NANYANG TECHNOLOGICAL UNIVERSITY

SYNTHESIS AND CHARACTERIZATION OF N-TYPE ORGANIC SEMICONDUCTORS AND THEIR POTENTIAL APPLICATIONS IN SOLAR CELLS AND SENSORS FOR SPORT

CHEN WANGQIAO

SCHOOL OF MATERIALS SCIENCE AND ENGINEERING

2016

SYNTHESIS AND CHARACTERIZATION OF N-TYPE ORGANIC SEMICONDUCTORS AND THEIR POTENTIAL APPLICATIONS IN SOLAR CELLS AND SENSORS FOR SPORT

CHEN WANGQIAO

SCHOOL OF MATERIALS SCIENCE AND ENGINEERING

A thesis submitted to the Nanyang Technological University
in partial fulfilment of the requirement for the degree of
Doctor of Philosophy

2016

Statement of Originality

I hereby certify that the work embodied in this thesis is the result of original research and has not been submitted for a higher degree to any other University or Institution.

.. . . . 30.09.2016 . . . .Chen wq . . . .
Date CHEN WANGQIAO

Abstract

During the past two decades, organic solar cells (OSCs) have attracted wide attention due to several advantages of light weight, low cost, easy processing and flexibility. Meanwhile, various usages of OSCs in wearable electronics recently imply the potential wide application of this technique in the area of sport. Growth of Power Conversion Efficiency of OSCs has reached higher than 10% for single junction OSCs mainly through design and synthesis of novel donors (p-type semiconductors materials), optimization of film morphology and device development. However, one lagging area is the development of novel electron acceptors (n-type semiconductors materials).

Nowadays, fullerene derivatives, such as $PC_{61}BM$ and $PC_{71}BM$, are still the dominant acceptors due to their superior charge transporting properties. However, these two acceptors suffer from some intrinsic shortcomings, such as high production cost, difficult functionalization and limited absorption etc. Therefore, developing novel acceptors that can overcome the above-mentioned disadvantages is highly desirable to obtain even higher PCE. In addition to the usage of n-type semiconductors in electronic materials, their usage in sensor is also important for providing novel materials to fulfill the rapid development of wearable sensor for in situ monitor. My Ph. D research, focusing on providing novel n-type semiconductors for OSCs and sensors, can be briefly divided into the following several parts.

Firstly, I focused on developing novel n-type building blocks for OSCs acceptors. By adopting the intramolecular double Friedel-Crafts-acylation (F-C acylation) method, various novel types of fused-heteroaromatic diones were obtained.

Secondly, I designed and synthesized two novel fullerene-based acceptors: TQMA and TQBA considering from the idea of increasing simultaneously the absorption and LUMO energy. Occupying the matched energy level and improved film morphology, acceptor TQMA exhibited best PCE of 2.8% with donor P3HT.

Thirdly, due to the toughness of functionalization for fullerene, I shifted the focus on developing other novel n-type semiconductor for non-fullerene acceptors. Considered that fullerene may have isotropic charge transport due to its 3D ball-like shape, I designed and synthesized a novel non-fullerene acceptor Me-PDI_4 with tetrahedral architecture based on PDI unit. It has complementary absorption with donor materials PBDTTT-C-T, amorphous film morphology and suitable energy level and exhibited moderate PCE of 2.73%.

Fourthly, I attempted to design and synthesize other novel n-type building block based on NDI. 1) I synthesized a novel NDI-core-extended building block NTI, which had single α thiophene vacant position for further transformation. Through coupling, I synthesized a series of NTI dimer and trimer, which showed not only good electron mobility, but also promising PCE about 2.5%. Further optimization elevated the value to 7%. 2) Through one-step simple thionation of NDI, I synthesized a series of S-NDI compounds with enhanced absorption and mobility as well as adjustable LUMO energy level. Although the PCE is not so promising, this method provides a useful way for further OSCs acceptor development.

Finally, I designed and synthesized a K^+ probe TM-1 based on n-type materials naphthalimide and 1-aza-18-crown-6 effectively within four steps. Interestingly, with different excited wavelength, it had different emission spectrum. The probing ability of TM-1 to K^+ ion was studied.

In conclusion, in this thesis, several n-type semiconductors for OSCs acceptors based on fullerene or non-fullerene materials have been designed and synthesized. Their photovoltaic properties were also investigated in depth. These works contributed, to some extent, to the development of the OSCs from the viewpoints of materials synthesis and methods innovations. In addition, n-type semiconductor used for sensor in this thesis also provides an alternative perspective to design novel sensor in the future.

Acknowledgements

The author would firstly acknowledge the scholarship from MSE and Institute for Sports Research (ISR) for financial support for the 4 years Ph. D study in NTU.
The author would like to take this opportunity to thank greatly his supervisor, Assoc. Prof. Qichun Zhang. His humble personality, broad knowledge, cutting-edge ideas and strict attitude to experimental result deeply impress me and will affect my academic career in the future.

The author would like to thank Prof. Chen Yongsheng in Nankai Univeristy, who gives us huge help in device fabrication and optimization.
The author would like to express special acknowledgements to Prof. Kazuo Takimiya, in RIKEN, Wako, Japan for giving me an internship chance to feel the difference research culture and group management.

The author would like to thank former Post Doc. Dr. Gang Li, Dr. Jianfeng Zhao, Dr Junkuo Gao, Dr Junbo Li et al for their kind assistance and discussion in daily lab work.

The author would like to thank Dr. Peiyang Gu, Dr. Weiwei Xiong, Dr.Guankui Long, Dr. Kaiqi Ye, Dr. Jiansheng Wu, Dr. Yi Zhou, Dr. Jun Zhao, Dr. Guodong Zhang, Dr. Liang Xu, Dr. Cui-e Zhao, Mrs. Li'na Nie, Mr. Bin Gu, Mr. Zilong Wang, Mr. Jian Xie and other group members for their valuable help and discussion.

He would like to acknowledge all the friends and colleagues who have helped in any way during his Ph. D. candidate. Finally, the author would like to my family members, who always support me in this four years.

Table of Contents

Table Captions

Scheme Captains

Figure Captions

Abbreviations

A	Acceptor
Al	Aluminium
BHJ	Bulk Hetero-Junction
CB	Chlorobenzene
CC	Column Chromatography
CE	Counter Electrode
CV	Cyclic Voltammetry
o-DCB	*o*-Dichlorobenzene
DCM	Dichloromethylene
Donor	D
DSC	Differential Scanning Calorimetry
$E_{p,a}$	Anodic Peak Potential
$E_{p,c}$	Cathodic Peak Potential
EA	Elemental Analysis
F-C	Friedel–Crafts
EQE	External Quantum Efficiency
FF	Fill Factor
HOMO	Highest Occupied Molecular Orbital
I_{sc}	Short Circuit Current
ITO	Indium Tin Oxide
I-V	Current-Voltage
LUMO	Lowest Unoccupied Molecular Orbital
MALDI-TOF	Matrix Assisted Laser Desorption Ionization-Time of Flight
MS	Mass Spectrum
NA	As-cast/Non Annealing
NDI	Naphthalene Diimides
NMR	Nuclear Magnetic Resonance
OSCs	Organic Solar Cells
OFET	Organic Field-Effect Transistor

OTFT	Organic Thin Film Transistor
P3HT	Poly(3-hexylthiophene-2,5-diyl)
$PC_{61}BM$	Phenyl-C61-Butyric Acid Methyl Ester
PE	Petroleum Ether
$PC_{71}BM$	Phenyl-C71-Butyric Acid Methyl Ester
PCE	Power Conversion Efficiency
PDI	Perylene Diimide
PEDOT:PSS	Poly(3,4-ethylenedioxythiophene):poly(styrenesulfonate
PXRD	Powder X-ray Diffraction
RE	Reference Electrode
TA	Thermally Annealing
TEM	Transmission Electron Microscopy
TGA	Thermogravimetric Analysis
UV	Ultraviolet Visible
V_{oc}	Open Circuit Voltage
WE	Working Electrode
XRD	X-ray Diffraction

Chapter 1

Introduction

In this chapter, the backgrounds of n-type semiconductor materials for OSCs acceptors as well as sensors are elaborated. Due to the difficult functionalization, air instability as well as the high cost of the known fullerene acceptor and extremely complex structure of probe for K^+, it is imperative to design and synthesize novel efficient and effective alternative n-type materials to solve the above-mentioned problems. The hypothesis is based on that through modification of the known efficient n-type building blocks (also fluorophore), such as PDI or NTI, some ideal target molecules can be obtained and subsequently the rational ideas verifying the hypothesis are exhibited. In addition, overview of the structure for this thesis is described as followed: firstly introduction, literature reviews and experimental methodology; secondly, the main discoveries during the Ph.D candidate period; finally, the summaries and future works. In the last part of this chapter, the main outcomes of research are briefly elaborated.

1.1 Hypothesis/Problem Statement

Fossil fuels, such as petroleum, coal and natural gas, are used widely in our daily life but contribute greatly to the environment pollution and global warming. Thus, scientists are trying to find alternative clean and efficient energy sources to replace the fossil fuels. Among all the new developed sources, solar energy, as a clean and renewable energy, provides a perfect solution to the present problem. Although commercially available silicon solar cells can show Power Conversion Efficiency (PCE) higher than 20%,[1] the energy production costs of such solar cells are still too high when compared with the energy cost to produce fossil fuels, which motivates us to find other kinds of low cost solar cells.

Table 1.1.1 Estimated cost for different OSCs technologies

Technology	Energy for production [M] W p^{-1}	CO_2 footprint [gr. CO_2 eq. W p^{-1}]	Energy payback time [years]
Flex OSCs	2.4	132	0.19
CdTe	9.5	542	0.75
mc-Si	24.9	1293	1.95
CIS	34.6	2231	2.71

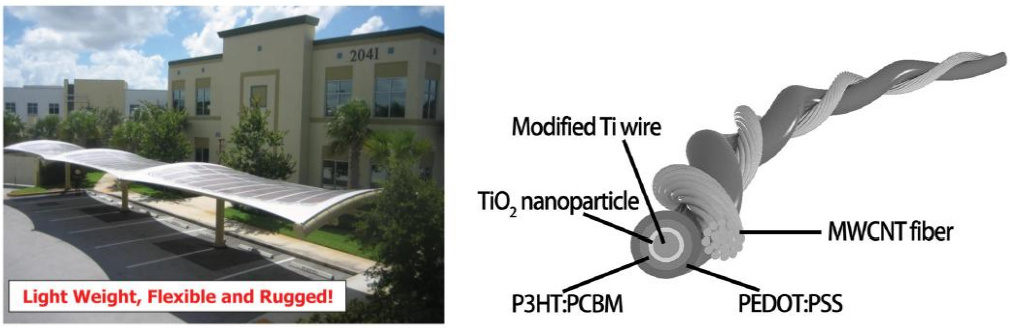

Fig. 1.1.1 Advantages of flexible OSCs

During the past two decades, compared with other solar cell technologies, OSCs (Organic Solar Cells) have attracted wide attention due to several advantages of light weight, low cost, easy process and flexibility[2-4](**Table 1.1.1** and **Fig.1.1.1**). In addition, the usage of OSCs in wearable electronics/fiber implies the potential wide application of this

technique, e.g. in sport. Generally speaking, an OSC device is a sandwiched structure in which there are two electrodes on the upper and bottom layers respectively. In the middle is the active layer consisting of donor (p-type semiconductor) and acceptor (n-type semiconductor) materials. In addition, the device also has both electron-transporting and hole-transporting layers. By designing and exploiting of novel donor/acceptor materials for the active layer and finding more efficient electron and hole transporting materials[5] as well as morphology optimization,[6] PCE increased gradually in the past decades. Especially in recent several years, the single junction OSCs have reached 10%,[7] thanks to the great contribution from development of the novel p-type semiconductor donor materials with broad light absorptions, low band gaps, high hole mobilities and finely-tuned electronic energy levels.[8-11] These achievements strongly encourage scientists to push the PCE into higher level. However, one lagging area is the development of novel n-type semiconductor electron acceptors. Especially, the rapid development of wearable electronics requires providing more and more efficient novel n-type materials.

Nowadays, almost all the efficient OSCs systems still adopt fullerene derivatives $PC_{61}BM$ and $PC_{71}BM$ as the electron acceptors due to their superior charge transporting properties. Nevertheless, this kind of acceptor also suffers from some intrinsic shortcomings, such as high production cost, difficulty in functionalization, and limited absorption of sunlight.[7] Therefore, developing novel acceptors, which can not only overcome the above-mentioned issues, but also mimic the electron transporting behavior of fullerene, is highly desirable. Moreover, n-type semiconductor materials can also be used in other optical fields. For example, progress in designing and synthesizing an efficient K^+ probe has been very slow over the past two decades and an efficient K^+ probe based on an organic semiconductor fluorophore has not been achieved yet.

Thus, the works in this dissertation are based on the several following hypothesis:

1) n-type building blocks are extremely important for the development of various organic functional materials. For example, the development of fullerene-based OSCs acceptor should benefit from the early discovery of the C_{60}. PDI building blocks have long been

demonstrated as powerful units for design and synthesis of various OSCs and OFETs materials. Given this point, a method to synthesize novel n-type diones-based building blocks is elaborated in this thesis.

2) Fullerene has been the dominant acceptor used in OSCs. In the past decade, bis-functionalization of fullerene to increase the LUMO energy level and the introduction of absorption groups to improve the J_{sc} have been proven as effective methods to obtain modified fullerene acceptors. What will be the OSCs performance for fullerene acceptors that possess two absorbing groups attached to the C_{60}? Two fullerene-based acceptors are designed and synthesized to test this hypothesis.

3) PDI has been proven as an effective building block for non-fullerene acceptor with a planar structure. For fullerene, it has been proven that the superior electron mobility can be partially ascribed to the ball-like configuration. What will be the OSCs performance for non-fullerene acceptor by combining PDI with a 3D configuration structure? A 3D non-fullerene acceptor Me-PDI_4 is designed and synthesized and its OSCs performance is demonstrated in this thesis.

4) NDI is another promising n-type material. Modification of NDI should provide an interesting building block for non-fullerene acceptors development. This hypothesis was tested by designing and synthesizing two NDI derivatives: NTI and S-NDI in this thesis.

5) Naphthalimide is a very interesting n-type organic building block and has been extensively adopted in various sensors. On the other hand, 1-aza-18-crown-6 is an effective response unit for K^+ ion. Thus, a sensor with a combination of these two building blocks may provide interesting results for K^+ probe.

1.2 Objectives and Scope

The motivation of this project is to design and synthesize novel n-type OSCs acceptors based on fullerene or non-fullerene materials to compete or even replace the standard OSCs acceptor PCBM and to improve the PCE eventually. Meanwhile, we will observe

the aspects that will have influence on the performance of OSCs and study the structure-property relationships between molecules and their performance. Moreover, designing and synthesizing K^+ probe has been an extremely difficult project over the past two decades and finding an efficient K^+ probe is still highly desirable.
The specific objectives are

(1) To design, synthesize and characterize novel fullerene-based acceptors or non-fullerene acceptors and investigate their OSCs performance.

(2) To investigate how the structure and the film morphology will affect the OSCs performance.

(3) To design and synthesize a novel K^+ probe based on n-type semiconductor materials naphthalimide.

1.3 Dissertation Overview

The thesis mainly focused on addressing the issue to develop n-type organic semiconductor building blocks, fullerene-based molecules and non-fullerene based molecules for OSCs acceptors.

Chapter 1 provides the rationality why we choose the OSCs acceptors as our research and the problem is carefully elaborated, then, the hypothesis was proposed. Secondly, the motivation and the object for the project were listed. Thirdly, the overview of the dissertation was briefly introduced. Finally, the finding/outcomes and originalities were emphasized.

Chapter 2 reviews the literature concerning the history of development of acceptors for organic solar cells. This chapter is mainly divided into two parts: the first part is the basic parameters regarding to the OSCs and the second part elaborates the development of the OSCs acceptors based on fullerene and non-fullerene compounds. Compared with fullerene acceptors, non-fullerene acceptors had a rapid progress in the past several years

from 2012 and I classify this section according to the main electron-efficient building blocks in the non-fullerene acceptors, such as PDI, NDI, DPP, etc.

Chapter 3 introduces the synthetic methods to prepare the desired molecules, the separation methods to purify them, the basic characterization techniques to confirm their structures and finally other technologies to elaborate the property performance for these novel molecules. For all the above-mentioned methods or technique, their basic procedures or principles are further explained through some examples.

Chapter 4 elaborates the design and synthesis of various novel building blocks containing fused heteroaromatic diones through one-step simple intramolecular double F–C acylation reaction. Different substrates ranging from simple bifuran, bipyrrole, bithiophene and biselenophene to more complex bibenzofuran, bibenzoindole and bibenzothiophene were studied. Their substrates give the desired products with 16%–85% yields.

Chapter 5 summarizes the design and synthesis of two novel C_{60} derivative acceptors monoadduct TQMA and bisadduct TQBA based on 2,3-bis(5-tert-butylthiophen-2-yl)-6,7-dimethylquinoxaline in aim to increase the absorption spectrum and V_{oc} of the device. Their physiochemical properties and the subsequent photovoltaic performance have been fully investigated. Optimized device by taking P3HT as donor and TQMA as acceptor exhibits the best PCE value of 2.8% with a V_{oc} of 0.76 V, which is about 0.12 V higher than that of $PC_{61}BM$ while TQBA display much poor PCE result due to the poor morphology.

Chapter 6 describes the design and synthesis of a novel 3D non-fullerene acceptor Me-PDI_4 with tetrahedral architecture based on PDI unit. The physiochemical properties were investigated. Solution-processed OSCs adopting Me-PDI_4 as the acceptor exhibited best PCE value of 2.73% at the optimized condition with inverted device structure. Our result indicates that design of 3D configuration of non-fullerene acceptor may be an alternative method to improve the OSCs performance in the future.

Chapter 7 elaborates the design and synthesis of a novel building block named naphtho[2,3-b]thiophenediimide (NTI) based on π-extended NDI unit. Taking advantage of the mono-functionalizeability of the NTI unit at the thiophene α-position, a simple NTI dimer and a trimer with a benzene core were synthesized and exhibited promising electron mobility up to 0.45 $cm^2V^{-1}S^{-1}$. and OSCs performance of 2.5% in the initial measurement.

Chapter 8 presents the design and synthesis of S-NDI compounds through one step thionation reaction by LR (Lawesson's Reagent). It's found out that after thionation, the sulfur substituted NDI has gradually red-shift absorption and the decreased LUMO energy level. In addition, the electron mobility increased simultaneously. Finally, the OSCs based on these materials as non-fullerene acceptor have been studied. However, the results are far away from expectations. From the morphology analysis through AFM, the large crystalline domain might account for that.

Chapter 9 elaborates the design and synthesis of a K^+ probe TM-1 based on naphthalimide building block and 1-aza-18-crown-6 within four steps. Interestingly, with different excited wavelength, this probe exhibited different emission spectrum. Although it turned out that this probe has weak response to K^+ in sweat, the other components in sweat, such as lactic acid, urea and Na^+, were proven to have no influence on this probe. It is inferred that the low efficiency for probing K^+ might result from the low steric effect and further improvement of the probe is underway.

Chapter 10 firstly summarizes the whole work in this dissertation. Secondly, I discuss the extent to which the hypothesis was proven/unproven as well as the reached/unreached targets. Finally, I propose the opportunities and the idea for the future works.

1.4 Findings and Outcomes/Originality

This research led to several novel outcomes indicated as following:

1. A concise and efficient method is discovered to synthesize n-type building block heteroaromatic diones through only one-step F-C reaction, which can be further transferred into other functionalized materials.

2. Designed and synthesized several novel OSCs acceptors based on fullerene and non-fullerene materials. Their basic physicochemical properties and photovoltaics properties were investigated deeply. It was found that the absorption range, the energy level, the electron mobility and more importantly, the morphology all played crucial effect on the final PCE result for the device. An extremely amorphous film or crystallaine film all brought negative effects on the device. In addition, as well as the reported NDI and PDI building blocks, another interesting building block NTI was developed in this thesis.

3. Due to the extremely complex synthetic route for the reported K^+ probes, design and preparation of novel K^+ probe with efficient synthetic route is highly desirable. In this thesis was designed and synthesized a novel K^+ probe based on n-type materials naphthalene within four steps and its response to potassium ions was investigated.

References

[1] M. A. Green, K. Emery, Y. Hishikawa, W. Warta and E. D. Dunlop, *Prog. Photovoltaics*, **2012**, 20, 12-20.

[2] S. Gunes, H. Neugebauer and N. S. Sariciftci, *Chem. Rev.*, **2007**, 107, 1324-1338.

[3] B. C. Thompson and J. M. J. Frechet, *Angew. Chem. Int. Edit.*, **2008**, 47, 58-77.

[4] A. L. Roes, E. A. Alsema, K. Blok and M. K. Patel, *Prog. Photovoltaics*, **2009**, 17, 372-393.

[5] R. Po, C. Carbonera, A. Bernardi and N. Camaioni, *Energ. Environ. Sci.*, **2011**, 4, 285-310.

[6] M. T. Dang, L. Hirsch, G. Wantz and J. D. Wuest, *Chem. Rev.*, **2013**, 113, 3734-3765.

[7] M. D. Linnik, J. Z. Hu, K. R. Heilbrunn, V. Strand, F. L. Hurley, T. Joh and L. I. Consortium, *Arthritis Rheum.*, **2005**, 52, 1129-1137.

[8] C. E. Small, S. Chen, J. Subbiah, C. M. Amb, S. W. Tsang, T. H. Lai, J. R. Reynolds and F. So, *Nat. Photonics*, **2012**, 6, 115-120.

[9] L. T. Dou, J. B. You, J. Yang, C. C. Chen, Y. J. He, S. Murase, T. Moriarty, K. Emery, G. Li and Y. Yang, *Nat. Photonics*, **2012**, 6, 180-185.

[10] J. Y. Zhou, X. J. Wan, Y. S. Liu, Y. Zuo, Z. Li, G. R. He, G. K. Long, W. Ni, C. X. Li, X. C. Su and Y. S. Chen, *J. Am. Chem. Soc.*, **2012**, 134, 16345-16351.

[11] H. J. Son, W. Wang, T. Xu, Y. Y. Liang, Y. E. Wu, G. Li and L. P. Yu, *J. Am. Chem. Soc.*, **2011**, 133, 1885-1894.

Chapter 2

Literature Review

To have a better understanding of the development history of the OSC acceptors, this chapter is mainly divided into two parts: the first part introduces the basic parameters regarding to the OSCs and the second part elaborates the development of the OSCs acceptors based on fullerene and non-fullerene. Compared with fullerene acceptors, non-fullerene acceptors have a rapid progress in the past several years from 2012 and they can be classified according to the main electron-deficient building blocks such as PDI, NDI, DPP. In addition, the history of development of sensors for K^+ is also briefly elaborated. Due to the difficult modification, air degradation issues as well as high cost of the known fullerene acceptors, unsatisfactory PCE performance for most non-fullerene acceptors and extremely complex structure of probes for K^+, it is still imperative to design and synthesize novel efficient and effective alternative n-type materials to solve the above-mentioned problems.

2.1 Overview

2.1.1 Basic principle of OSCs and device structure

As displayed in **Fig. 2.1.1.1**, an OSCs device is normally a sandwiched structure in which there is one low work function Al metal electrode on the top of the device and another transparent ITO electrode on the bottom of the device connecting with the glass substrate. In the middle of the structure is the active layer that typically consists of π-conjugated polymers/small molecules as donor materials and fullerene-based or non-fullerene compounds as acceptor materials. PEDOT: PSS is utilized as a hole transporting layer. Within the active layer, the heterojunction structure contains the donor and acceptor materials that absorb the solar irradiation to create excitons, which diffuse to the Donor-Acceptor (D-A) interface, and then dissociate into free holes and electrons. Once separation of the electrons and holes has occurred, the built in potential will cause these holes and electrons to pass through the pathways formed in the BHJ donor and acceptor blended films to the cathodes and anode, respectively. Finally, they are collected on the corresponding electrodes, generating the current that enters the outer circuit.[1]

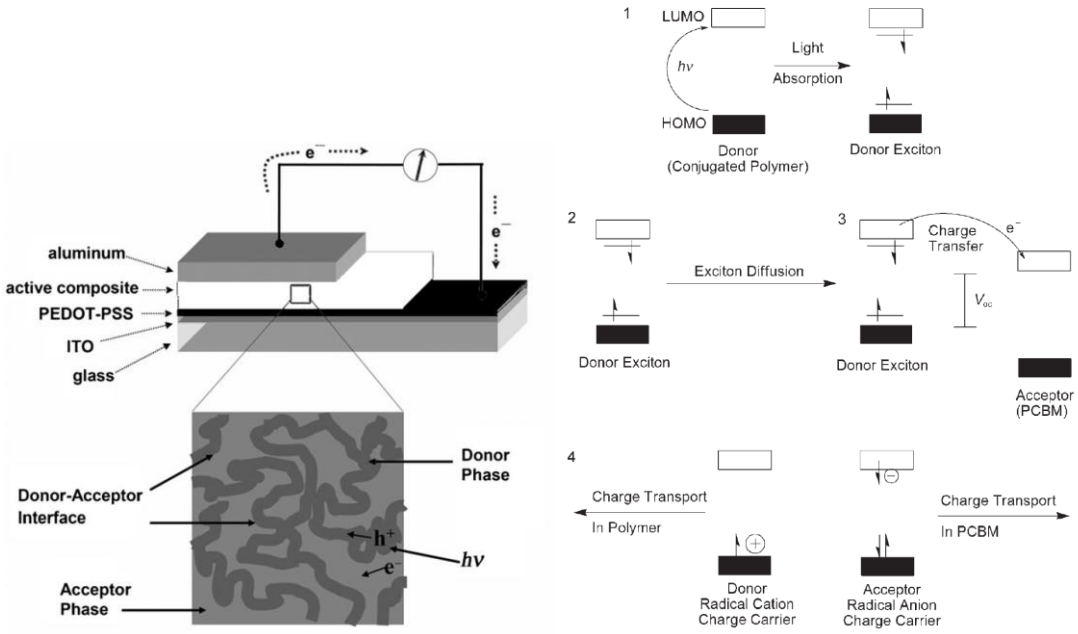

Fig. 2.1.1.1 Diagrams for the device structure and photo energy conversion in OSCs (Reproduced from Ref. 1)

D-A heterojunctions structures can be simply classified into two main types of architectures: bilayer heterojunctions[2] and bulk heterojunctions (BHJ).[3](**Fig. 2.1.1.2**) For **Fig.2.1.1.1**, the formed excitons must diffuse into the D/A interface area firstly and afterwards can be dissociated into the electrons and holes to form the electricity. Therefore, the diffusion distance and the D-A contacting interface area are two significant factors that affect the final PCE performance. For the bilayer heterojunction, there is only limited interface area between the planar donor and acceptor layers. In addition, only the excitons within 5-20 nm of the D/A interface area have chance to form the current eventually.[4] The excitons formed farther than 20 nm away will quench to the ground state again before they reach the D/A interface due to the long diffusion distance. Thus, the OSCs performance for bilayer heterojunctions is seriously limited due to these two disadvantages. To improve this situation, the BHJ structure was developed. Compared with the bilayer heterojunction structure, D/A interface area in the BHJ structure increases dramatically due to the interpenetrating and bicontinuous configuration within donor and acceptor blend films, which will be beneficial for the dissociation of the excitons. In addition, the phase separation in BHJ structure is much improved due to the nanoscale network, which provides more pathways shorter than 5-20 nm for the diffusion. Therefore, BHJ structure exhibits better OSC performance and is used prevalently in OSCs.

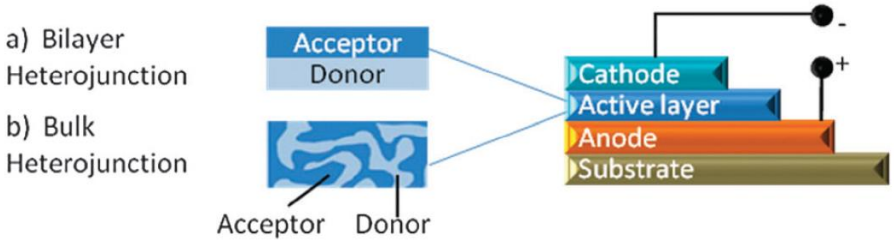

Fig. 2.1.1.2 Architectures of the OSCs device structures: a) bilayer heterojunction; b) BHJ (Reproduced from ref: *Chem. Soc. Rev.*, **2012**, *41*, 4245)

2.1.2 Basic parameters regarding to OSCs

A typical *J*-*V* curve for a OSCs device is shown in **Fig. 2.1.2.1**.

(a) $\boldsymbol{I_{SC}}$: The short circuit current (I_{sc}) is the maximum current that the device reaches when the voltage is zero. I_{sc} is affected by several factors, such as the number of photons

absorbed/photoexcitations, the quantum efficiency for charge separation and the transport ability of the charge carriers within the material. Generally speaking, a broad absorption spectrum is advantageous to harvest as large as amount of the photons from the sun fraction as possible.

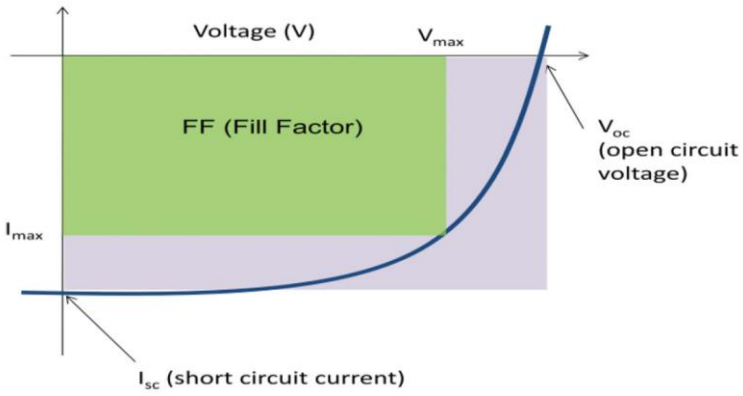

Fig. 2.1.2.1 *J-V* curve for current density vs. voltage (reproduced from ref: *Adv. Mater.*, **2014**, *26*, 10)

(b) $\boldsymbol{V_{oc}}$: Open circuit voltage (V_{oc}) is the maximum voltage exhibited by OSCs device when there is no flow of current. V_{oc} is determined by the difference in the quasi-Fermi levels of the phase separated donor and acceptor domains as sketched below. The third term in Equation 1 below arises from the temperature dependence of the quasi-Fermi levels. The open circuit voltage is given by Equation 1 (see **Fig. 2.1.2.2**):

$$V_{OC} \approx E_{\text{fullerene(LUMO)}} + E_{\text{polymer (HOMO)}} + k_B/e\{\ln (n_e n_h / N_c^2)\} \quad (1)$$

where n_e and n_h are the electron and hole densities, respectively; and N_c is the corresponding density of states near the acceptor LUMO energy and the donor HOMO, assumed to be equal for simplicity. This equation was initially verified by correlating the difference between HOMOs of the donor materials and LUMOs of the acceptor materials in BHJ solar cells fabricated with 26 different donor polymers.[5] However, the excellent correlation required the addition of an additional 0.3 eV of unknown origin. As shown by Cowen et al.,[6] the "mysterious" 0.3 eV results directly from the third term in Equation 1 . In principle, V_{oc} can be increased by the difference in work functions of the anode and cathode. However, the use of interlayers (electron transport/hole blocking and hole

transport/electron blocking) tends to decouple the V_{oc} from the difference in the anode and cathode work functions.

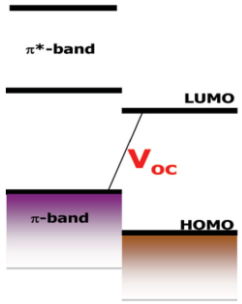

Fig. 2.1.2.2 Diagram for the origin of the V_{oc} in OSCs (reproduced from ref: *Adv. Mater.*, **2014**, *26*, 10)

(c) **FF**: the fill factor (FF) is the ratio between the green and the gray areas in **Fig. 2.1.2.1.** The FF is determined by the competition between sweep-out of the photogenerated carriers and the recombination of carriers to the ground state.

The maximum power generated in the external circuit is the product of the following three:

$\boldsymbol{P}$ **max =** $\boldsymbol{I_{sc}}$ $\boldsymbol{V_{oc}}$ **FF/** Power (solar in) (2) The incident light power is usually standardized to be equivalent to AM 1.5 solar spectrum (i.e., the spectrum of the solar radiation received on the surface of the earth 100 mW/cm^2).

2.1.3 OSCs acceptors based on fullerenes and their derivatives

Fullerene based compounds are among the earliest used n-type semiconductor OSCs acceptors for both the bilayer hetero-junction and BHJ device structures. These acceptors have several superior advantages to be acceptors:

Firstly of all, their suitable electron affinities enable them to have the strong inclination to receive the electrons from donor materials.

Secondly, these acceptors can form favorable morphologies with nanoscale networks upon mixing with donor materials, which facilities the transportation and dissociation of the electrons and holes and contributes to an improved OSCs performance.

In 1985, Kroto and his coworkers discovered the ball-like compound C_{60}.[7a] Compared with the planar structure compounds, C_{60} has a spherical shape with 12 pentagons and 20

hexagons all containing C=C double bonds, which facilitates superior isotropic electron accepting and transporting ability. Thus, it is expected that C_{60} is a good acceptor matching with donor materials. One disadvantage of C_{60} is that it has poor absorption in the visible range due to its high symmetric configuration that makes the lowest-energy transitions formally dipole forbidden.[7b] Later on, to overcome this limitation, the analogous compound C_{70} was also developed and due to its lower symmetry to relax some forbidden transition, it had much improved absorption in the long-wavelength part of spectrum.[7b] Leo and coworkers used C_{60} and C_{70} in the OSCs device with donor material ZnPc, obtaining PCEs of 2.27% and 2.87%, respectively. It has been found that the 25% improvement in device performance from C_{60} to C_{70} can be attributed to an increase in the J_{sc} (from 7.52 to 9.88 mA/cm^2) due to improved absorption of C_{70} as compared to C_{60}.(**Fig. 2.1.3.1**)

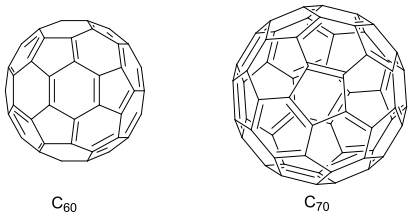

Fig. 2.1.3.1 Structures of C_{60} and C_{70}

The poor solubility of C_{60} as well as C_{70} in most organic solvents limits their wide application in organic electronics and various soluble groups were designed and connected onto them to increase their solubility. The $PC_{61}BM$, which containing a phenyl and butyric acid methyl ester, was synthesized and applied in photophysical studies by Hummelen and his coworkers toward amelioration of photo-induced electron transfer efficiencies in the photo-diodes and photo-detectors devices.[8] (**Fig. 2.1.3.2)** It was found out that $PC_{61}BM$ exhibits much better solubility for most organic solvents than its precursor C_{60}. In 1995, Yu and his coworkers investigated the OSCs performance of taking $PC_{61}BM$ as acceptor material and the conjugated polymer MEH-PPV as donor material employing the breakthrough concept of BHJ.[3] Afterwards, $PC_{61}BM$ became more and more prevalent as the acceptor in OSCs. However, there are several limitations associated with $PC_{61}BM$ compound: a) $PC_{61}BM$ has poor absorption in the visible region due to the highly symmetric ball-like structure of C_{60}, b) the LUMO energy level of $PC_{61}BM$ is relatively low especially which may lead to V_{oc} loss in OSCs when it is

blended with conjugated donor with a high HOMO energy level and further limit the PCE performance.

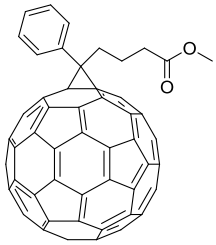

$PC_{61}BM$

Fig. 2.1.3.2 Structure of $PC_{61}BM$

Regarding to the above limitations, there are two main ways to solve them. The first way is to improve the visible absorption of acceptors. Wienk and his coworkers designed and synthesized the analogous compound $PC_{71}BM$ that possesses better absorption than $PC_{61}BM$ between 400 and 700 nm.[9] Since then, $PC_{61}BM$ and $PC_{71}BM$ have been widely used in the fabrication of BHJ OSCs and generally speaking, the BHJ OSCs based on $PC_{71}BM$ have higher PCE performance than $PC_{61}BM$. Adopting the same idea, Sharma and coworkers designed and synthesized a novel fullerene-based acceptor **F** with an absorption group cyanostilbenzene containing two electron-withdrawing groups –CN and $–NO_2$. It is demonstrated that this novel acceptor F exhibited enhanced absorption compared with $PC_{61}BM$ while at the same time, its solubility remains good in common organic solvents. After optimizing device fabrication conditions, the best PCE value for F by taking P3HT as donor can be up to 5.3%. (**Fig. 2.1.3.3**)

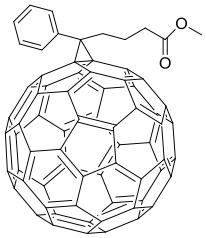

$PC_{71}BM$

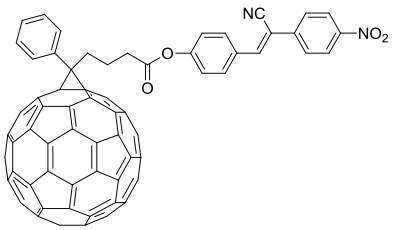

F

Fig. 2.1.3.3 Structures of $PC_{71}BM$ and **F**

The second way is multi-functionalization of C_{60}. (**Fig. 2.1.3.4**) For example, by adding one more phenyl and butyric acid methyl ester group on the $PC_{61}BM$, a novel bis-adducted fullerene based acceptor bis-$PC_{61}BM$ was designed and synthesized by the

Blom group.[10] It was discovered that the LUMO energy level of this acceptor was 0.1 V higher than that of $PC_{61}BM$ through CV measurements. More importantly, by taking P3HT as the donor material, bis-adduct PCBM displayed a PCE of 4.5% compared to 3.8% obtained with $PC_{61}BM$, which was ascribed to the increase of the V_{oc} value (from 0.58 V to 0.74). Later on, following this method, Li and coworkers also developed two novel fullerene acceptors by adding indene unit on the C_{60}, indene-C_{60} bisadducted ($IC_{60}BA$)[11, 12] and indene-C_{70} bisadducted ($IC_{70}BA$),[13, 14] which exhibited LUMO value up-shifted by 0.17 and 0.19 eV, respectively, compared with $PC_{61}BM$ and $PC_{71}BM$. Still using P3HT as the donor materials, these two acceptors all displayed high PCE values up to 6.55% and 5.64% respectively (For comparison, 3.8% PCE for $PC_{61}BM$) with the high *Voc* value of 0.84 eV, which was 0.26 V higher than that of the devices using $PC_{61}BM$ as acceptor (0.58 V). [11, 13]

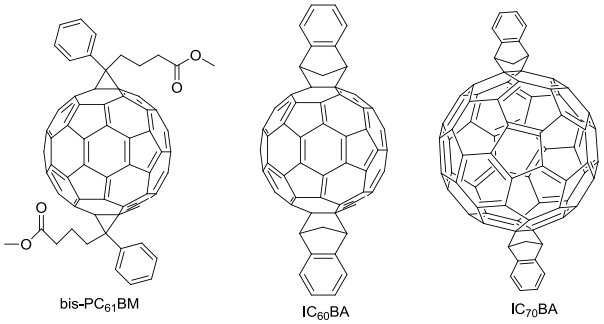

Fig. 2.1.3.4 Structures of bis-$PC_{61}BM$, $IC_{60}BA$ and $IC_{70}BA$

During the past decades, fullerene-based acceptors have achieved great success in parallel to the boost development of highly efficient donor materials and especially for $PC_{61}CM$ and $PC_{71}BM$, they are the predominant acceptors used in OSCs. Although other strategies such as increasing the LUMO energy of fullerene through multiple-functionalization or increasing the absorption through introducing different absorption groups were also designed, investigated and proved effectively with donor P3HT. Their status still can't surpass that of $PC_{61}BM$ and $PC_{71}BM$. At the same time, non-fullerene n-type semiconductor acceptors also attracted much attention due to the versatility of the building blocks and easy modification of these non-fullerene acceptors.

2.1.4 OSCs acceptors based on non-fullerenes

Before the intense study of the non-fullerene acceptors, various efficient n-type organic materials with high electron mobility have been developed and utilized in OFETs. Therefore, these materials were also borrowed and utilized to design and synthesize the non-fullerene acceptors for OSCs by some researchers. Rylene diimides compounds, such as PDI and NDI, have attracted broad interest and employed as the early building blocks for developing non-fullerene acceptors because they possess several superior advantages: [15]

1) Excellent photo-stability and absorption spectrum
2) Suitable HOMO and LUMO energies level, similar to that of Fullerene.
3) High electron mobilities and affinities.

More importantly, it is very difficult to synthesize or modify the fullerene-based acceptor. For these PDI and NDI compounds, all of the above-mentioned three merits can be tuned readily through different modifications. The detailed examples will be discussed in the following text.

2.1.4.1 Perylenediimide (PDI) acceptors

PDI based compounds are investigated earliest as non-fullerene acceptors used in OSCs. Simply by the addition of two 1,2-diamine benzene group onto the PDI plane, a large conjugated molecule with extremely insolubility **PDI-1** was synthesized. (**Fig. 2.1.4.1.1**) Tang did the pioneer working by fabricating this non-fullerene acceptor into the bilayer heterojunction OSCs device through vacuum deposition method, yielding a PCE performance of 0.95% by taking CuPc as the donor material.[2] This value increased to 1.3% when the donor material was changed to ZnPc.[16]

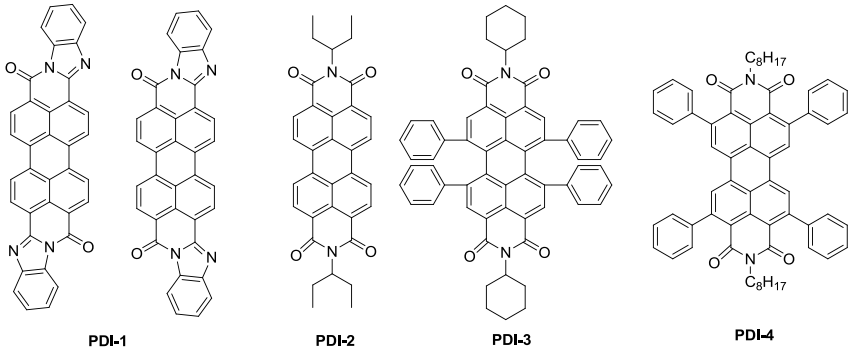

Fig. 2.1.4.1.1 Structures of **PDI-1**, **PDI-2**, **PDI-3** and **PDI-4**

In 2013, by combining the donor p-DTE($FBTTH_2$)$_2$ and **PDI-2**, a PCE up to 3% was obtained by Bazan and his coworkers, which was among the best results for mono-PDI acceptor at that time.[17] However, due to the strong tendency for π–π stacking between PDI molecules resulting from their large planar conjugation structure, it is easy for them to form large aggregates in the film, facilitating the recombination of the excitons and deteriorating in the PCE performance. To solve this problem, Sun and his coworkers recently reported acceptor **PDI-3** with 1,6,7,12-tetraphenyl groups. Interestingly, they found that the absorption spectra of this acceptor in solution and in neat film were very similar to each other, which indicated that the aggregation behavior was significantly suppressed by introducing the phenyl groups and a cyclohexyl group onto the nitrogen atom. After blending with the donor polymer PTB7-Th as well as taking 1% chloronaphthalene (CN) as the solvent additive, **PDI-3** could exhibit a PCE value of 4%.[18] With a very similar structure, Wasielewski and coworkers developed another efficient acceptor **PDI-4** by placing the four phenyl groups onto the 2, 5, 8 and 12-positions. Surprisingly, this acceptor exhibited a very high V_{oc} value of 1.0V, which contributed to an excellent PCE performance of which 3.7%. They demonstrated that the molecular strategy: formation of slip-stacking of the PDI unit is crucial to prevent the coupling necessary for rapid excimer formation.[19]

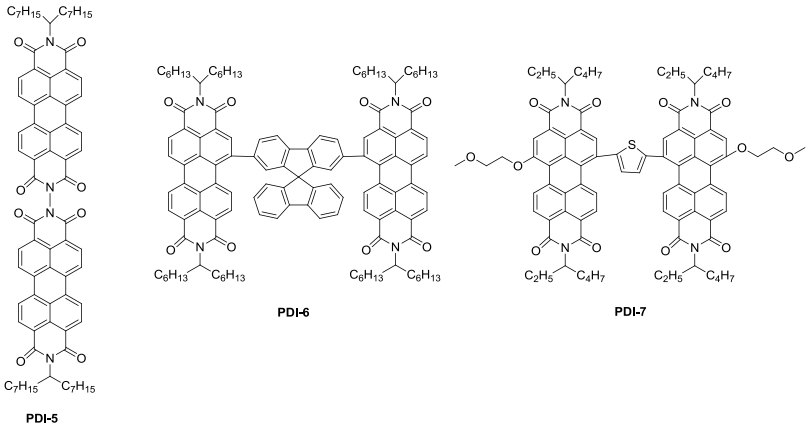

Fig. 2.1.4.1.2 Structures of **PDI-5**, **PDI-6**, **PDI-7**

From the above discussion, acceptors based on mono-PDI ordinarily display low PCE results < 5% and this makes researchers switch to other non-fullerene acceptors built from multiple PDI units. Dimeric PDI with twisted conformation was designed and synthesized since it can not only reduce the aggregation tendency, but also guarantee the

soluble process of the device. Generally speaking, there are two ways to construct the twisted PDI dimmers: one is to connect two PDI monomers through the nitrogen atom on the imide group and the other one is to form PDI bridged through the bay position as shown in **Fig. 2.1.4.1.2**, In 2012, Narayan and his coworkers reported pioneering work on acceptor PDI dimer **PDI-5**, in which two PDI units were connected through the N atoms on the imide groups. They illustrated that the usage of donor material PBDTTT-C-T could afford a PCE value around 2.8%, which is about 20-time higher than the PCE (0.13%) of a controlled group based on a planar mono-PDI. In their work, they demonstrated effectively that disrupting the crystallinity without adversely impacting the charge-transfer properties of PDIs was an important design principle.[20] In 2013, Zhao, Pei and their coworkers reported a PDI dimer acceptor **PDI-6** with spirobifluorene linkers in the bay positions. They also introduced other linkers such as thiophene, phenyl etc and investigated their PCE performance with donor P3HT. It turned out that the device based on **PDI-6** showed the best PCE of 2.3%, which they ascribed to the suppression of self-aggregation of PDI units by the non-planar, 3D twisted structure.[21] Almost at the same time, Yao and his coworkers reported a similar structure acceptor **PDI-7** with thiophene as the linker and two 2-methoxyethoxyl groups as the solubilising groups. By using the polymer donor PBDTTT-C-T, the device showed PCE of 4.03%, which was the best OSCs system based on non-fullerene system at that time.[22] Later, the PCE reached 6.1% for the same system by using the solvent vapor annealing (SVA) method. The authors ascribed them to the improved molecular organization and the reduced excition recombination due to slow evaporation of the host solvent.[23]

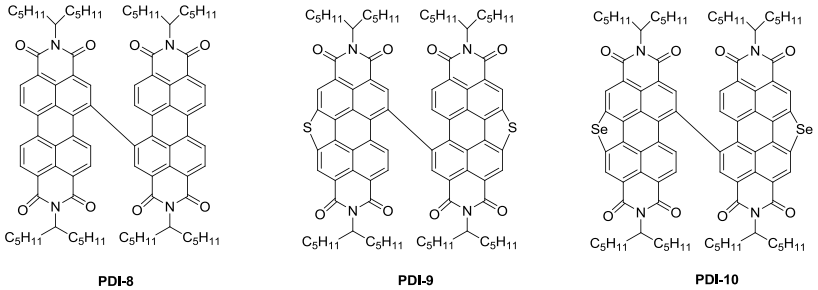

Fig. 2.1.4.1.3 Structures of **PDI-8**, **PDI-9** and **PDI-10**

In 2014, Jen and his coworkers reported an acceptor **PDI-8** with direct linkage of two PDI units through the bay position. After various optimization, such as using a fullerene

self-assembled monolayer ($PC_{61}BM$-SAM)-modified zinc oxide (ZnO) interlayer to enhance charge extraction, an invert device architecture of (ITO/ZnO/PTB_7-Th:s-diPBI/MoO_3/Ag), the efficient donor materials PTB7-Th, the device showed a best result of 5.90%.[24] Very recently, Wang and his coworkers reported a series of acceptors **PDI-9** and **PDI-10** as shown in **Fig. 2.1.4.1.3**.[25, 26] It was found that introduction of sulfur and selenium atom into the PDI plane has several major advantages:

1. The fused thiophene or selenophene ring increases the rigidity of the whole molecule, thus **PDI-9** and **PDI-10** have very twisted structures. The dihedral angle between the two PDI subunits was 80 ^{o}C and 77 ^{o}C respectively for **PDI-9** and **PDI-10**. This change would account for weak aggregation for these two acceptors in the solid film.

2. Due to the electron-donating property of the sulfur atom or selenium atom, it is envisioned that the LUMO for these two acceptors would be raised and the V_{oc} of the device would also improve at the same time. The V_{oc} values for the two acceptors **PDI-9** and **PDI-10** are 0.90 V and 0.96 V with donor PDBT-T1, respectively.

3. Selenium has a bigger and more polarizable electron cloud than sulfur, which should enhance the orbital overlap and charge carrier mobility of **PDI-10**. The hole and electron mobility for **PDI-10** is 3.6 × 10^{-3} cm^2 V^{-1} s^{-1} and 4.8 × 10^{-3} cm^2 V^{-1} s^{-1}, which is higher than that of **PDI-9**: 1.2 × 10^{-3} cm^2 V^{-1} s^{-1} and 2.8 × 10^{-3} cm^2 V^{-1} s^{-1}. With DIO as the additive, both acceptors **PDI-9** and **PDI-10** showed very high PCE results of 7.2% and 8.4% with donor polymer PDBT-T1, respectively.

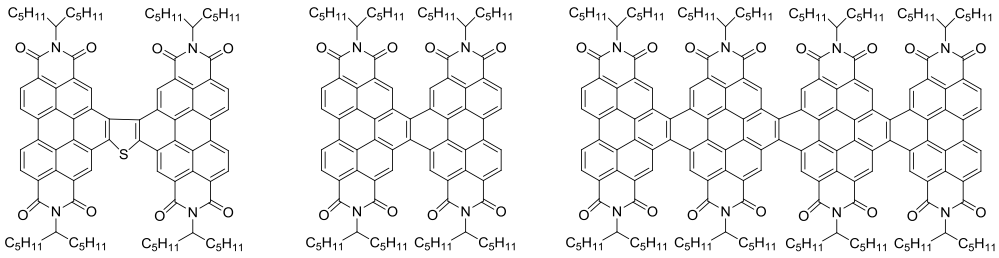

Fig. 2.1.4.1.4 Structures of **PDI-11**, **PDI-12** and **PDI-13**

Very recently, acceptors **PDI-11**, **PDI-12**, **PDI-13** shown in **Fig. 2.1.4.1.4** based on fused ring between the bay position of the subunit of PDI were designed and synthesized.[27-29] These molecules have the following two features:

1. The fused rings, to some extent, increase the effective conjugation between the PDI subunit and decrease the rotational disorder as well as the reorganization energy, which may be beneficial for better charge mobility and morphology in the solid films.
2. Although the conjugation is increased through the whole molecules, these acceptors still possess a non-planar geometry, which will ensure the inhibition of strong aggregation of the films and formation of a bicontinuous network with the donor materials.

For **PDI-11**, the optimized PCE reached up to 6.72% for the inverted device architecture ITO/ZnO/PTB_7-Th:**PDI-11**/MoO_3/Ag using 1-chloronaphthalene (CN) as the solvent additives.

For **PDI-12** and **PDI-13**, the PDI units were covalently linked by one or more ethylene bridges. Because of their twisted structures, they showed weak aggregation but better electron mobility and electron accepting ability, for instance, tetramer **PDI-13** can accept up to 5 electrons from the electrochemical measurements. With solvent additive, these two acceptors showed very high PCEs of 6.05% and 8.3% respectively.

From the above discussion, the most successful non-fullerene acceptors originated from the PDI building block, demonstrating the huge advantages of PDI compared with other building locks.

2.1.4.2 Naphthalene diimide (NDI) acceptors

NDI is another extensively studied building block for developing novel non-fullerene acceptors. However, NDI has relatively poor absorption in the visible range (λ_{onset} is below 400 nm) due to the smaller conjugation plane, which results in a large bandgap of more than 3.0 eV. Therefore, OSCs device based on NDI non-fullerene acceptors normally exhibits poorer PCE performance than PDI. For example, although acceptor **NDI-1** has a similar structure to the acceptor **PDI-1** except for the decreased conjugated ring numbers, it only displayed a PCE of 0.54%, much lower than the PCE value of 1.30% for **PDI-1** with ZnPC as the donor material.[30] Jenekhe and coworkers reported acceptor **NDI-2** with oligothiophene arms attached to the NDI core. (**Fig. 2.1.4.2**) After optimizing the conditions of annealing temperature and additive concentration, the best PCE value for the P3HT : **NDI-2** device is up to 1.5%.[31, 32]. Recently, considering the success of

acceptor **PDI-7**, Zhan and his coworkers synthesized a similar acceptor **NDI-3** based on NDI, in which two NDI units were connected by a thiophene group linker. The acceptor exhibited good absorption between the 300 to 700 nm and suitable LUMO energy around –3.80 eV. However, a lower J_{sc} was observed due to the weak ICE absorption. When taking the PBDTTT-C-T as the donor material, **NDI-3** yielded a PCE value of 1.31% with a high V_{oc} of 0.95–0.96 V.[33] Russell and coworkers synthesized another NDI dimer acceptor **NDI-4** with a vinyl double bond as the bridge. As a matter of fact, **NDI-4** showed high electron mobility of 0.365 $cm^2\ V^{-1}\ s^{-1}$ based on thin film transistor. Meanwhile, it also exhibited moderate PCE performance of 2.41% when using 0.5% DIO as the additive, which is among the highest results for the small molecule acceptors based on NDI.[34] Very recently, an interesting molecular structure combining a superior intermolecular orbital overlap, improved carrier mobilities, optical and electronic properties as well as tunable electronic structure (**NDI-5)** has also been introduced by Jenekhe and coworkers. It has an electron mobility of 0.12 $cm^2\ V^{-1}\ s^{-1}$ with a PCE of 1.8%.[35] Further modification of the **NDI-5** by employing thiophene as the bridge gave the novel acceptor **NDI-6**. The alkyl group on the thiophene affects the PCE performance significantly and it founded out that when adopting 3,4-dimethyl thiophene as the linker, **NDI-6** exhibited best PCE value of 6.4%. It is expected that due to the more twisted conformation caused by steric interactions with the methyl groups, there was more efficient molecular packing and improved isotropic charge transport [36]

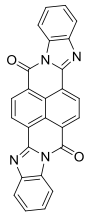

NDI-1

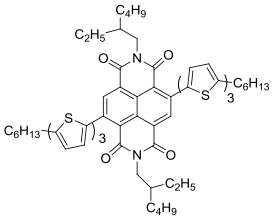

NDI-2

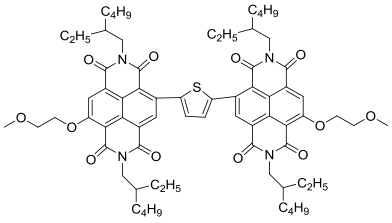

NDI-3

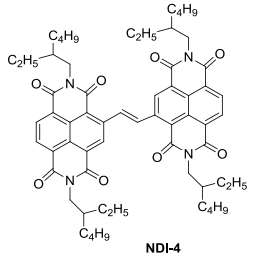

NDI-4

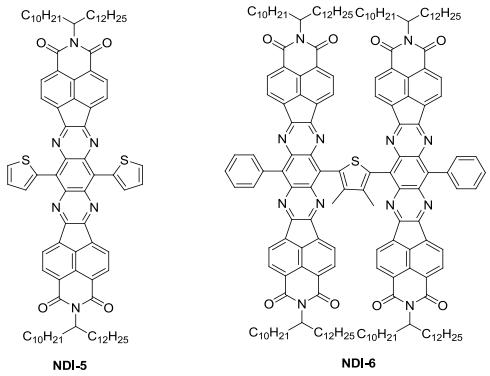

Fig. 2.1.4.2 Structures of NDI-based acceptors

From the above discussion, PDI and NDI based non-fullerene acceptors have achieved much success just during the past 3 years and the best PCE values rival the result for the same donor using $PC_{61}BM$ as the acceptor. However, there is one apparent limitation pertaining to these types of non-fullerene acceptors: the large π-conjugated plane. Due to the large π-π intermolecular interactions between these conjugated planes, the PDI-based non-fullerenes tend to aggregate readily, which is detrimental to the film morphology and further decreases the film electron mobility as well as the final PCE performance. Therefore, various strategies, such as the twisted strategies, were developed to solve this problem and the situation improved to some extent. But most novel PDI acceptors still need to overcome the obstacles to match with various donors while still keeping the high PCE performance. At the same time, non-fullerene acceptors based on other electron-withdrawing building blocks have been investigated as discussed in the following text.

2.1.4.3 Diketopyrrolepyrrole (DPP) acceptors

DPP, as an electron-withdrawing unit, has been demonstrated as a powerful Acceptor (A) building block for synthesizing many promising donors materials for OSCs.[37] Various non-fullerene acceptors based on DPP have been developed in which DPP is combined with other electron-donating or electron withdrawing groups. Based on this thought, acceptor **DPP-1** was designed and synthesized. For this acceptor, it was demonstrated that the DPP's intrinsic electron affinity was much enhanced by the electron-withdrawing group CF_3. Finally, **DPP-1** produced the best PCE value of 1.0% when taking P3HT as the donor material.[38] (**Fig. 2.1.4.3**) Later on, acceptor **DPP-2** with sila-fluorene core and two DPP units as wing was developed and its BHJ devices blended with P3HT resulted in

a PCE of 2.05%.[39] AFM images showed the films had interpenetrating networks with long fibrils 20 nm in diameter, indicating a desirable phase separation. In 2015, Jo and co-workers reported an A−π−A−π−A type acceptor **DPP-3**, in which two DPP units are covalently linked to the central benzothiadiazole unit through thienyl bridges.[40] This structure had low lying LUMO and HOMO energies (−4.33 and −5.85 eV, respectively) and exhibited an absorption band between 450 and 800 nm. A PCE of 5% was obtained for the **DPP-3**:PTB7 blend. Recently, Chen and his co-workers reported the study of a diketopyrrolopyrrole (DPP)-based organic acceptor, **DPP-4**, in which four DPP moieties are covalently linked through a spirobifluorene core. It has suitable LUMO and HOMO energies of −3.60 and −5.26 eV, respectively. Its absorption spectrum was similar to those of most DPP-based small molecules with a localized band between 480 and 680 nm, which is complementary to the absorption of P3HT. The **DPP-4**:P3HT blend had a PCE value of 3.63% with a high V_{oc} of 1.10 V.[41] Based on these results, the DPP unit appears to be a promising building block for which to construct novel small molecule acceptors, due in part to the facile synthesis, long wavelength absorption, and low-lying LUMO levels.[39]

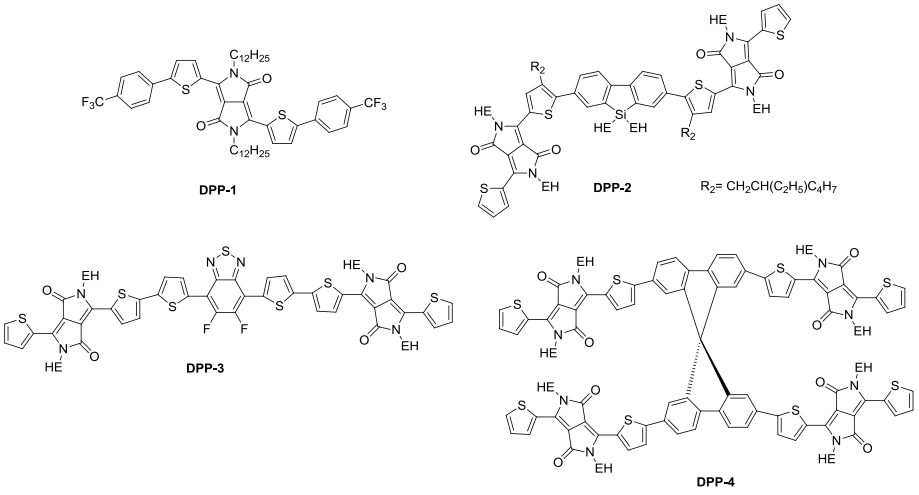

Fig. 2.1.4.3 Structures of DPP-based acceptors

2.1.4.4 Subphthalocyanines based acceptors

Subphthalocyanines, particular boron SubPc chlorides, are another class of materials used as non-fullerene acceptors in OSCs.(**Fig. 2.1.4.4**) In 2014, Kjellcnops and his coworker developed the acceptors **SubPc-1** and **SubPc-2**.[42] They found that these acceptors

afforded high PCE of 4.69% and 6.02% respectively by employing the simple bilayer devices. Interestingly, a remarkable efficiency up to 8.40% was achieved with a simple three-layer device architecture comprising both **SubPc-1** and **SubPc-2**. The three photoactive materials have complementary optical absorption profiles and both internal (IQE) and external quantum efficiency (EQE) spectra show efficient photocurrent generation within all three absorbing materials. Interestingly, **SubPc-2** was also used as a donor material in conjunction with chlorinated electron acceptor **SubPc-3**.[43] A planar hetero-junction was utilized again, and with interlayer optimization, a PCE of 6.4% was achieved owing to the high J_{sc}, V_{oc}, FF values of 9.0 mA.cm^{-2}, 1.03 V and 71%. Compared with the corresponding device with C_{60} as the electron acceptor, an increased current with **SubPc-3** was attributed to strong and complementary absorption profiles, while the greatly improved fill factor was explained by decreased recombination of either charge-transfer states or trapped charges.

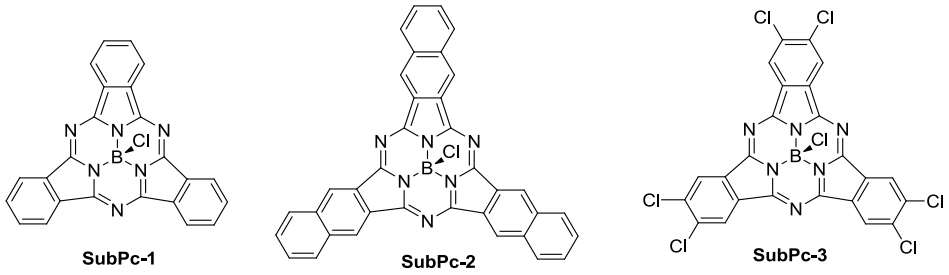

Fig. 2.1.4.4 Structures of subphthalocyanines-based acceptors

2.1.4.5 Typical A-D-A structure acceptors

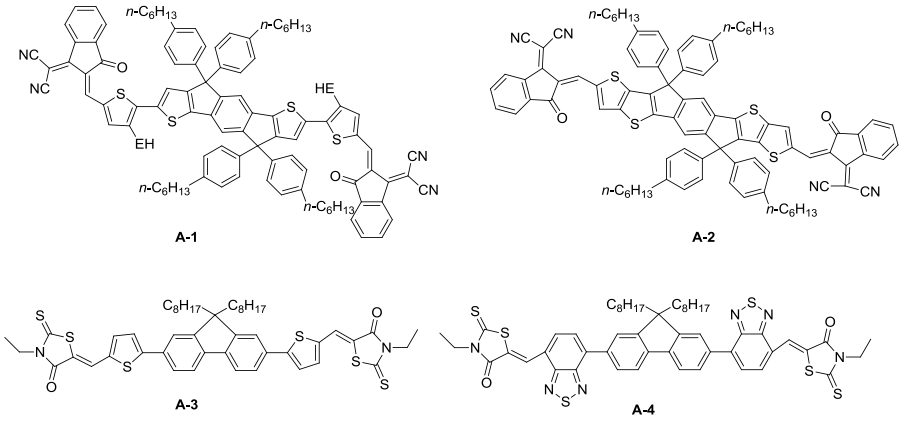

Fig. 2.1.4.5 Structures of A-D-A type acceptors

Small molecules with A-D-A structure or polymers with D-A structures have been studied intensively as OSCs donor materials and great progress has been achieved. By choosing suitable D and A units to ensure the electron affinity of the designed molecules, they can also be used as OSCs acceptors and very good results have been obtained. (**Fig. 2.1.4.5**) Recently, Zhan and his coworkers reported a series of efficient large π-conjugation A-D-A acceptors **A-1** and **A-2**,[44, 45] where A represents electron-withdrawing group: 2-(3-oxo-2,3-dihydroinden-1-ylidene) malononitrile while D represents two typical electron-donating ladder-type groups: indaceno[1,2-b:5,6-b']dithiophene (IDT)[46] and indacenodithieno[3,2-b]thiophene (IDTT)[47]. Four phenyl groups are introduced on the D unit to adjust the solubility of these two acceptors. These two acceptors showed high PCE results of 6.31% and 6.80% results, respectively when employing PTB7-Th as the donor materials. Lim and coworkers reported acceptors **A-3** with the same idea, where A part is rhodanine rather than the 2-(3-oxo-2,3-dihydroinden-1-ylidene) malononitrile while D part is just a simple fluorene group.[48] Acceptor **A-3** exhibited PCE value of 3.08% by adopting P3HT as the donor material. Similarly, by changing the linker thiophene to the benzothiadiazole, acceptor **A-4** with A-A-D-A-A structure was designed and synthesized, which showed best PCE result of 4.11% with donor P3HT.[49]

2.1.4.6 Other highly efficient acceptors

Except for the above-discussed acceptors, other various types of non-fullerene acceptors were also developed during the past several years as shown in **Fig. 2.4.6.** Pei and his coworkers designed and synthesized the novel electron acceptor **A-5** based on a fluoranthene-fused imide scaffold with a CN^- functional group.[50] The study of the physiochemical properties of this acceptor indicated that it had a suitable LUMO energy of –3.5 eV, matching well with the donor material P3HT and the work function of the metal electrode. After TA post treatment, the OSCs device based on P3HT:**A-5** (1:2) blended film gave a PCE value of 1.86%, with V_{oc} value of 0.76 V, much higher than the value 0.58 V obtained by the controlled P3HT:$PC_{61}BM$ device. Wudl and coworkers designed and synthesized another interesting non-fullerene acceptor **A-6** based on a 9,9'-bifluorenylidene structure.[51, 52] It was discovered that the 9,9'-bifluorenylidene building block is especially good at stabilizing a negative charge resulting both from the steric and

electronic effects because after accepting one electron, the tension force for the planar structure can be relieved and hence it possesses the aromaticity property. Meanwhile, through changing the functional groups on the aromatic periphery, the LUMO energy level for this acceptor can be readily modified. When blending with donor material P3HT, this acceptor exhibited a surprisingly high V_{oc} of 1.10 V and finally a moderate PCE value of 1.7%. Wudl and his coworkers also reported a symmetric electron-deficient decacyclene-based triimide acceptor A-7.[53, 54] It founded out that this acceptor worked well with kinds of other donor materials and showed PCE ranging from 0.75% to 1.47%. It found that the low PCE results partially ascribed to the low fill factors. Recently, Sauvé and coworkers reported one very interesting acceptor bis[2,6-diphenylethynyl-1,3,7,9-tetraphenyl-azadipyrromethene] zinc(II), **A-8**, in which there were two highly twisted azadipyrromethene planes pointing in four directions.[55] Its intense absorption ranges from 580 to 800 nm, which is complementary to P3HT, and suitable low-lying LUMO and HOMO levels about −3.85 and −5.60 eV enable it the potential candidate to be the OSCs acceptor material. Actually, the optimized **A-8**:P3HT blend films yielded a PCE value of 4.10% while the PCE is only 3.7% for the controlled device of the $PC_{61}BM$:P3HT. This work shows that organic-metal coordinated complexes might have potential for use as alternative non-fullerene acceptors. Another type of non-fullerene acceptor **A-9** is based on truxenone derivatives. The dicyanovinylene motif in **A-9** results in an EA of approximately 4.1 eV and give a PCE around 1.0%, which outperforms $PC_{61}BM$ in a bilayer OPV structure.[56]

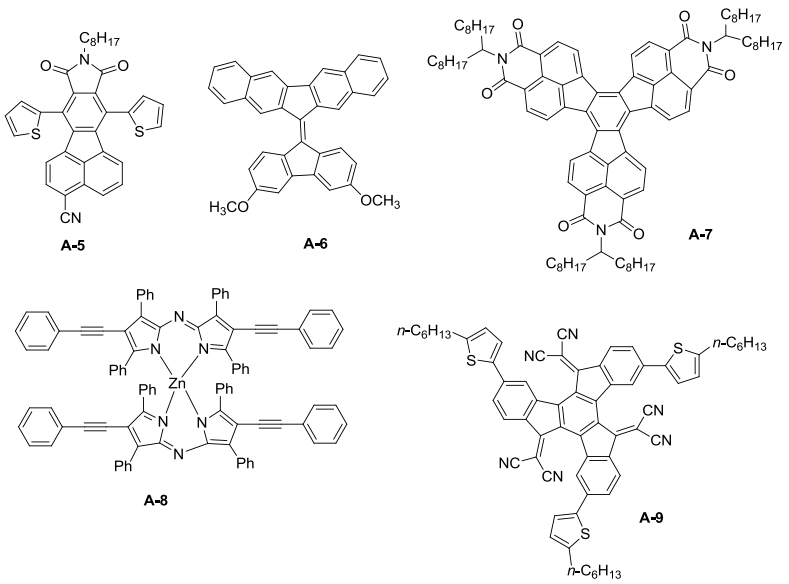

Fig. 2.1.4.6 Structures of acceptors **A-5** to **A-9**

2.1.4.7 Polymer acceptors

By comparison with fullerene derivatives, n-type semiconducting polymers, which can also be used as acceptors in OSCs with polymer/small molecules donors, possess the advantages of strong and broad absorption spectra and easily tuned energy levels. In addition, all-PSCs are suitable for the large area fabrication methods, such as roll-to-roll coating and printing technique. Due to the good ambient and thermal stability, high electron affinity and high electron mobility, rylene diimide is still usually adopted as the core of the polymer in designing the polymer acceptor as shown in **Fig. 2.1.4.7.** For example, Facchetti et al have reported a NDI-bithiophene based polymer **NDI-P1**, which showed a PCE result of 5% recently using donor PPDT2FBT. [57] Later on, various small molecule and polymer donor materials were used together with this acceptor, for example, PTB7-Th, and showed PCE value of 5.5%.[58] Very recently, Jen and coworkers reported one modified acceptor similar to **NDI-P1** just by introducing two fluorine atoms onto the bithiophene unit, from which a PCE of 6.7% was obtained.[59] Compared with NDI unit, PDI is also a very common acceptor building block for synthesizing polymer acceptor. As shown in **Fig. 2.1.4.7**, acceptor **PDI-P2** blended with P3HT showed PCE of 2.17%.[60]

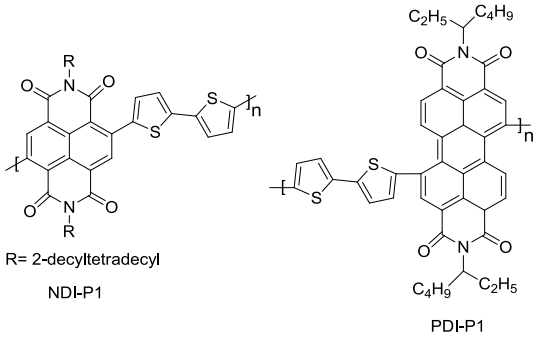

Fig. 2.1.4.7 Structures of **PNDIBS** and **PC-PDI**

The above review discusses the development history of representative fullerene or non-fullerene OSCs acceptors. However, due to the limited space for the thesis, not every reported work regarding to the OSCs acceptor can be included in this thesis. For further information, please refer to the following reviews:

For fullerene acceptors, check the references here:[61]

For small molecule non-fullerene acceptor, check the references here:[62-66]

For polymer non-fullerene acceptors, check references here:[57, 67]

2.1.5 Sensor for K^+

Potassium ion (K^+) is one of the most abundant physiological metal ions in living organisms where it plays particularly important roles in biological processes including heartbeat, muscle contraction, nerve transmission and kidney function.[68] It makes up about 0.4 percent of the mass of the human body, functionalizing as maintaining intracellular and extracellular osmotic pressure and electrolyte balance as well as modulating biochemical signal transduction throughout the nervous system of organisms.[69] Moreover, normal serum potassium levels are maintained within a fairly narrow concentration range from 3.5-5.5 mM by a renal excretion mechanism.[70] High serum potassium levels (45.5 mM) are referred to as hyperkalemia, and when in the low (5.5-6.0 mM) range or moderate (6.1-6.9 mM) range, it causes nausea, fatigue, muscle weakness, and/or bearable cardiac arrhythmia. Hyperkalemia commonly causes cardiac arrest and even death when it is associated with a K^+ concentration of 7.0 mM.[71] Therefore, sensitive and selective methods for detecting potassium in living organisms are in great need.

Due to the excellent coordination property of crown and aza-crown ether unit for potassium ion, they have been widely adopted as accepting parts in fluorescent probes. In the 90's of last century, Garlid and his coworkers designed and synthesized a novel and now the only commercial available potassium probe KS-1 based on benzofuran isophthalate (PBFI), which used to measure the fluorescence response to potassium and sodium ions in the beef heart and mouse liver mitochondrial.[72] This study observed the existence of K^+/H^+ antiporter in these tissues for the first time. However, KS-1 is still not an ideal probe due to its insufficient binding capability to K^+ and interference from the coexisting sodium ions. Regarding to this problem, novel probes containing cryptand architecture are designed and KS-2 based on [2,2,2] cryptand and coumarin dye was synthesized.[73] It's found out that this probe have good sensing behavior to K^+ ion selectively. In addition, it apparently inhibited the pH interferences. But KS-2 also suffered restricting rotation about the trigger nitrogen-carbon bond. He et al. discovered that this rotational restriction is responsible for large changes in the fluorescence efficiency that occurs upon K^+ binding.[74] To alleviate this problem, an aza-cryptand ligand TAC was designed and synthesized and became the most frequently utilized receptor for potassium probe.

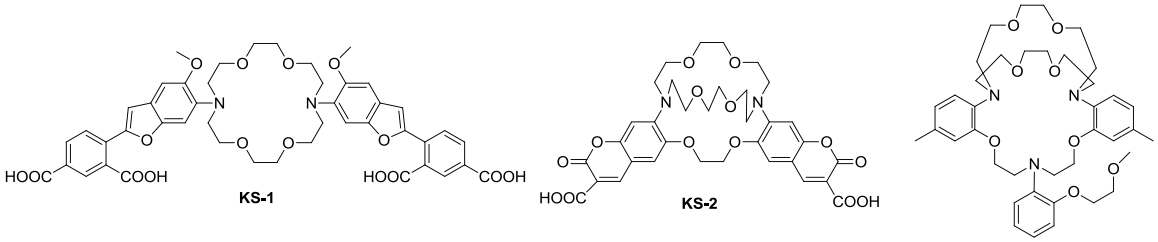

Fig. 2.1.5.1 Structures of **KS-1** and **KS-2**

By combining the TAC acceptor part and the fluorophore part 3,6-bis(dimethylamino)xanthylium, Verkman and his coworker designed and synthesized a novel potassium probe KS-3,[75] which possess several exciting properties: 1) it had emission spectrum in the visible range of 570 nm and the intensity increased by more than 23 folds as the K^+ concentration increased from 0 to 200 mM; 2) High selectivity of K^+/Na^+ ions ratio around 37; 3) high sensitivity for K^+ around 0 to 40 mM. In addition, it's demonstrated the KS-3 could be adopted for visualizing potassium waves in the brain cortex of mice. By changing the fluorophore to BODIY, probe KS-4 was designed and

synthesized.[76] Further functionalization of KS-4 with amino-dextrain produced a polymer-based probe, which could be employed to be a cellular K^+ channel mimicking the potassium ions transporting behaviors and monitoring K^+ in the airway surfaces. For the above-discussed probes, they displayed high selectivity and sensitivity for detecting extracellular K^+ ion ranging around 5 mM. However, the intracellular K^+ ions was in much higher concentration of 150-475 mM. Thus, a suitable probe for K^+ detection at this level is highly desirable. For the purpose, probe KS-5 with a pull-push electron system was designed and synthesized by connecting 2-dicyanomethylene-3-cyano-4,5,5-trimethyl-2,5-dihydrofuran fluorophore with the cryptand architecture.[77] It was found out that this probe responded to K^+ ions over a broad and high concentration range (up to 1.6 M). Although KS-3, KS-4 and KS-5 and other probes based on cryptand structure TAC exhibited excellent selectivity and sensitivity for K^+ ions, their synthesis was complex and lengthy. Therefore, a simple strategy to discover other K^+ probes is still on high demand. Regarding to this, Holdt and his coworkers designed and synthesized probe KS-6 through click reaction based on phenylaza-18-crown-6 and coumarins.[78] The lariat moiety played crucial effect on the stability of this probe and KS-6 displayed high selectivity towards K^+ over Na^+ under simulated physiological conditions.

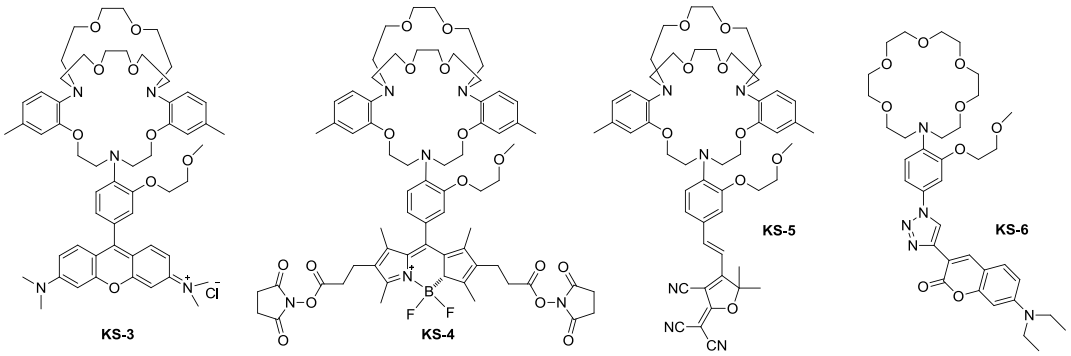

Fig. 2.1.5.2 Structures of **KS-3 to KS-6**

Aside from the coumarin and BODIY fluorophores, n-type rylenes compounds are another group materials which also display fluorescene and most of them are cheap and commercial available. As a matter of fact, by attaching a naphthalimide building block with the cryptand TAC structure, probe KS-7 was developed,[79] which showed excellent respond to K^+ at 540 nm. Moreover, the 40 fold coexisting Na^+ ions had almost no effect on the selectivity of K^+ ions for this probe.

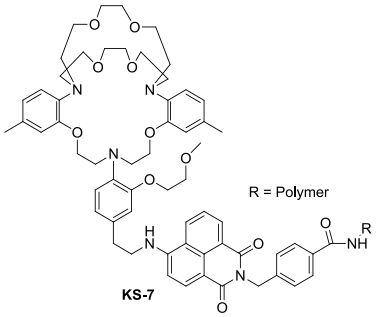

Fig. 2.1.5.3 Structures of **KS-7**

For the mechanism of the probing, as displayed in **Fig. 2.1.5.4**,[80] before binding the K^+ ions, there is electron transfer process from the donor cryptand part to the fluorophore part, which the accounts for the weak fluorenscene of the probes. After binding the K^+ ions, the electron transfer process is inhibited and the fluorophore regains its fluorescence efficiency.

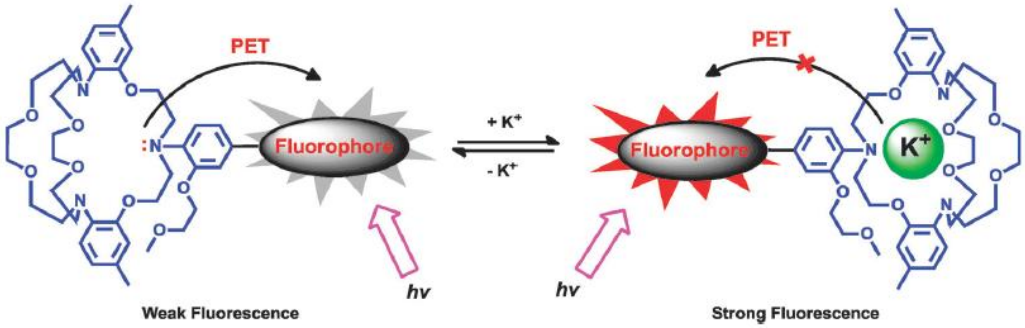

Fig. 2.1.5.4 Diagram for the mechanism of photoinduced electron transfer (Reproduced from ref. *Chem. Soc. Rev.*, **2015**, *44*, 4619)

2.2 Questions to answer based on literature

Chemical functionalization allows researchers design and synthesize various acceptors based on different structures. Thus, the aim to control the overall absorption spectrum and energy levels of non-fullerene acceptors is achieved.

However, compared to fullerene-based acceptors, non-fullerene acceptors generally exhibit inferior performance in OSCs devices for most cases when compared with PCBM acceptor.

Secondly, one universal non-fullerene acceptor like PCBM that can match and work with various polymer/small molecules donor materials have not been obtained and proved. Thirdly, compared with the nanoscale phase separation and suitable morphology for PCBM films, it needs much work to optimize the non-fullerene based device morphology to obtain the best PCE performance.

Finally, there is large variation for the charge transport property in neat film and in the blended film. While many of these non-fullerene acceptor materials displayed good measured electron mobilities for neat films, the mobilities for blended films with the donor material will generally decrease significantly. It's also demonstrated with different morphology for the films, the PCE results vary significantly. The next step in the development of new non-fullerene acceptors may involve developing multi-dimensional structures.

For the K^+ ion probe, the field was developed very slowly during the past decades and the successful examples generally need multiple steps to achieve and the cost is extremely high. In addition, the probe was frequently built up from known dyes, such as BODIY etc. A novel K^+ ion probe that can be obtained through efficient synthesis and development of novel fluorophore part for the K^+ probe is still highly desirable.

2.3 PhD in context of literature

For the literature review, the first part is mainly about the development history of fullerene based acceptors. There are two main methods to improve the efficiency of the fullerene acceptors. One is through introducing the absorption group to increase the I_{sc} of the acceptor, another one is through multi-functionalization to increase the LUMO energy level to increase V_{oc} of the device. What will happen by combing these two methods

together to introducing two absorption group onto C_{60}? Following this idea, TQBA was designed and synthesized but as will be shown herein, it was found out that the V_{oc} indeed increased but J_{sc} and FF decreased, which indicated that it was necessary to balance these three parameters well to obtain ideal PCE, which was the basis for subsequent design.

The second part of the literature review focuses on non-fullerene acceptors. For PDI based non-fullerene acceptor, a lot of successful examples were developed. We followed the tendency to design a 3D acceptor based on PDI and checked its photovoltaic performance. It turned out that the 3D shape was beneficial for inhibiting aggregation of PDI unit, but might result in too amorphous film and lower electron mobility. Aside from PDI, we also designed and synthesized non-fullerene acceptor based on NDI. Core-extended-NDI molecule NTI was obtained and it's demonstrated to be a powerful n-type building block for OSCs. Another one was S-NDI compound obtained from NDI through thionation reaction. This method was powerful in adjusting the absorption, bandgap and energy level. But at the same time, the crystalline for these kinds of molecules also increased. We need to balance these change to obtain the desired target we expect. In addition to design and synthesis of novel non-fullerene acceptor based on PDI and NDI, we also developed a novel building block heteroaromatic diones through one step F-C reaction.

The third part is about the probes for K^+. The project was so difficult that there were no more than 50 examples during the past 30 years. The successful examples are based on multiple cryptand architecture TAC to coordinate with K^+ with a fluorophore, mainly dyes. But one big problem is that they are too complex. I designed and synthesized a probe for K^+ mainly based on efficient synthesis and easily available n-type building block naphthalimide and studied its response to K^+.

References

[1] B. C. Thompson and J. M. J. Frechet, *Angew. Chem. Int. Edit.*, **2008**, 47, 58-77.

[2] C. W. Tang, *Appl. Phys. Lett.*, 1986, **48**, 183-185.

[3] G. Yu, J. Gao, J. C. Hummelen, F. Wudl and A. J. Heeger, *Science*, **1995**, 270, 1789-1791.

[4] R. R. Lunt, N. C. Giebink, A. A. Belak, J. B. Benziger and S. R. Forrest, *J. Appl. Phys.*, **2009**, 105.

[5] M. C. Scharber, D. Wuhlbacher, M. Koppe, P. Denk, C. Waldauf, A. J. Heeger and C. L. Brabec, *Adv. Mater.*, **2006**, 18, 789-794.

[6] S. R. Cowan, A. Roy and A. J. Heeger, *Phys. Rev. B*, **2010**, 82.

[7] a) H. W. Kroto, J. R. Heath, S. C. Obrien, R. F. Curl and R. E. Smalley, *Nature*, **1985**, 318, 162-163; 7b) J. W. Arbogast, C. S. Foote, *J. Am. Chem. Soc.* **1991**, 113, 8886-8889.

[8] J. C. Hummelen, B. W. Knight, F. Lepeq, F. Wudl, J. Yao and C. L. Wilkins, *J. Org. Chem.*, **1995**, 60, 532-538.

[9] M. M. Wienk, J. M. Kroon, W. J. H. Verhees, J. Knol, J. C. Hummelen, P. A. van Hal and R. A. J. Janssen, *Angew. Chem. Int. Ed.*, **2003**, 42, 3371-3375.

[10] M. Lenes, G. J. A. H. Wetzelaer, F. B. Kooistra, S. C. Veenstra, J. C. Hummelen and P. W. M. Blom, *Adv. Mater.*, **2008**, 20, 2116-2119.

[11] Y. J. He, H. Y. Chen, J. H. Hou and Y. F. Li, *J. Am. Chem. Soc.*, 2010, 132, 1377-1382.

[12] G. J. Zhao, Y. J. He and Y. F. Li, *Adv. Mater.*, **2010**, 22, 4355-4358.

[13] Y. J. He, G. J. Zhao, B. Peng and Y. F. Li, *Adv. Funct. Mater.*, **2010**, 20, 3383-3389.

[14] Y. P. Sun, C. H. Cui, H. Q. Wang and Y. F. Li, *Adv. Energy Mater.*, **2011**, 1, 1058-1061.

[15] X. W. Zhan, A. Facchetti, S. Barlow, T. J. Marks, M. A. Ratner, M. R. Wasielewski and S. R. Marder, *Adv. Mater.*, **2011**, 23, 268-284.

[16] S. Erten, F. Meghdadi, S. Gunes, R. Koeppe, N. S. Sariciftci and S. Icli, *Eur. Phys. J-Appl. Phys.*, **2006**, 36, 225-229.

[17] a) A. Sharenko, C. M. Proctor, T. S. van der Poll, Z. B. Henson, T. Q. Nguyen and G. C. Bazan, *Adv. Mater.*, **2013**, 25, 4403-4406; b) L.Schmidt-Mende, A. Fechtenktter.,

K. Mullen., E. Moons, R. H. Friend, and J. D. MaeKenzie, *Science*, **2001**, *293*, 1119; c) J. Li, F. Dierschke, J. Wu, A. C. Grimsdale and K. Müllen, *J. of Mater. Chem.*, **2006**, *16*, 96

[18] Y. H. Cai, L. J. Huo, X. B. Sun, D. H. Wei, M. S. Tang and Y. M. Sun, *Adv. Energy Mater.*, **2015**, 5, 1500032.

[19] P. E. Hartnett, A. Timalsina, H. S. S. R. Matte, N. J. Zhou, X. G. Guo, W. Zhao, A. Facchetti, R. P. H. Chang, M. C. Hersam, M. R. Wasielewski and T. J. Marks, *J. Am. Chem. Soc.*, **2014**, 136, 16345-16356.

[20] S. Rajaram, R. Shivanna, S. K. Kandappa and K. S. Narayan, *J. Phys. Chem. Lett.*, **2012**, 3, 2405-2408.

[21] Q. F. Yan, Y. Zhou, Y. Q. Zheng, J. Pei and D. H. Zhao, *Chem. Sci.*, **2013**, 4, 4389-4394.

[22] X. Zhang, Z. H. Lu, L. Ye, C. L. Zhan, J. H. Hou, S. Q. Zhang, B. Jiang, Y. Zhao, J. H. Huang, S. L. Zhang, Y. Liu, Q. Shi, Y. Q. Liu and J. N. Yao, *Adv. Mater.*, **2013**, 25, 5791-5797.

[23] X. Zhang, C. L. Zhan and J. N. Yao, *Chem Mater*, **2015**, 27, 166-173.

[24] Y. Zang, C. Z. Li, C. C. Chueh, S. T. Williams, W. Jiang, Z. H. Wang, J. S. Yu and A. K. Y. Jen, *Adv. Mater.*, **2014**, 26, 5708-5714.

[25] D. Meng, D. Sun, C. M. Zhong, T. Liu, B. B. Fan, L. J. Huo, Y. Li, W. S. Jiang, H. S. Choi, T. Kim, J. Y. Kim, Y. M. Sun, Z. H. Wang and A. J. Heeger, *J. Am. Chem. Soc.*, **2016,** 138, 375-380.

[26] D. Sun, D. Meng, Y. H. Cai, B. B. Fan, Y. Li, W. Jiang, L. J. Huo, Y. M. Sun and Z. H. Wang, *J. Am. Chem. Soc.*, **2015**, 137, 11156-11162.

[27] H. L. Zhong, C. H. Wu, C. Z. Li, J. Carpenter, C. C. Chueh, J. Y. Chen, H. Ade and A. K. Y. Jen, *Adv. Mater.*, **2016**, 28, 951-958.

[28] Y. Zhong, M. T. Trinh, R. S. Chen, W. Wang, P. P. Khlyabich, B. Kumar, Q. Z. Xu, C. Y. Nam, M. Y. Sfeir, C. Black, M. L. Steigerwald, Y. L. Loo, S. X. Xiao, F. Ng, X. Y. Zhu and C. Nuckolls, *J. Am. Chem. Soc.*, **2014**, 136, 15215-15221.

[29] Y. Zhong, M. T. Trinh, R. S. Chen, G. E. Purdum, P. P. Khlyabich, M. Sezen, S. Oh, H. M. Zhu, B. Fowler, B. Y. Zhang, W. Wang, C. Y. Nam, M. Y. Sfeir, C. T. Black,

M. L. Steigerwald, Y. L. Loo, F. Ng, X. Y. Zhu and C. Nuckolls, *Nat. Commun.*, **2015**, 6, 8242.

[30] S. Erten and S. Icli, *Inorg. Chim. Acta.*, **2008**, 361, 595-600.

[31] G. Q. Ren, E. Ahmed and S. A. Jenekhe, *Adv. Energy Mater.*, **2011,** 1, 946-953.

[32] E. Ahmed, G. Q. Ren, F. S. Kim, E. C. Hollenbeck and S. A. Jenekhe, *Chem. Mater.*, **2011**, 23, 4563-4577.

[33] X. Wang, J. H. Huang, Z. X. Niu, X. Zhang, Y. X. Sun and C. L. Zhan, *Tetrahedron*, **2014**, 70, 4726-4731.

[34] Y. Liu, L. Zhang, H. Lee, H. W. Wang, A. Santala, F. Liu, Y. Diao, A. L. Briseno and T. P. Russell, *Adv. Energy Mater.*, **2015**, 5, 1500195.

[35] H. Y. Li, F. S. Kim, G. Q. Ren, E. C. Hollenbeck, S. Subramaniyan and S. A. Jenekhe, *Angew. Chem. Int. Ed.*, **2013**, 52, 5513-5517.

[36] H. Y. Li, Y. J. Hwang, B. A. E. Courtright, F. N. Eberle, S. Subramaniyan and S. A. Jenekhe, *Adv. mater.*, **2015**, 27, 3266-3272.

[37] Z. T. Liu, G. X. Zhang, Z. X. Cai, X. Chen, H. W. Luo, Y. H. Li, J. G. Wang and D. Q. Zhang, *Adv. Mater.*, **2014**, 26, 6965-6977.

[38] P. Sonar, G. M. Ng, T. T. Lin, A. Dodabalapur and Z. K. Chen, *J. Mater. Chem.*, **2010**, 20, 3626-3636.

[39] Y. Z. Lin, Y. F. Li and X. W. Zhan, *Adv. Energy Mater.*, **2013**, 3, 724-728.

[40] J. W. Jung and W. H. Jo, *Chem. Mater.*, **2015**, 27, 6038-6043.

[41] X. F. Wu, W. F. Fu, Z. Xu, M. M. Shi, F. Liu, H. Z. Chen, J. H. Wan and T. P. Russell, *Adv. Funct. Mater.*, **2015**, 25, 5954-5966.

[42] K. Cnops, B. P. Rand, D. Cheyns, B. Verreet, M. A. Empl and P. Heremans, *Nat. Commun.*, **2014**, 5, 3406.

[43] B. Verreet, K. Cnops, D. Cheyns, P. Heremans, A. Stesmans, G. Zango, C. G. Claessens, T. Torres and B. P. Rand, *Adv . Energy Mater.*, **2014**, 4, 1301413.

[44] Y. Z. Lin, Z. G. Zhang, H. T. Bai, J. Y. Wang, Y. H. Yao, Y. F. Li, D. B. Zhu and X. W. Zhan, *Energ. Environ. Sci.*, **2015**, 8, 610-616.

[45] Y. Z. Lin, J. Y. Wang, Z. G. Zhang, H. T. Bai, Y. F. Li, D. B. Zhu and X. W. Zhan, *Adv. Mater.*, **2015**, 27, 1170-1174.

[46] C. P. Chen, S. H. Chan, T. C. Chao, C. Ting and B. T. Ko, *J. Am. Chem. Soc.*, **2008**, 130, 12828-12833.

[47] Y. X. Xu, C. C. Chueh, H. L. Yip, F. Z. Ding, Y. X. Li, C. Z. Li, X. S. Li, W. C. Chen and A. K. Y. Jen, *Adv. Mater.*, **2012**, 24, 6356-6361.

[48] Y. Kim, C. E. Song, S. J. Moon and E. Lim, *Chem. Commun.*, **2014**, 50, 8235-8238.

[49] S. Holliday, R. S. Ashraf, C. B. Nielsen, M. Kirkus, J. A. Rohr, C. H. Tan, E. Collado-Fregoso, A. C. Knall, J. R. Durrant, J. Nelson and I. McCulloch, *J. Am. Chem. Soc.*, **2015**, 137, 898-904.

[50] Y. Zhou, L. Ding, K. Shi, Y. Z. Dai, N. Ai, J. Wang and J. Pei, *Adv. Mater.*, **2012**, 24, 957-961.

[51] F. G. Brunetti, X. Gong, M. Tong, A. J. Heeger and F. Wudl, *Angew. Chem. Int. Edit.*, **2010**, 49, 532-536.

[52] X. Gong, M. H. Tong, F. G. Brunetti, J. Seo, Y. M. Sun, D. Moses, F. Wudl and A. J. Heeger, *Adv. Mater.*, **2011**, 23, 2272.

[53] T. V. Pho, F. M. Toma, M. L. Chabinyc and F. Wudl, *Angew. Chem. Int. Edit.*, **2013**, 52, 1446-1451.

[54] T. V. Pho, F. M. Toma, B. J. T. de Villers, S. Wang, N. D. Treat, N. D. Eisenmenger, G. M. Su, R. C. Coffin, J. D. Douglas, J. M. J. Frechet, G. C. Bazan, F. Wudl and M. L. Chabinyc, *Adv. Energy Mater.*, **2014**, 4, 1301007.

[55] Z. H. Mao, W. Senevirathna, J. Y. Liao, J. Gu, S. V. Kesava, C. H. Guo, E. D. Gomez and G. Sauvé, *Adv. Mater.*, **2014**, 26, 6290-6294.

[56] C. B. Nielsen, E. Voroshazi, S. Holliday, K. Cnops, B. P. Rand and I. McCulloch, *J. Mater. Chem. A*, **2013**, 1, 73-76.

[57] a) A. Facchetti, *Mater. Today*, **2013**, 16, 123-132. b) H. Kang,; M. A. Uddin,; C. Lee,; K.-H. Kim,; T. L. Nguyen,; W. Lee,; Y. Li,; C. Wang,; H. Y. Woo,; B. J. Kim, *J. Am. Chem. Soc.*, **2015**, 137, 2359-2365.

[58] D. Mori, H. Benten, I. Okada, H. Ohkita and S. Ito, *Energ. Environ. Sci.*, **2014**, 7, 2939-2943.

[59] J. W. Jung, J. W. Jo, C. C. Chueh, F. Liu, W. H. Jo, T. P. Russell and A. K. Y. Jen, *Adv. Mater.*, **2015**, 27, 3310-3317.

[60] Y. Zhou, Q. F. Yan, Y. Q. Zheng, J. Y. Wang, D. H. Zhao and J. Pei, *J. Mater. Chem. A*, **2013**, 1, 6609-6613.

[61] Y. J. He and Y. F. Li, *Phys. Chem. Chem. Phys.*, **2011**, 13, 1970-1983.

[62] C. L. Zhan, X. L. Zhang and J. N. Yao, *RSC Adv.*, **2015**, 5, 93002-93026.

[63] C. L. Zhan and J. N. Yao, *Chem. Mater.*, **2016**, 28, 1948-1964.

[64] C. B. Nielsen, S. Holliday, H. Y. Chen, S. J. Cryer and I. McCulloch, *Acc. Chem. Res.*, **2015**, 48, 2803-2812.

[65] Y. Z. Lin and X. W. Zhan, *Mater. Horizons*, **2014**, 1, 470-488.

[66] A. F. Eftaiha, J. P. Sun, I. G. Hill and G. C. Welch, *J. Mater. Chem. A*, **2014**, 2, 1201-1213.

[67] Y. Kim and E. Lim, *Polymers*, **2014**, 6, 382-407.

[68] F. He, Y. L. Tang, S. Wang, Y. L. Li and D. B. Zhu, *J. Am. Chem. Soc.*, **2005**, 127, 12343-12346.

[69] J. M. Burnell, M. F. Villamil, B. T. Uyeno and B. H. Scribner, *J. Clin. Invest.*, **1956**, 35, 935-939.

[70] A. Thibon and V. C. Pierre, *J. Am. Chem. Soc.*, **2009**, 131, 434-435.

[71] H. R. Yu, X. J. Ju, R. Xie, W. Wang, B. Zhang and L. Y. Chu, *Anal. Chem.*, **2013**, 85, 6477-6484.

[72] P. Jezek, F. Mahdi and K. D. Garlid, *J. Biol. Chem.*, **1990**, 265, 10522-10526.

[73] R. Crossley, Z. Goolamali and P. G. Sammes, *J. Chem. Soc. Perk. Trans. 2*, **1994**, 1615-1623.

[74] H. R. He, M. A. Mortellaro, M. J. P. Leiner, S. T. Young, R. J. Fraatz and J. K. Tusa, *Anal. Chem.*, **2003**, 75, 549-555.

[75] P. Padmawar, X. M. Yao, O. Bloch, G. T. Manley and A. S. Verkman, *Nat. Methods*, **2005**, 2, 825-827.

[76] W. Namkung, P. Padmawar, A. D. Mills and A. S. Verkman, *J. Am. Chem. Soc.*, **2008**, 130, 7794-7795.

[77] X. F. Zhou, F. Y. Su, Y. Q. Tian, C. Youngbull, R. H. Johnson and D. R. Meldrum, *J. Am. Chem. Soc.*, **2011**, 133, 18530-18533.

[78] S. Ast, T. Schwarze, H. Muller, A. Sukhanov, S. Michaelis, J. Wegener, O. S. Wolfbeis, T. Korzdorfer, A. Durkop and H. J. Holdt, *Chem-Eur. J.*, **2013**, 19, 14911-14917.

[79] H. R. He, M. A. Mortellaro, M. J. P. Leiner, R. J. Fraatz and J. K. Tusa, *J. Am. Chem. Soc.*, **2003**, 125, 1468-1469.

[80] W. Zhang, Z. Ma, L. P. Du and M. Y. Li, *Analyst*, **2014**, 139, 2641-2649.

Chapter 3

Experimental Methodology

In this chapter, first, the synthetic methods are introduced including classical coupling reactions and Friedel–Crafts reaction, which are reliable to repeat, easy to use for obtaining the desired molecules. Second, the purification methods to purify the product, including the most frequently used method column chromatography and other ones, such as recrystallation and extraction, are described. Third, the basic material characterization techniques to confirm the target molecule's structure are elaborated. Of these NMR technique plays an irreplaceable role in confirming the structure of most organic compounds. Finally various technologies, such as UV-Vis, TGA, DSC, AFM, TEM, are elaborated to study the electrochemical or physicochemical properties for these novel functional molecules. For all the above-mentioned methods or techniques, their basic procedures or principles are further explained through some examples.

3.1 Rationale for Selection

The selection of the following sections for synthetic methods, purification methods, basic characterization techniques and physical and photoelectrical characterization techniques are based on the following ideas: 1) How to obtain the target molecules; 2) How to purify them; 3) How to confirm their structures; 4) How to evaluate their properties.

For the first part of the synthetic methods to obtain the target molecules, the employed reaction must be reliable to repeat, with high yields and easy to operate. Thus, in this section, I simply elaborate the lithiation reaction, the coupling reaction, the radical reaction and the Friedel–Crafts (F-C) reaction.

For the second part of purification methods to obtain the target molecules in pure form, various complementary methods: column chromatography (CC), recrystallization, sublimation, extraction and filtration are elaborated. Some methods are used for removing impurity roughly, such as filtration and extraction. While some methods are employed in order to obtain the target molecule in pure form, such as CC and recrystallization methods. Especially for sublimation method, the purified compound has very high purity even for electronic device fabrication.

For the third part of basic materials characterization techniques to confirm the structures of unknown compounds, Nuclear Magnetic Resonance (NMR), Mass Spectroscopy (MS) and Elemental Analysis (EA) techniques are necessary to realize this aim. Generally speaking, ^{1}H-NMR and ^{13}C-NMR are the most frequently used and most reliable technique for confirming the unknown compounds that has good solubility in common organic solvents. Through the further MS or EA data, the structure can definitely be confirmed.

For the final part of physical and photoelectrical characterization techniques, Ultraviolet-Visible (UV), Fluorescence, Cyclic Voltammetry (CV), Thermogravimetric Analysis (TGA), Differential Scanning Calorimetry (DSC), Atomic-Force Microscopy (AFM), X-ray Diffraction (XRD), Transmission Electron Microscopy (TEM) are elaborated to investigate the intrinsic physicochemical properties for the novel molecule developed in this dissertation and their corresponding films information that has crucial effect on the OSCs or electron mobility performance.

3.2 Synthesis Methods

3.2.1 Lithiation Reaction

Lithiation reaction is to use lithium reagents, such as *n*-butylithium or lithium diisopropylamide, to remove one or more H atoms of the reactant to form one nucleophilic intermediate, which subsequently reacts with an electrophilic reagent to form the target molecule. (**Scheme 3.2.1**) The mechanism of this reaction is that, due to the much higher relative pK_a of alkyl hydrogen than aryl hydrogen, there is a strong driving force for the lithium reagent to combine with the hydrogen atom on thiophene molecule to form one alkane and another lithium intermediate. In this thesis, it was used to introduce different alkyl groups or silyl group to bithiophene, bifuran and bipyrrole etc as showed in **scheme 3.2.1**. The advantages of this reaction are following 1) Easy to introduce different functional groups. 2) High yields.

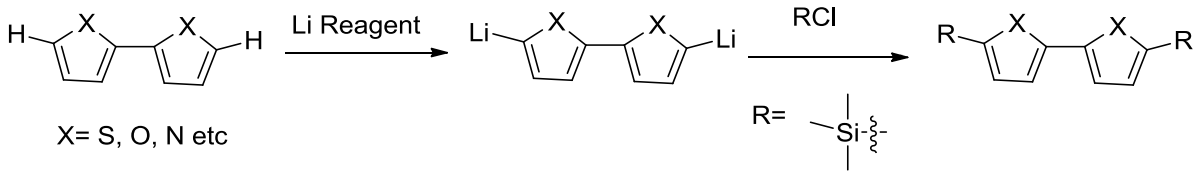

Scheme 3.2.1 Reaction procedure for lithium reagent

3.2.2 Coupling Reactions

A coupling reaction is one which connects two hydrocarbon units with the aid of a metal catalysis. It is one of the most frequently used organic reactions in organic chemistry. There are several coupling reactions named after famous chemists who discovered or developed them, such as Suzuki coupling reaction, Negishi coupling reaction and Heck coupling. As showed in the **Scheme 3.2.2**, one major difference between these reactions is that the coupling reactant is different in each case. For the Suzuki reaction, the reactant is a boron reagent while for the Negishi reaction, the reactant is a zinc reagent. Therefore, researchers can choose different coupling reactions according to the different reaction conditions.

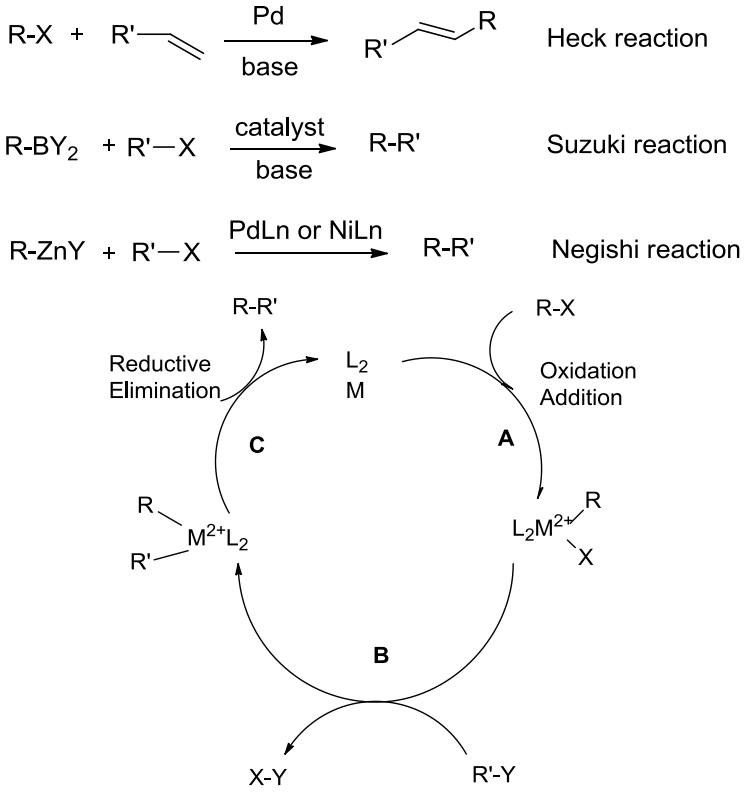

Scheme 3.2.2 Coupling reaction types and the general reaction mechanism

The reaction mechanism contains three steps **A, B** and **C** as showed in **scheme 3.2.2**. For step **A**, firstly there is an oxidative addition reaction in which the organic halide reactant R-X reacts with the metal catalysis Pd or Ni to form the metal intermediate. In step **B**, subsequently, the metal intermediate reacts with another reactant R'-Y to undergo the transmetallation, forming another metal intermediate containing the two coupling units R and R' on the metal center while eliminating the functional group X-Y. For the final step **C,** there is a reductive elimination reaction in which the target molecule R-R' was produced while the catalyst regenerates and afterwards takes part into the reaction in the next cycle again. In this thesis, for some substrates, such as the bipyrrole, biindole, etc, they are synthesized through the coupling reaction. The coupling reactions have the following advantages: 1) easy to operate. 2) reliable to repeat 3) various target molecules can be synthesized by alternating different coupling units.

3.2.3 Free Radical Reaction

Free radical reaction is a reaction involving free radical during the reaction process,

which is provided by radical initiator, such as peroxides PBO as showed in **Scheme 3.2.3**. Generally speaking, this reaction is frequently employed to introduce Br atom into the reactant to form brominated molecule that can be used for further transformation. In this thesis, I used this radical reaction to form the precursor for synthesizing the fullerene based acceptors. The mechanism is drawn as displayed in **scheme 3.2.3**: firstly, the initiator peroxides cleave to form free radicals under the thermal activation and secondly, these radicals activate the Br source (NBS) and the Br atoms adds to the reactant one by one and finally form the target molecule. The advantage of the radical reaction is that the number of Br atoms can be adjusted by controlling the amount of the Br source, NBS.

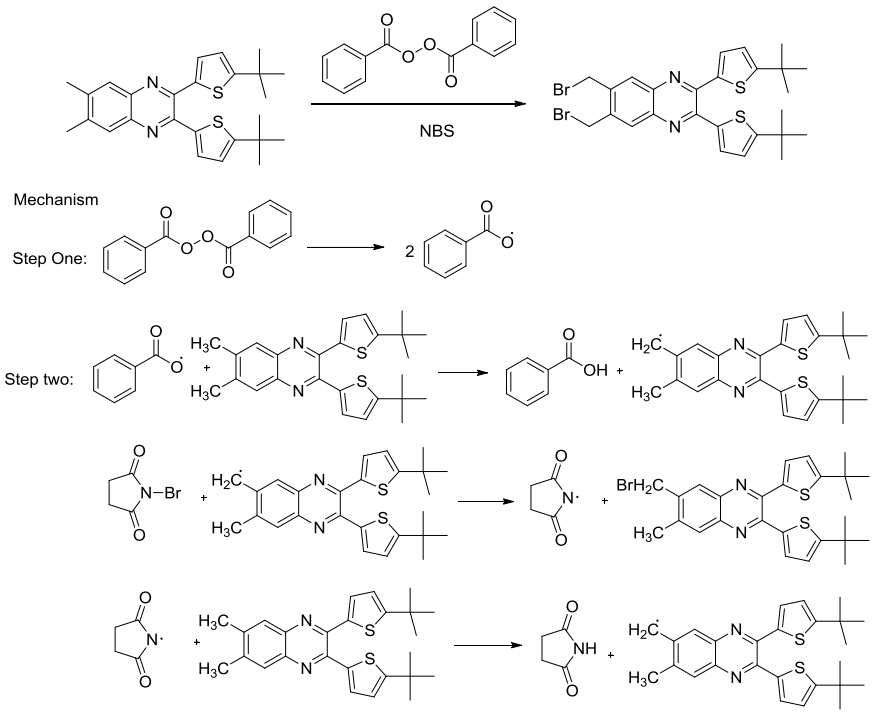

Scheme 3.2.3 Typical radical reaction and the general reaction mechanism

3.2.4 Friedel–Crafts (F-C) Reaction

F-C acylation is the reaction between the aromatic/heteroatom aromatic reactant with an acyl chloride under the catalysis of a strong lewis acid, such as $AlCl_3$ as showed in **Scheme 3.2.4.** F-C acylation is also possible by taking acid anhydrides as the acylation reagent. This reaction has several advantages over the alkylation reaction:

1) No multiple acylation will happen due to the lower reactivity of the ketone product than the original molecule.

2) No carbocation rearrangement will happen because the carbonium ion is very stable due to the molecular resonance.

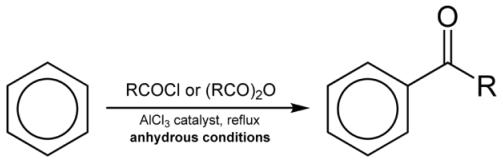

Scheme 3.2.4 Typical procedure for Friedel–Crafts acylation

3.3 Purification Methods

3.3.1 Column Chromatgraphy (CC) Technology

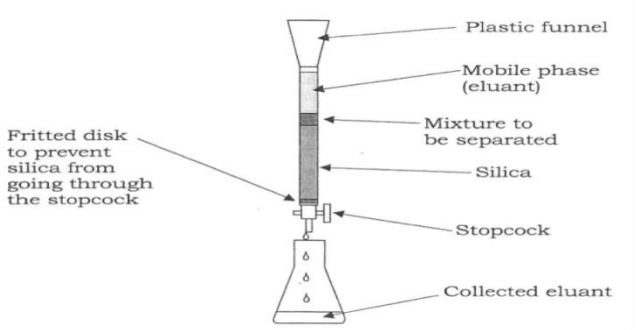

Fig. 3.3.1 Diagram of a column chromatography

Column chromatography is used for the separation of mixture of the product through glass column or tube. (**Fig. 3.3.1**) It contains two important parts:

1. Stationary phase, mainly silica gel. Due to the different binding forces with the silica gel for the components in a mixture, their speeds passing through the column are also different. Thus, each component can be separated respectively in order of increasing binding to silica.

2. Mobile phase. Mobile phase consists of a pure solvent, such as hexane or DCM. But more frequently, it is a mixture of solvents, such as hexane/ethyl acetate, or hexane/ DCM etc, which pushes forward the product moving on the column. In addition, by changing the volume ratio of the solvents, the required time for separation of the product is also controlled. For example, when increasing the volume of DCM in a mixture solvent of DCM/hexane, its polarity will increase and the product will move faster on the column.

Advantages:

1. The relatively low cost

2. Avoidance of cross-contamination for different batches of product due to the disposability of the silica gel in the process.

Disadvantages: Loss of product on the column and sometimes operation time is long.

3.3.2 Recrystallization

Recrystallization means a purification process to remove the impurity from target organic compound which are solid at room temperature. (**Fig. 3.2.2**) The basic principle is that most organic compounds have different solubility in some particular solvents at different temperatures. Thus, when heating the solvent, the organic compound and impurity all dissolve. However, when the solution cools down, crystals will form, grow and precipitate out from the solution and leave small amounts of the organic compound as well as the impurity (small amounts of impurity will sufficiently dissolve in the solution-circle as shown in the right figure in **Fig. 3.2.2**) in the so called 'mother solution'. Therefore, recrystallization is a good method to purify some organic compounds, whose solubility vary significantly at different temperature and contains small amount of impurity.

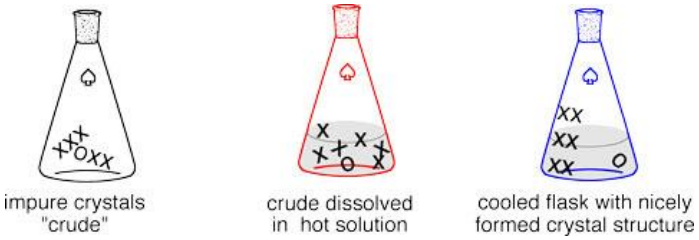

Fig. 3.3.2 Diagram for recrystallation

Advantage:

1. To obtain compound in high purity.
2. Almost no loss when the compound is stable at high temperature.
3. Operation time is short compared with column chromatography.

3.3.3 Sublimation

Sublimation is phenomenon that indicates the transition of a substance directly from the solid to the gas phase without passing through the intermediate liquid phase. Sublimation

is also a technique used to purify compounds. As displayed in **Fig. 3.3.3,** a solid is typically placed in a sublimation chamber (area 1) and a pump evacuates the gas out to maintain the chamber under vacuum condition. Under this reduced pressure, the solid is heated (area 1) and volatilizes and then cools down to form a purified compound in the cooled area (area 2), leaving a non-volatile residue of impurity behind. To future purifying the solid, gradient temperature heat can be used to remove the volatile impurities (area 3). Vacuum sublimation is important for the electronic device because very high purity is needed to achieve high device performance.

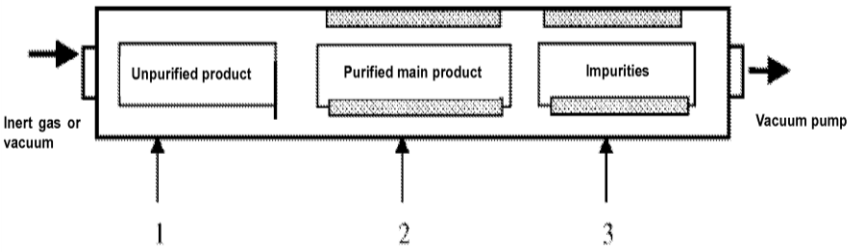

Fig. 3.3.3 Diagram for the sublimation procedure in a chamber

3.3.4 Extraction

Extraction is a frequently used operation in the lab by using two immiscible phases to purify the organic compounds roughly in the first place. For a reaction which contains organic compounds and salt dissolved in H_2O, by adding the organic solvent (hexane or dichloromethylene etc) and H_2O simultaneously and shaking the mixture solvent intensively. The organic compounds will dissolve into the organic solvent, forming the so-called oil phase while the salt will dissolve into the water, forming the so-called water phase. Upon leaving the solvent mixture to stand still for some time, the oil phase/water phase separates. After removing the water phase and repeating this procedure for around 3 times, the majority of impurities dissolved in water will be removed depending upon partition constant.

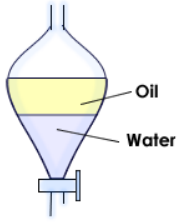

Fig. 3.3.4 Diagram for extraction

3.3.5 Filtration method

Filtration is a process that separates the solid phase from the liquid phase.(**Fig. 3.3.5**) Filtration is very useful in work up of the reaction. If the target molecule is in the filtrate, after filtration and evaporating the solvent in the filtrate, the crude target molecule can be obtained. When doing the recrystallization operation, filtration is a necessary step to separate the crystal solid from the mother solution.

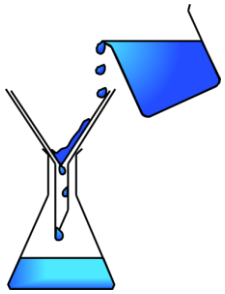

Fig. 3.3.5 Diagram for filtration

3.4 Basic material characterization

3.4.1 ^{1}H-NMR and ^{13}C-NMR

Proton nuclear magnetic resonance (^{1}H-NMR) is a spectroscopic technique probing the nature of hydrogen-1 nuclei within a molecule through nuclear magnetic resonance. Through ^{1}H-NMR, the structure of the measured molecule can be determined. The information of a ^{1}H-NMR mainly comes from two parameters: chemical shifts and the spin-spin coupling.

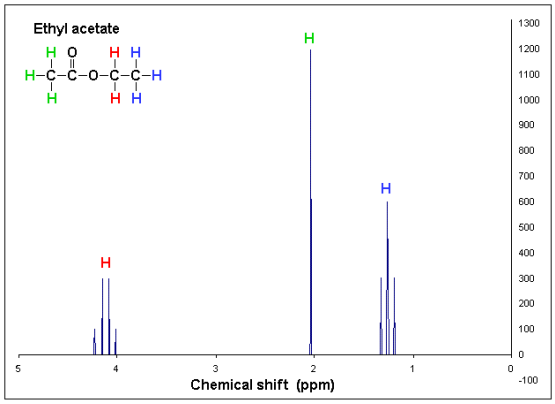

Fig. 3.4.1.1 ^{1}H-NMR spectrum for $CH_3COOC_2H_5$

The chemical shift is the resonant frequency of a nucleus relative to a standard in a magnetic field. The electrons around a nucleus will circulate in a magnetic field and create a secondary induced magnetic field. This field opposes the applied field as stipulated by Lenz's law and atoms with higher induced fields (i.e., higher electron density) are therefore called *shielded*, relative to those with lower electron density. The chemical milieu of an atom can influence its electron density through the polar effect. Electron-donating alkyl groups lead to increased shielding while electron-withdrawing substituent such as nitro group lead to *deshielding* of the nucleus. For example, the chemical shift of H atoms on CH_3 group is around 1.0 ppm (**Fig. 3.4.1.1**). When it is connected with C=O group of $CH_3COOC_2H_5$, the value will shift to low field around 2.0 ppm.

Spin-spin coupling is the coupling of the intrinsic angular momentum (spin) of different particles. Such coupling between pairs of nuclear spins is an important feature of nuclear magnetic resonance (NMR) spectroscopy as it can provide detailed information about the structure and conformation of molecules. Still taking the ethyl acetate $CH_3COOC_2H_5$ as the example, (**Fig. 3.4.1.1**) from the above analysis, it is known that the chemical shift position of H atoms on CH_3 group will appear at around 2.0 ppm. In addition, because there is no other H (only C=O group) connecting to the CH_3 group, therefore, the peak should not split and there is only a single peak. By combining these two analysis, it can be confirmed the molecule contains the CH_3 group that connects with C=O group. Following the same method, we can confirm the other functional groups.

Similar with ^{1}H-NMR, Carbon nuclear magnetic resonance (^{13}C-NMR) is spectroscopy/technique regarding to the Carbon-13 nuclei within a molecule through nuclear magnetic resonance. The main parameter is the still the chemical shift. For ^{13}C NMR, it has several features:

1). Carbon-12 is the main isotope of carbon while carbon-13 is present naturally only in 1.1% abundance. Thus, the sensitivity of ^{13}C-NMR is much weaker than H-NMR.

2). One bond J-coupling constants between carbon and hydrogen (typically from 100 to 250 Hz) results in potential complications. In order to suppress these couplings, which would otherwise complicate the spectra and further reduce sensitivity, carbon NMR spectra are usually proton decoupled to remove the signal splitting. Couplings between

carbons can be ignored due to the low natural abundance of ^{13}C. Hence in contrast to typical proton NMR spectra which show multiplets for each proton position, carbon NMR spectra show a single peak for each chemically non-equivalent carbon atom. (**Fig. 3.4.1.2**)

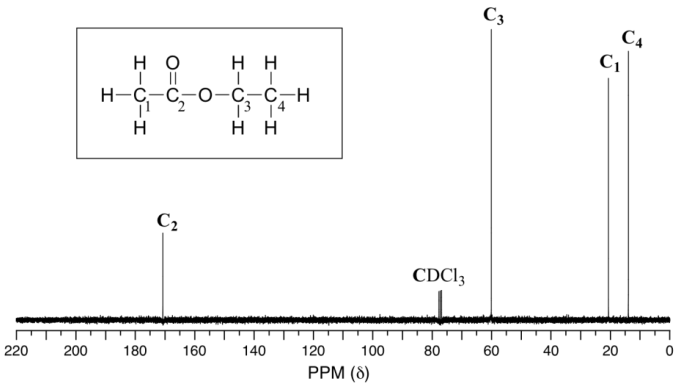

Fig. 3.4.1.2 ^{13}C-NMR spectrum for $CH_3COOC_2H_5$

3.4.2 HRMS/MALDI-TOF

Mass Spectrum is a spectrum that displays the peaks of ions by mass to charge ratio, denoted as m/z. Through analyzing the m/z values, which come from the molecule of the given substance $M+H^+$ as well as its fragments, the structure of the measured substance can be primarily determined. In an electron impact mass spectrometer, a high energy beam of electrons is used to displace an electron from the organic molecule to form a radical cation known as the molecular ion as schemed below**.**

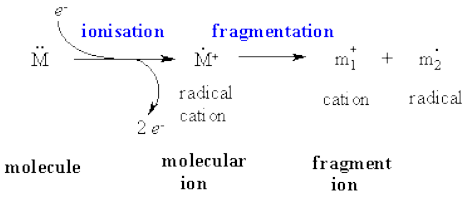

As showed in the **Fig. 3.4.2**, there is a M^+ peak at 298 and we can speculate that the molecular weight of the unknown compound is 298. It is a very useful complementary technique combined with H-NMR to eventually decipher the unknown compounds.

For normal mass spectrum, it is difficult to differentiate the compounds that have the same relative molecular mass. For high resolution MS, it enables us to distinguish between different molecular formulae which have the same relative molecular mass to

the nearest whole number.

In some cases, MALDI-TOF (matrix-assisted laser desorption/ionization time of flight), which is a soft ionization technique, is another choice to solve this problem. Charged ions of various sizes are generated. As the potential difference V_0 is constant with respect to all ions, ions with smaller m/z value (lighter ions) and more highly charged ions move faster through the drift space until they reach the detector. Consequently, the time of ion flight differs according to the mass-to-charge ratio (m/z) value of the ion.

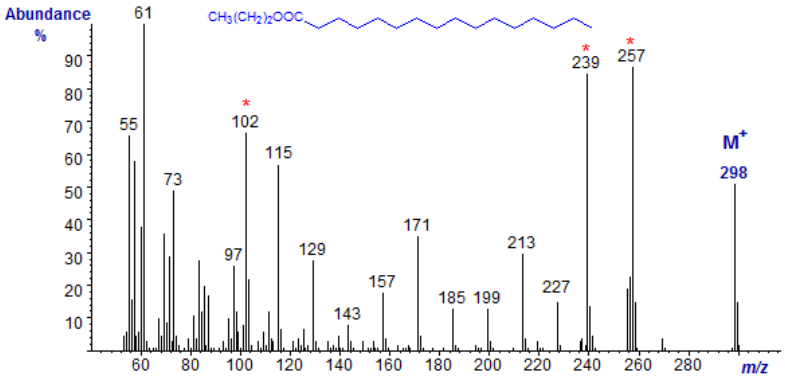

Fig. 3.4.2 A typical MS spectrum

3.4.3 Elemental Analysis (EA)

EA is a technique that through analyzing the elements report, such as Carbon (C), Hydrogen (H), Nitrogen (H) and Heteroatom (X, sulfur etc), regarding to the weight distribution for a measured sample, the purity of a sample or the structure of a known/unknown compound can be confirmed.

Taking the compound $C_{201}H_{212}N_8O_{16}$ as an example, the calculated mass fractions (%) for the CHN are C: 80.58, H: 7.13, N: 3.74 respectively, the obtained experimental data for the mass fractions (%) are: C: 80.72, H: 7.21, N: 3.99. Because the deviation for each element are all below 0.5% (C: 0.14%, H: 0.08%, N: 0.25%), thus, we can conclude that the compound $C_{201}H_{212}N_8O_{16}$ is the desired compound with high purity.

The detailed operation procedure is that after we load the sample, it will be burned in the instrument with excessive of oxygen gas to produce the combustion residual of water, CO_2 and the nitric oxide. And the measured weight for these compounds transfers into weight fraction calculated based on the H, C, N element.

3.3.4 Melting Point (m.p.)/Boilong Point (b.p)

The m.p. for a solid is the temperature when it changes from the solid state into the liquid state. M.p. is a basic physical property for the solid compounds and generally speaking, different solid compounds possess different m.p values. When measuring the m.p., the purity of the sample can be judged approximately because if the melting process for a solid lasts for a wide temperature range (> 5 ^{o}C), it implies that the solid may contain small amount of other impurity. If the solid is very pure, the melting temperature range will below 2 ^{o}C. Corresponding to the m.p, b.p. is the temperature when a liquid changes from the liquid state into the gaseous state. B.p is another basic physical property for the various solvents used in the lab. The b.p. must be checked carefully especially when doing different refluxing reactions.

3.5 Physical or Photoelectrical Characterizations

3.5.1 Ultraviolet–visible Spectroscopy (UV-Vis)

UV-Vis spectroscopy refers to an absorption spectrum ranging from the ultraviolet to visible region for samples in the solution or in the solid state. This technique has wide application for measuring inorganic metal ions, organic π-conjugated molecules or even biological macromolecules. In analytic chemistry, it can be used to determine quantitatively the regarding analytes through the internal calibration while in organic chemistry, the bandgap can be calculated by using the formula $E_g = 1240/\lambda_{max}$ (λ_{max} is the onset absorption of the UV-Vis spectrum). For the compound in the **Fig. 3.5.1.1**, the bandgap E_g can be calculated to be $E_g = 1240/560 = 2.21$ eV. Information for structure and molecule packing properties also can be roughly obtained by elucidating the various maximum absorption peaks.

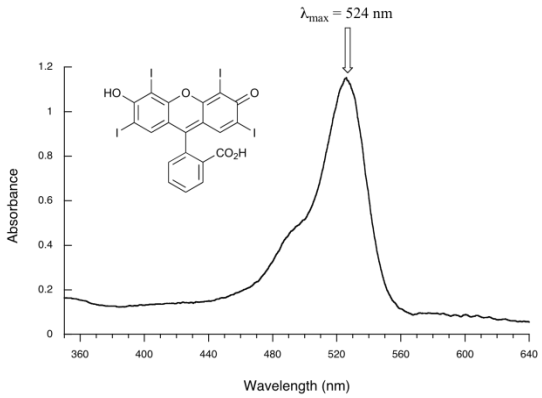

Fig. 3.5.1.1 A typical UV-Vis Spectrum

The principle is as showed in **Fig. 3.5.1.2**. For the molecules used for UV-Vis measurement, it normally has five energy levels: σ bonding & σ* anti-bonding; π bonding & π anti-bonding as well as the n non-bonding. The energy disparity between any of these energy levels is different from each other. Thus, when different energy in the form of ultraviolet or visible light acts on these energy levels, the electrons will absorb these energies and be excited to the high anti-bonding energy level and the UV-vis spectrum forms. The more difficult to excite the electrons, the shorter the onset wavelength for the spectrum and the larger the bandgap for the measured molecule is and vice versa. As showed in **Fig. 3.5.1.2**, the lowest bandgap for the measured molecule is from the n non-bonding energy level to π* anti-bonding energy level while the largest bandgap for the measured molecule is from the σ bonding energy level to the σ* anti-bonding energy level.

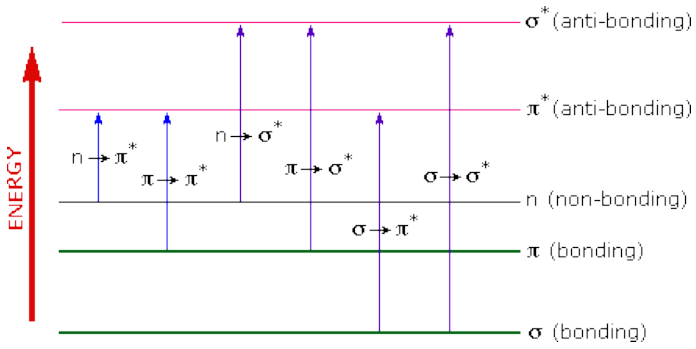

Fig. 3.5.1.2 Energy level diagram for a UV-Vis spectrum

UV/Vis **spectrophotometer** is the instrument used for the UV-Vis spectrum measurement. Firstly, the pure solvent was put into the holder and the intensity of the

light passing through this solvent was recorded as $\boldsymbol{I_o}$. Afterwards, the solution containing the measured sample was put into the holder again and the intensity of the light passing through this solution was recorded as (***I***). The absorbance, ***A*** , is calculated based on the following equation:

$$A = -\log(\%T/100\%)$$

Where *T* is often called the *transmittance (ratio of* $\boldsymbol{I}/\boldsymbol{I_o}$*), which is normally denoted as* as a percentage (%T). It is also denoted as Beer-Lambert Law shown in the following equation:

$$A = \varepsilon \; b \; c$$

Where ε is called the Molar Absorptivity, having unit of $M^{-1}cm^{-1}$, b is path length (cm) and the concentration of the absorbing species is measured in Molarity.

The basic parts of the spectrophotometer contain several parts as displayed in **Fig. 3.5.1.3**: the light source, monochromator, the holder for the sample/reference solution and the detector.

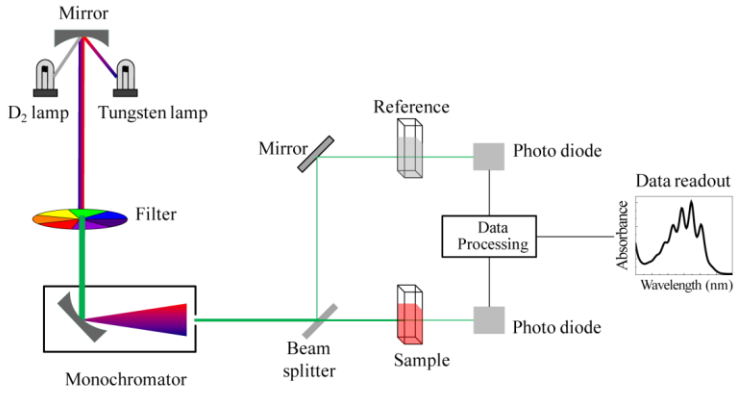

Fig. 3.5.1.3 Diagram of the spectrophotometer

The light source provides the light from ultraviolet region (190-400 nm) to visible region. Monochromator guarantees that the intensity is measured as a function of wavelength. Double holder contains reference holder, which allows transmission of 100% and the sample holder.

3.5.2 Fluorescence Spectroscopy

Fluorescence is the property of some atoms and molecules to absorb light at a particular

wavelength and to subsequently emit light of longer wavelength after a brief interval, termed the fluorescence lifetime. Fluorescence spectroscopy refers to an emission spectrum when a sample is excited. This technique has wide applications in measuring the quantum efficiency for a sample in solution, selecting the appropriate organic materials for OLED application and biological application for in vivo image or probe for detecting harmful substance in human bodies, etc.

The principle for the fluorescence mechanism is displayed as Jablonski diagram in **Fig. 3.5.2.1**. After an electron absorbs a high energy photon, the system is excited electronically and vibrationally. The system relaxes vibrationally, and eventually fluoresces at a longer wavelength. Because the energy associated with fluorescence emission transitions is typically less than that of absorption, the resulting emitted photons have less energy and are shifted to longer wavelengths.

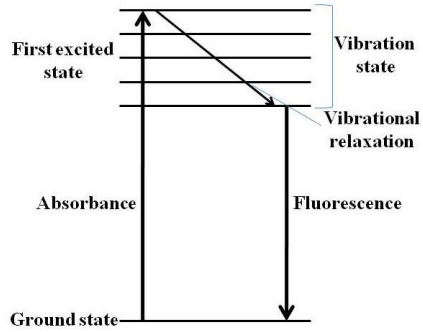

Fig. 3.5.2.1 Jablonski diagram of fluorescence

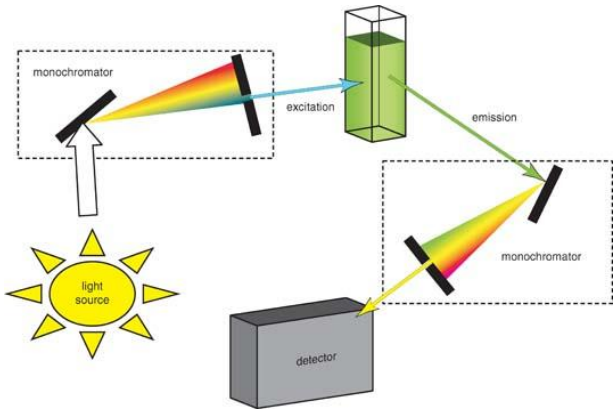

Fig. 3.5.2.2 Diagram of a fluorescence spectrometer

Light source

Light source provides the excitation energy in the form of UV-Vis light that ensures to

excite the measured sample from ground state to the excited state. There are various types of lamps used for light source, such as the Xe-Hg lamp, high-pressure Hg lamp arc and incandescent Xe lamp, etc.

Monochromator

Monochromator is utilized for providing the experimentally required light with a wavelength variation within 10 nm. There are two main types of monochromator: Diffraction grating and Prism..

Optical filter

Optical filter is another component inserted into the instrument for purifying the light again besides the monochromator. There are two classifications for the optical filter: colored filter and thin film filter. They are complementary to each other for the fluorescence measurement.

Detector

Detector is the component (an InGaAS array) used for accepting the emission light and transferring them into the corresponding spectrum rapidly and robustly.

3.5.3 Cyclic Voltammetry (CV)

CV is an electrochemical measurement to determine the electron transfer kinetics of the analyte, the possible intermediates in the redox reaction or the reduction/oxidation potential of an analyte. In this thesis, the CV technique is mainly used to obtain the data regarding to the onset of the reduction potential and oxidation potential of the organic semiconductor and calculate their LUMO and HOMO energy level. In addition, the bandgap of the organic molecule can also be obtained. The typical curve of CV is shown as follows: the working electrode potential is changed versus time.

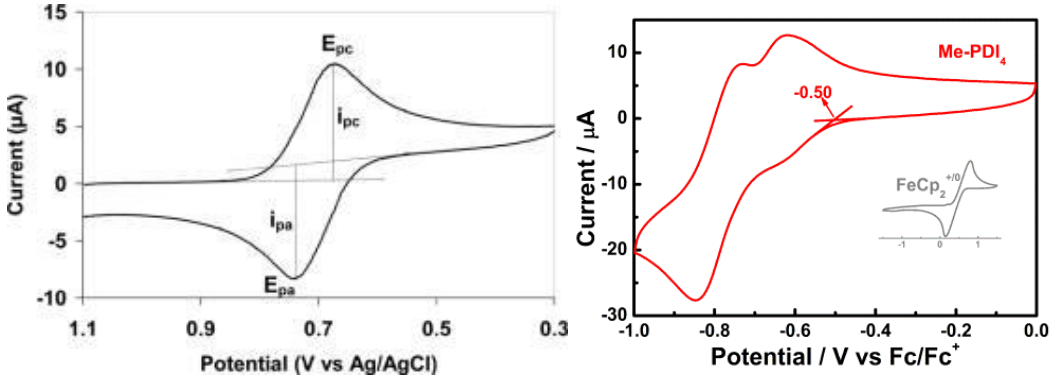

Fig. 3.5.3.1 Typical curve of CV

In **Fig. 3.5.3.1**(left) is shown the typical cyclic voltammogram where i_{pc} and i_{pa} display the peak cathodic and anodic current respectively for a reversible reaction. For the CV curve of Me-PDI_4, it is important to calculate its approximate LUMO energy. Hence, in the reduction region between 0 and –1.0 V, the E_{red}^{onset} = –0.5 V is firstly defined and then according to further calculation, its LUMO energy can be calculated.

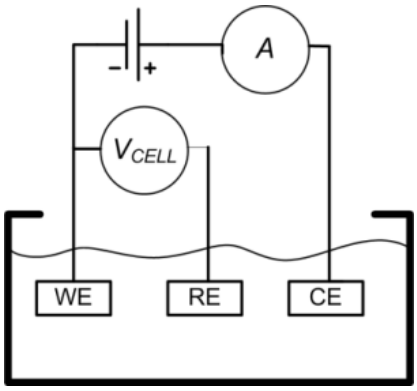

Fig. 3.5.3.2 Three-electrodes setup of CV measurement

A standard CV measurement setup contains three electrodes: working electrode (WE), reference electrode (RE) and counter electrode (CE), sometimes referred to a three-electrodes setup as displayed in **Fig. 3.5.3.2**. The three electrodes are immersed into the solution containing the measured sample. Between the WE and the RE is applied a voltage while at the same time, the current flowing between the WE and the CE is recorded and these data are exhibited as curves showed in **Fig. 3.5.3.1** by taking current (*i*) as Y-axis and potential (*E*) as X-axis. Electrolyte is usually added to ensure the sufficient conductivity.

3.5.4 Thermogravimetric Analysis (TGA)

TGA is a technique in which the changing amount of mass for the sample is measured as a function of temperature. (**Fig. 3.5.4.1**) The basic principle is that, at higher temperature, the measured TGA sample will lose or gain weight due to decomposition, oxidation reaction or leaving of the volatile components within the sample. Therefore, TGA can be used in the following fields:

1) To measure the decomposition temperature and learn the stability property for the

materiasl.

2) To investigate the behavior of the volatile components in a organic or inorganic materiasl.

3) To determine the content of the inorganic element (e.g. ash) in a sample, which can be used to predict the structure for the sample and simply as chemical analyzing method.

4) To study the decomposition mechanism for the measured materials.

As displayed in the Fig. **3.5.4.1**, the volatile components' behavior in the grease can be obtained through its TGA diagram. There are two types of volatiles in the grease: the high volatiles below 150 ^{o}C and the medium volatiles between 150 ^{o}C and 650 ^{o}C. In addition, when the temperature reaches higher than 750 ^{o}C, the inorganic ash will forms and the inorganic components in the sample can be determined.

In this thesis, TGA is mainly used for measuring the decomposition temperature for the newly developed molecules and their stability property.

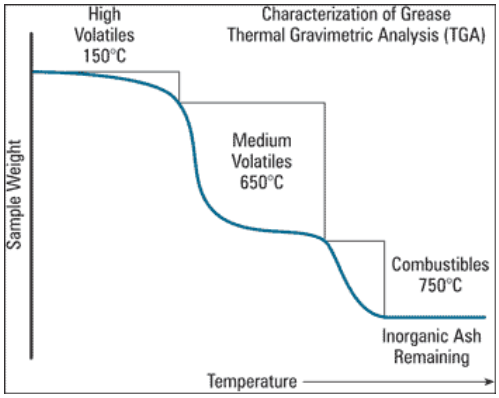

Fig. 3.5.4.1 A typical TGA curve for grease

Thermogravimetric instrumentation should include several basic components to provide the flexibility necessary for the production of useful analytical data:

a) A balance; b) A heating device,

c) A unit for temperature measurement and control,

d) A means for automatically recording the mass and temperature changes,

e) A system to control the atmosphere around the sample.

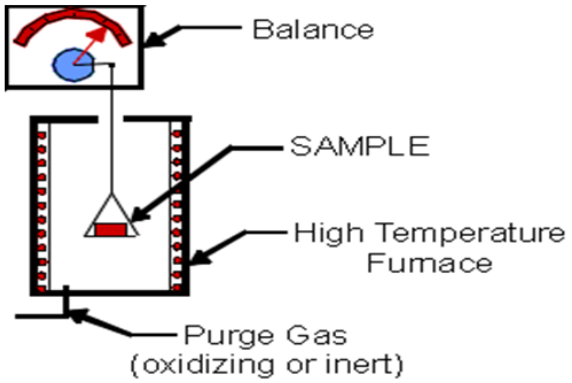

Fig. 3.5.4.2 Structure of a thermogravimetry

3.5.5 Differential Scanning Calorimetry (DSC)

Similar to TGA, DSC is another thermo-analytical technique in which the changing amount of heat for the sample is recorded as a function of temperature, while the measurements are controlled by a temperature program.

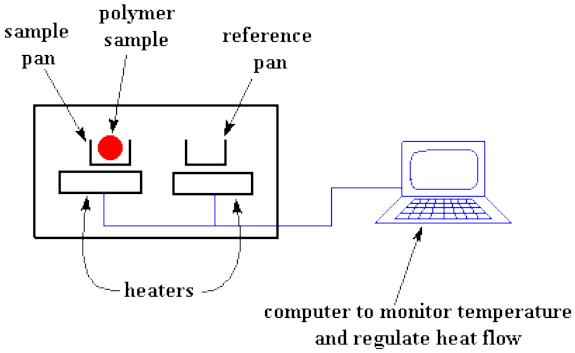

Fig. 3.5.5.1 Structure of a DSC instrument

For the instruments, there are two pan holders, heaters and recording computer. For the pans, one is for reference and another one is for holding the sample. Each pan is put on top of a heater during the measuring process. The heating rate is kept exactly constant through the whole experiment to minimize the systematic error. (**Fig.3.5.5.1**)

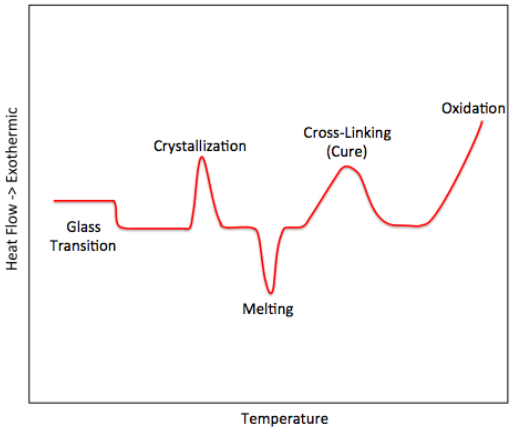

Fig. 3.5.5.2 A typical curve of a DSC

When there are phase transition companied with exothermic or endothermic phenomena, they will be displayed as crystallization peak or melting peak. As displayed in **Fig. 3.5.5.2**, when a sample is heated up and reaches the crystalline region, it will release heat due to the phase transition. In this case, with the excessive heat imported by the sample, the instrument needs to decrease the heat supply to keep the heat rate constant. Thus, the decreased amount of heat is displayed as the crystallization peak on a DSC curve. On the contrary, when the temperature continues increase and the sample reaches the melting region, it needs absorb excessive energy to finish the transfer from the solid state to the liquid state. In this case, the instrument needs to provide more heat to keep the heating rate constant. Hence, there will be a melting peak indicating these additional heats.

3.5.6 Atomic-force Microscopy (AFM)

AFM is a scanning probe technique to move on the sample surface and provide the information of the sample surface with very high resolution on the order of nanometer level, about 1000 fold better than the optical diffraction limit. (**Fig. 3.5.6.1**)

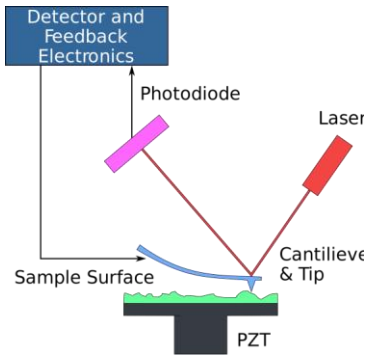

Fig. 3.5.6.1 Structure of the AFM instrument

The instrument mainly contains tips, cantilever tip, photodiode and detectors. The AFM works by employing an ultra-fine needle attached to a cantilever beam. The tip of the needle runs over the ridges and valleys on the surface of the material being imaged. As the tip moves up and down due to the roughness of the surface, the cantilever deflects at the same time. In one basic configuration, a laser shines on the cantilever at an oblique angle, and allows for the direct measurement of the deflection in the cantilever by simply changing the angle of incidence for the laser beam. In this way, an image may be created revealing the configuration of the molecules being imaged by the machine

The AFM has been widely applied in various disciplines, including surface chemistry, polymer chemistry and physics, solid state films, cell biology, molecular biology, and medicine.

For example, in the surface and solid state physics fields, the AFM is used for (a) the identifying the behavior of atom in a pattern on a surface, (b) evaluating the interactions between a specific atom and its neighboring atoms. In this thesis, the AFM is an important technique to investigate the surface morphology of the device film and speculate the relationship between the device performance and the film morphology.

3.5.7 X-ray Powder Diffraction (XRD)

XRD is widely used analytical technique to decipher the internal information for a crystalline materials sample, providing structure data regarding to unit cell dimensions. The primary principle for XRD technique is based on the constructive interference between X-rays and the internal atoms/molecules within the sample. As showed in **Fig. 3.5.7.1**, when the X-rays are irradiated into the crystalline sample, these lights will interact with the atoms or molecules within the sample to produce the constructive interference, leading to the refraction of these lights. When some of these X-rays meet the conditions for the following Bragg's law:

$n\lambda=2d\sin\theta$

The diffracted X-rays will be detected and processed. By changing the scanning 2θ angles with the sample, all the possible diffraction information about the internal lattices/elements within the crystalline sample could be obtained because of the casual

directions for the powdered sample.

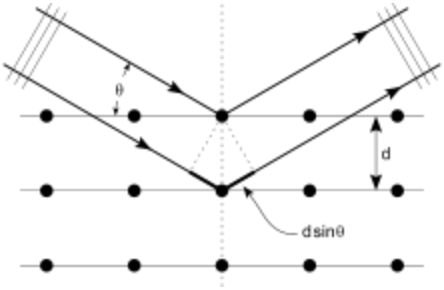

Fig. 3.5.7.1 Interaction between the incident X-ray and the atoms within a sample

XRD data was collected through the X-ray diffractometers that is generally constituted by three basic components: the X-ray tube, a sample holder and the detector.(**Fig. 3.5.7.2**) X-rays tube is used for generating the X-rays through heating a filament to produce the high energy electrons, which are accelerated under the assistance of a applied voltage. These electrons will bombard the target sample to dislodge inner shell electrons and the corresponding XRD curve spectrum will be formed.

The sample holder is used to hold the sample and receive the X-rays functions

The X-rays detector receives the diffraction and transfers these data into XRD spectrum.

The dynamic behavior to collect XRD data from a sample for an X-ray diffractometer is that the sample rotates with an angle θ in the diffractometer on the pathway of the collimated X-ray beam while the X-ray detector rotates with an angle of 2θ to collect the diffracted X-rays data.

Filtering is sometimes necessary to produce experimentally needed monochromatic X-rays for diffraction, realized by monochrometer or foil component. Single crystal structure is very important for explaining the materials properties due to the different packing for organic conjugation molecules. With Cu K_α radiation = 1.5418Å, copper is the mostly utilized target metal for single-crystal diffraction. These X-rays are collimated to irradiate onto the measured crystalline sample. The intensity of the reflected X-rays is recorded down when the detector and the sample rotate.

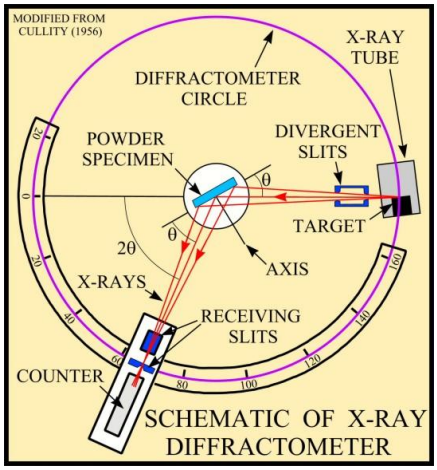

Fig. 3.5.7.2 Structure of x-ray diffractometer

For typical powder patterns, data is collected at 2θ from ~5 to 70 angles that are preset in the X-ray. (**Fig. 3.5.7.3**) Conversion of the diffraction peaks to *d*-spacings allows confirmation of the mineral sample because each mineral sample has a series of its own *d*-spacings values. Normally, this is achieved by comparing the experimentally obtained d-spacing data with standard database reference patterns. XRD technique is frequently utilized for identifying the unknown crystalline samples (e.g. minerals, organic compounds, inorganic compounds etc). It is used to 1) characterize the crystalline samples; 2) identify the components for some fine-grained minerals samples that are difficult to analyze through optical methods, e.g. clays; and 3) identify the unit cell. In this thesis, the XRD is used to characterize the device film and investigate the packing information of the active materials within the film and speculate the correlation between the device performance with the packing mode.

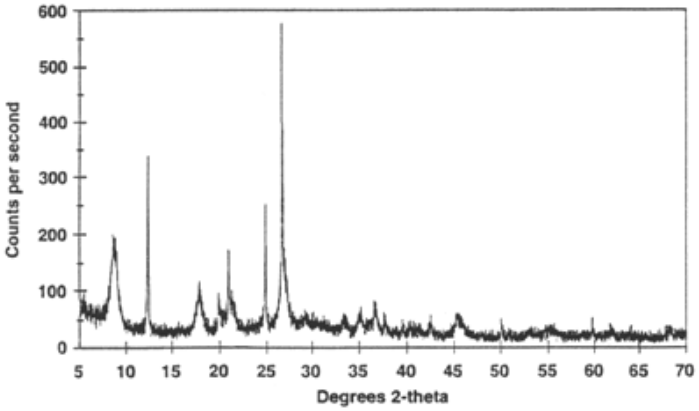

Fig. 3.5.7.3 A typical XRD curve

3.5.8 Transmission Electron Microscopy (TEM)

Similar with the AFM technique, TEM is another microscopy technique with high resolution to provide the surface information for an ultra-thin sample. The basic principle is that the electron gun emits electrons with very high energy to the surface of the specimen. (**Fig. 3.5.8**) Afterwards, these electrons will interact with atoms/elements within the samples and passed through the film. An image will be formed from interaction of the transmitting electrons, magnified and focused on one fluorescent screens. Within a TEM instrument, the lens functionalizes to magnify the image for the samples. The objective lens normally is the most significant lens because it determines how the sample will be illuminated with electrons.

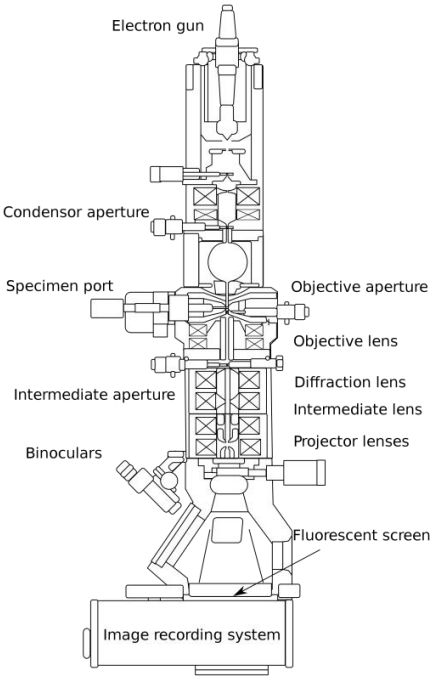

Fig. 3.5.8 A TEM instrument

TEM is also widely in various fields ranging from chemical, physical, materials science to biological science. Due to the extremely short de Broglie wavelength for the electrons, TEM has the capability to image the sample with much higher resolution than the normal optical microscopes. Therefore, the measured substance, as small as atomic level, can still be imaged and studied through the TEM technique. Hence, the detailed information for a specimen can be obtained and analyzed. For a sample with higher thickness, due to the

loss of electrons absorbed by the sample, there are smaller magnifications TEM image contrast. In this thesis, TEM technique is used for investigating the film morphology information for the donor and acceptor materials distribution and summarizing the relationship between the PCE performance and the morphology.

Chapter 4

Preparation of the Novel Fused-Heteroaromatic-Diones through a Concise and Efficient Double F-C Acylation Reaction

Development of novel building block is very important for design and synthesis of novel organic functional materials for OSCs. In this chapter, the intramolecular double F–C acylation method is adopted to obtain various novel fused heteroaromatic diones (12 samples using 2,2'-dithiophene, 2,2'-difuran, 2,2'-diselenophene, and 2,2'-dipyrrole as cores) with 16%–85% yield, which are promising n-type semiconductor materials for various applications. It is found out that the electron-donating groups favor the reaction and bulky substituted group can increase the reaction yield. The fact that the yield is low to moderate may be ascribed to the low reaction selectivity of 3, 4 positions on thiophene. In addition, substrates with electron-withdrawing groups show no reaction.

*This section has been published substantially as: W. Chen *et al*, *Org. Chem. Front*., **2014**, *1*, 391–394 (2014 hot paper)

4.1 Introduction

Developing novel n-type organic semiconductor building blocks for organic solar cells and organic field-effect transistor is a long-term target for chemist and materials science researchers. During the past decades, various efficient units have been developed as shown below (**Fig. 4.1.1**) and used widely in organic electronics.[1-3]

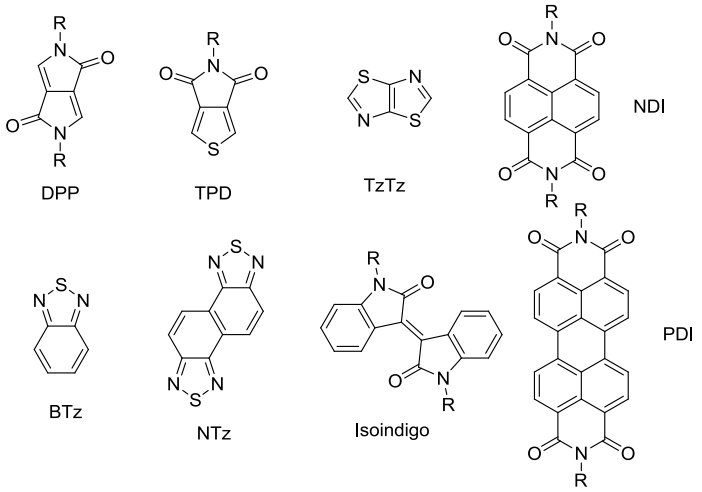

Fig. 4.1.1 Reported electron-deficient building blocks for n-type semiconductors

Among all of these building block, the fused aromatic/hetero-aromatic diones have been proven as powerful building blocks to construct various π-conjugated compounds ranging from small molecules to large π-conjugated polymers, which are commonly applied for OSCs, [4, 5] OFETs,[6-8] lithium-ion batteries,[9] sensors[10-12] phototransistor devices,[13] and optical waveguides,[14]. Especially, fused hetero-aromatic diones are appealing because by varying the position, type as well as valence of hetero-atoms, the properties and characteristics of new materials could also be tuned.[15] Thus, it is very interesting to develop an efficient method for preparing these fused hetero-aromatic diones.

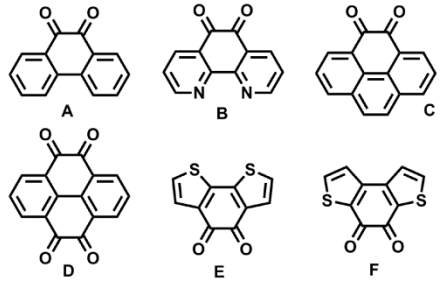

Fig. 4.1.2 Reported structures of fused diones

However, for the fused heteroaromatic diones, there are still not efficient and universal methods to obtain them. Taking the benzo-[2,1-b:3,4-b']-dithiophene-4,5-dione (BDTD) core as an example, there are generally three methods to prepare it (**Scheme 4.1.1**):

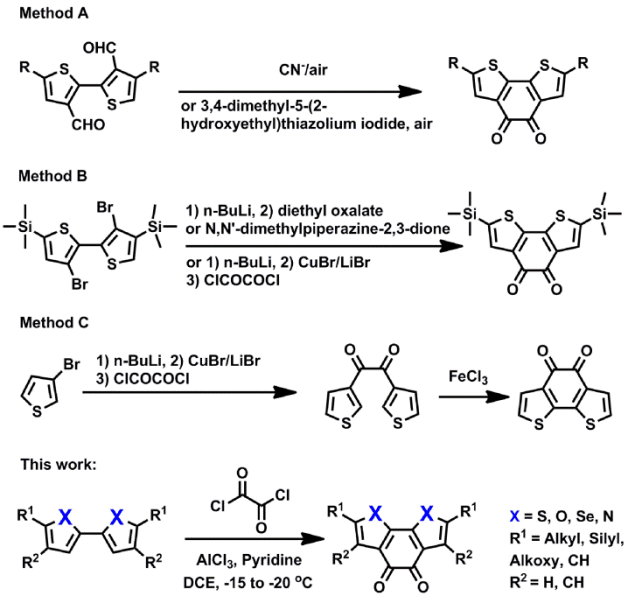

Scheme 4.1.1 The synthetic methods to prepare the fused heteroaromatic diones

a) Substituted 3,3-dialdehyde-2,2'-bithiophene substrate undergoes the intramolecular benzoin condensation in the presence of cyanide reagent or 3,4-dimethyl-5-(2-hydroxyethyl)thiazolium iodide followed by aerial oxidation. (Method A)[16, 17]

b) The bithiophene substrate with two Br groups on the 3,3 positions reacts with n-butyllithium reagent to form the lithium intermediate, which is subsequently converted into diones by reacting with the electrophile reagent N,N'-dimethylpiperazine-2,3-dione or diethyl oxalate or by reacting with CuBr/LiBr followed by oxalyl chloride (Method B) [15, 18]

(c) 3-Bromo-thiophene first reacts with n-butyllithium and is then transformed to diones by reaction with N,N'-dimethylpiperazine-2,3-dione or oxalyl chloride reagent. Subsequently, the target fused heteroaromatic dione molecule can be obtained in high yield through the carbon-carbon coupling reaction between two thiophenes using $FeCl_3$ as the catalyst. (Method 2c). [18, 19]

However, these above-mentioned methods might not be applicable for synthesizing other types of interesting fused heteroaromatic diones with bipyrrole, bifuran and biselenophene cores due to the following several points:

(1) Certain intermediates need multiple steps to prepare and they are not commercial available.

(2) Each time, only one kind of dione can be obtained.

(3) Some of the chemical reagents, such as cyanide, are very poisonous and harmful to the environment.

Thus, it should be highly desirable and challenging to develop a general, concise and efficient method to address these problems. In this work, various novel fused heteroaromatic diones (X= S, Se, O, N) are designed and synthesized through a one-step simple intramolecular double F-C acylation.

4.2 Experimental Methods

4.2.1 Preparation of various substrates and the analytical data

5,5'-di-*t*-butyl-2,2'-bithiophene(1b)[20]:

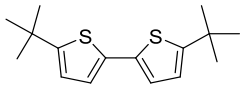

The title compound was prepared based on the modified literature method. $PdCl_2(PhCN)_2$ (0.132 g, 0.34 mmol), 2-*t*-butylthiophene[21] (0.80 g, 5.71 mmol) and anhydrous DMSO (30.0 mL) were placed in a two-neck 100 mL flask. To this was added silver(I) fluoride (1.53 g, 12.0 mmol), and the resulting mixture was stirred at 60 ℃ for 6 h under Argon atmosphere. The resulting mixture solution was cooled down to r.t. and passed through a pad of Celite, which was successively washed well with DCM. The filtrate was washed with water (60 mL) and the aqueous layer was extracted with DCM (100 mL x 3). The combined organic layer was dried over anhydrous Na_2SO_4 and then concentrated under reduced pressure to leave a crude product. Purification by CC using hexane gave 5,5'-di-*t*-butyl-2,2'-bithiophene (white solid, 450 mg, 56% yield).^{1}H-NMR (Chloroform-d**,** 400 MHz): δ 1.39 (s, 18H), 6.70 (d, *J* = 3.6 Hz, 2H), 6.90 (d, *J* = 3.6 Hz, 2H); ^{13}C-NMR (Chloroform-d, 100 MHz): δ 32.4, 34.6, 121.8, 122.3, 134.8, 156.2; HRMS: calculated for $C_{16}H_{22}S_2 + H^+$, 279.1241; found: 279.1252 (M+).

5,5'-Bis(trimethylsilyl)-2,2'-bithiophene (1d)[22]:

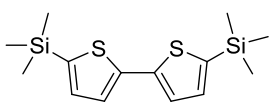

The title compound was prepared using the literature method. ^{1}H-NMR (Chloroform-d, 300 MHz): δ 0.33 (s, 18H), 7.13 (d, *J* = 3.6 Hz, 2H), 7.23 (d, *J* = 3.3 Hz, 2H).

5,5'-Bis(triisopropylsilyl)-2,2'-bithiophene (**1e**)[23]:

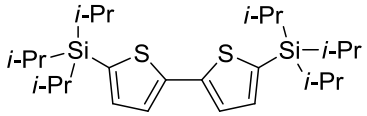

The title compound was prepared using the modified literature method. *n*-BuLi (2.5M in hexane, 5.0 mL, 12.5 mmol) was injected drop by drop to a solution of 2,2-bithiophene (1.0 g, 6.0 mmol) in 22 mL anhydrous THF at −78 ℃ in Argon atmosphere. The mixtures solution was stirred at −78 °C for 30 min, followed by addition of triisopropylsilyl chloride (2.4 g, 2.75 mL, 12.6 mmol). After stirring at r.t for 3 hrs, hexane was added and the organic phase was separated and washed with water, dried through anhydrous Na_2SO_4, filtered. The solvent in the filtrate was removed *in vacuo* to give the residue, which was subjected to CC (hexane as eluent) to give **1e** (white solid, 2.1 g, 73%). ^{1}H-NMR (Chloroform-d, 300 MHz): δ 1.15–1.13 (d, 36H), 1.41–1.28 (m, 6H), 7.16 (d, *J* = 3.6 Hz, 2H), 7.31 (d, *J* = 3.3 Hz, 2H),; ^{13}C-NMR (Chloroform-d, 75 MHz): δ 11.8, 18.6, 124.7, 133.5, 136.4, 142.4; HRMS: calculated for $C_{26}H_{46}S_2Si_2 + H^+$, 479.2658; found: 479.2690 (M+).

5,5'-dimethoxyl-2,2'-bithiophene(1f)[24]:

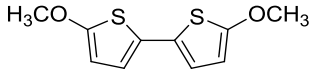

The title compound was prepared using the literature method. ^{1}H-NMR (Chloroform-d, 300 MHz): δ 3.88 (s, 6H), 6.07 (d, *J* = 3.9 Hz, 2H), 6.61 (d, *J* = 3.9 Hz, 2H),

5,5'-diacetyl-2,2'-bithiophene(1g)[25]:

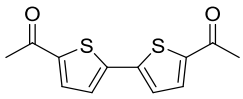

The title compound was prepared using the literature method. ^{1}H-NMR (Chloroform-d, 300 MHz): δ 2.57 (s, 6H), 7.30 (d, *J* = 3.0 Hz, 2H), 7.61 (d, *J* = 3.0 Hz, 2H).

5,5'-Bis(trimethylsilyl)-2,2'-bifuran(3a)[26]:

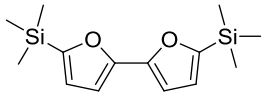

The title compound was prepared using the modified literature method. *n*-BuLi (2.5M in

hexane, 4.0 mL, 10.0 mmol) was injected drop by drop into a solution of 2,2'-bifuran (600 mg, 4.48 mmol) in 40 mL anhydrous THF at −78 °C in Argon atmosphere. The solution was stirred at −78 °C for 30 mins and at r.t. for another 1 h. The solution was cooled down again to −78 °C and the chlorotrimethylsilane (1.07 g, 1.28 mL, 9.8 mmol) was added dropwise. After stirring at r.t. for 3 hrs, the mixture was quenched with water, extracted with hexane, dried through anhydrous Na_2SO_4, filtered, and concentrated *in vacuo* to give the residue, which was subjected to CC (hexane as eluent) to give **1j** (white solid, 312 mg, 25%). ^{1}H-NMR (Chloroform-d, 400 MHz): δ 0.29 (s, 18H), 6.57 (s, 2H), 6.65 (s, 2H),; ^{13}C-NMR (Chloroform-d, 100 MHz): δ –1.57, 105.4, 121.1, 150.8, 159.8; HRMS: calculated for $C_{16}H_{22}O_2Si_2 + H^+$, 279.1237; found: 279.1246 (M+).

5,5'-Bis(trimethylsilyl)-2,2'-biselenophene(3b)[27]:

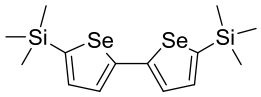

The title compound was prepared using the modified literature method. *n*-BuLi (2.5M in hexane, 1.8 mL, 4.5 mmol) was injected drop by drop to a solution of 2,2'-biselenophene (520 mg, 2.0 mmol) in 20 mL anhydrous THF at −78 °C in Argon atmosphere. The mixture solution was stirred at −78 °C for 30 mins and at r.t. for another 1 h. The solution was cooled down again to −78 °C and the chlorotrimethylsilane (480 mg, 0.56 mL, 4.4 mmol) was added dropwise. After stirring at r.t. for 6 hrs, hexane was added and the organic phase was separated and washed with water, dried through anhydrous Na_2SO_4, filtered, and concentrated *in vacuo* to give the residue, which was subjected to CC (hexane as eluent) to give **1i** (white solid, 210 mg, 26%). ^{1}H-NMR (Chloroform-d, 400 MHz): δ 0.32 (s, 18H), 7.31 (d, *J* = 2.8 Hz, 2H), 7.38 (d, *J* = 3.2 Hz, 2H); ^{13}C-NMR (Chloroform-d, 100 MHz): δ 0.22, 128.5, 136.9, 148.3, 149.4; HRMS: calculated for $C_{14}H_{22}Se_2Si_2 + H^+$, 406.9669; found: 406.9667 (M+).

1,1-dimethyl-5,5'-dimethyl-2,2'-bipyrrole(3c)[28]:

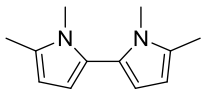

The title compound was prepared using the modified literature method. *N,N'*-dimethyl-2,2'-bipyrrole[29] (1.6 g, 10 mmol) and THF (20 mL) were added to a nitrogen purged three-neck round-bottom flask and cooled down to –78 ℃. *n*BuLi (2.5M in hexane, 10

mL, 25 mmol) was injected drop by drop and the solution was stirred overnight, allowing to warm slowly to r.t.. The solution was again cooled down to –78 ℃ and methyl iodide (1.86 mL, 30 mmol) was added in slowly. The reaction was stirred at –78 ℃ for 4 h and was then allowed to warm slowly for 24 h. The reaction was quenched by adding H_2O (20 mL) and was then extracted with Et_2O. The organic phase was separated and dried with anhydrous $MgSO_4$, filtered, and concentrated *in vacuo* to give the residue, which was subjected to CC using neutral aluminum oxide (hexane: EA = 30:1) to give **1k** (white solid, 242 mg, 13%).^{1}H-NMR (Chloroform-d, 400 MHz): 2.28 (s, 6H), 3.35 (s, 6H), 5.95 (d, *J* = 2.8 Hz, 2H), 6.06 (d, *J* = 3.2 Hz, 2H); ^{13}C-NMR (Chloroform-d, 100 MHz): δ 12.7, 31.0, 105.7, 109.4, 124.9, 129.5; HRMS: calculated for $C_{12}H_{16}N_2 + H^+$, 189.1392; found: 189.1386 (M+).

2,2'-Bibenzofuran(5a)[30]:

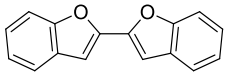

The title compound was prepared using the literature method. ^{1}H-NMR (Chloroform-d, 400 MHz): δ 7.17 (s, 2H), 7.35–7.26 (m, 4H), 7.55 (d, *J* = 8.0 Hz, 2H), 7.63 (d, *J* = 8.0 Hz, 2H).

2,2'-Bibenzothiophene(5b)[31]:

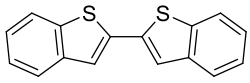

The title compound was prepared using the literature method. ^{1}H-NMR (Chloroform-d, 400 MHz): δ 7.37–7.31 (m, 4H), 7.52 (s, 2H), 7.83–7.76 (m, 4H).

1-*n*-hexylindole[32]:

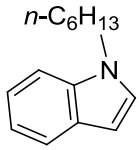

The title compound was prepared using the literature method. ^{1}H-NMR (Chloroform-d, 400 MHz): δ 0.89 (t, *J* = 6.4 Hz, 3H), 1.32 (s, 6H), 1.87–1.81 (m, 2H), 4.13 (t, *J* = 6.8 Hz, 2H), 6.50 (d, *J* = 2.4 Hz, 1H), 7.13–7.10 (m, 1H), 7.26–7.20 (m, 1H), 7.36 (d, *J* = 8.4 Hz, 1H), 7.65 (d, *J* = 8.0 Hz, 1H).

1,1'-di-*n*-hexyl-2,2'-Bibenzoindole(5c)[33]:

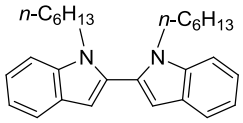

The title compound was prepared using the modified literature method. *n*-BuLi (1.6M in hexane, 6.3 mL, 10.0 mmol) was injected drop by drop to a solution of 1-*n*-hexylindole (1.7 g, 8.5 mmol) in dry 30 mL THF at 0 ℃ under an Argon atmosphere. The mixture was heated at refluxing temperature for 4 hrs and then cooled down to r.t.. Anhydrous $CuCl_2$ (0.94 g, 7 mmol) was then added in one portion and the mixture again heated under refluxing for 2 hrs. After being allowed to cool to r.t., the mixture was left to stand for 1 hour before poured into ice/water. The dirty brown-green precipitate was filtered off and washed with DCM, the organic layer was separated, and the aqueous phase was extracted with DCM two times. The combined organic phase was dried with anhydrous Na_2SO_4, filtered, and concentrated *in vacuo* to give the residue, which was subjected to CC (hexane: DCM = 20:1) to give **1n** (sticky liquid, 565 mg, 33%). ^{1}H-NMR (Chloroform-d, 400 MHz): δ 0.82 (t, *J* = 6.4 Hz, 6H), 1.21 (s, 12H), 1.73–1.68 (m, 4H), 4.10 (t, *J* = 7.6 Hz, 4H), 6.65 (s, 2H), 7.20 (t, *J* = 7.6 Hz, 2H), 7.31 (t, *J* = 7.6 Hz, 2H), 7.45 (d, *J* = 8.0 Hz, 2H), 7.72 (d, *J* = 8.0 Hz, 2H); ^{13}C-NMR (Chloroform-d, 100 MHz): δ 13.9, 22.5, 26.5, 30.0, 31.3, 44.1, 104.6, 110.1, 119.7, 120.9, 122.0, 127.8, 131.1, 136.8; HRMS: calculated for $C_{28}H_{36}N_2 + H^+$, 401.2957; found: 401.2979 (M+).

4.2.2 Typical procedure of the Friedal-Crafts acylation and the analytical data

Typical procedures of the Friedal-Crafts Acylation with substrate **5,5'-dimethyl-2,2'-bithiophene(1a):**

600 mg $AlCl_3$ (4.5 mmol) was added into a flask under an Argon atmosphere, 15 ml 1,2-DCE was injected into the flask and the solution was cooled down to –20 ℃ using a NaCl ice bath. Subsequently, 0.5 ml 1,2-DCE containing 229 mg of oxalyl chloride (1.8 mmol) was added slowly into the solution firstly and secondly, another 1.0 ml 1,2-DCE containing 292 mg dimethyl-2,2'-bithiophene **1a** (1.5 mmol) and 284 mg pyridine (3.6 mmol) was injected into the solution dropwise through 0.5 hrs. After finishing the injection, the reaction was kept with stirring between –20 °C and –15 °C for about 20 mins and the temperature was raised to 0 °C. The mixture was dropped onto ice and extracted

with DCM. The organic DCM layer was washed with water several times, saturated NaCl solution one time, dried through anhydrous $MgSO_4$, filtrated and concentrated in vacuo to give the residue, which was purified by CC taking DCM as eluent to give **2a** as a blue solid (120 mg, 32%).

2,7-dimethylbenzo[2,1-b:3,4-b']dithiophene-4,5-diones(2a):

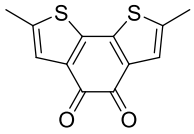

Yield: 32%. Blue solid; ^{1}H-NMR (Chloroform-d, 300 MHz): δ 2.45 (s, 6H), 7.08 (s, 2H); ^{13}C-NMR (Chloroform-d, 100 MHz): δ 15.2, 125.2, 134.8, 140.4, 142.7, 174.4; HRMS: calculated for $C_{12}H_8O_2S_2 + H^+$, 249.0044; found: 249.0027 (M+).

Typical ^{1}H-NMR for **2a**

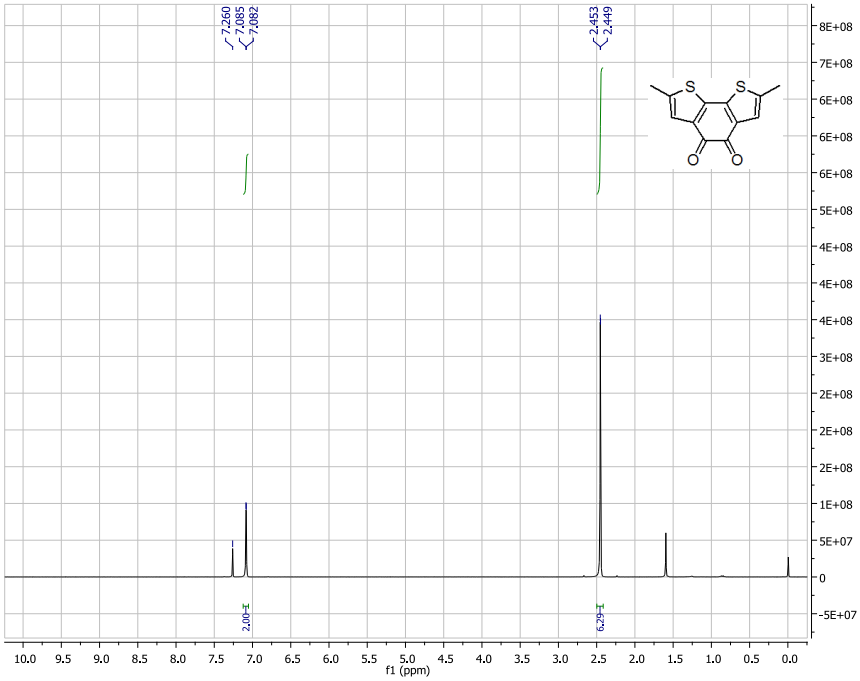

Typical ^{13}C-NMRfor **2a**:

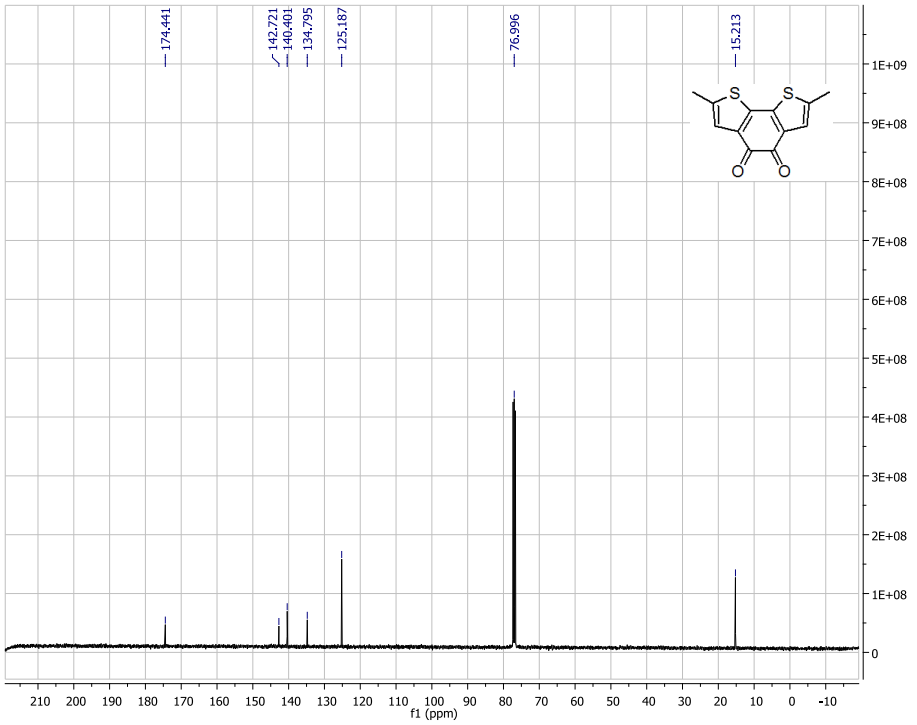

Typical HR MS spectrum for **2a:**

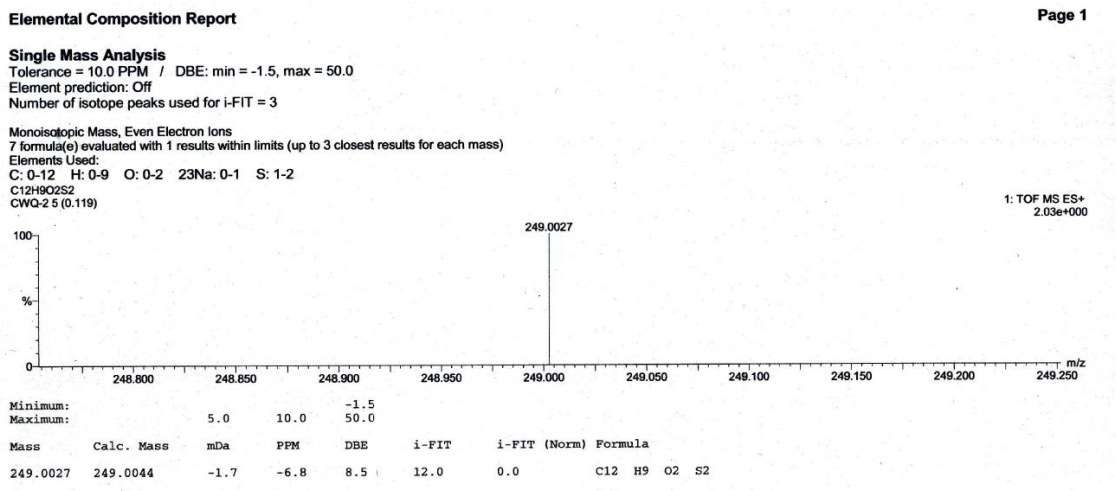

The following compounds were obtained using a similar method to that described above. For the CC condition, the ratio of DCM : hexane ranges from 1:1 to pure DCM. For some substrates, due to their low solubility, they needed to be sonicated for 10 min to 30 min to make them easy to inject into the flask.

2,7-di-*t*-butylbenzo[2,1-b:3,4-b']dithiophene-4,5-diones(2b):

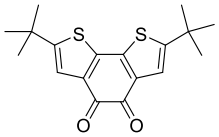

Yield: 48%. Blue solid; ^{1}H-NMR (Chloroform-d, 300 MHz): δ 1.38 (s, 18H), 7.16 (s, 2H); ^{13}C-NMR (Chloroform-d, 75 MHz): δ 32.0, 34.9, 121.4, 134.4, 142.3, 158.3, 174.8; HRMS: calculated for $C_{18}H_{20}O_2S_2 + H^+$, 333.0983; found: 333.0981 (M+).

2,7-di-*n*-hexylbenzo[2,1-b:3,4-b']dithiophene-4,5-diones(2c):

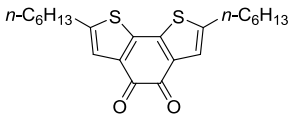

Yield: 37%. Blue solid; ^{1}H-NMR (Chloroform-d, 300 MHz): δ 0.90 (t, *J* = 6.6 Hz, 6H), 1.39–1.25 (s, 12H), 1.74–1.32 (m, 4H), 2.75 (t, *J* = 7.5 Hz, 4H), 7.11 (s, 2H); ^{13}C-NMR (Chloroform-d, 100 MHz): δ 14.0, 22.5, 28.5, 29.8, 30.9, 31.4, 124.0, 134.6, 142.6, 146.5, 174.7; HRMS: calculated for $C_{22}H_{28}O_2S_2 + H^+$, 389.1609; found: 389.1613 (M+).

2**,7-Bis(trimethylsilyl)benzo[2,1-b:3,4-b']dithiophene-4,5-diones(2d)**[15]:

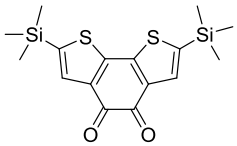

Yield: 28%. ^{1}H-NMR (Chloroform-d, 400 MHz): δ 0.34 (s, 18H), 7.57 (s, 2H).

2,7-Bis(triisopropylsilyl)benzo[2,1-b:3,4-b']dithiophene-4,5-diones(2e):

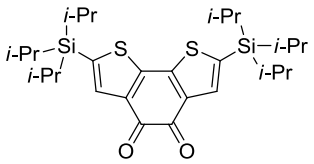

Yield: 45%. Blue solid; ^{1}H-NMR (Chloroform-d, 300 MHz): δ 1.13–1.11 (d, 36H), 1.40–1.30 (m, 6H), 7.62 (s, 2H); ^{13}C-NMR (Chloroform-d, 100 MHz): 11.6, 18.4, 135.7, 135.9, 136.8, 148.4, 175.3; HRMS: calculated for $C_{28}H_{44}O_2S_2Si_2 + H^+$, 533.2400; found: 533.2394.2690 (M+).

2,7-dimethoxylbenzo[2,1-b:3,4-b']dithiophene-4,5-diones(2f):

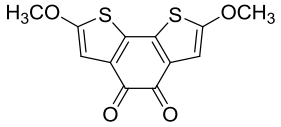

Yield: 25%. Blue solid; ^{1}H-NMR (Chloroform-d, 300 MHz): δ 3.92 (s, 6H), 6.48 (s, 2H); ^{13}C-NMR (Chloroform-d, 100 MHz): δ 60.5, 102.1, 132.6, 133.0, 165.2, 174.0; HRMS: calculated for $C_{12}H_9O_4S_2 + H^+$, 280.9942; found: 280.9941 (M+).

2,7-Bis(trimethylsilyl)benzo[2,1-b:3,4-b']difuran-4,5-diones(4a):

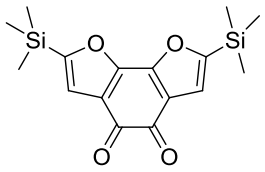

Yield: 16%. Red solid. ^{1}H-NMR (Chloroform-d, 400 MHz): δ 0.35 (s, 18H), 6.96 (s, 2H); ^{13}C-NMR (Chloroform-d, 100 MHz): δ –1.94, 118.5, 120.1, 155.5, 165.7, 176.0; HRMS: calculated for $C_{16}H_{22}S_2 + H^+$, 279.1237; found: 279.1246 (M+). HRMS: calculated for $C_{16}H_{20}O_4Si_2 + H^+$, 333.0556; found: 333.0569 (M+).

2,7-Bis(trimethylsilyl)benzo[2,1-b:3,4-b']diselenophene-4,5-diones(4b)[15]:

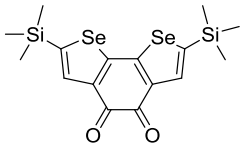

Yield: 37%. ^{1}H-NMR (Chloroform-d, 400 MHz): δ 0.34 (s, 18H), 7.91 (s, 2H).

1,1-dimethyl-2,7-dimethylbenzo[2,1-b:3,4-b']dipyrrole-4,5-diones(4c):

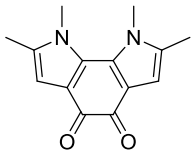

Yield: 32%. Deep-Blue solid. ^{1}H-NMR (Chloroform-d, 400 MHz): δ 2.15 (s, 6H), 3.61 (s, 6H), 6.20 (s, 2H); ^{13}C-NMR (Chloroform-d, 100 MHz): δ 12.6, 35.8, 109.3, 120.0, 134.0, 134.1, 176.9; HRMS: calculated for $C_{14}H_{14}N_2O_2 + H^+$, 243.1134; found: 243.1128 (M+).

Dibenzo[d,d']benzo[2,1-b:3,4-b']difuran-6,7-diones(6a):

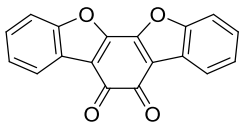

Yield: 35%. Dark-purple solid. ^{1}H-NMR (Chloroform-d, 400 MHz): δ 7.48–7.46 (m, 4H), 7.67–7.65 (m, 2H), 8.14–8.12 (m, 2H); ^{13}C-NMR (Chloroform-d, 100 MHz): δ 112.4, 116.6, 122.3, 123.5, 126.4, 127.6, 153.1, 156.4, 175.5; HRMS: calculated for $C_{18}H_8O_4 + H^+$, 289.0501; found: 289.0494 (M+).

Dibenzo[d,d']benzo[2,1-b:3,4-b']dithiophene-6,7-diones(6b):

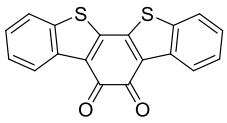

Yield: 58 %. Dark-brown solid. ^{1}H-NMR (Chloroform-d, 400 MHz): δ 7.46 (t, *J* = 7.6 Hz, 2H), 7.55 (t, *J* = 7.6 Hz, 2H), 7.85 (d, *J* = 8.0 Hz, 2H), 8.68 (d, *J* = 8.4 Hz, 2H); ^{13}C-NMR (Chloroform-d, 100 MHz): δ 122.6, 125.4, 127.0, 127.7, 128.7, 137.0, 146.6, 175.0; HRMS: calculated for $C_{18}H_8O_2S_2 + H^+$, 321.0044; found: 321.0036 (M+).

1,1'-di-*n*-hexylbenzo[2,1-b:3,4-b']diindole-6,7-diones(6c):

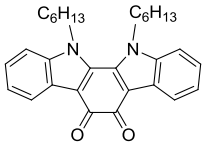

Yield: 85%. Dark-green solid.^{1}H-NMR (Chloroform-d, 400 MHz): δ 0.75 (t, *J* = 6.0 Hz, 6H), 1.17 (s, 12H), 1.86–1.81 (m, 4H), 4.40 (t, *J* = 7.6 Hz, 4H), 7.31–7.28 (m, 4H), 7.42–7.40 (m, 2H), 8.28–8.26 (m, 2H); ^{13}C-NMR (Chloroform-d, 100 MHz): 13.7, 22.3, 26.2, 29.5, 31.0, 48.3, 112.1, 115.1, 122.2, 124.7, 124.8, 127.4, 139.5, 139.6, 177.1,; HRMS: calculated for $C_{30}H_{34}N_2O_2 + H^+$, 455.2699; found: 455.2677 (M+).

4.3 Principal outcomes

4.3.1 Study of substrates based on bithiophene

Firstly, 2,2'-bithiophene was used as a substrate and the effect of different substituted groups in 5 and 5' positions, such as electron-donating group and electron-withdrawing group was investigated (**Scheme 4.3.1**) on the reactivity of the acylation reaction. The reaction conditions are: keeping the amount of dithiophene substrate to be 1.0 eq, the amount of oxalyl chloride and $AlCl_3$ to be 1.2 eq. and 3.0 eq., respectively. As shown in Scheme 4.3.1, for all the substrates with electron-donating groups, such as the alkyl, silyl and alkoxy groups, the F-C reaction underwent well and low to moderate yields could be obtained (**2a** to **2f**). However, for the substrate with electron-withdrawing group, such as the acetyl group, there was no reaction happened due to the low reactivity for the substrate. (**1g**) Although substrate **1h** disappeared as reaction proceeded, no target molecule dione was observed and complex by-products were formed.

It is also found out that if the substituted R group became bulky by changing from the methyl group to *t*-butyl group, the yield increased from 32% to 48%. (**2a** and **2b**) The same tendency was also observed for the substrates **1d** and **1e**. The formation of by-product **2i** might account for the low yield for the substrate **1d**, which had intermolecular F-C acylation reaction due to the broken of C-Si bond. Therefore, our study indicated that electron-rich substrates favoured the intramolecular double F-C reaction and the bulky substituted group was beneficial for improving the reaction yield.

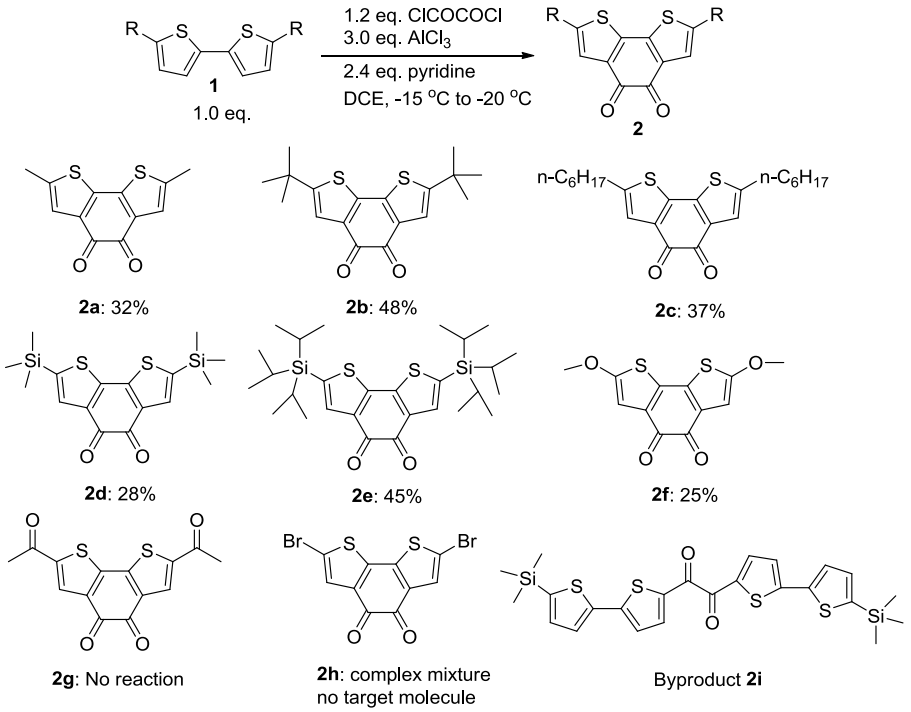

Scheme 4.3.1 F–C acylation reaction with various bithiophene substrates

4.3.2 Study of the substrates based on bifuran, bipyrrole and biselenophene core

After studying successfully the intramolecular double F-C acylation of bithiophene derivatives, we determine to expand the method to other di-hetero systems containing 2,2'-biselenophene, 2,2'-bifuran, and N,N'-dimethyl-2,2'-bipyrrole as cores. As shown in **Scheme 4.3.2.1**, due to its high reactivity, substrate 3a conducted other reactions to form complex by-products under the normal reaction condition (–15 ^{o}C) and only by decreasing the reaction temperture to –50 ^{o}C, the target dione product (**4a**) could be obtained in 16% yield. As to 2,2'-biselenophene (**3b**) and N,N'-dimethyl-2,2'-bipyrrole (**3c**), the reactions could proceed successfully with medium yields of 37% and 32%

respectively. It is worth to mention that it is the first time to report intramolecular double F-C acylation to obtain the corresponding diones molecule on these systems containing 2,2'-bifuran, 2,2'-biselenophene or N,N'-dimethyl-2,2'-bipyrrole as cores.

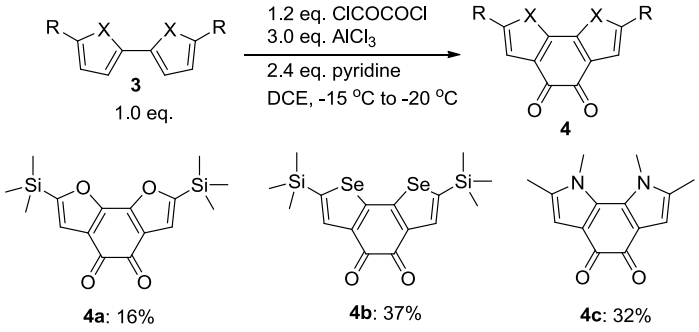

Scheme 4.3.2.1 F–C acylation with bifuran, biselenophene and bipyrrole substrates

The further exploration of intramolecular double F-C acylation with more complex substrates (e.g. 2,2'-bibenzofuran, 2,2'-bibenzothiophene, and 1,1'-dihexyl-1H,1'H'-2,2'-biindole) have also been investigated (**Scheme 4.3.2.1**). All reactions gave good yields (35-85%) under similar reaction conditions. Our methods provide some hints for synthesizing large π conjugation heteroatomic diones functional materials in the future.

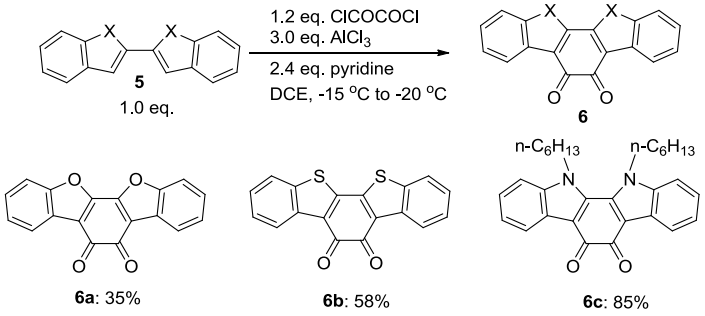

Scheme 4.3.3.2 F–C acylation with bibenzofuran, bibenzothiophene and biindole substrates

4.4 Conclusions

In this chapter, various novel building blocks fused heteroaromatic diones were simply synthesized through one-step F-C acylation reaction. The substrates ranging from simple bifuran, bipyrrole, bithiophene and biselenophene compounds to the more complex bibenzofuran, bibenzoindole and bibenzothiophene compounds were all studies. It was discovered that electron-donating groups favor the reaction. Meanwhile, one limitation for this reaction is that the selectivity is not very satisfactory yet due to the intermolecular reaction, which accounts for the low yield for some substrates. These fused heteroaromatic diones can be employed to develop more functional organic materials in the future and the corresponding work is underway.

References

[1] Z. T. Liu, G. X. Zhang, Z. X. Cai, X. Chen, H. W. Luo, Y. H. Li, J. G. Wang and D. Q. Zhang, *Adv. Mater.*, **2014**, 26, 6965-6977.

[2] K. Takimiya, I. Osaka and M. Nakano, *Chem. Mater.*, **2014**, 26, 587-593.

[3] R. Stalder, J. G. Mei, K. R. Graham, L. A. Estrada and J. R. Reynolds, *Chem. Mater.*, **2014**, 26, 664-678.

[4] C. Y. Mei, L. Liang, F. G. Zhao, J. T. Wang, L. F. Yu, Y. X. Li and W. S. Li, *Macromolecules*, **2013**, 46, 7920-7931.

[5] R. Mondal, N. Miyaki, H. A. Becerril, J. E. Norton, J. Parmer, A. C. Mayer, M. L. Tang, J. L. Bredas, M. D. McGehee and Z. A. Bao, *Chem. Mater.*, **2009**, 21, 3618-3628.

[6] R. Mondal, S. W. Ko, E. Verploegen, H. A. Becerril, M. F. Toney and Z. A. Bao, *J. Mater. Chem.*, **2011**, 21, 1537-1543.

[7] Y. A. Getmanenko, M. Fonari, C. Risko, B. Sandhu, E. Galan, L. Y. Zhu, P. Tongwa, D. K. Hwang, S. Singh, H. Wang, S. P. Tiwari, Y. L. Loo, J. L. Bredas, B. Kippelen, T. Timofeeva and S. R. Marder, *J. Mater. Chem. C*, **2013**, 1, 1467-1481.

[8] Y. F. Xie, T. Fujimoto, S. Dalgleish, Y. Shuku, M. M. Matsushita and K. Awaga, *J. Mater. Chem. C*, **2013**, 1, 3467-3481.

[9] T. Nokami, T. Matsuo, Y. Inatomi, N. Hojo, T. Tsukagoshi, H. Yoshizawa, A. Shimizu, H. Kuramoto, K. Komae, H. Tsuyama and J. Yoshida, *J. Am. Chem. Soc.*, **2012**, 134, 19694-19700.

[10] G. Li, Y. C. Wu, J. K. Gao, J. B. Li, Y. Zhao and Q. C. Zhang, *Chem-Asian J.*, **2013**, 8, 1574-1578.

[11] M. Alfonso, A. Tarraga and P. Molina, *Org. Lett.*, **2011**, 13, 6432-6435.

[12] R. Satapathy, Y. H. Wu and H. C. Lin, *Chem. Commun.*, **2012**, 48, 5668-5670.

[13] Y. C. Wu, Z. Y. Yin, J. C. Xiao, Y. Liu, F. X. Wei, K. J. Tan, C. Kloc, L. Huang, Q. Y. Yan, F. Z. Hu, H. Zhang and Q. C. Zhang, *Acs Appl. Mater. Inter.*, **2012**, 4, 1883-1886.

[14] Z. H. Guo, T. Lei, Z. X. Jin, J. Y. Wang and J. Pei, *Org. Lett.*, **2013**, 15, 3530-3533.

[15] Y. A. Getmanenko, C. Risko, P. Tongwa, E. G. Kim, H. Li, B. Sandhu, T. Timofeeva, J. L. Bredas and S. R. Marder, *J. Org. Chem.*, **2011**, 76, 2660-2671.

[16] J. A. Letizia, S. Cronin, R. P. Ortiz, A. Facchetti, M. A. Ratner and T. J. Marks, *Chem-Eur J.*, **2010**, 16, 1911-1928.

[17] Y. Didane, A. Kumagai, N. Yoshimoto, C. Videlot-Ackermann and H. Brisset, *Tetrahedron*, **2011**, 67, 1628-1632.

[18] F. A. Arroyave, C. A. Richard and J. R. Reynolds, *Org. Lett.*, **2012**, 14, 6138-6141.

[19] J. E. Zhang, W. Z. Cai, F. Huang, E. G. Wang, C. M. Zhong, S. J. Liu, M. Wang, C. H. Duan, T. B. Yang and Y. Cao, *Macromolecules*, **2011**, 44, 894-901.

[20] K. Masui, H. Ikegami and A. Mori, *J. Am. Chem. Soc.*, **2004**, 126, 5074-5075.

[21] J. Nagakubo, M. Ashizawa, T. Kawamoto, A. Tanioka and T. Mori, *Phys. Chem. Chem. Phys.*, **2011**, 13, 14370-14377.

[22] O. V. Borshchev, S. A. Ponomarenko, N. M. Surin, M. M. Kaptyug, M. I. Buzin, A. P. Pleshkova, N. V. Demchenko, V. D. Myakushev and A. M. Muzafarov, *Organometallics*, **2007**, 26, 5165-5173.

[23] J. H. Choi, D. W. Cho, H. J. Park, S. H. Jin, S. Jung, M. Yi, C. K. Song and U. C. Yoon, *Synthetic Met.*, **2009**, 159, 1589-1596.

[24] T. Tsuchimoto, M. Iwabuchi, Y. Nagase, K. Oki and H. Takahashi, *Angew. Chem. Int. Edit.*, **2011**, 50, 1375-1379.

[25] H. Wynberg and A. Logothetis, *J. Am. Chem. Soc.*, **1956**, 78, 1958-1961.

[26] O. Gidron, Y. Diskin-Posner and M. Bendikov, *J. Am. Chem. Soc.*, **2010**, 132, 2148.

[27] W. H. Lee, S. K. Lee, S. K. Son, J. E. Choi, W. S. Shin, K. Kim, S. H. Lee, S. J. Moon and I. N. Kang, *J. Polym. Sci. Polym. Chem.*, **2012**, 50, 551-561.

[28] J. E. Taylor, M. D. Jones, J. M. J. Williams and S. D. Bull, *Org. Lett.*, **2010**, 12, 5740-5743.

[29] G. W. Gribble, D. H. Blank and J. P. Jasinski, *Chem. Commun.*, **1999**, 2195-2196.

[30] S. Matsuda, M. Takahashi, D. Monguchi and A. Mori, *Synlett.*, **2009**, 1941-1944.

[31] T. Qi, Y. L. Guo, Y. Q. Liu, H. X. Xi, H. J. Zhang, X. K. Gao, Y. Liu, K. Lu, C. Y. Du, G. Yu and D. B. Zhu, *Chem. Commun.*, **2008**, 6227-6229.

[32] D. Saha, R. Ghosh and A. Sarkar, *Tetrahedron*, **2013**, 69, 3951-3960.

33. U. Pindur, Y. S. Kim and D. Schollmeyer, *J. Heterocyclic Chem.*, **1994**, 31, 377-386.

Chapter 5

Design and Synthesis of Quinoxaline-Functionalized C_{60} Compounds as OSCs Acceptors

For fullerene based acceptor, increasing the J_{sc} and V_{oc} at the same time may be an efficient method to improve the OSCs device performance. In this chapter, two novel C_{60} derivative acceptors monoadduct TQMA and bisadduct TQBA based on 2,3-bis(5-tert-butylthiophen-2-yl)-6,7-dimethylquinoxaline were designed and synthesized in order to increase the absorption and V_{oc} of the device. Their physiochemical properties and the subsequent photovoltaic performance have been fully investigated. An optimized device using P3HT as donor and TQMA as acceptor exhibits the best PCE value of 2.8% with a V_{oc} of 0.76 V, which is about 0.12 V higher than that device using $PC_{61}BM$ while TQBA displays much poorer PCE due to the poor film morphology, although it has an expected high V_{oc} value of 0.84 V.

*This section has been published substantially as: W. Chen *et al*, *RSC Adv.*, **2014**, *4*, 25291–25301

5.1 Introduction

For OSCs, as discussed in the literature review, the progress in the research of new acceptors is relatively slow. Generally speaking, the acceptors in OSCs can be briefly divided into two groups: fullerene-based and non-fullerene acceptors. For this chapter, we mainly focused on the fullerene-based OSCs acceptors.

For the fullerene-based acceptors, the classical acceptor $PC_{61}BM$ and $PC_{71}BM$ are still the dominated acceptor due to their superior electron mobility and compatibility with different donor materials.[1] However, there are two apparent disadvantages associated with $PC_{61}BM$: (a) the LUMO energy level of $PC_{61}BM$ is relatively low, accounting for the low V_{oc} of the OSCs and affecting the final PCE result; and (b) $PC_{61}BM$ has weak absorption in the visible region, which may affect the I_{sc} of the solar cells. Therefore, new fullerene based acceptors were designed and synthesized with the aim of solving these two problems.

As showed in **Fig. 5.1.1**, Method A is to increase the LUMO value of the acceptor because V_{oc} strongly relates to the difference between the LUMO value of the acceptor and the HOMO value the donor.[2] The concrete procedure is through 4+2 ring addition to one more double bond of fullerene. By taking this strategy, acceptors bis-$PC_{61}BM$[3] [4]and $IC_{60}BA$[5, 6] were synthesized and it has been found that they work well with P3HT as donor material showing PCE results of 4.5% and 6.5% respectively, which are higher than the acceptor $PC_{61}BM$ under the same conditions. Further examples of this strategy include acceptors dihydronaphthyl-$C_{60/70}$ bisadduct ($NC_{60}BA$ and $NC_{70}BA$), thieno-o-quinodimethane-C_{60} (bis-TOQC) and di(4-methylphenyl)methano-C_{60} bisadduct (DMPCBA). [7-11]

The other Method B is to broaden the absorption of the acceptor in the visible range to obtain higher absorption efficiency of the active layer. The concrete procedure is to introduce different absorbing groups onto the fullerene acceptor. For example, the Mikroyannidis [12, 13]and Wudl[14] groups separately replaced the methoxy (–OMe) group of the $PC_{61}BM$ with a 4-nitro-40-hydroxy-α-cyanostilbene (F) and visible-light sensitizer (DR). For the acceptor F, the PCE shows a higher result of 5.25% while the acceptor PCBDR only produces PCE of 0.9%. By analyzing the structures for these two novel acceptors F and PCBDR, it can be observed that these new acceptors retain the basic part

(PCB) of the classical PCBM acceptor and the absorbing groups are introduced at the outer end of the PCBM to replace methyl group. Thus, they provide no guideline as to what the OSCs performance will be if the absorption groups are directly attached on the C_{60} backbone. Regarding this point, in 2012, Saravanan et al[15] designed and synthesized a novel acceptor 3Th-C_{60} with a terthiophene absorption group through a 1,3-dipolar cycloaddition reaction between the corresponding precursor azomethine ylide and C_{60}. Although there is a contribution of 3T excitons to the photocurrent, this novel acceptor gave a PCE value of only about 2.54%, which was still lower than the compared $PC_{61}BM$ group.

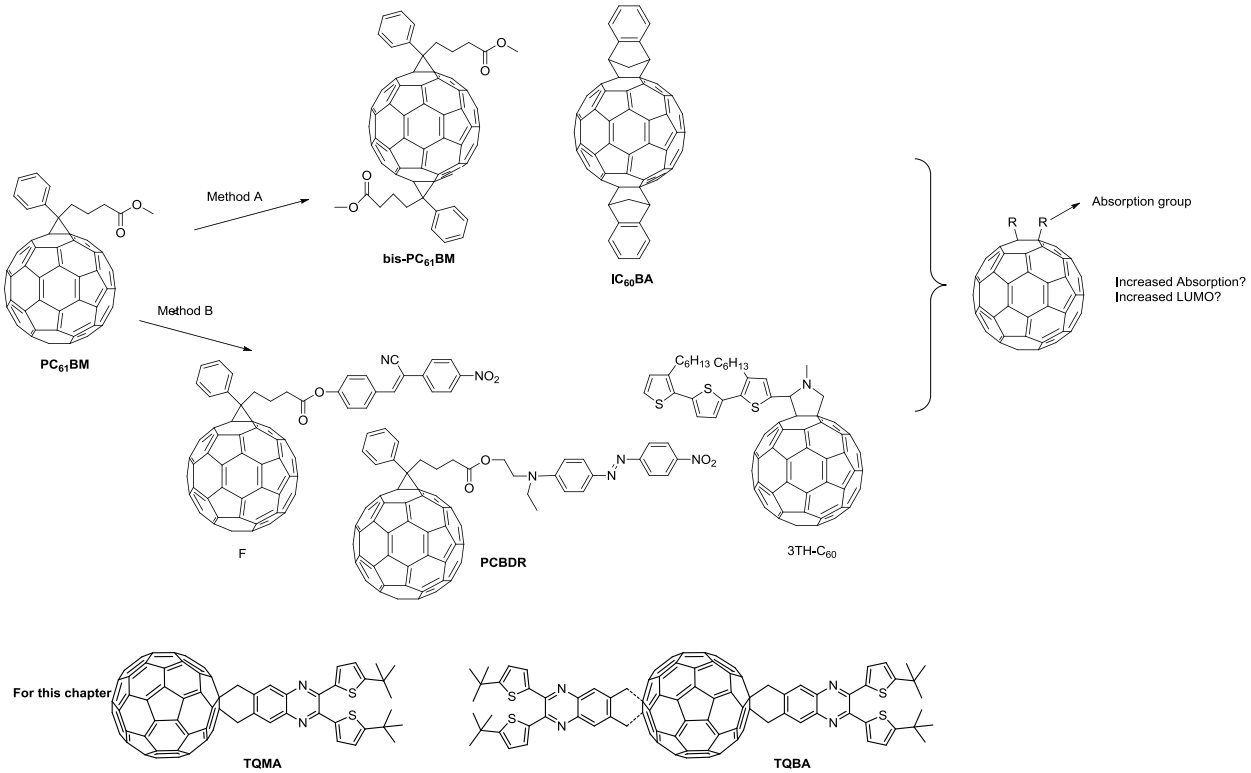

Fig. 5.1.1 Structure of OSCs acceptor based on fullerene

From the above discussion, Method A and Method B are two effective methods to improve the efficiency of the novel fullerene-based acceptors by increasing the V_{oc} and J_{sc} values respectively. Therefore, what will the OSCs performance be for a novel fullerene-based acceptor with increased LUMO energy and absorption through introducing two absorption functional groups onto the C_{60}? Following this idea, in this chapter, two novel acceptors are designed and synthesized: mono-adducted TQMA and bis-adducted TQBA based on quinoxaline absorbing group with thiophene units through

D-A addition reaction. In addition, their physiochemical properties and the subsequent photovoltaic performance have been fully investigated.

5.2 Experimental methods

Device Fabrication: Unless otherwise stated, the mixtures of donor P3HT and acceptors (TQMA, TQBA or $PC_{61}BM$) were prepared in *o*-DCB (10 mg :8 mg wt%) and stirred overnight at 70 °C under N_2 protection in glovebox. The OSCs devices were fabricated on pre-patterned ITO-coated glass substrates, which were sequentially cleaned by ultra-sonication in DI water, acetone and isopropanol each for 15 min. Subsequently, PEDOT:PSS was spin coated at 3000 rpm for 60 s. The substrates were then baked at 140 °C for 10 min followed by spin-coating of blend solutions at 700 rpm for 120 s in N_2 atmosphere. The blend films were annealed at 150 °C for 20 min, and were spin coated with TiO_x solution (in isopropanol). The hydrolysis of TiO_x precursors occurred in ambient for approximately 45 min. The samples were transferred to N_2 glove box again for Al deposition (10^{-6} mbar). The active area of the device was 0.1 cm^2.

1,2-bis(5-*tert*-butylthiophen-2-yl)ethane-1,2-dione(R2):

To a sealed flask with 2.8 g $AlCl_3$ (21.0 mmol) was added 10 mL of 1,2-DCE and cooled down to –20 °C, then 1.5 mL 1,2-DCE containing 0.54 g oxalyl chloride (4.3 mmol) was slowly added into the flask again. Afterwards, 3.0 mL 1,2-dichloroethane containing a mixture solution of 1.4 g 2-*tert*-butylthiophene (**R1**, 10.0 mmol) and 0.79 g of pyridine (10.0 mmol) was injected dropwise by syringe. After finishing the injection, the reaction was stirred of –20 °C to –15 °C for about 20 mins and the temperature was then raised to 0 °C. The mixture was poured onto ice and extracted with DCM. The organic DCM layer was washed with water several times and saturated NaCl solution one time, dried over anhydrous $MgSO_4$, then filtrated and concentrated under reduced pressure to give a crude product, which was purified by CC (eluent: PE: Ethyl acetate = 5:1, V/V) to give orange solid product (1.17 g, 81%). Further purification was obtained through recrystallization (800 mg in 30 mL PE, refluxing, up to 70% yield). ^{1}H-NMR (Chloroform-d, 300 MHz): 1.42 (s, 18H), 6.95 (d, *J* = 3.0 Hz, 2H), 7.85 (d, *J* = 3.0 Hz, 2H); ^{13}C-NMR (Chloroform-d, 300 MHz) δ: 32.1, 35.3, 123.8, 135.8, 137.5, 171.3, 183.0; MALDI-TOF MS: calculated for $C_{18}H_{22}O_2S_2 + H^+$, 335.1139; found: 335.1143 (M+).

2,3-bis(5-*tert*-butylthiophen-2-yl)-6,7-dimethyl quinoxaline (R3): In a 50 ml flask, 334 mg **R2** (1.0 mmol) and 163 mg 4,5-dimethyl-1,2-phenylenediamine (1.2 mmol) was added into 30 mL anhydrous ethanol subsequently. Then, the solution was stirred at r.t. for about 24 h under argon protection and during which a yellow solid precipitated from the solution. The reaction was monitored until the dione had all disappeared by TLC. The solution was filtrated and a bright yellow solid was obtained (412 mg, 95%). ^{1}H-NMR (Chloroform-d, 300 MHz) δ: 1.42 (s, 18H), 2.46 (s, 6H), 6.75 (d, *J* = 3.0 Hz, 2H), 7.04 (d, *J* = 3.0 Hz, 2H), 7.79 (s, 2H); ^{13}C-NMR (Chloroform-d, 300 MHz) δ: 20.3, 32.4, 34.8, 122.0, 127.8, 128.6, 138.7, 139.4, 140.3, 146.0, 161.0; MALDI-TOF MS: calculated for $C_{26}H_{30}O_2S_2 + H^+$, 435.1929; found: 435.1919 (M+).

6,7-bis(bromomethyl)-2,3-bis(5-tert-butylthiophen-2-yl)quinoxaline(R4): 434 mg **R3 (**1.0 mmol), 427 mg NBS (2.4 mmol, 2.4 eq. to **R3**) and catalytica amount of benzoyl peroxide (BPO, 24 mg, 0.1 mmol, 10% eq. to **R3**) was added into a flask and proteced under Argon atomospher. Anhydrous benzene was added and the mixture was refluxed for 6 h. After cooling down to r.t., the benzene was removed under vacuum to give the residual solid, which was purified by CC (PE: DCM=3: 1) to obtain an orange viscous liquid: 350 mg, 59%. ^{1}H-NMR (Chloroform-d, 300 MHz) δ: 1.44 (s, 18H), 4.81 (s, 4H), 6.75 (d, *J*= 3.0 Hz, 2H), 7.18 (d, *J*= 3.0 Hz, 2H), 8.01 (s, 2H); ^{13}C-NMR(Chloroform-d, 300 MHz) δ: 29.8, 32.5, 35.0, 122.3, 129.5, 131.0, 137.9, 138.1, 140.2, 147.8, 162.2; (**Fig. 5.2.1** and **Fig. 5.2.2**.) MALDI-TOF MS: calculated for $C_{26}H_{28}Br_2O_2S_2 + H^+$, 593.0118; found: 592.9991 (M+).

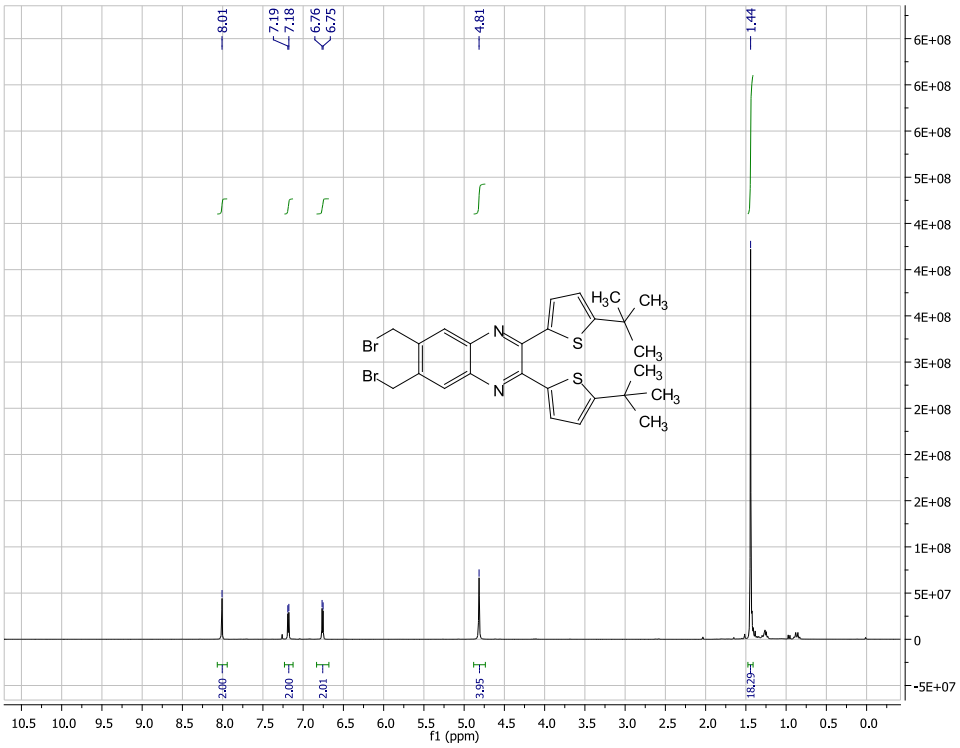

Fig. 5.2.1 ^{1}H-NMR of R4

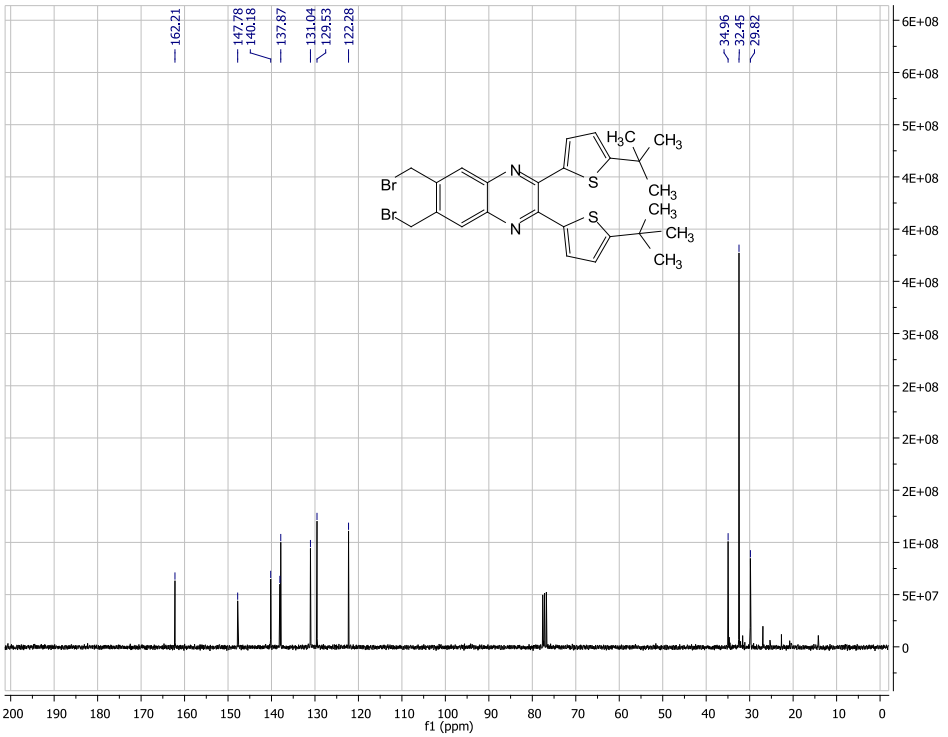

Fig. 5.2.2 ^{13}C-NMR of R4

2,3-bis(5-*tert*-butylthiophen-2-yl)-6,7-dimethylquinoxaline-C60-monoadduct (TQMA) and (2,3-bis(5-*tert*-butylthiophen-2-yl)-6,7-dimethylquinoxaline-C60-bisadduct) TQBA: 306 mg C_{60} (0.43 mmol, 1.0 eq.), 300 mg **R4** (0.51 mmol, 1.2 eq. to C_{60}), 399 mg KI (2.04 mmol, 4.0 eq. to **R4**) and 539 mg 18-crown-6 (2.04 mmol, 1.0 eq. to KI) was added into a flask under an Argon atmosphere. 20 mL of anhydrous *o*-DCB was injected into the flask and the mixture was refluxed for 48 h in the dark. The solvent was removed under reduced pressure after cooling to r.t. The resulting solid was transferred into methanol (10 mL × 3), sonicated and centrifuged. The residual solid was purified by CC with toluene. The separated mono-adduct TQMA was 170 mg, yield, 35%. ^{1}H-NMR (Chloroform-d, 300 MHz) δ: 8.32 (s, 2H), 1.46 (s, 18H), 4.64 (d, *J* = 15Hz, 2H), 5.07 (d, *J* = 15 Hz, 2H), 6.79 (d, *J*= 3.0 Hz, 2H), 7.23 (d, *J* = 3.0Hz, 2H); MALDI-TOF MS: calculated for $C_{86}H_{28}N_2S_2$ + H^+, 1153.1772; found: 1153.0865 (M+). (**Fig. 5.2.3**) Bisadduct TQBA was 51 mg, yield, 8%.^{1}H-NMR (Chloroform-d, 300 MHz) δ: 1.57–1.41 (m, 36H), 5.30–4.01 (m, 8H), 6.82–6.69 (m, 4H), 7.32–7.11 (m, 4H), 8.44–8.00 (m, 4H); MALDI-TOF MS: calculated for $C_{112}H_{56}O_4S_4$ + H^+,1585.34; found: 1585.33. (**Fig. 5.2.4**)

Minimum:				-1.5			
Maximum:		5.0	200.0	100.0			
Mass	Calc. Mass	mDa	PPM	DBE	i-FIT	i-FIT (Norm)	Formula
1153.0865	1153.1772	-90.7	-78.7	73.5	11.5	0.0	C86 H29 N2 S2

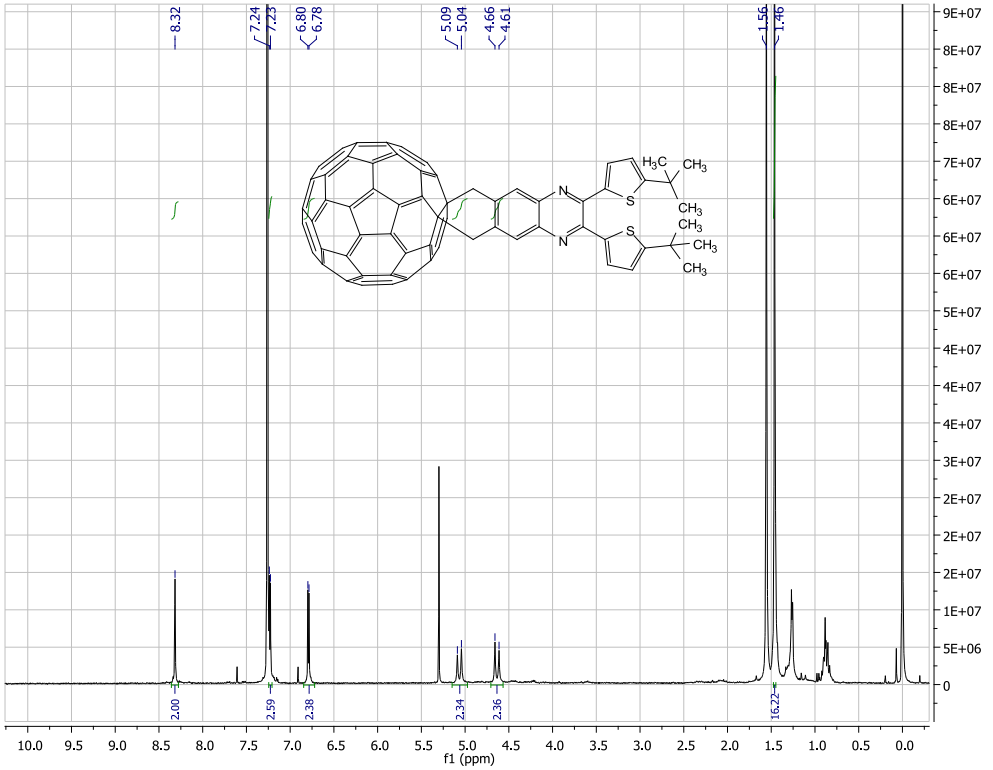

Fig. 5.2.3 MS spectrum and ^{1}H-NMR of TQMA

TQBA

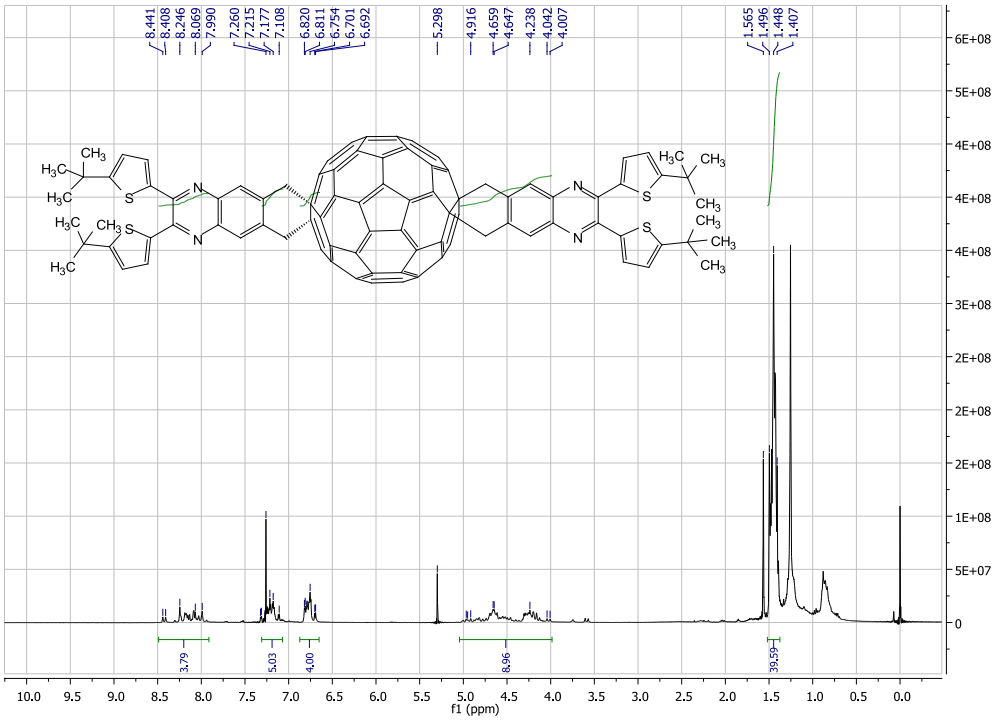

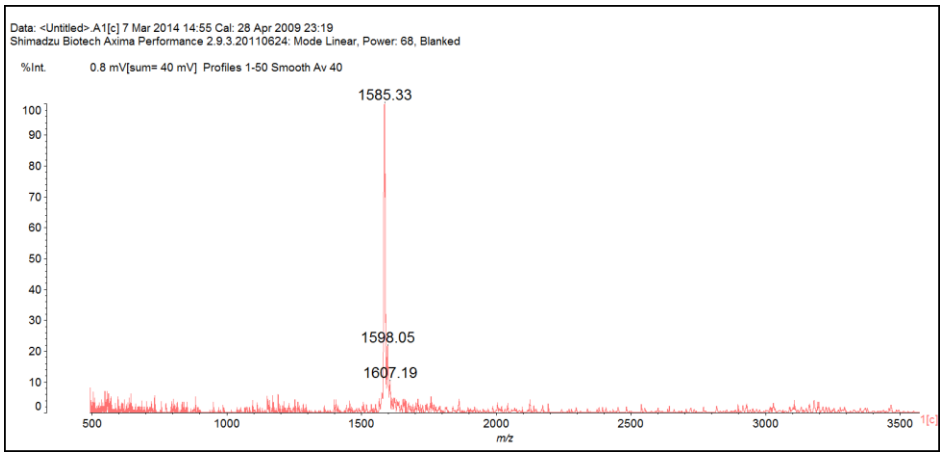

Fig. 5.2.4 ^{1}H-NMR and Maldi-TOF of TQBA

5.3 Principal outcomes

5.3.1 Synthetic route for TQMA and TQBA

The synthetic route for the target molecules TQMA and TQBA was displayed in **Scheme 5.3.1** and Diels-Alder (D-A) reaction was utilized as the key reaction for the final step.[16] Precursor **R1** was synthesized according to the literature[17] and transformed into intermediate **R2** through double F-C reaction,[18] which reacted with 4,5-dimethyl-1,2-phenylenediamine in ethanol at r.t to form the intermediate **R3** in almost quantitative yield.[19] The dibromo precursor **R4** was obtained through the NBS free radical reaction by taking the benzoyl peroxide (BPO) as the initiator according to the procedure used to make similar molecules in literature.[20] TQMA and TQBA were synthesized through the D-A [2+4] addition reaction of C_{60} and the in-situ generated 2,3-bis(5-*tert*-butylthiophen-2-yl)-6,7-dimethenequinoxaline by a published method used to make similar molecules.[21] 1.2 equiv. of precursor was employed in the reactions in order to render TQMA as the main product. The yield is 35% for mono-adduct TQMA and 8% for bis-adduct TQBA.

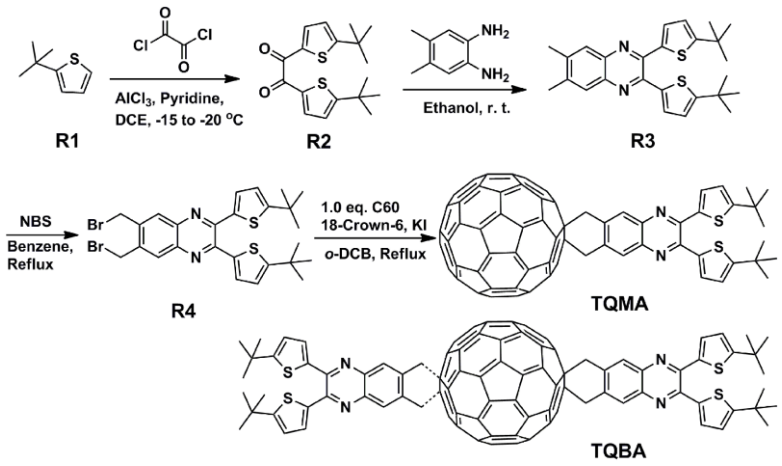

Scheme 5.3.1 Synthetic route for acceptors TQMA and TQBA

5.3.2 Physicochemical properties for TQMA and TQBA

The optical spectra of the precursor **R3** and the acceptors TQMA, TQBA and $PC_{61}BM$ are shown in **Fig. 5.3.2.1**. (Measured on a UV-Vis-NIR Spectrophotometer, UV-3600, Shimadzu). For the precursor **R3**, λ_{onset} absorption is 450 nm and according to the equation: $E_g^{opt} = 1240/\lambda_{onset}$, its bandgap is calculated to be 2.81 eV. **R3** also has fluorescence appearing in the range of 410 – 570 nm. Nevertheless, when it is attached on the C_{60}, the fluorescence quenches completely, which may indicate a possible electron transfer from the quinoxaline unit to the C_{60} and contribute to the photocurrent of the device.[54] With the same concentrations in chloroform, TQMA and TQBA show apparently enhanced absorption in the 300 – 450 nm range comparing with $PC_{61}BM$ after attaching quinoxaline **R3** groups. In addition, according to the above-mentioned equation, these two novel acceptors all have the same badgap of 2.0 V as $PC_{61}BM$ due to their similar λ_{onset} around 450 nm.

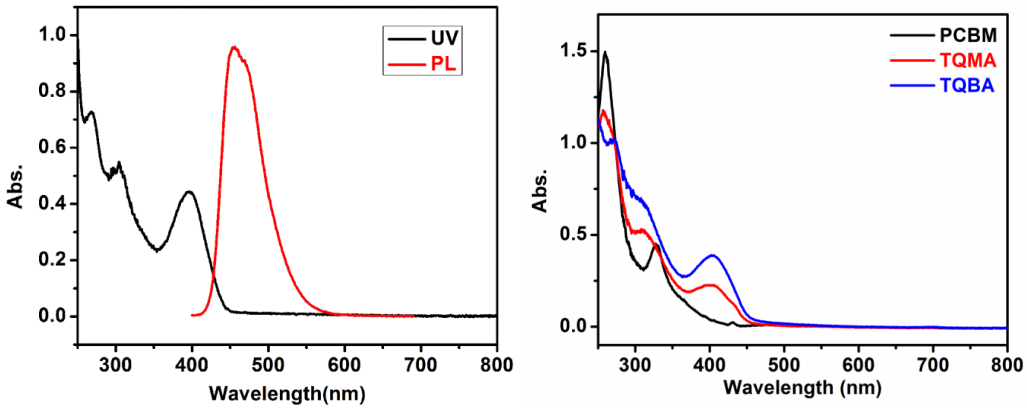

Fig. 5.3.2.1 Left: UV-Vis and Fluorescence spectra of precursor R3; Right: UV-Vis spectra of the acceptors (10^{-5} mol/L in chloroform)

The electrochemical properties of the acceptors are studied by CV on CHI 660C Electrochemical Workstation and measured by 3-electrodes method (Pt disk: WE; Pt wire: CE and Ag/Ag^{+} electrode: RE) in a mixed solution of *o*-DCB: CH_3CN (5:1 v/v) with 0.1 M Bu_4NPF_6 at 100 mV s^{-1}. **Fig. 5.3.2.2** shows the CV diagrams of the acceptors and precursor **R3**. For the negative potential area between 0 to –2.0 V, all the acceptors exhibit three reversible peaks while **R3** shows one reduction peak around –2.0 V. In addition, the three reduction peaks of E_1, E_2 and E_3 are almost the same for acceptors TQMA and $PC_{61}BM$. While for TQBA, they are all left shifted about 0.15 V due to its increased LUMO energy. **Table 5.3.2.1** lists all the half-wave potentials for E_1, E_2 and E_3 (denoted as $E = 1/2(E_{p,c} + E_{p,a})$.

The LUMO energy levels for all the acceptors can be calculated according to the following equation,[22]

$E_{LUMO} = -e(E_{red}^{on} + 4.71)[eV]$

The E_{red}^{on} value for the acceptor TQMA is – 0.82 eV, thus, according to this equation, the LUMO energy level for TQMA is calculated to be –3.89 eV. With the same method, the LUMO energy values for TQBA, $PC_{61}BM$ and R3 can be calculated to be –3.76, –3.91 and –2.91 eV respectively. All the corresponding data are summarized in **Table 5.3.2** and the energy level diagrams is drawn in **Fig. 5.3.2.3**., which indicates it is energetically favourable for the excitons to move from the quinoxaline to the fullerene part due to the large Δ_{LUMO}.

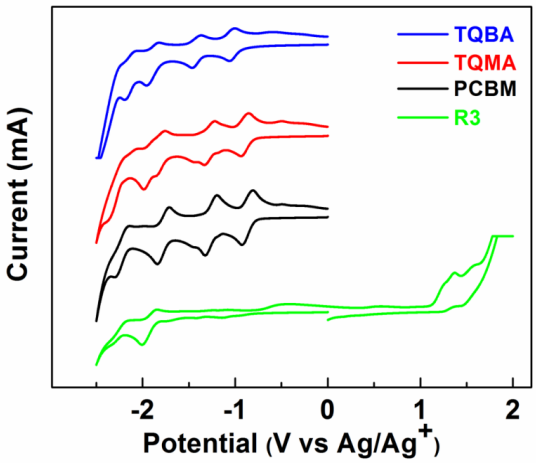

Fig. 5.3.2.2 CV diagrams of the acceptors and precursor R3

Table 5.3.2 Electrochemical properties of TQMA, TQBA and $PC_{61}BM$

Acceptor	E_1 [V]	E_2 [V]	E_3 [V]	E_{red}^{on}	E_{LUMO}	E_{HOMO}^{a}	$E_g^{opt\ b}$
TQMA	–0.90	–1.28	–1.81	–0.82	–3.89	–5.89	2.0
TQBA	–1.04	–1.42	–1.90	–0.95	–3.76	–5.76	2.0
$PC_{61}BM$	–0.87	–1.26	–1.78	–0.80	–3.91	–5.93	2.02
R3	–1.90			–1.80	–2.91	–5.72	2.81

[a] $E_{HOMO} = E_{LUMO} - E_g^{opt}$

[b] $E_g^{opt} = 1240/\lambda_{onset}$

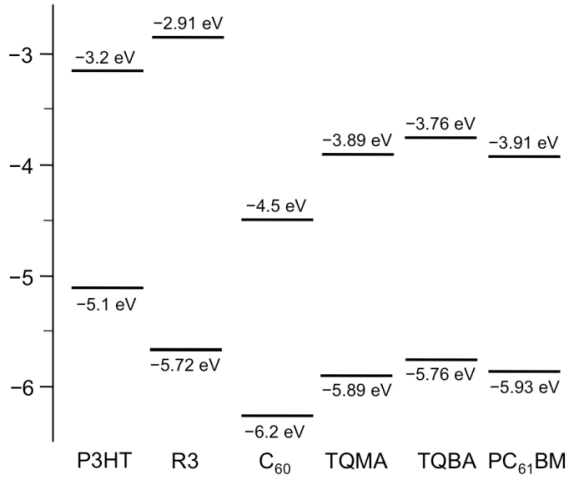

Fig. 5.3.2.3 Energy level diagram of the molecules

5.3.3 Photovoltaic performance and characterization of the device

UV-Vis spectra of the active layer blended films with different acceptors by taking P3HT as donor material (as cast: NA and thermally annealed: TA) are displayed in **Fig. 5.3.3.1**. There are 3 points that need to pay attention to:

1) For the acceptors TQMA and TQBA, there are slightly enhanced absorptions between 350 nm and 450 nm, which correspond well with the **R3** absorption group. However, acceptor TQBA with two absorption group does not exhibit stronger absorption compared with TQMA. This implies that connecting absorbing functional groups onto the C_{60} will improve the whole absorption for the device to some extent but may not as large in solid state as that in solution. (**Fig. 5.3.2.1**)

2) TA post-treatment is an effective method to facilitate the molecule reorganization and to improve the device absorption. After TA, all the three acceptors have enhanced

absorption due to the molecular reorganization and improved intermolecular stacking.[23] However, it seems that both the blended films for TQMA and $PC_{61}BM$ are more susceptible to heat treatment and have more extensive red-shift and enhanced absorption due to the significantly improved molecular packing.

3) The NA blended film for TQMA displays the poorest absorption with λ_{max} at 500 nm and two shoulders at 560 and 610 nm respectively compared with other two acceptors with λ_{max} at 520 nm. This may indicate that TQMA blended film possesses the most prominent extent of disorder.

Furthermore, the shoulder peak around 620 nm ascribed to the donor P3HT become much more apparent after TA, which indicates an improved packing for P3HT which should produce more efficient charge transport within the film.

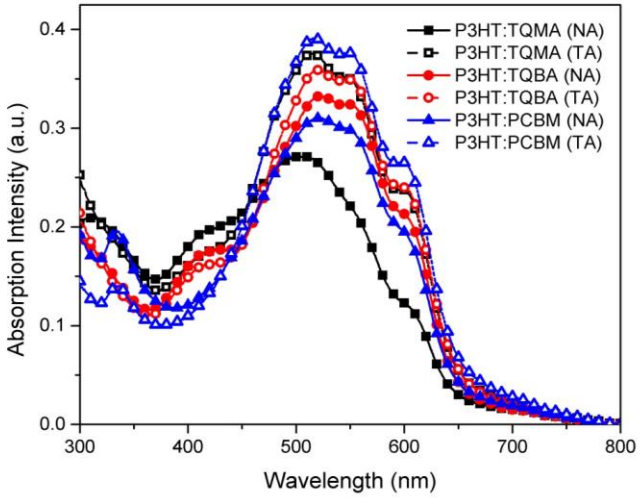

Fig. 5.3.3.1 UV-Vis spectra of the active layer blended film with D-A ratio of 10 : 6

Although there are similar absorption behaviors for these acceptors, their devices with different blended films after TA exhibit different OSCs performance, which were measured under N_2 atmosphere with Agilent 4155C Semiconductor Analyzer under AM 1.5G (100 mW cm^{-2}) illumination. **Fig. 5.3.3.2a** shows typical *J*–*V* curves for the various devices, whose structures are ITO/PEDOT:PSS/Active Layer/TiO_x/Al and their regarding device data are summarized in **Table 5.3.3.1**. The as-cast P3HT:TQMA and P3HT:TQBA all exhibit poor PCE of 0.5 and 0.06% respectively. The subsequent *R*s data reveals that without any heat treatment, both P3HT:TQMA and P3HT:TQBA has internal resistance all higher than 200, which indicates that although these film absorption are

similar with $PC_{61}BM$, the photons are either not effectively converted into free carriers or the charges are not effectively transported across the blended films. For comparison, the as-cast $PC_{61}BM$-based OSCs exhibit PCE of 2.71%. Upon TA treatment, the device performance for P3HT:TQMA blended film improves significantly and results in J_{sc}, V_{oc}, FF and PCE of 6.2 mA cm^{-2}, 0.76 V, 0.51 and 2.4%, respectively. On the other hand, P3HT:TQBA also experiences a 6-fold improvement in OSCs performance but still with a very high *R*s value. TA treatment seems to be more effective in generating percolation pathways for efficient hole and electron transport in P3HT:TQMA than in P3HT:TQBA. From the above discussion, we can summarize briefly the following several points: 1) the V_{oc} of P3HT:TQBA (0.84 V, TA) is higher than that of P3HT:TQMA (0.76V, TA), which correlates well with the LUMO trend as expected when we designed the molecules. However, simply introduction of the bis-adducted absorption groups on TQBA don't guarantee good J_{sc} and FF, eventually bringing seriously damage to PCE performance. 2) For mono-adducted acceptor TQMA, it surprisingly also displays higher LUMO (0.76 V) than $PC_{61}BM$ (0.64), which offset the decreased value of J_{sc} and FF to some extent.

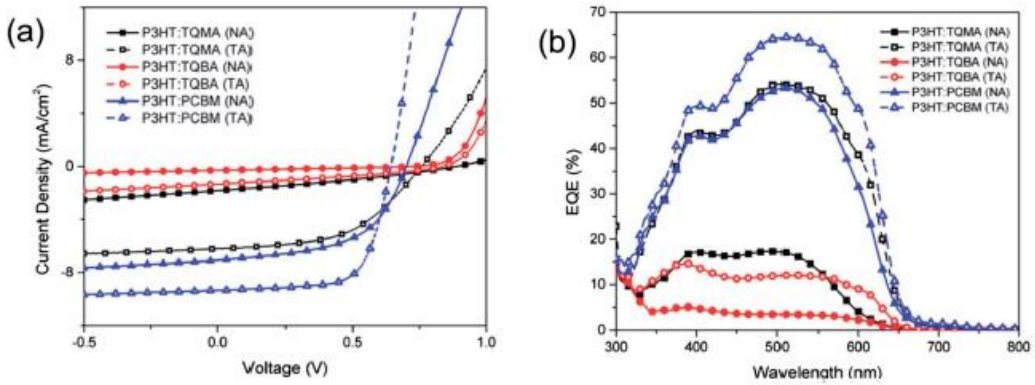

Fig. 5.3.3.2 a) *J*–*V* performance curves; b) Corresponding EQE spectra data

Table 5.3.3.1 Summary of device data for P3HT with different acceptors

Acceptor	Annealing	J_{sc} [mA cm^{-2}]	V_{oc} [V]	FF	PCE [%]	*R*s [**Ω** cm^{-2}]	*R*p [**Ω** cm^{-2}]
TQMA	n/a	1.84	0.89	0.31	0.50	269.6	6.6×10^2
	150 °C	6.20	0.76	0.51	2.40	40.4	1.1×10^3
TQBA	n/a	0.29	0.72	0.26	0.06	1041.7	2.6×10^3
	150 °C	1.34	0.84	0.32	0.36	207.8	8.8×10^2

$PC_{61}BM$	n/a	7.06	0.70	0.55	2.71	19.5	5.9×10^2
	150 °C	9.34	0.64	0.68	4.10	9.6	1.5×10^3

Fig. 5.3.3.2b shows the EQE spectra of devices measured by Merlin radiometer (Newport) under monochromatic light illumination. For the TQBA, the EQE curve doesn't have significant increment after TA treatment (from 5% to 10%), which corresponds well with the *J*–*V* data. However, for TQMA and $PC_{61}BM$, the EQE of the devices after TA treatment reach the highest value of 54% and 65% respectively. The slightly lower EQE for acceptor TQMA compared with controlled acceptor $PC_{61}BM$ may indicate that there is less efficient charge transport within the P3HT and TQMA blended film resulting from less efficient percolation pathways.

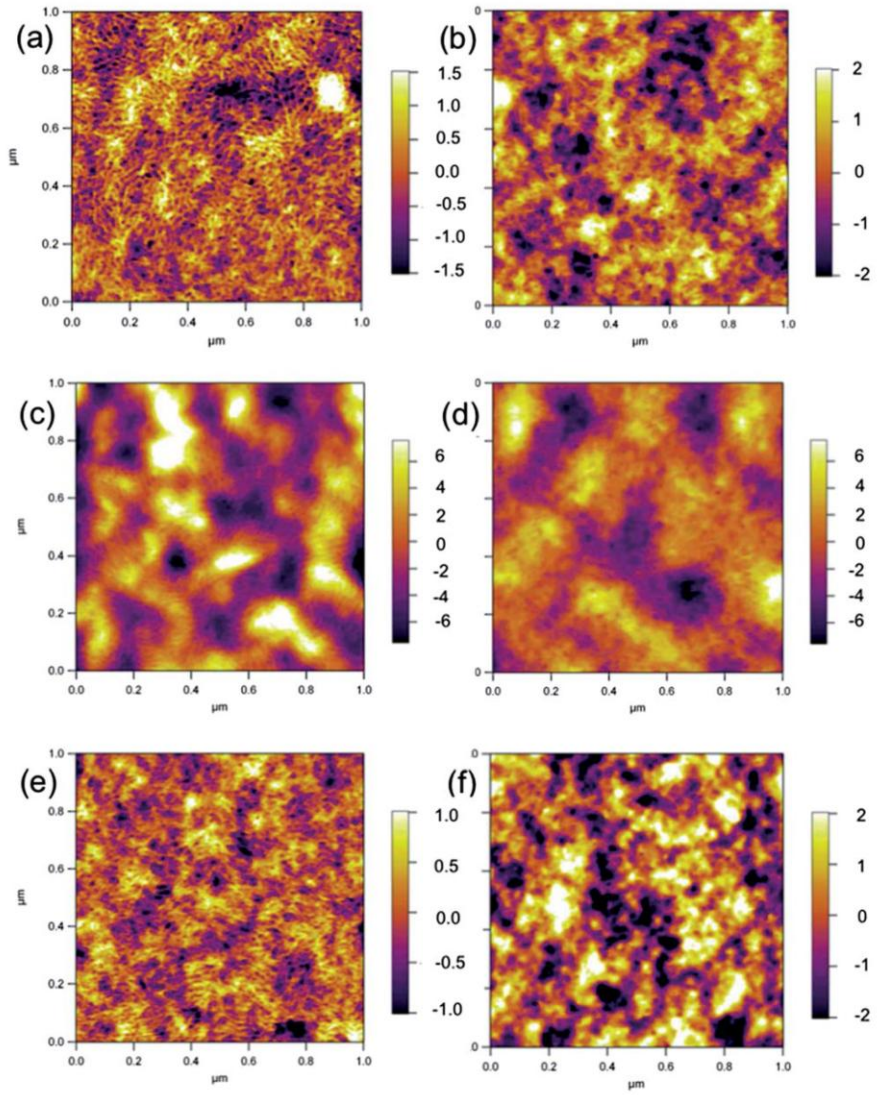

Fig. 5.3.3.3 AFM height images for P3HT:TQMA (a & b); P3HT:TQBA(c & d) as well as P3HT:$PC_{61}BM$ (e & f). NA films for a, c, e and TA films for b, d, f.

To further study the reasons accounting for the PCE results, atomic force microscopy (AFM) was performed on the blend films with an Asylum Research (MFP-3D-BIO) to investigate the surface morphologies. **Fig. 5.3.3.3** displays the tapping-mode AFM height images of P3HT blends with various acceptors. Both as-cast P3HT:TQMA and P3HT:$PC_{61}BM$ blends exhibit smooth morphologies before and after thermally annealing (TA), except slightly increment of the surface roughness (for TQMA, σ_{RMS} increasing from 0.64 nm to 0.96 nm; for PCBM, σ_{RMS} increasing from 0.39 nm to 0.88 nm).(**Fig. 5.3.3.3a, e, b, f**). In both types of blends, TA does not cause any significant roughening of the blend surface. As a result, these devices are not expected to suffer from poor charge extraction. On the other hand, P3HT:TQBA (**Fig. 5.3.3.3c**) adopts different morphology and there is a substantial roughening of the blend surface with σ_{RMS} of 3.75 nm, which may contribute to the poor charge extraction and dissociation. After the heat treatment, P3HT:TQBA device (**Fig. 5.3.3.3d**) reduced the surface roughening to σ_{RMS} 2.63 nm. From the above discussion, we can conclude that the TA of the blend molecules triggers reassembling of blend morphology, leading to formation of fewer aggregates which is beneficial for increasing the J_{sc}, V_{oc} and FF parameters and eventually improving the PCE values.

This set of data demonstrates the truth that the number of functional groups connecting to fullerene molecules has crucial effect on the device properties. While there are a lot of other successful fullerene bisadducts used in OSCs,[5, 8] this work proves that mono-adducted C_{60} acceptor may exhibit better PCE performance than the bis-adducted C_{60} acceptor if there is an obvious defect in the film morphology caused by introducing large bulky functional group.

Due to the promising PCE performance obtained for acceptor TQMA than TQBA, the optimization for P3HT:TQMA device was further studied. The solvents and the D/A ratio were first investigated. The solvent chlorobenzene (CB) was selected due to its lower boiling point, which may be beneficial for forming thick active layers and so improving the light absorption. **Table 5.3.3.2** summarizes the corresponding device data. Upon increasing the loading of acceptor in the blend films, both J_{sc} and V_{oc} decrease

simultaneously due to the decreased absorption in the high wavelength (480–700 nm) contributed from P3HT because there is less P3HT in the blend. However, the fill factor (FF) increases from 0.42 to about 0.50, which indicates that increased amount of acceptor in the active layer improve the film morphology and electron charge transport without perturbing the hole transport channels. This can also be proved by the decreased series resistance (*R*s) value from 50 to around 40. The optimized PCE value of 2.8% is obtained with J_{sc} of 7.25 mA cm^{-2}, a V_{oc} of 0.75, an FF of 0.51.

Table 5.3.3.2 Summary of the P3HT:TQMA device data with different D : A weight ratio

Ratio	J_{sc} [mA cm^{-2}]	V_{oc} [V]	FF	PCE [%]	*R*s [**Ω** cm^{-2}]	*R*p [**Ω** cm^{-2}]
10 : 6	7.76	0.77	0.42	2.50	50.32	5.89×10^2
10 : 7	7.25	0.75	0.51	2.80	39.60	7.33×10^2
10 : 8	6.98	0.74	0.50	2.60	41.06	8.31×10^2

5.4 Conclusions

In conclusion, two novel fullerene acceptors have been designed and synthesized: mono-adduct TQMA and bis-adduct TQBA with quinoxaline-based absorping groups connected to the C_{60} with the aim of improving the J_{sc} and V_{oc} of the device and so the final PCE value. It turned out that TQMA and TQBA acceptors do have enhanced absorption around 250-410 nm in solution at the same concentration. However, their enhancements become much narrower when it comes to the blend films with donor P3HT and thus, both of them do not show any apparent elevation in the J_{sc}. Particularly for the acceptor TQBA, it has an extremely low J_{sc} value despite exhibiting a high V_{oc} value of 0.84 V as was expected when designing this molecule. From AFM analysis, the poor morphology may contribute to the low J_{sc} and PCE result (0.36%) for TQBA. For TQMA, the high V_{oc} value of 0.74 V offsets the low J_{sc} and FF values and in addition to the more optimal morphology, a best PCE of 2.8% was obtained. The work in this chapter proves that the number, type of the functional groups connecting to C_{60} has crucial effect on the novel fullerene acceptors' performance in OSCs.

References

[1] Y. J. He and Y. F. Li, *Phys. Chem. Chem. Phys.*, **2011**, 13, 1970-1983.

[2] C. J. Brabec, A. Cravino, D. Meissner, N. S. Sariciftci, T. Fromherz, M. T. Rispens, L. Sanchez and J. C. Hummelen, *Adv. Funct. Mater.*, **2001**, 11, 374-380.

[3] M. Lenes, G. J. A. H. Wetzelaer, F. B. Kooistra, S. C. Veenstra, J. C. Hummelen and P. W. M. Blom, *Adv. Mater.*, **2008**, 20, 2116-2119.

[4] M. Lenes, S. W. Shelton, A. B. Sieval, D. F. Kronholm, J. C. Hummelen and P. W. M. Blom, *Adv. Funct. Mater.*, **2009**, 19, 3002-3007.

[5] Y. J. He, H. Y. Chen, J. H. Hou and Y. F. Li, *J. Am. Chem. Soc.*, **2010**, 132, 1377-1382.

[6] G. J. Zhao, Y. J. He and Y. F. Li, *Adv. Mater.*, **2010**, 22, 4355-4358.

[7] E. Voroshazi, K. Vasseur, T. Aernouts, P. Heremans, A. Baumann, C. Deibel, X. Xue, A. J. Herring, A. J. Athans, T. A. Lada, H. Richter and B. P. Rand, *J. Mater. Chem.*, **2011**, 21, 17345-17352.

[8] K. H. Kim, H. Kang, S. Y. Nam, J. Jung, P. S. Kim, C. H. Cho, C. Lee, S. C. Yoon and B. J. Kim, *Chem. Mater.*, **2011**, 23, 5090-5095.

[9] Y. J. Cheng, M. H. Liao, C. Y. Chang, W. S. Kao, C. E. Wu and C. S. Hsu, *Chem. Mater.*, **2011**, 23, 4056-4062.

[10] C. Y. Zhang, S. Chen, Z. Xiao, Q. Q. Zuo and L. M. Ding, *Org. Lett.*, **2012**, 14, 1508-1511.

[11] X. Y. Meng, W. Q. Zhang, Z. A. Tan, Y. F. Li, Y. H. Ma, T. S. Wang, L. Jiang, C. Y. Shu and C. R. Wang, *Adv. Funct. Mater.*, **2012**, 22, 2187-2193.

[12] J. A. Mikroyannidis, A. N. Kabanakis, S. S. Sharma and G. D. Sharma, *Adv. Funct. Mater.*, **2011**, 21, 746-755.

[13] J. A. Mikroyannidis, D. V. Tsagkournos, S. S. Sharma and G. D. Sharma, *J. Phys. Chem. C*, **2011**, 115, 7806-7816.

[14] M. F. Wang, E. Chesnut, Y. M. Sun, M. H. Tong, M. Guide, Y. Zhang, N. D. Treat, A. Varotto, A. Mayer, M. L. Chabinyc, T. Q. Nguyen and F. Wudl, *J. Phys. Chem. C*, **2012**, 116, 1313-1321.

[15] C. Saravanan, C. L. Liu, Y. M. Chang, J. D. Lu, Y. J. Hsieh, S. P. Rwei and L. Wang, *Acs Appl. Mater. Inter.*, **2012**, 4, 6133-6141.

[16] S. A. Backer, K. Sivula, D. F. Kavulak and J. M. J. Frechet, *Chem. Mater.*, **2007**, 19, 2927-2929.

[17] J. Nagakubo, M. Ashizawa, T. Kawamoto, A. Tanioka and T. Mori, *Phys. Chem. Chem. Phys.*, **2011**, 13, 14370-14377.

[18] T. Dallos, M. Hamburger and M. Baumgarten, *Org. Lett.*, **2011**, 13, 1936-1939.

[19] V. Lukes, M. Breza, D. Vegh, P. Hrdlovic, J. Krajeovic and V. Laurinc, *Synthetic Met*, **2001**, 124, 279-286.

[20] R. Neidlein and D. Knecht, *Chem Ber-Recl*, **1987**, 120, 1593-1595.

[21] U. M. FernandezPaniagua, B. M. Illescas, N. Martin and C. Seoane, *J. Chem. Soc. Perk. T 1*, **1996**, 1077-1079.

[22] J. Pommerehne, H. Vestweber, W. Guss, R. F. Mahrt, H. Bassler, M. Porsch and J. Daub, *Adv. Mater.*, **1995**, 7, 551-554.

[23] Y. Xia, C. Musumeci, J. Bergqvist, W. M, F. Gao, Z. Tang, S. Bai, Y. Jin, C. Zhu, R. Kroon, C. Wang, M. R. Andersson, L. Hou, O. Inganas and E. Wang, *J. Mater. Chem.* A, **2016**, *4*, 3835–3843.

Chapter 6

Design and Synthesis of a 3D non-Fullerene Acceptor Me-PDI_4 with Tetrahedral Architecture Based on PDI

PDI is a powerful building block for non-fullerene acceptor development while the fullerene PCBM has been the dominant acceptor due to its superior 3D isotropic electron transporting ability. In this chapter, by combining PDI unit and the 3D concept, a novel 3D non-fullerene acceptor Me-PDI_4 with tetrahedral architecture has been designed and synthesized. The physicochemical properties were investigated. Solution-processed OSCs adopting Me-PDI_4 as the acceptor exhibited a best PCE value of 2.73% under optimized conditions with an inverted device structure. This new design with the idea of 3D or tetrahedral configuration provides an alternative method to improve the OSCs performance based on non-fullerene acceptors in the future.

*This section has been published substantially as: W. Chen *et al*, *J. Mater. Chem. C*, **2015**, *3*, 4698–4705 (2015 most accessed)

6.1 Introduction

In the last chapter was discussed the design and synthesis of OSCs acceptors TQMA and TQBA based on fullerene. Although they exhibited a moderate PCE result of 2.8%, it seems very difficult to make further improvement by modification on the fullerene ball and so researchers have turned their sights onto acceptor based on non-fullerene acceptors. Regarding to the types as well as the development history of these acceptors, they have been reviewed in Chapter 2. For non-fullerene acceptors, they can be simply classified as two groups: small molecule acceptors and polymer acceptors. In this chapter, the focus is on the non-fullerene acceptors based on small molecules.

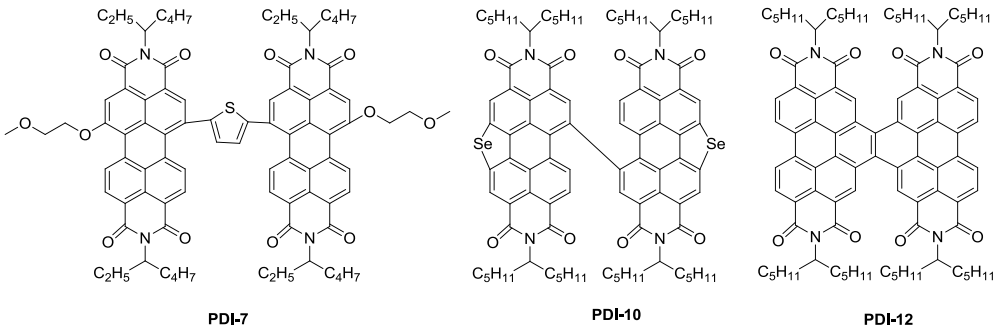

Fig. 6.1.1 Structures of PDI based acceptors

Non-fullerene acceptors developed slowly before 2013 and generally the PCE was lower than 3%.[1] For PDI, one member of the non-fullerene acceptors family, this problem existed due to its strong tendency to aggregate and produced poor morphology of the device film. However, a breakthrough with the acceptor **PDI-7**[2] in 2013 was reported by Yao and his coworkers as shown in **Fig. 6.1.1**. This acceptor has a twisted structure formed by two PDI units with a thiophene molecule as a linker and by combination with donor materials PTB7-Th, a PCE of 4.03% was achieved, which was among the best OSCs results based on a non-fullerene acceptor and demonstrated the effectiveness of the building block PDI. PDI has been known for a long time as an n-type organic semiconductor with excellent thermal, chemical and light stability. In addition, it has several advantages for use as an OSCs acceptor building block: 1) It shows strong absorption in the visible region as well as in the NIR area 2) It has a suitable LUMO energy (ca. –4.0 eV) and high electron mobility, which make it a good match to the donor materials.[3, 4] 3) Their solubility, optoelectronic and self-assembling properties can be

tuned finely through proper modification.[5, 6] Due to these advantage of PDI and the promising result obtained by Yao and his coworkers, following the twisted structure idea, various non-fullerene acceptors based on PDI as well as its derivatives were designed and synthesized,[7, 8] some being shown in **Fig. 6.1.1** (for more examples, see chapter 2). They showed very good PCE results with the best being >8%.

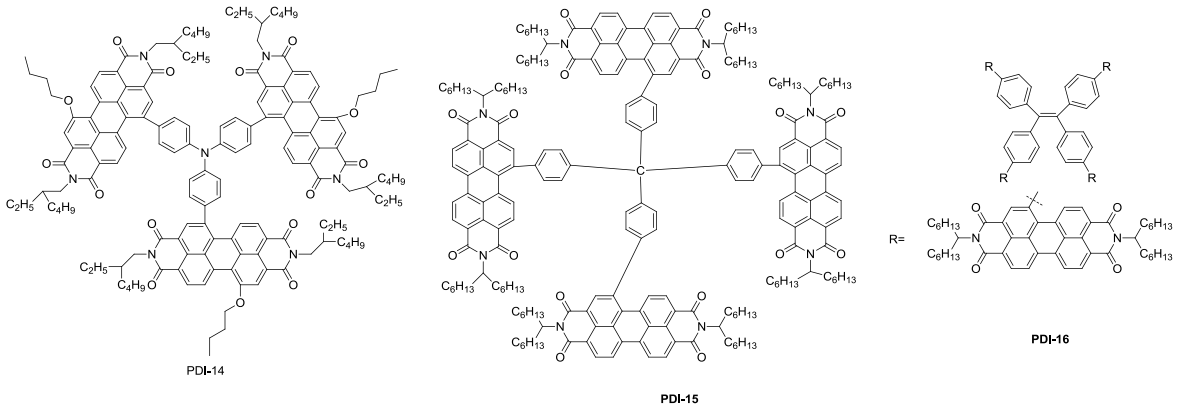

Fig. 6.1.2 Structures of 3D PDI based acceptors

Although these efforts are impressive, further improving the performance of PDIs in OSCs further is still highly desirable. Researchers once speculated that the reason that OSCs based on fullerene acceptors exhibit excellent results was ascribed to the isotropic charge transport ability of these materials due to their ball-like structure.[9-11] Thus, design and synthesis of novel non-fullerene acceptors with a 3D architecture to mimic the behavior of fullerene-based acceptor may be beneficial for enhancing the OSCs performance. Several molecules based on this idea have been produced by different research groups. (**Fig. 6.1.2**) For example, Zhan and his coworkers reported a novel quasi-3D non-fullerene acceptor **PDI-14** by taking triphenylamine as core and PDI as peripheral units, which yielded a PCE performance as high as 3.32% using compound PBDTTT-C-T as donor .[12, 13] When the triphenylamine core was changed to a tetraphenyl methane core, acceptor **PDI-15** was designed and synthesized, which showed an improved PCE result of 4.3% mixing with donor PffBT4T-2DT.[14] Yan and his coworkers designed and synthesized another novel non-fullerene acceptor **PDI-16** by adopting tetraphenylethylene as the core. Taking the donor polymer PBDTT-F-TT, the best PCE performance for this acceptor was 5.53%.[15] These examples imply that non-fullerene acceptors with 3D architecture can be an effective method to elevate the PCE value.

In this chapter, a novel 3D non-fullerene acceptor Me-PDI_4 with tetrahedral architecture based on PDI has been designed and synthesized. Solution-processed OSCs adopting Me-PDI_4 as the acceptor and PBDTTT-C-T as the donor exhibited best PCE value of 2.73% at the optimized condition with inverted device structure. Our new design with the idea 3D or tetrahedral configuration provides an alternative method to improve the OSCs performance based on non-fullerene acceptor in the future. (**Fig. 6.1.3**)

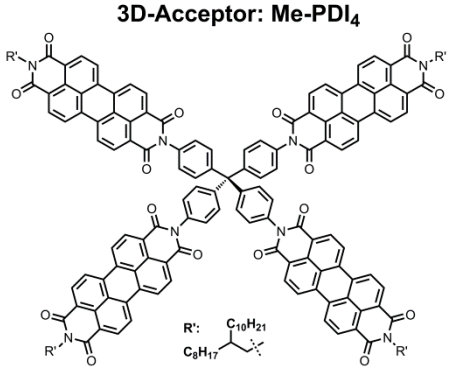

Fig. 6.1.3 Acceptor Me-PDI_4 designed and synthesized in this chapter

6.2 Experimental Methods

6.2.1 General information

NETZSCH STA 409PC instrument was used for TGA measurement at a constant heating rate a 10 ℃ min^{-1} under purified nitrogen gas flow. Bruker AV 300/400 Spectrometer was the instrument used for NMR spectra measurement. Instrument TAQ-10 was the instrument used for DSC recording at a constant heating rate of 10 ℃ min^{-1} under a nitrogen atmosphere. Shimadzu Biotech Axima Performance system was used for taking MALDI-TOF MS data and Bruker Autoflex Ⅲ was another instrument for taking HRMS data. Vario EL Cube instrument was used for the Elemental Analysis (EA) data collection. JASCO V-570 spectrophotometer was the instrument used for obtaining the UV–Vis spectrum data. CV experiments were performed with a LK98B II and all CV data were obtained through employing 3-electrodes system (Glassy carbon electrode as WE, saturated calomel electrode as RE and Pt wire as the CE). Microcomputer-based Electrochemical Analyzer is the CV measurement instrument. Tetrabutylammonium phosphorus hexafluoride (Bu_4NPF_6, 0.1 M) in dichloromethane was used as the supporting electrolyte, and the scan rate was 100 mV s^{-1}. Multimode 8 atomic force

microscope in tapping mode was used for performing ADM experiments. Philips Technical G2 F20 at 200 kV was utilized for TEM study. The specimen for TEM measurement was prepared by spin casting the blend solution on ITO/PEDOT:PSS substrate, then floating the film on a water surface, and transferring to TEM grids. SCLC mobility was measured using a diode configuration of ITO/PEDOT:PSS/active layer/Au for hole and Al/active layer/Al for electron by taking the dark current density in the range of 0-8 V and fitting the results to a space charge limited form, where SCLC is described by:

$$J = \frac{9\varepsilon_0\varepsilon_r\mu_0 V^2}{8L^3}\exp\left(0.89\beta\sqrt{\frac{V}{L}}\right)$$

where ε_0, ε_r, μ_0 represent for permittivity of free space (8.85×10^{-12} F m^{-1}), dielectric constant for the transport material and electron or hole mobility; *J*, *V*, *L* represent for the current density, internal voltage denoted as V_{appl} - V_{bi} (V_{appl}: the applied voltage and V_{bi} is: the built-in voltage) and film thickness for the active layer respectively.

6.2.2 Preparation of precursors M1-M4

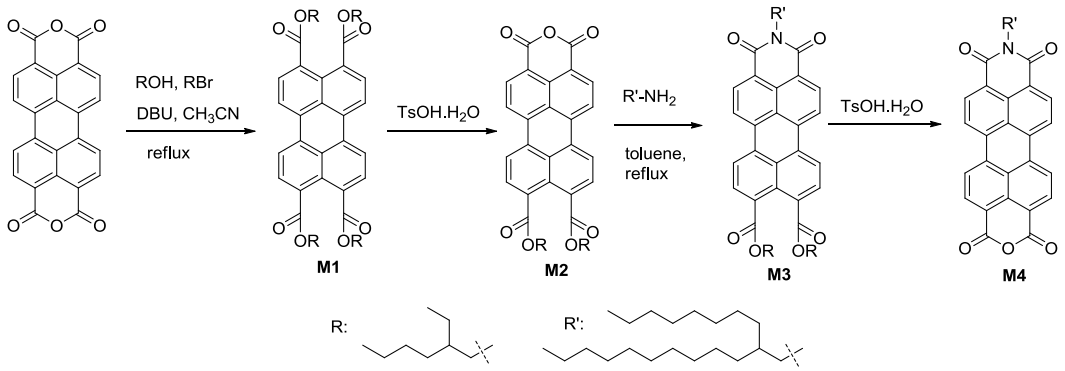

Scheme 6.2.2.1 Synthetic route for intermediate of M1 to M4

Synthesis of M1

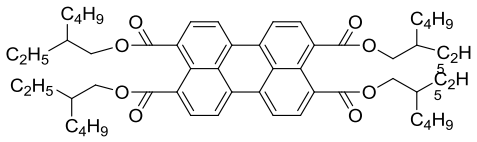

The title compound was prepared based on the modified literature method.[16] To a suspension of the dianhydride PDA (5.0 g, 12.8 mmol) in 200 ml of acetonitrile was added 2-ethyl-1-hexanol (9.9 g, 76.5 mmol), 2-ethylhexyl bromide (14.7 g, 76.5 mmol)

and 1,8-diazabicyclo[5.4.0]undec-7-ene (DBU) (15.5 g, 102.4 mmol). The mixture was heated under refluxing for 24 hrs and then cooled down to r.t.. After the removal of acetonitrile under reduced pressure, the residual was dissolved in chloroform again and dropped into methanol solution. Large amount of solid precipitated in the methanol and was collected by filtration. The crude product obtained was further purified by CC using DCM as the eluent to obtain 8.2 g of pure product. Known compound.[17] Yield: 73%. ^{1}H-NMR (Chloroform-d, 400 MHz): δ 0.99–0.89 (m, 24H), 1.54–1.33 (m, 32H), 1.81–1.75 (m, 4H), 4.30–4.22 (m, 8H), 8.02 (d, *J* = 8.0 Hz, 4H), 8.30 (d, *J* = 8.0 Hz, 4H).

Synthesis of M2

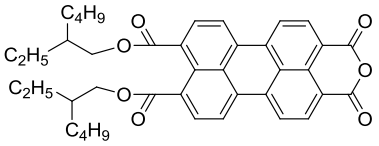

The title compound was prepared based on the modified literature method.[18, 19] A 10 mL round-bottomed flask was charged with 1.752 g (2.0 mmol) **M1**, 0.5 ml toluene and 2.5 ml *n*-dodecane before being heated to 95 ^{o}C. After the yellow powder **2** was all dissolved, 380 mg (2.0 mmol) *p*-toluenesulfonic acid monohydrate (TsOH·H_2O) was added to the solution and the solution was stirred at 95 ℃ for 5 hours. Then the dark red mixture was dissolved in $CHCl_3$. Afterwards, the chloroform solution was dropped into methanol solution and a large amount of red solid precipitated, which was collected by filtration and could be used directly in the next step. The product could be further purified by CC with DCM as the eluent. Dark red solid, 1.2 g, yield: 95%. Known compound.[17] ^{1}H-NMR (Chloroform-d, 400 MHz): δ 1.01–0.92 (m, 12H), 1.53–1.37 (m, 16H), 1.82–1.77 (m, 2H), 4.30–4.27 (m, 4H), 8.06 (s, 2H), 8.42 (s, 4H), 8.57 (s, 2H).

Synthesis of M3:

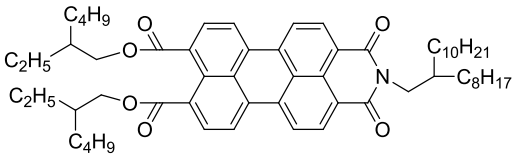

A mixture of **M2** (1.75 g, 2.76 mmol) and 2-octyldodecylamine (984 mg, 3.31 mmol) was refluxed in 40 ml toluene under argon protection for 48 hrs until the anhydride disappeared through TLC monitor. After the removal of toluene under reduced pressure, the residual was dissolved in minimal chloroform and dropped into methanol solution. A

large amount of solid precipitated from the methanol and was collected by filtratration. The crude product so obtained can be used in the next step without further purification. The product could be further purified by CC with DCM as eluent. Dark red solid, 2.34 g, yield 93%. ^{1}H-NMR (Chloroform-d, 400 MHz): δ 1.01–0.82 (m, 18H), 1.53–1.21 (m, 48H), 1.83–1.76 (m, 2H), 2.09 (m, 1H), 4.13 (d, J= 7.2 Hz, 2H), 4.33–4.24 (m, 4H), 8.02 (d, *J*= 8.0 Hz, 2H), 8.33 (d, *J* = 8.0 Hz, 4H), 8.52 (d, *J*= 8.0 Hz, 2H); ^{13}C-NMR(Chloroform-d, 100 MHz): δ 11.0, 14.1, 22.6, 23.0, 23.9, 26.5, 29.0, 29.3, 29.6, 30.1, 30.5, 31.7, 31.9, 36.6, 38.8, 44.6, 68.1, 121.5, 121.9, 122.3, 125.6, 128.8, 128.9, 129.1, 129.8, 131.1, 131.7, 131.9, 135.0, 163.7, 168.2. MALDI-TOF MS: calculated for $C_{60}H_{83}NO_6 + H^+$, 914.62; found: 914.61 (M+).

Synthesis of M4

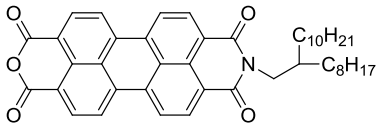

The title compound was prepared based on the modified literature method.[20] A 100 mL round-bottomed flask was charged with 2.30 g (2.52 mmol) **2**, 40 ml toluene and heated to 100 ^{o}C. After the solid was all dissolved, 570 mg (3.0 mmol) TsOH·H_2O was added to the solution and the solution was stirred at 100 ℃ for 5 hours. Then the dark red mixture was dissolved in 40 mL $CHCl_3$. Then, due to the low solubility of the product in $CHCl_3$, the chloroform solution was filtered and the crude product was obtained. The product can be further purified by CC with $CHCl_3$: acetone = 20 : 1 (v/v) as the eluent. Know compound.[21] Dark red solid, 1.6 g, yield: 95%. ^{1}H-NMR (Chloroform-d, 400 MHz): δ 0.86–0.82 (m, 6H), 1.25–-1.21 (m, 32H), 2.04–1.97 (m, 1H), 4.174 (d, *J* = 7.2 Hz, 2H), 8.68–8.66 (m, 4H), 8.74–8.71 (m, 4H).

Synthesis of Me-PDI$_4$

51 mg (0.135 mmmol) of tetra(4-aminophenyl) methane and 403 mg (0.60 mmol) **M4** as well as a catalytic amount of of anhydrous $Zn(OAc)_2$ was added into 10 mL quinoline. The mixture solution was refluxed for 36 hrs until the reaction was complete by TLC. Then, the reaction solution was cooled down to r.t. and dropped into diluted 2N HCl solution. A large amount of precipitate appeared immediately and the solution was stirred for about 20 min. The red precipitated solid was afterwards collected by filtration and

washed several times with H_2O and then with methanol. The crude product can be further purified by CC by using the eluent chloroform: methanol = 100 : 1.5 (V/V). Deep red solid, 221 mg, yield: 55%. ^{1}H-NMR (chloroform-d, 400 MHz): 0.84–0.81 (m, 24H), 1.36–1.21 (m, 128H), 2.01 (m, 4H), 4.18 (m, 8H), 7.65–7.57 (m, 16H, aromatic H), 8.09–8.07 (m, 16H, perylene aryl H), 8.43 (m, 16H, perylene aryl H); ^{13}C-NMR(100 Hz-$CDCl_3$): 14.0, 22.6, 26.5, 29.3, 29.6, 29.7, 30.1, 36.7, 44.8, 64.8, 122.6, 123.0, 123.1, 125.2, 128.1, 128.5, 130.6, 133.2, 133.6, 148.7, 162.7, 163.1. MALDI-TOF MS: calculated for $C_{201}H_{212}N_8O_{16}$ + H^+, 2993.60; found: 2994.61. Elemental analysis: calculated $C_{201}H_{212}N_8O_{16}$, C: 80.58, H: 7.13, N: 3.74; experimental data: C: 80.72, H: 7.21, N: 3.99. (**Fig. 6.2.2.1**)

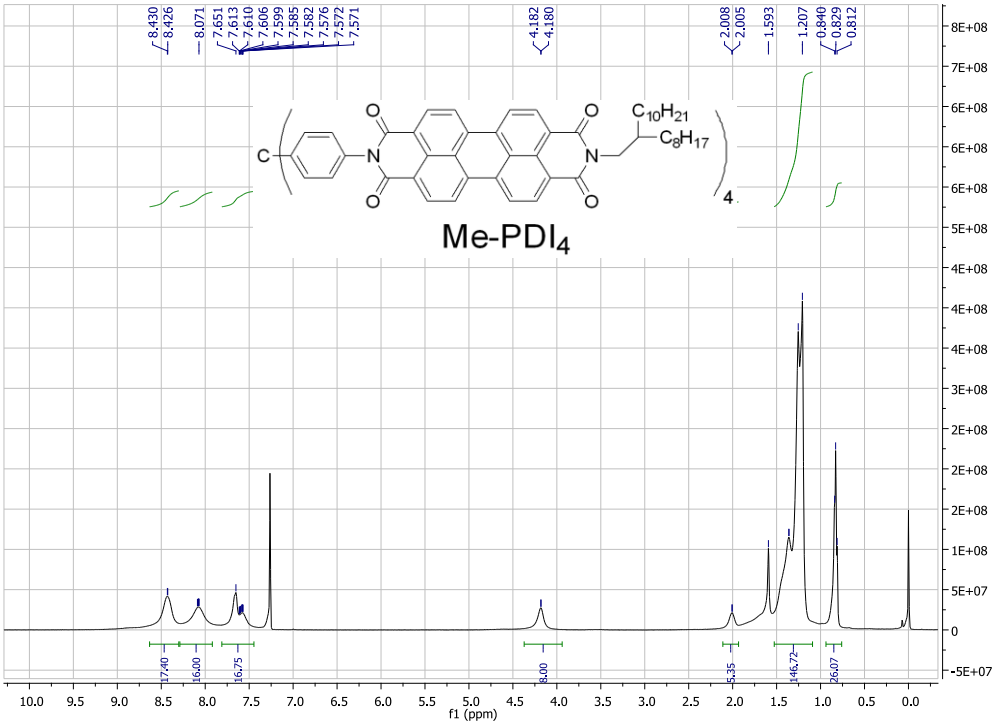

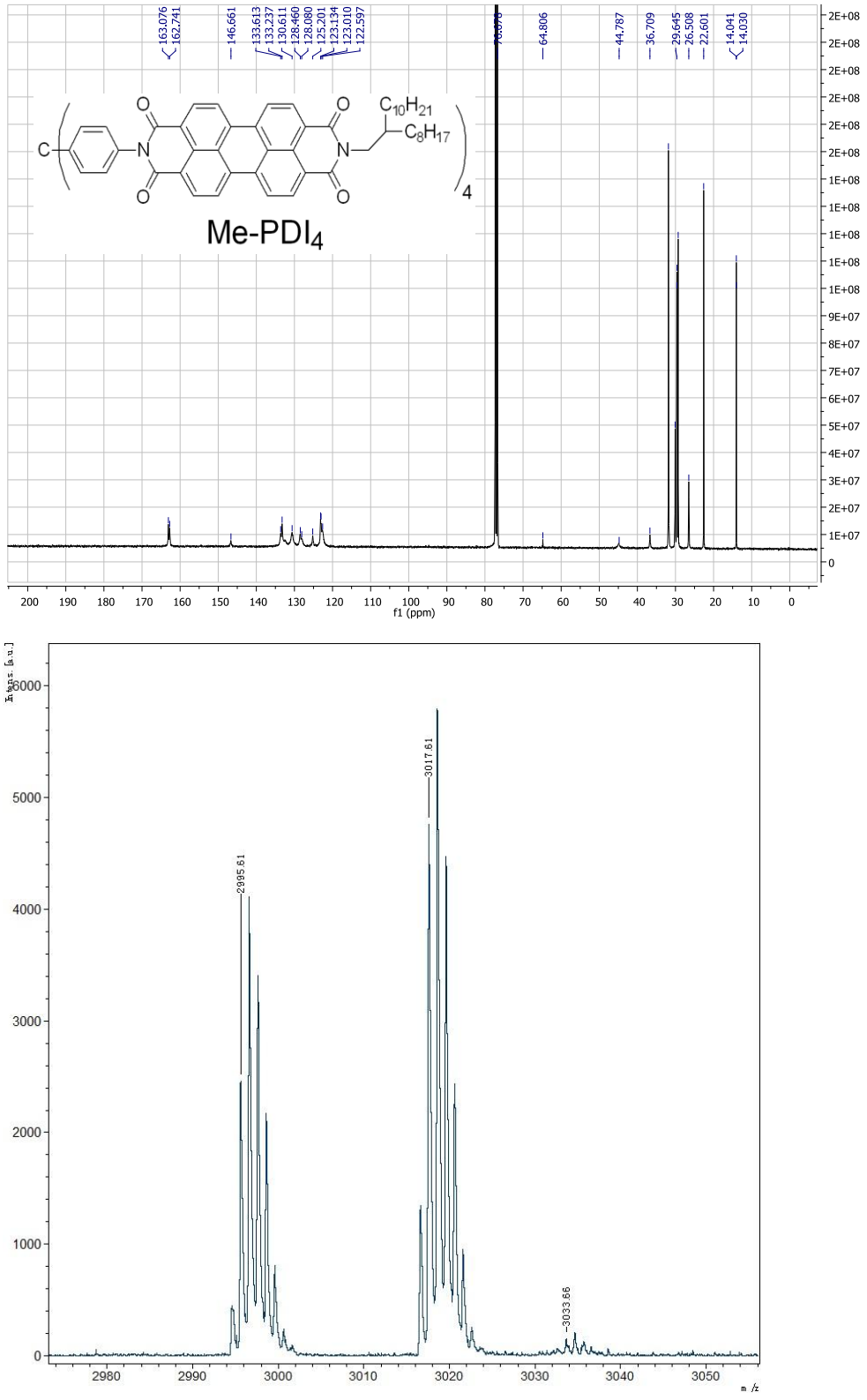

Fig. 6.2.2.1 NMR and MS spectra of the **Me-PDI$_4$**

6.2.3 Device fabrication and measurements

The conventional device structure was fabricated as glass/ITO/PEDOT:PSS/PBDTTT-C-T:Me-PDI_4/Ca/Al. Patterned ITO-coated substrates were firstly cleaned using a detergent scrub and subsequently immersed in an ultrasonic bath to be treated successively with soap in DI water, DI water, acetone and isopropyl alcohol for 15 minutes respectively. These ITO substrates were dried with a stream of N_2 gas and put into UVO machine to dry for 20 minutes. A PEDOT:PSS layer of around 30 nm (Clevios P VP AI 4083, filtered at 0.45 mm) was then spin-coated onto the ITO substrates at the spinning rate of 4500 rpm/min and baked at 150 ^oC in an oven under ambient conditions for 20 minutes. Afterwards, the substrates were transferred quickly into the argon protected glovebox. Subsequently, a blended solution of the donor and acceptor materials PBDTTT-C-T:Me-PDI_4 in *o*-DCB (w/w = 1 : 1, totally 30 mg mL^{-1}) with DIO additive at various concentrations was spin-coated above the PEDOT:PSS layer at 1500 rpm. After TA for 10 minutes at required temperature, a metal Ca layer (around 20 nm thick) and the metal electrode Al (around 100 nm thick) in succession were deposited on the active layer under high vacuum.

The inverted device structure was fabricated as glass/ ITO/ZnO nanoparticles (NPs)/PBDTTT-C-T:Me-PDI_4/modified PEDOT: PSS/Ag. ZnO NPs were prepared according to the literature published by Beek et al.[22] ITO substrates were cleaned following the procedures described in last paragraph and spin-coated with the filtrated ZnO NP solution in n-BuOH at 3000 rpm (~30 nm). After being baked at 120 ^oC for 30 minutes, these substrates were quickly transferred into an argon protected glove box. The active layer solution was subsequently spin-coated onto the ZnO layer under the same conditions using the conventional device. Then the modified PEDOT:PSS[23, 24] was spin-coated onto the active layer, followed by TA for 10 minutes at 100 ^oC. Finally, a metal Ag layer for 100 nm was deposited on the active layer.

6.3 Principal outcomes

6.3.1 Synthetic route for Me-PDI_4

As shown in **scheme 6.3.1**, Me-PDI_4 was synthesized through one-step reaction by refluxing the reactants amine and the anhydrous **M4** in a quinoline solution for 48 h at 180 ^oC in the present of small amount of catalytic anhydrous $Zn(OH)_2$. The intermediate compound **M4** was designed and synthesized through several steps according to the procedures described in the **6.2.2 experimental methods** part. The as-prepared deep red target molecule Me-PDI_4 was obtained in 55% yield after purification and fully characterized by ^1H-NMR, ^{13}C-NMR and MALDI-TOF. Importantly, Me-PDI_4 had very good solubility (>20 mg mL^{-1}) in various common solvents including DCM, chloroform, chlorobenzene and *o*-DCB, which is favorable for the solution processed fabrication of devices.

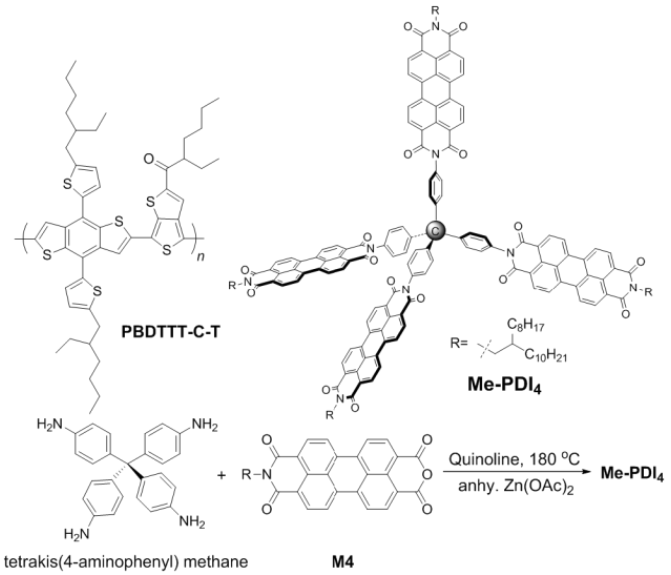

Scheme 6.3.1 Synthetic route for Me-PDI_4 and structure for donor PBDTTT-C-T

6.3.2 Physicochemical properties of Me-PDI_4

Thermal properties

TGA and DSC spectra of Me-PDI_4 were measured as displayed in **Fig. 6.3.2.1** to investigate its thermal properties. It can be observed that from the TGA diagram, Me-PDI_4 has a relative high degradation temperature at 364 ^oC with 5% weight loss and can be stable up to 310 ^oC. For the DSC spectrum, there is no peak observed between 50 and 300 ^oC for any melting or crystalline phase transition, which indicates that Me-PDI_4 may have low crystallinity.

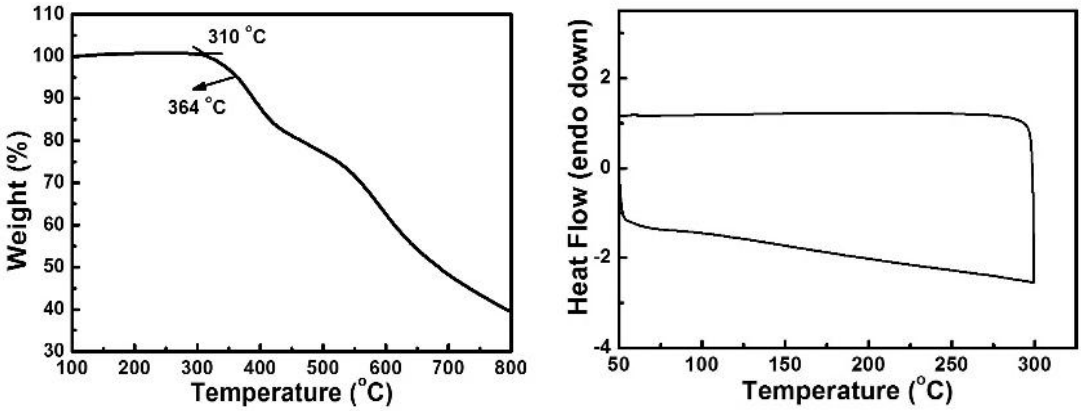

Fig. 6.3.2.1 TGA and DSC spectra of **Me-PDI$_4$**

Simulation of Me-PDI$_4$

Theoretical DFT calculation of energy level for PDI-M$_4$ was based on B3LYP/6-31G* and carried out using Gaussian 09. The longer C_{20} alkyl chain was substituted by a shorter ethyl group. Me-PDI$_4$ compound possesses a high symmetric structure and there is a dihedral angle of 110.171 between the phenyl and the PDI units, which means the tetraphenyl methane core separates the four PDI units very well. In addition, this molecule is predicted have the ability to receive up to eight electrons due to the four degenerated LUMO energy levels, which is very similar to the behavior of acceptor $PC_{61}BM$ with three quasi-degenerated LUMOs (**Fig. 6.3.2.2**).[25] Besides this, it is expected that there will be intramolecular interaction between the PDI units due to the 3D configuration of Me-PDI$_4$ acceptor, which may facility the electron-coupling when charge transfer happens.

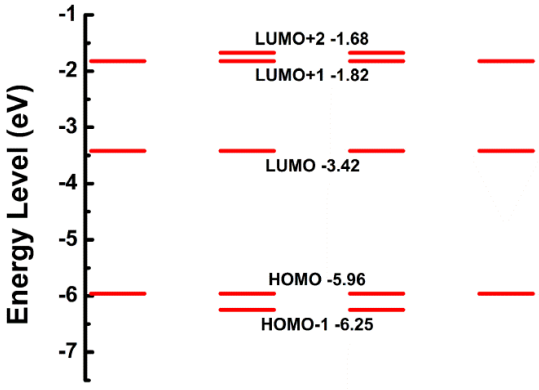

Fig. 6.3.2.2 Theoretical calculations of energy level **Me-PDI$_4$**

Electronic and optical properties

The normalized UV-Vis spectra about Me-PDI_4 in solution and film are shown in **Fig. 6.3.2.3**. For the absorption in solution, Me-PDI_4 displays a similar behavior to the mono-PDI molecule with a narrow absorption region between 420 to 550 nm and two peaks at 490 nm and 530 nm. For the absorption in neat film, Me-PDI_4 exhibited an intense and broader absorption in comparison with its absorption in solution, indicating the enhanced packing of the molecule. As to the blended film absorption for the PBDTTT-C-T:Me-PDI_4 active layer, a wide absorption spectrum covering from 300 nm to 780 nm forms due to the complementary absorption of the donor and acceptor materials, which indicates that both the donor and acceptor materials may contribute to the J_{sc} for the OSCs device. The bandgap for Me-PDI_4 can be calculated to be 2.14 eV according to the equation $E_g^{opt} = 1240nm/\lambda_{onset}$.

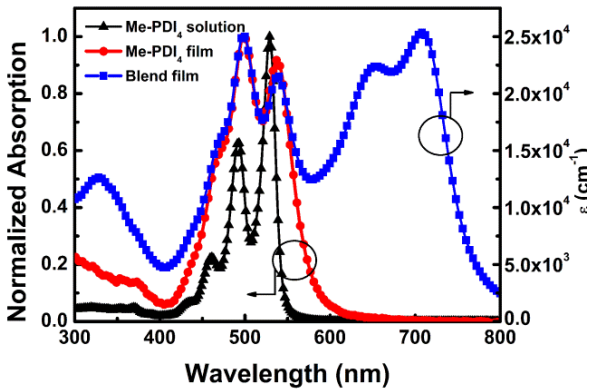

Fig. 6.3.2.3 UV-Vis spectra of **Me-PDI_4** and its blended film with PBDTTT-C-T

CV diagram for Me-PDI_4 was measured in 0.1 M *n*-Bu_4NPF_6 anhydrous DCM solution to study its electrochemical properties. In Fig. **6.3.2.4a**, the onset of reduction potential E_{red}^{onset} was measured to be –0.98 V versus $FeCp^2$ +/0 (+0.48 V). Thus, according to the following equation:

$E_{LUMO} = -(E_{red}^{onset} + 4.8)$ eV,

The LUMO value for Me-PDI_4 can be calculated to be –3.82 eV assuming the absolute energy level for $FeCp^2$ +/0 is 4.8 eV below vacuum.[26] The HOMO value can be further calculated to be –5.96 eV by the LUMO and the E_g^{opt}. All the corresponding data are summarized in Table **Table 6.3.2**.

The energy level diagram for the donor and acceptor materials is drawn in **Fig. 6.3.2.4b.** The LUMO values for the donor and acceptor are –3.25 eV and –3.82 eV respectively

and the offset for their LUMOs can be calculated to be 0.56 eV, which is large enough to guarantee the dissociation of excitons and the electron transfer within the blended film since the minimal required value is around 0.3 eV for such offset.[27]

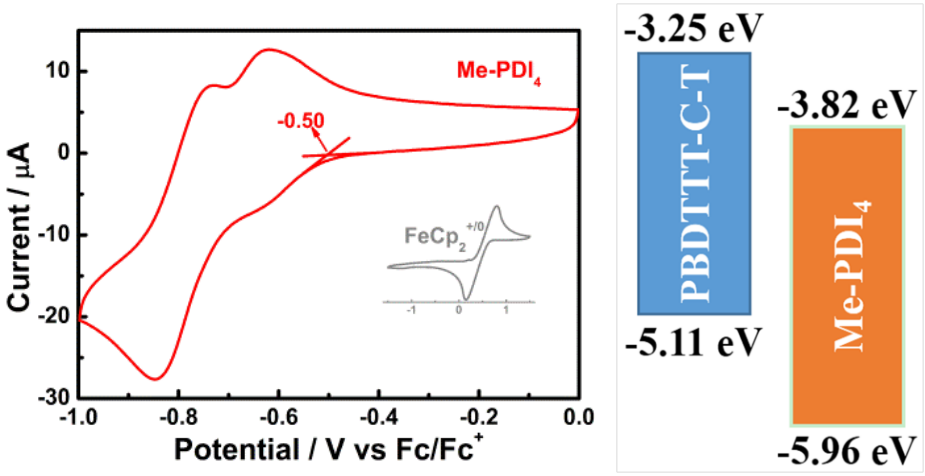

Fig. 6.3.2.4 a) CV diagram for **Me-PDI$_4$**; b) Schematic diagram for the donor and acceptor energy levels

Table 6.3.2 Physicochemical properties of **Me-PDI$_4$**

	λ_{onset} [a] [nm]	LUMO[b] [eV]	E_g^{opt} [c] [nm]	HOMO[d] [eV]
Me-PDI$_4$	580	–3.82	2.14	–5.96

[a] Obtained from UV-Vis spectrum for the neat film

[b] Measured by CV

[c] Estimated according to the equation: $E_g^{opt} = 1240m/\lambda_{onset}$

[d] Calculated according to the equation: HOMO = LUMO – E_g^{opt}

6.3.3 Photovoltaic performances and characterization of the devices

The OSCs performances for Me-PDI$_4$ were studied under standard AM1.5 solar illumination at 100 mW.cm^{-2} and the corresponding *J*–*V* curves and EQE curves are showed in **Fig. 6.3.3.1**. The detailed values for J_{sc}, V_{oc}, FF and PCE etc are summarized in table **Table 6.3.3.** The fabrication procedures for conventional and inverted device structure are described in **Experimental Methods 6.2.3** section. It was found that the concentration additive, TA treatment[28] and the device structure[39, 155, 156] all have crucial effect on the PCE performance. A low PCE of 0.9% was achieved without any additive and TA treatment, but the value increased to 2.04% with 3% DIO as additive. Further TA treatment elevated the PCE value to 2.35% with J_{sc}, V_{oc}, FF values of 6.47 mA cm^{-2}, 0.77

V and 47.2% respectively. As well as the slight improvement of the V_{oc} value (from 0.71V to 0.77 V), the significantly increased value for J_{sc}, FF values indicated that the additive and TA treatment for the device enhanced the reorganization and packing for the donor and acceptor molecules within the film, forming favorable nanoscale phase transition which facilitated the charge dissocation and transportation. At the optimized fabrication condition with 3% DIO concentration and 180 ^{o}C TA treatment, the OSCs performance with inverted structure reached to 2.73% finally, which mainly resulted from the increment of J_{sc} from 6.47 to 7.83 mA cm^{-2}. The similar FF values were obtained for both the conventional and inverted structure, indicated similar exciton combination rates in both device. Therefore, it is speculated that the elevated value for J_{sc} resulted mainly from the enhanced absorption within the active blended film.

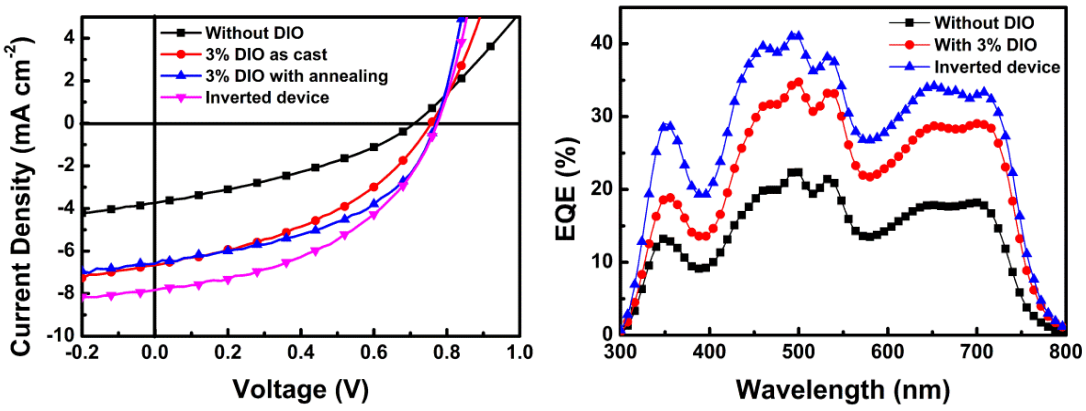

Fig. 6.3.3.1 a) *J-V* curves of devices; b) EQE spectra of the blended films

EQE spectra for the donor and acceptor blend films (**Fig. 6.3.3.1b**) display the same tendency on the J_{sc} change in *J–V* curves for the devices. It can be observed:

1) EQE spectrum becomes stronger and stronger for the films without DIO, with DIO and the inverted structure.

2) EQE spectrum show a broad spectrum ranging from 300–800 nm, which correspondes with the wide UV-Vis absorption spectrum also ranging from 300–800 nm.

3) Attributed to the contribution from Me-PDI$_4$, there is strong photo response ranging from 400–550 nm, indicating that the novel acceptor Me-PDI$_4$ play an irreplaceable role to improve the overall device photocurrent. Especially the higher EQE value of 40% at 500 nm (from acceptor) than the EQE value about 32% above 600 nm (from donor) emphasizes the significance of absorption of acceptor when designing and synthesizing of

novel non-fullerene acceptors. The calculated J_{sc} integrated from the EQE spectra for the conventional device without DIO, with 3% DIO and the inverted device is 4.004, 6.464 and 7.825 mA cm^{-2} respectively, which corresponds well with the experimental data with mismatch 7%, 3% and 1%.

Table 6.3.3 Device data for PBDTTT-C-T: **Me-PDI$_4$**

DIO [%]	V_{oc} [V]	J_{sc} [mA cm^2]	FF [%]	PCE [%] [c]
0	0.71	3.74	34.5	0.92 (0.90)
1	0.75	4.07	38.9	1.19 (1.17)
3	0.76	6.66	40.4	2.04 (1.98)
5	0.77	3.31	42.0	1.07 (1.00)
3[a]	0.77	6.47	47.2	2.35 (2.25)
3[b]	0.77	7.83	45.0	2.73 (2.47)

[a]: Conventional device with TA treatment at 180 ^{o}C for 10 min

[b]: Inverted device at the optimal condition

[c]: Average value in parenthesis

Morphological properties

In **Fig. 6.3.3.2** and **Fig.6.3.3.3**, AFM and TEM images were carried out to study the PBDTTT-C-T: **Me-PDI$_4$** blended film morphology change and elucidate its effect on the OSCs performance. The films were fabricated with different additive condition and TA treatment. Without any additive, there was no apparent phase separation for the film, obtaining a smooth morphology with a comparatively small room mean square (σ_{rms}) roughness value of 0.695 nm. Addition of 3% of DIO as the additive resulted in the formation of a particle-like domain and the σ_{rms} rms roughness increased to 0.884 nm. This change was confirmed by the corresponding phase image and the diameter of the bright domain increased to about 40 nm. Meanwhile, TEM results were consistent with the phase separation phenomena observed in AFM. The J_{sc} value enhanced from 3.74 to 6.66 mA cm^{-2} due to the improved film morphology.[29, 30] Further treatment with TA based on 3% DIO caused a more uniform film morphology with interpenetrating network and the σ_{rms} roughness value elevated again to 0.964 nm, accounting for the increment of FF from 0.404 to 0.472. During fabricating the blend films, the slow evaporation rate of DIO due to its high boiling point, may provide sufficient time for the acceptor to grow larger phase domains and produce more favorable phase separation.

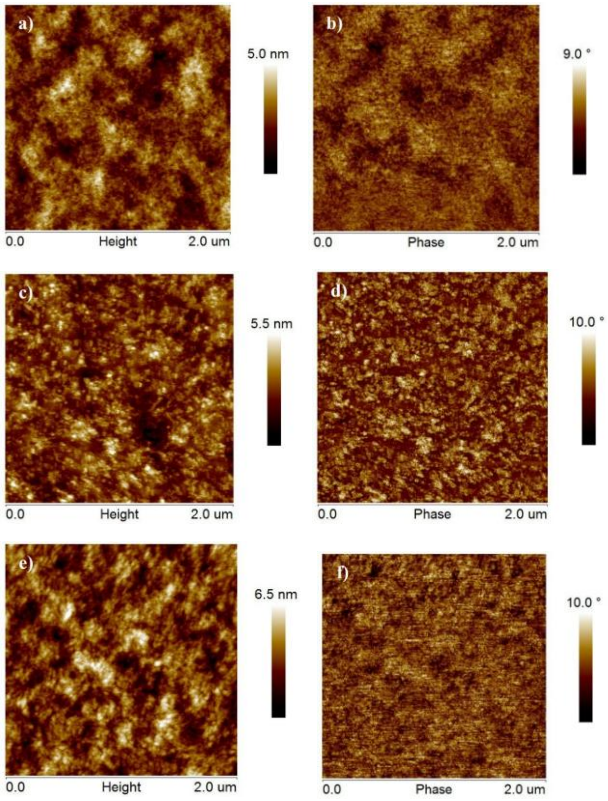

Fig. 6.3.3.2 AFM height (a, c, e) and phase (b, d, f) images of PBDTTT-C-T: **Me-PDI$_4$** blended film treated without DIO (a, b); with 3% DIO (c, d); with 3% DIO and 180 ^{o}C TA treatment (e, f).

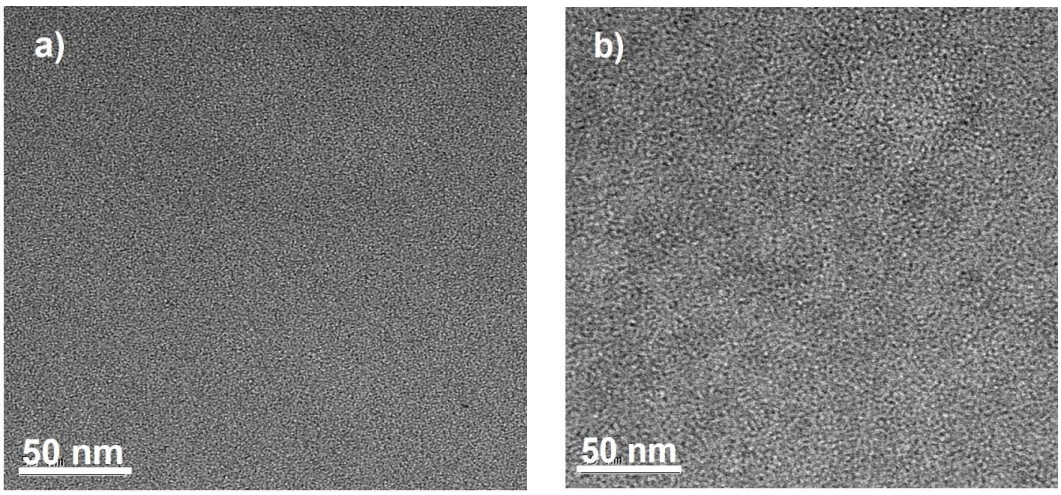

Fig. 6.3.3.3 TEM images of PBDTTT-C-T: **Me-PDI$_4$** blended films treated without DIO (a); with 3% DIO (b)

Charge transport properties

The hole and electron mobilities of the PBDTTT-C-T:Me-PDI$_4$ blended films was measured to investigate their carrier transport properties through the space charge limited

current (SCLC) method. The fitting curves for the hole-only device and the electron-only device are depicted in **Fig. 6.3.3.4**. The measured hole mobility and electron mobility for the as-fabricated film at the optimized condition was 5.55×10^{-5} cm^2 V^{-1} s^{-1} and 1.78×10^{-6} cm^2 V^{-1} s^{-1} respectively. The unbalanced electron-hole mobility (μ_e / μ_h = 0.032) may be responsible for the relatively low FF (<0.5).[31]

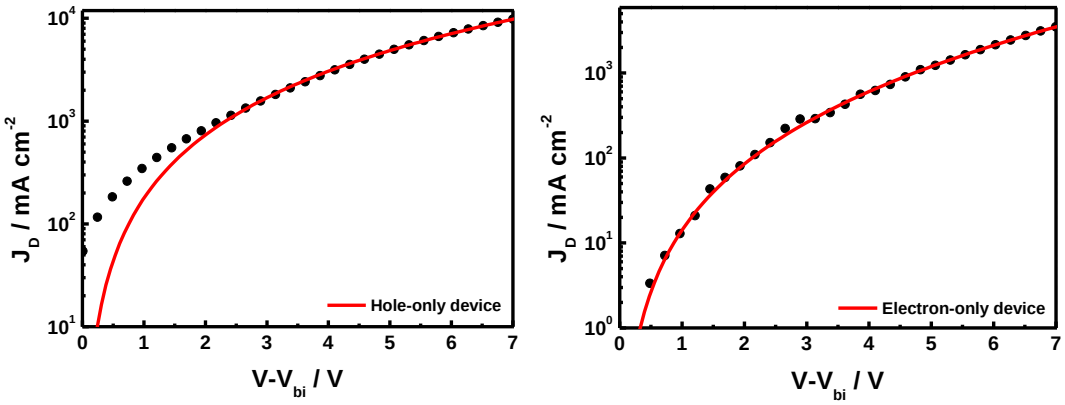

Fig. 6.3.3.4 Hole-only and electron-only device SCLC curves for PBDTTT-C-T: **Me-PDI$_4$** blended films with 3% DIO and 180 ^{o}C TA treatment

6.4 Conclusions

In this chapter, a novel non-fullerene 3D acceptor with tetrahedral architecture based on PDI was explored and synthesized. The physicochemical study indicated this acceptor possessing suitable LUMO energy level and complementary absorption spectrum compared with intended donor materials. Optimized OSCs device based on PBDTTT-C-T and Me-PDI_4 with DIO as additive and TA post treatment yielded a PCE value as high as 2.73%, which demonstrated that the 3D architecture could be an effective strategy for future design of novel acceptors.

References

[1] A. F. Eftaiha, J. P. Sun, I. G. Hill and G. C. Welch, *J. Mater. Chem. A*, **2014**, 2, 1201-1213.

[2] X. Zhang, Z. H. Lu, L. Ye, C. L. Zhan, J. H. Hou, S. Q. Zhang, B. Jiang, Y. Zhao, J. H. Huang, S. L. Zhang, Y. Liu, Q. Shi, Y. Q. Liu and J. N. Yao, *Adv. Mater.*, **2013**, 25, 5791-5797.

[3] A. F. Lv, S. R. Puniredd, J. H. Zhang, Z. B. Li, H. F. Zhu, W. Jiang, H. L. Dong, Y. D. He, L. Jiang, Y. Li, W. Pisula, Q. Meng, W. P. Hu and Z. H. Wang, *Adv. Mater.*, **2012**, 24, 2626-2630.

[4] M. C. R. Delgado, E. G. Kim, D. A. da Silva and J. L. Bredas, *J. Am. Chem. Soc.*, **2010,** 132, 3375-3387.

[5] X. W. Zhan, A. Facchetti, S. Barlow, T. J. Marks, M. A. Ratner, M. R. Wasielewski and S. R. Marder, *Adv. Mater.*, **2011**, 23, 268-284.

[6] C. Li and H. Wonneberger, *Adv. Mater.*, **2012**, 24, 613-636.

[7] D. Meng, D. Sun, C. M. Zhong, T. Liu, B. B. Fan, L. J. Huo, Y. Li, W. S. Jiang, H. S. Choi, T. Kim, J. Y. Kim, Y. M. Sun, Z. H. Wang and A. J. Heeger, *J. Am. Chem. Soc.*, **2016**, 138, 375-380.

[8] Y. Zhong, M. T. Trinh, R. S. Chen, W. Wang, P. P. Khlyabich, B. Kumar, Q. Z. Xu, C. Y. Nam, M. Y. Sfeir, C. Black, M. L. Steigerwald, Y. L. Loo, S. X. Xiao, F. Ng, X. Y. Zhu and C. Nuckolls, *J. Am. Chem. Soc.*, **2014**, 136, 15215-15221.

[9] J. Roncali, P. Leriche and A. Cravino, *Adv. Mater.*, 2007, 19, 2045-2060.

[10] B. A. Gregg, *J. Phys. Chem. Lett.*, **2011**, 2, 3013-3015.

[11] A. L. Kanibolotsky, I. F. Perepichka and P. J. Skabara, *Chem. Soc. Rev.*, **2010**, 39, 2695-2728.

[12] Y. Z. Lin, P. Cheng, Y. F. Li and X. W. Zhan, *Chem. Commun.*, **2012**, 48, 4773-4775.

[13] Y. Z. Lin, Y. F. Wang, J. Y. Wang, J. H. Hou, Y. F. Li, D. B. Zhu and X. W. Zhan, *Adv. Mater.*, **2014**, 26, 5137-5142.

[14] Y. H. Liu, J. Y. L. Lai, S. S. Chen, Y. K. Li, K. Jiang, J. B. Zhao, Z. K. Li, H. W. Hu, T. X. Ma, H. R. Lin, J. Liu, J. Zhang, F. Huang, D. M. Yu and H. Yan, *J. Mater. Chem. A*, **2015**, 3, 13632-13636.

[15] Y. H. Liu, C. Mu, K. Jiang, J. B. Zhao, Y. K. Li, L. Zhang, Z. K. Li, J. Y. L. Lai, H. W. Hu, T. X. Ma, R. R. Hu, D. M. Yu, X. H. Huang, B. Z. Tang and H. Yan, *Adv. Mater.*, **2015**, 27, 1015-1020.

[16] Y. Y. Jiang, L. H. Lu, M. Y. Yang, C. Zhan, Z. Z. Xie, F. Verpoort and S. Q. Xiao, *Polym. Chem.*, **2013**, 4, 5612-5620.

[17] A. Wicklein, M. A. Muth and M. Thelakkat, *J. Mater. Chem.*, 2010, 20, 8646-8652.

[18] C. M. Xue, R. K. Sun, R. Annab, D. Abadi and S. Jin, *Tetrahedron Lett.*, **2009**, 50, 853-856.

[19] R. Z. Wang, Z. Q. Shi, C. C. Zhang, A. D. Zhang, J. Chen, W. W. Guo and Z. Z. Sun, *Dyes Pigments*, **2013**, 98, 450-458.

[20] S. Sengupta, R. K. Dubey, R. W. M. Hoek, S. P. P. van Eeden, D. D. Gunbas, F. C. Grozema, E. J. R. Sudholter and W. F. Jager, *J. Org. Chem.*, **2014**, 79, 6655-6662.

[21] B. Saibal, A. Z. Ashar, R. N. Devi, K. S. Narayan and S. K. Asha, *Acs Appl. Mater. Inter.*, **2014**, 6, 19434-19448.

[22] W. J. E. Beek, M. M. Wienk, M. Kemerink, X. N. Yang and R. A. J. Janssen, *J. Phys. Chem. B*, **2005**, 109, 9505-9516.

[23] M. Vosgueritchian, D. J. Lipomi and Z. A. Bao, *Adv. Funct. Mater.*, **2012**, 22, 421-428.

[24] Y. L. Chen, W. S. Kao, C. E. Tsai, Y. Y. Lai, Y. J. Cheng and C. S. Hsu, *Chem. Commun.*, **2013**, 49, 7702-7704.

[25] Y. J. He and Y. F. Li, *Phys. Chem. Chem. Phys.*, **2011**, 13, 1970-1983.

[26] J. Pommerehne, H. Vestweber, W. Guss, R. F. Mahrt, H. Bassler, M. Porsch and J. Daub, *Adv. Mater.*, **1995**, 7, 551-554.

[27] M. F. Falzon, M. M. Wienk and R. A. J. Janssen, *J. Phys. Chem. C*, **2011**, 115, 3178-3187.

[28] E. Verploegen, R. Mondal, C. J. Bettinger, S. Sok, M. F. Toney and Z. A. Bao, *Adv. Funct. Mater.*, **2010**, 20, 3519-3529.

[29] C. W. Schlenker and M. E. Thompson, *Chem. Commun.*, **2011**, 47, 3702-3716.

[30] B. Y. Qi and J. Z. Wang, *Phys. Chem. Chem. Phys.*, **2013**, 15, 8972-8982.

[31] D. Credgington and J. R. Durrant, *J. Phys. Chem. Lett.*, **2012**, 3, 1465-1478.

Chapter 7

Naphtho[2,3-*b*]thiophenediimide (NTI): a Mono-Functionalizable NDI-Core-Extended Building Block for Versatile Electron-Deficient Architectures

This chapter describes a new π-extended naphthalene dimide with one fused thiphene ring, namely, naphtho[2,3-b]thiophenediimide (NTI) and characterizes its molecular and packing structure as well as electronic structure. Taking advantage of the mono-functionalizeability of the NTI unit at the thiophene α-position, a simple dimer of NTI and a trimer with a benzene core, as potential n-type organic semiconductors, are easily derived. These extended NTI derivatives can functionalize as n-type semiconductors in photovoltaic cells or thin-film transistors, exhibiting a PCE of 2.5% in preliminary tests and an electron mobility of 0.4–0.5 $cm^2 V^{-1} s^{-1}$.

*This section has been published substantially as: W. Chen *et al*, *J. Mater. Chem. C,* **2016**, *4*, 8879-8883

7.1 Introduction

In the previous chapters, it was shown that PDI is a good basis for non-fullerene acceptors candidate due to the three unique advantages: 1) good absorption in visible region to almost 600 nm 2) suitable LUMO energy level (–4.0 eV) to match most low bandgap donor polymer 3) proper electron affinity and mobility. Based on PDI unit, a non-fullerene acceptor **Me**-PDI_4 was designed and synthesized, which shows a PCE of 2.73%. Combined with the PDI acceptors discussed in the Literature Review chapter, it has been demonstrated that developing suitable building blocks (such as PDI) is very important for developing organic semiconductor materials.[1] Compared with PDI, NDI is another traditional n-type organic semiconductor for photoelectronic materials. However, NDI has several intrinsic disadvantages, which may limit its wide application as OSCs acceptor: 1) The NDI has poor absorption and large bandgap. The λ_{max} of NDI is usually around 400 nm, and thus the bandgap is around 3.0 eV according to the empirical equation $E_{gap} = 1240/\lambda_{max}$. 2) NDI has higher LUMO energy level than PDI. Due to the wide bandgap, the LUMO energy level is elevated to around –3.7 eV. 3) Charge transport ability is poor. Therefore, to design and synthesize good non-fullerene acceptors based on NDI, researchers need to overcome these obstacles. The first and most efficient method is to design D-A polymers with NDI as the A unit. Facchetti et al have reported a NDI-bithiophene based polymer **NDI-P1**, which showed a PCE result of 5% recently using donor PPDT2FBT.[2] One other strategy is to functionalize/extend the core of NDI in the horizontal direction. In this relation, recently, a novel building block naphtho[2,3-*b*:6,7-*b'*]dithiophene diimide (NDTI) based on a core-extended NDI with two fused-thiophene rings at the both sides of the naphthalene part have been reported by Takimiya and coworkers,[3, 4] in which the vacant thiophene α-positions can be effectively functionalized to elaborate various NDTI-based semiconducting materials, including small-molecule and polymers semiconducting that serve as the active material for the n-type/ambipolar semiconducting layer in OFETs and the acceptor materials in OPVs.[5-7]

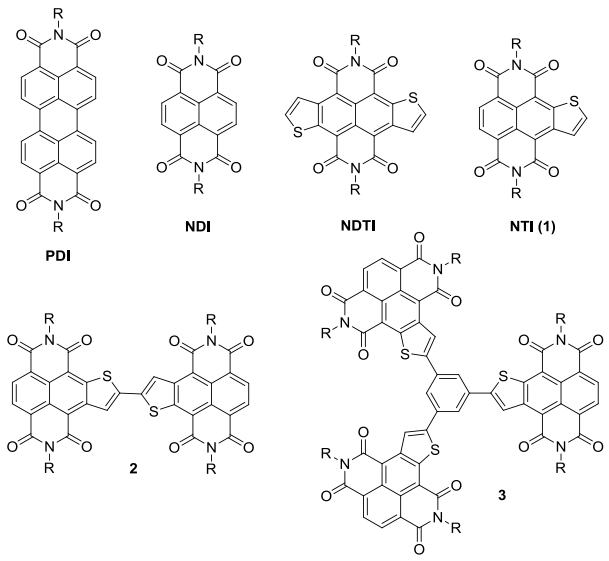

Fig. 7.1 Structures of PDI, NDI, NDTI and NTI as well as its derivatives

Since the NDTI core has two equivalent functionalization sites at the thiophene α-positions, the core is suitable to utilize in the synthesis of polymers and symmetrical oligomers, in which the NDTI part bears two other π-conjugated units. On the other hand, to ensure further designability of thiophene-fused NDIs, it would be desirable to have mono-functionalizable derivative, namely naphtho[2,3-*b*]thiophene diimide (NTI, **1**). In the present chapter, the synthesis and characterization of NTI and its utilization in the synthesis of NTI-based molecular architectures such as a dimer (**2**) and a dendritic trimer (**3**) is described. Their electronic properties and potentials as n-type organic semiconductors are also investigated by fabricating and evaluating their thin-film devices.

7.2 Experimental Methods

General

All chemicals and solvents are of reagent grade unless otherwise indicated. DCM and THF were purified by standard procedures prior to use. *N*,*N*′-Dioctyl-2-bromo-1,4,5,8-naphthalene tetracarboxylic acid diimide[8] and *N*,*N*′-bis(2-ethylhexyl)-2-bromo-1,4,5,8-naphthalene tetracarboxylic acid diimide were synthesized according to the reported procedures. Nuclear magnetic resonance[9] spectra were obtained in deuterated chloroform ($CDCl_3$) with TMS as internal reference unless otherwise stated; chemical shifts (δ) are reported in parts per million. IR spectra were recorded using a KBr pellet. EI-MS spectra

were obtained using an electron impact ionization procedure (70 eV). The molecular ion peaks of the bromine and/or sulfur containing compounds showed a typical isotopic pattern, and all the mass peaks are reported based on ^{32}S, or ^{77}Br, respectively. ESI-MS spectra were obtained using an electrospray ionization method under ambient pressure. HRMS were carried out at Materials Characterization Support Unit, RIKEN Advanced Technology Support Division.

_N,N′_-dioctyl-2-[2-(trimethylsilyl)ethynyl)]-1,4,5,8-naphthalene tetracarboxylic acid diimide (5a)

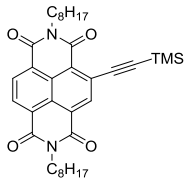

To a stirred solution of *N,N′*-dioctyl-2-bromo-1,4,5,8-naphthalene tetracarboxylic acid diimide (47mg, 0.083 mmol) in toluene (4 mL), $PdCl_2(PPh_3)_2$ (5.8mg, 0.008mmol) was added, and the resulting solution was further stirred for 30 min. at room temperature under an argon atmosphere. Then, tributyl(trimethylsilylethynyl)tin (96 mg, 0.025 mmol) was added, and the mixture was refluxed for 1 h. After cooling down, the mixture was evaporated under vacuum, and the residue was purified by CC eluting with hexane-DCM (v/v = 1:2 to 1:4) to afford a green solid (40 mg, 82%). Mp: 145–146 °C; IR (KBr): = 1707 cm^{-1}, 1662 cm^{-1} (C=O);^{1}H-NMR (400 MHz): 8.72 (d, *J* = 8.0 Hz, 1H), 8.70 (s, 1H), 8.67 (d, *J* = 8.0 Hz, 1H), 4.17–4.13 (m, 4H), 1.76–1.67 (m, 4H), 1.44–1.26 (m, 20H), 0.88–0.84 (m, 6H), 0.38 (s, 9H). ^{13}C-NMR(100 MHz): 162.56, 162.19, 162.17, 161.18, 137.36, 131.20, 130.67, 127.09, 126.99, 126.30(two carbons), 126.23, 125.53, 125.22, 110.40, 103.23, 40.97, 40.94, 31.78, 31.75, 29.22(two carbons), 29.16, 29.13, 27.97, 27.89, 27.04, 27.01, 22.61, 22.59, 14.06(two carbons), –0.33. HRMS (ESI) *m/z* calcd for $C_{35}H_{46}N_2O_4Si$: $[M]^+$ 586.3227. Found: 586.3235.

***N,N′*-Bis(2-ethylhexyl)-2-[2-(trimethylsilyl)ethynyl]-1,4,5,8-naphthalene tetracarboxylic acid diimide (5b)**

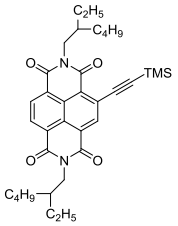

The title compound was synthesized from *N,N′*-bis(2-ethylhexyl)-2-bromo-1,4,5,8-naphthalene tetracarboxylic acid diimide in the same manner as described above for **5a** to yield a white solid, 73%. Mp: 129–131 ^{o}C; IR (KBr): = 1707 cm^{-1}, 1663 cm^{-1} (C=O);^{1}H-NMR (400 MHz): 8.77 (s, 1H), 8.76 (d, *J* = 8.0 Hz, 1H), 8.71 (d, *J* = 8.0 Hz, 1H), 4.19–4.07 (m, 4H), 1.99–1.88 (m, 2H), 1.41–1.29 (m, 16H), 0.95–0.86 (m, 12H), 0.37 (s, 9H). ^{13}C-NMR(100 MHz) 163.06, 162.73(two carbons), 161.59, 137.47, 131.36, 130.84, 127.24, 127.08, 126.41, 126.35, 126.29, 125.67, 125.22, 110.28, 103.30, 44.53, 44.43, 37.87, 37.67, 30.63, 30.51, 28.60, 28.40, 23.95(two carbons), 23.10(two carbons), 14.11, 14.09, 10.55(two carbons), –0.36; HRMS (ESI) *m/z* calcd for $C_{35}H_{46}N_2O_4Si$: $[M]^+$ 586.3227. Found: 586.3226.

***N,N′*-Dioctyl-2-(trimethylsilyl)naphtho[2,3-*b*]thiophene-4,5,8,9-diimide (6a)**

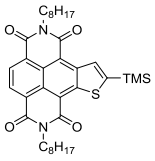

Under argon atmosphere, sodium sulfide hydrate ($Na_2S•9H_2O$, 5.76 g, 24.0 mmol), was added to a stirred suspension of **5a** (2.35 g, 4.0 mmol) in 2-methoxyethanol (400 mL) and acetic acid (8.0 mL) at 60 ^{o}C. After stirring at the same temperature for 12 h, the mixture was stirred again at room temperature for 3 h. Then, the mixture was dropped into stirring water (400 mL) to precipitate a red solid. The precipitate was collected by filtration and washed successively with water and methanol. The product was further purified by column chromatography on silica gel eluting with hexane: dichloromethane (1:3 v/v) to give an orange solid (1.61g, 65%). Mp: 183–184 ^{o}C; IR (KBr): = 1698 cm^{-1}, 1655 cm^{-1} (C=O); ^{1}H-NMR (400 MHz,): 8.93 (s, 1H), 8.63 (s, 2H), 4.23–4.17 (m, 4H), 1.80–1.72 (m, 4H), 1.47–1.24 (m, 20H), 0.89–0.86 (m, 6H), 0.54 (s, 9H). ^{13}C-NMR(100 MHz) 163.10, 163.07, 162.53, 162.46, 159.46, 147.94, 143.92, 130.21, 130.06(two carbons),

126.28, 125.36, 124.52, 123.04, 117.96, 117.58, 41.16, 41.07, 31.8(two carbons), 29.33, 29.29, 29.22(two carbons), 28.09, 28.04, 27.19, 27.16, 22.62(two carbons), 14.09(two carbons), –0.60; HRMS (ESI) *m/z* calcd for $C_{35}H_{46}N_2O_4SSi$: $[M]^+$ 618.2948. Found: 618.2952.

_N,N′_-Bis(2-ethylhexyl)-2-(trimethylsilyl)naphtho[2,3-*b*]thiophene-4,5,8,9-diimide (6b)

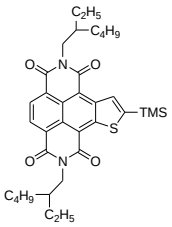

6b was synthesized from **5b** in the same manner as was used to make **6a**. Yield: 56%. Mp: 214–215 °C; IR (KBr): = 1697 cm^{-1}, 1655 cm^{-1} (C=O); ^{1}H-NMR (400 MHz): 8.95 (s, 1H), 8.67 (s, 2H), 4.22–4.10 (m, 4H), 2.04–1.92 (m, 2H), 1.43–1.24 (m, 16H), 0.96–0.86 (m, 12H), 0.54 (s, 9H). ^{13}C-NMR(100 MHz) 163.50, 163.46, 163.03, 162.97, 159.26, 148.09, 144.04, 130.35, 130.18(two carbons), 126.31, 125.37, 124.68, 123.22, 118.04, 117.68, 44.79, 44.61, 37.79(two carbons), 30.61(two carbons), 28.57(two carbons), 23.96, 23.93, 23.09(two carbons), 14.09(two carbons), 10.65, 10.57, –0.56; HRMS (ESI) *m/z* calcd for $C_{35}H_{46}N_2O_4SSi$: $[M]^+$ 618.2948. Found: 618.2948.

_N,N′_-Dioctylnaphtho[2,3-*b*]thiophene-4,5,8,9-diimide (NTI, 1a)

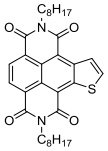

Under argon atmosphere, **6a** (990 mg, 1.6 mmol) was dissolved in THF (120 mL) and acetic acid (1.2 mL), and then, tetra-*n*-butylammmonium fluoride (1.0 M in THF, 16 mL) was added to the solution at 0 °C. After stirred for 3h at room temperature, the solution was diluted with methanol (120 mL). The resulting precipitate was collected by filtration and washed with methanol and purified by column chromatography on silica gel (hexane: dichloromethane: 1 : 3 v/v) to afford **1a** as a orange solid. (790 mg, 90%). Mp: 224–225 °C; IR (KBr): = 1695 cm^{-1}, 1649 cm^{-1} (C=O); ^{1}H-NMR (400 MHz): 8.96 (d, *J* = 8.0 Hz, 1H), 8.84 (s, 2H), 8.16 (d, *J* = 8.0 Hz), 4.29–4.24 (m, 4H), 1.82–1.75 (m, 4H), 1.48–1.29 (m, 20H), 0.90–0.86 (m, 6H). ^{13}C-NMR(100 MHz): 163.04, 163.00, 162.57,

162.50, 144.69, 142.74, 140.11, 130.34, 130.24, 126.40, 125.46, 124.56, 123.94, 123.30, 118.60, 118.33, 41.14, 41.03, 31.80(two carbons), 29.32, 29.30, 29.22(two carbons), 28.07, 28.06, 27.17, 27.15, 22.63(two carbons), 14.09(two carbons). HRMS (ESI) *m/z* calcd for $C_{32}H_{38}N_2O_4S$: $[M]^+$ 546.2552. Found: 546.2562.

***N,N′*-Dioctyl-2-bromonaphtho[2,3-*b*]thiophene-4,5,8,9-diimide (7a)**

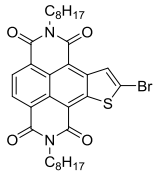

Under argon atmosphere, bromine (960 mg, 6.0 mmol) was added to a stirred suspension of **6a** (248 mg, 0.4 mmol) in dichloromethane (40 mL) at room temperature. After stirring at 40 ^oC for 15 h, the mixture was quenched with diluted $NaHSO_3$ aqueous solution and extracted with dichloromethane. The combined organic layer was washed with saturated NaCl solution, dried (Na_2SO_4), and then concentrated. The resulting crude product was purified by column chromatography on silica gel (eluent, hexane: dichloromethane = 1: 3 v/v) to give **7a** as an orange solid (190 mg, 76%). Mp: 175–176 ^oC; IR (KBr): = 1697 cm^{-1}, 1647 cm^{-1} (C=O); ^{1}H-NMR (400 MHz): 8.64 (s, 2H), 8.58 (s, 1H), 4.15–4.10 (m, 4H), 1.77 –1.69 (m, 4H), 1.46–1.28 (m, 20H), 0.89–0.86 (m, 6H); ^{13}C-NMR(100 MHz): 162.60, 162.47, 162.13, 162.03, 145.24, 141.63, 132.27, 130.54, 130.45, 126.19, 126.10, 125.21, 124.31, 122.68, 117.10, 116.40, 41.11, 41.00, 31.79(two carbons), 29.30, 29.26, 29.22(two carbons), 27.99, 27.96, 27.16, 27.11, 22.63(two carbons), 14.09(two carbons); HRMS (ESI) *m/z* calcd for $C_{32}H_{37}BrN_2O_4S$: $[M]^+$ 624.1657. Found: 624.1662.

***N,N′*-Bis(2-ethylhexyl)-2-bromonaphtho[2,3-*b*]thiophene-4,5,8,9-diimide (7b)**

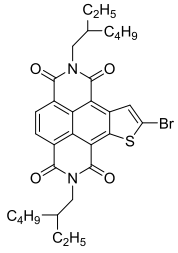

7b was synthesized from **6b** in the same manner as was used to make **7a**. Yield: 64%. Mp: 239–240 ^oC; IR (KBr): = 1697 cm^{-1}, 1647 cm^{-1} (C=O); ^{1}H-NMR (400 MHz): 8.88 (s, 1H), 8.78 (s, 2H), 4.22–4.11 (m, 4H), 2.02–1.90 (m, 2H), 1.43–1.31 (m, 16H), 0.97–0.87 (m, 12H); ^{13}C-NMR(100 MHz): 163.45, 163.29, 162.97, 162.86, 145.94, 142.34,

132.26, 130.78, 130.69, 126.60, 126.47, 125.58, 124.93, 123.32, 117.66, 116.98, 44.79, 44.63, 37.92, 37.85, 30.70, 30.61, 28.63, 28.53, 24.03, 23.98, 23.06(two carbons), 14.09(two carbons), 10.62, 10.58; HRMS (ESI) *m/z* calcd for $C_{32}H_{37}BrN_2O_4S$: $[M]^+$ 624.1657. Found: 624.1647.

[2,2′]Bi[naphtho[2,3-*b*]thienyl]-*N*,*N*′,*N*″,*N*‴-tetraoctyl-4,4′,5,5′,8,8′,9,9′-tetraimide (NTI-dimer-C8) (2a)

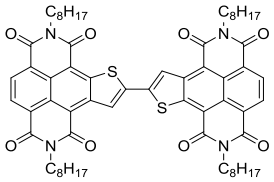

Hexamethylditin (26mg, 0.08mmol, 0.017 mL) was added to a solution of **7a** (94 mg, 0.15 mmol), and tetrakis(triphenylphosphine)palladium(0) ($Pd(PPh_3)_4$, 0.015 mmol, 18 mg) in 20 mL of toluene under an argon atmosphere. The solution was heated to 95 ^oC for 3 h and then to 105 ^oC for 10 h. After the solution was cooled down, the resulting precipitate was collected by filtration to obtain the crude product, which was dissolved in hot *o*-dichlorobenzene (>150 ^oC), and the hot solution was filtered to remove the insoluble particles. Recrystallization from *o*-DCB twice afforded analytically pure **2a** (60 mg, 73% yield). Mp: > 350 ^oC; IR (KBr): = 1697 cm^{-1}, 1649 cm^{-1} (C=O); ^{1}H-NMR (400 MHz, *o*-dichlorobenzene-d_4): 9.53 (s, 2H), 8.65 (s, 4H), 4.37 (s, 8H), 1.97–1.94 (m, 8H), 1.57–1.30 (m, 40H), 0.88 (s, 12H); HRMS (ESI) *m/z* calcd for $C_{64}H_{74}N_4O_8S_2$: $[M]^+$ 1090.4948. Found: 1090.4950.

No signal was observed in the 13C-NMRspectrum even after 20,000 scans, owing to the low solubility of **2a**.

[2,2′]Bi[naphtho[2,3-*b*]thienyl]-*N*,*N*′,*N*″,*N*‴-tetrakis(2-ethylhexyl)-4,4′,5,5′,8,8′,9,9′-tetraimide (2b) (NTI-dimer-C2C6)

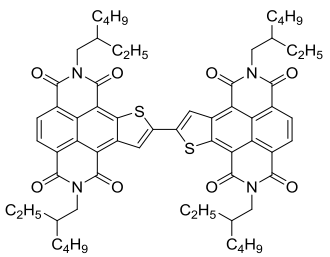

2b was synthesized from **7b** in the same manner as was used to make **2a**. Yield: 74%. Mp: > 350 ^oC; IR (KBr): = 1699 cm^{-1}, 1648 cm^{-1} (C=O); ^{1}H-NMR (400 MHz, *o*-

dichlorobenzene-d_4): 9.51 (s, 2H), 8.64 (s, 4H), 4.35–4.25 (m, 8H), 2.19–2.12 (m, 4H), 1.54–1.32 (m, 32H), 1.02-0.86 (m, 24H); HRMS (ESI) *m/z* calcd for $C_{64}H_{74}N_4O_8S_2$: $[M]^+$ 1090.4948. Found: 1090.4973. No signal was observed in 13C-NMRspectrum even after 20,000 scans, owing to the low solubility of **2b**.

1,3,5-Tris(naphtho[2,3-*b*]thiophen-2-yl)benzen-*N*,*N′*,*N″*,*N‴*,*N⁗*,*N⁗′*-hexakis(2-ethylhexyl)-4,4′,4″,5,5′,5″,8,8′,8″,9,9′,9″-hexaimide (Trimer-ph-C2C6) (3b)

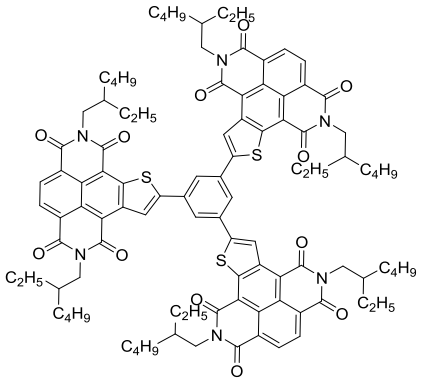

Under an argon atmosphere, aqueous sodium carbonate solution (2 M, 0.75 mL, 1.5 mmol) was added to a solution of **7b** (113 mg, 0.18 mmol), 1,3,5-tris(4,4,5,5-tetramethyl-1,3,2-dioxaborolan-2-yl)benzene (21 mg, 0.045 mmol), and tetrakis(triphenylphosphine)palladium(0) ((Pd(PPh_3)$_4$, 0.007 mmol, 8.0 mg) in 10 mL of dioxane, and the resulting mixture was refluxed for 36 h. After cooling, the reaction mixture was added dropwise into 100 mL water to precipitate a red solid, which was collected by filtration, washed successively with water and methanol. The crude product was dissolved into dichloromethane, and the solution was absorbed onto a short silica gel column, eluted first with neat dichloromethane to remove less-polar impurities, and then with dichloromethane: methanol(100: 1 v/v) to obtain **3b** as an orange solid (60 mg, 58% yield). Mp: 330–331 ^oC; IR: (KBr): = 1699 cm^{-1}, 1655 cm^{-1} (C=O). ^{1}H-NMR (400 MHz):

9.22 (s, 3H), 8.57 (d, *J* = 8.0 Hz, 3H), 8.53 (d, *J* = 8.0 Hz, 3H), 8.35 (s, 3H), 4.34–4.17 (m, 12H), 2.07–2.19 (m, 6H), 1.48–1.29 (m, 48H), 1.00–0.83 (m, 36H); ^{13}C-NMR(100 MHz): 163.05(two carbons), 162.61, 162.48, 154.86, 144.91, 143.48, 135.42, 130.21, 130.01, 127.56, 126.06, 125.06, 124.76, 123.32, 121.04, 117.99, 117.76, 44.82, 44.68, 37.86, 37.78, 30.76, 30.67, 28.61, 28.55, 24.12, 23.98, 23.12(two carbons), 14.08(two carbons), 10.77, 10.62. HRMS (ESI) *m/z* calcd for $C_{102}H_{114}N_6O_{12}S^3$: $[M]^+$ 1710.7657.

Found: 1710.57.

7.3 Principal Outcomes

7.3.1 Synthetic route for NTI and its derivatives

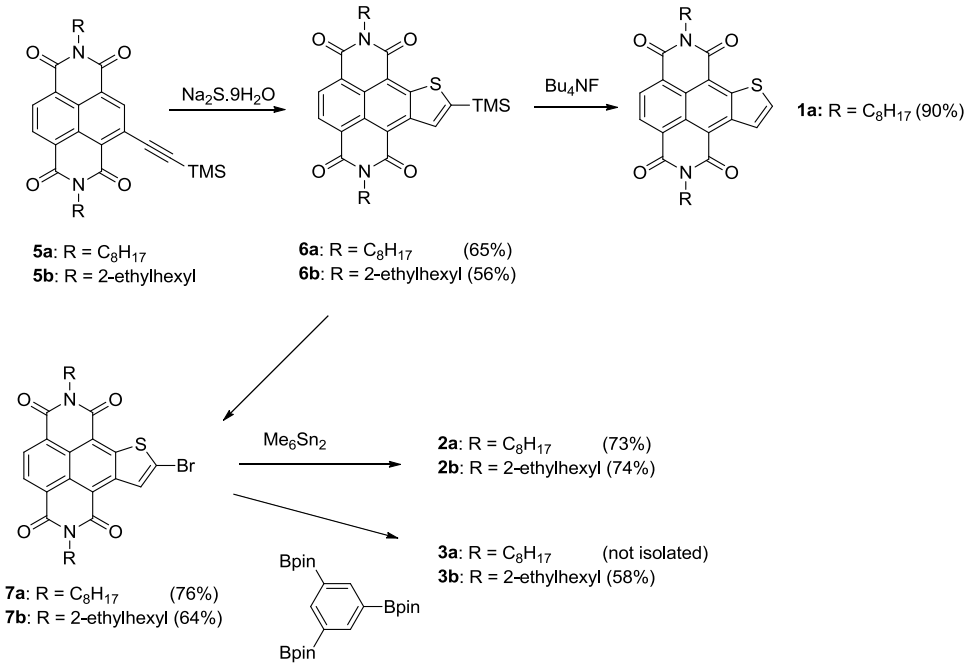

Scheme 7.3.1.1 Synthetic route for NTI and its derivatives

As we have already reported, the thiophene-annulation reaction on the NDI core can take place via the nucleophilic hydrogen substitution (S_NH) effected by sodium sulfite hydrate.[10] Following this strategy, *N,N'*-dioctyl-2-trime-thylsilylethynyl-NDI (**5a**) was first synthesized from the corresponding 2-bromo-NDI. As demonstrated in Scheme 1, **5a** was effectively converted into **6a** in a 65% isolated yield. The trimethylsilyl group was readily removed to give **1a** (90% yield) or converted into the bromide group by the treatment with bromine to give **7a** in a 76% isolated yield. **1a** was fully characterized by spectroscopic analysis (see Supporting Information) and single crystal X-ray analysis (**Fig. 7.3.1**). Although the position of the sulfur atom in the thiophene ring is disordered in the crystal structure, almost a planar molecular structure is confirmed as its analogous compound, NDTI. The brominated NTI (**7a**) turned out to be a useful compound to derive the NTI dimer (**2**) and trimer (**3**). Treatment of **7a** with hexamethylditin in the presence of tetrakis(triphenylphosphine)palladium gave **2a** as a poorly soluble solid in a 73% isolated

yield. Although the dendritic trimer with the central benzene core (**3a**) was obtained via a Suzuki-Miyaura coupling reaction of **7a** with 1,3,5-tris(4,4,5,5-tetrame-thyl-1,3,2-dioxaborolan-2-yl)benzene, concomitant **2a** formation prevented isolation of **3a** in a pure from, because of poor solubilities of **2a** and **3a**. Instead, introduction of 2-ethylhexyl group on NTI core improved the solubility of the dimer (**2b**) and trimer (**3b**) greatly, and as a result, both **3b** as well as **2b** with improved solublities were isolated as pure forms in reasonable yields. All the NTI derivatives except for **3a** were characterized by spectroscopic analysis.

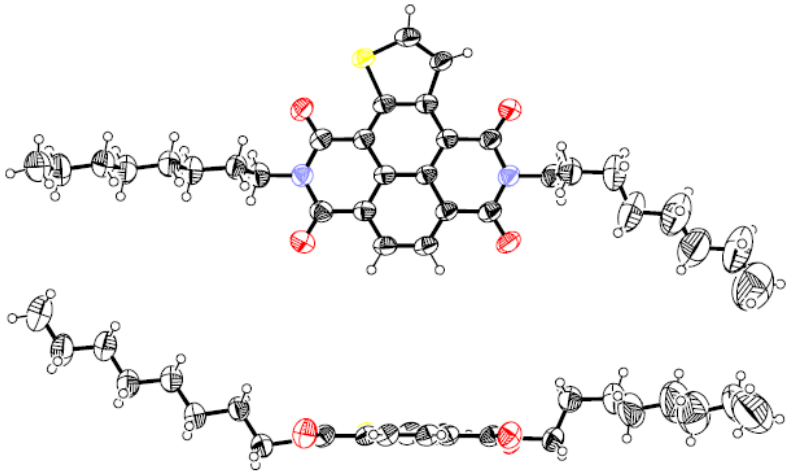

Fig. 7.3.1 Single crystal structure of **1a**

7.3.2 Physicochemical properties for NTI and its derivatives

The electronic structures of the NTI derivatives were elucidated by absorption spectroscopy and solution electrochemistry. As clearly observed in **Fig. 7.3.2.2a**, **1a** with one annulated thiophene ring shows medium absorption band (λ_{max}: 482 nm) between those of NDI (λ_{max}: 379 nm) and NDTI (λ_{max}: 548 nm). This can be qualitatively understood by the fact that the thiophene-annulation rises the energy level of HOMO without significant perturbation to the energy level of LUMO. This trend was reproduced by the theoretical calculations by the DFT methods (**Fig. 7.3.2.1**). Extension of the conjugation system by accumulation of the NTI cores brings bathochromic shifts; the absorption maximum of dimer (**2b**) shifts to ca. 542 nm, whereas that of the trimer with the benzene core (**3b**) is 506 nm (**Fig. 7.3.2.2b**). This is clearly explained by the nature of connection of the NTI units; for **2b**, the thiophene-thiophene junction between the two

NTIs allows effective conjugation, whereas the benzene linker through its *meta*-positions is less effective for the electronic communication between the NTI units, resulting in smaller extent of bathochromic shift. On the other hand, accumulation of three NTI units enhances the extinction coefficient relative to that of NTI (**1a**) and dimer (**2b**) (**Table 7.1.3.1**).

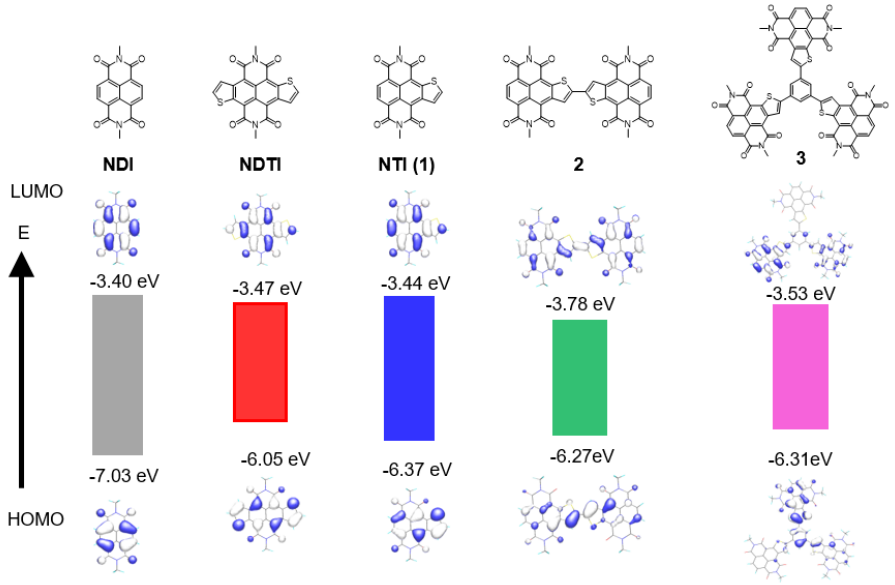

Fig. 7.3.2.1 Calculated LUMO and HOMO energy levels

As predicated by the theoretical calculations (**Fig. 7.3.2.1**), the LUMO energy levels (E_{LUMO}) are not significantly affected by the thiophene annulation on the NDI core; electrochemically estimated LUMO energy levels of NDI (3.8 eV below the vacuum level), NTI (**1a**, −3.9 eV) and NDTI (−4.0 eV) are only slightly different (**Fig. 7.3.2.2c** and **Table 7.3.2**). On the other hand, E_{LUMOs} can be tuned by the accumulation of the NTI units. The direct dimerization of two NTI units effectively lowers the E_{LUMO}, which is explained by the effective conjugation of two NTIs through the thiophene-thiophene junction; the E_{LUMO} of **2b** is lower than the monomer (**1a**) by ca 0.3 eV. On the other hand, the E_{LUMO} of **3b** is only slightly lowered (by ca. 0.1 eV), owing to less effective conjugation between NTI units through the benzene *meta*-position (**Fig. 7.3.2.2d**). The shapes of reduction wave in the voltammograms are also affected by the accumulation of NTI units. Likely owing to deposition of reduced species on the working electrode, an irreversible reduction wave was observed for **2b**. On the other hand, **3b** showed multiple

reduction processes, in sharp contrast to the simple two-stage stepwise reduc-tion process of NTI (**1a**). With the aid of differential pulse voltammetry (DPV) technique, we conclude that the first reduction process is one-electron reduction (half-wave re-duction potential, $E_{red}^{1/2}$ = −0.40 V), followed by two-electron reduction process at E_{red} 1/2 = −0.50 V, which results in triple NTI-mono-anions, and the second reduction of each NTI unit occurs simultaneously as tree-electron reduction process at $E_{red}^{1/2}$ = −0.90 V to create the triple NTI-dianions (Figure S2). It is interesting to note that similar but slightly different stepwise redox behaviors have been reported for NDI trimers.[11, 12]

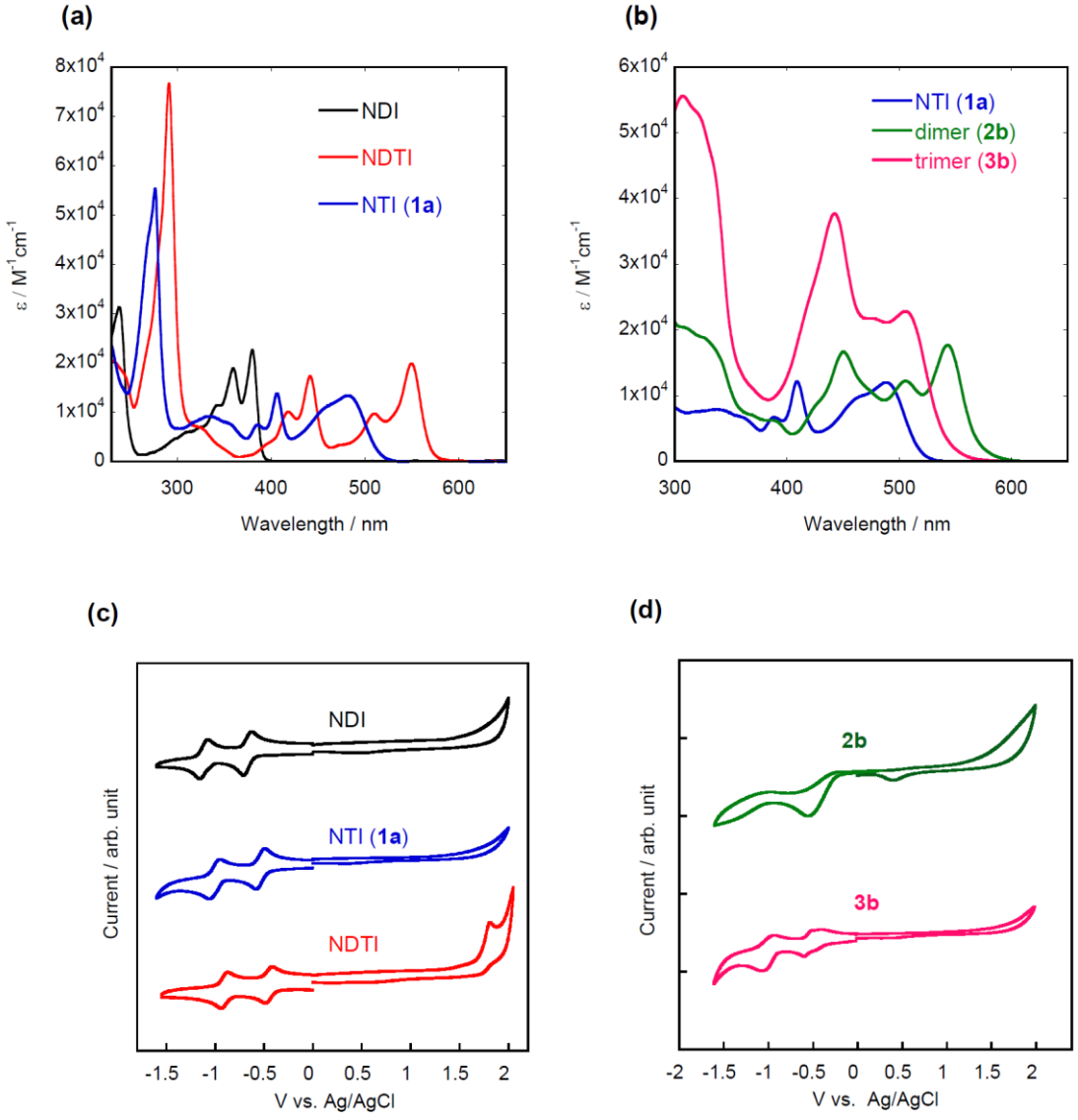

Fig. 7.3.2.2 UV-Vis and CV spectra for NTI and its derivatives

Table 7.3.2 Physicochemical properties of NTI and its derivatives

	E_{red}^{onset} / V [a]	E_{LUMO} /eV [b]	λ_{max} (Log ε)	λ_{edge} / nm	E_g^{opt} / eV [c]
NTI (1a)	–0.48	–3.9	482 (4.13)	510	2.43
			407 (4.14)		
2b	–0.26	–4.2	543 (4.25)	575	2.15
			505 (4.09)		
			451 (4.22)		
3b	–0.34	–4.0	506 (4.36)	540	2.29
			442 (4.58)		
NDI	–0.59	–3.8	380 (4.35)	390	3.17
			360 (4.28)		
NDTI	–0.36	–4.0	548 (4.30)	570	2.17
			510 (4.29)		

[a] V vs. Ag/AgCl

[b] Electrochemical E_{LUMO} were estimated from E (eV) = –4.4– E_{red}^{onset}

[c] Estimated from the absorption edge

[d] Alkyl group on the imide nitrogen atom is *n*-octyl group

7.3.3 OFET and OSCs performance for NTI derivatives

As clearly demonstrated by the electrochemical evaluations, dimers (**2a** and **2b**) and trimer (**3b**) with low-lying E_{LUMOs} seem to be promising as n-type organic semiconductors. To confirm the utility of these NTI-based materials as organic semiconductors, we took **2b** and **3b** as the model compounds for device applications. It is assumed that the dimers (**2**) can be suitable as the active materials in thin film transistors, as the naphtho[*b*]thiophene dimer and its related compounds behave as potential organic semiconductors for hole transport.[13] **2b**-based field-effect transistors were first fabricated by vapor-deposition on Si/SiO2 substrates modified with octyltrichlorosilane (OTS) (**Fig 7.3.3a, b**). As expected from its low-lying E_{LUMO}, the device worked under ambient conditions, and the extracted electron mobility was up to 0.4–0.5 $cm^2\ V^{-1}\ s^{-1}$. Although the electron mobility is moderate, operation under ambient conditions with negligible hysteresis are good signs for further optimization of the molecular structure for better n-type organic semiconductors for transistor applications. Solar cells were also fabricated consisting of a bulkheterojunction layer made with 1:1 equimolar mixture of poly[4,8-

bis(5-(2-ethylhexyl)thiophen-2-yl)benzo[1,2-*b*;4,5-*b*']dithiophene-2,6-diyl-alt-(4-(2-ethylhexyl)-3-fluorothieno[3,4-*b*]thiophene-)-2-carboxylate-2-6-diyl)] (PTB7-Th) and **3b** as p- and n-type material, respectively. As demonstrated by the absorption spectrum of each component, they show complementary absorption band effectively covering almost whole the visible range. Although the present cells showed limited power conversion efficiency up to 2.46% with short circuit current density of 6.86 mA^{-1}, open-circuit voltage of 0.76 V, and fill factor of 47% (**Fig. 7.3.3.c, d**), these result demonstrate that NTI-based small molecules can be active n-type materials in photovoltaic cells.

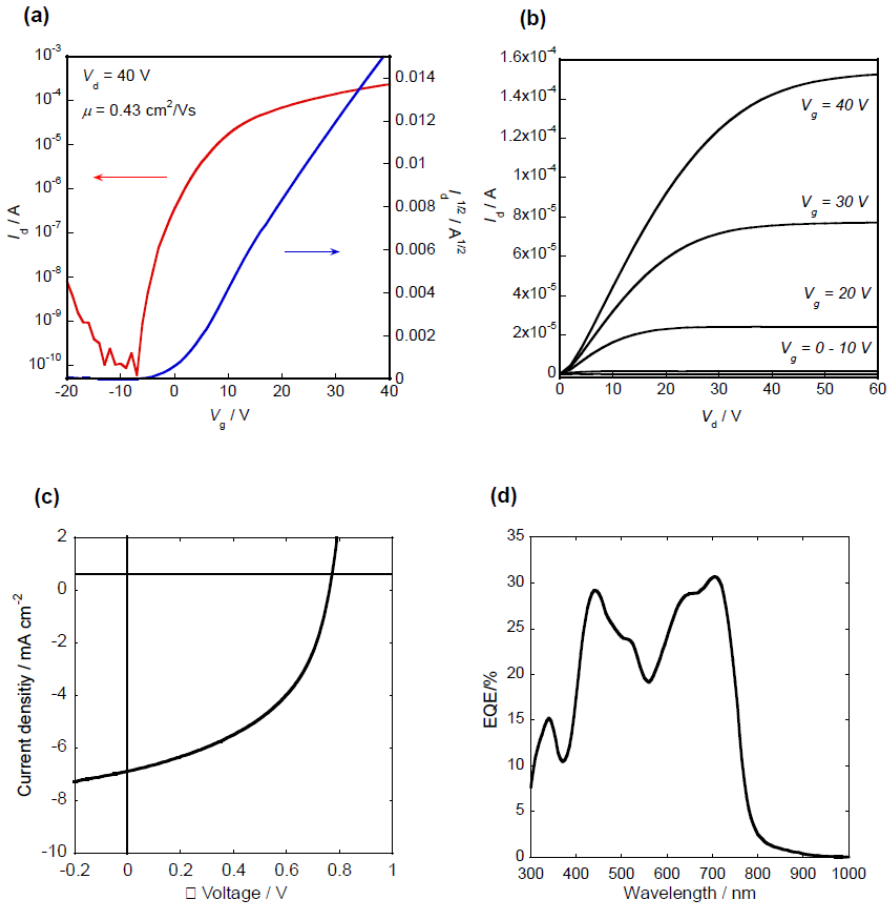

Fig. 7.3.3 a and **b**) OFET transfer and output curves device data for **2b**; **c** and **d**) OPV *J-V* curve and EQE device data for **3b**

7.4 Conclusions

In summary, a mono-thiophene-fused naphthalene dimide has been synthesized, i.e., naphtho[2,3-*b*]thiophene diimide (NTI) with selective mono-functionalizeability. By using the general coupling chemistry at the thiophene α-position, the NTI unit was readily integrated into multi-NTI compounds, e.g., the simple dimer and trimer with the central benzene core, which were also used as n-type organic semiconductors for organic field-effect transistors and organic photovoltaic cells, respectively. Although the performances of the present devices are still low, the NTI unit has proven to be useful for designing versatile electron-deficient molecular architectures.

References

[1] C. B. Nielsen, S. Holliday, H. Y. Chen, S. J. Cryer and I. McCulloch, *Acc. Chem. Res.*, **2015**, 48, 2803-2812.

[2] a) A. Facchetti, *Mater. Today*, **2013**, 16, 123-132. b) H. Kang,; M. A. Uddin,; C. Lee,; K.-H. Kim,; T. L. Nguyen,; W. Lee,; Y. Li,; C. Wang,; H. Y. Woo,; B. J. Kim, *J. Am. Chem. Soc.*, **2015**, 137, 2359-2365.

[3] Y. Fukutomi, M. Nakano, J. Y. Hu, I. Osaka and K. Takimiya, *J. Am. Chem. Soc.*, **2013**, 135, 11445-11448.

[4] M. Nakano, I. Osaka, D. Hashizume and K. Takimiya, *Chem. Mater.*, **2015**, 27, 6418-6425.

[5] E. J. Zhou, M. Nakano, S. Izawa, J. Z. Cong, I. Osaka, K. Takimiya and K. Tajima, *Acs Macro. Lett.*, **2014**, 3, 872-875.

[6] M. Nakano, I. Osaka and K. Takimiya, *Macromolecules*, **2015**, 48, 576-584.

[7] K. Nakano, M. Nakano, B. Xiao, E. J. Zhou, K. Suzuki, I. Osaka, K. Takimiya and K. Tajima, *Macromolecules*, **2016**, 49, 1752-1760.

[8] B. A. Jones, A. Facchetti, T. J. Marks and M. R. Wasielewski, *Chem. Mater.*, **2007**, 19, 2703-2705.

[9] S. F. Volker, A. Schmiedel, M. Holzapfel, C. Bohm and C. Lambert, *Phys. Chem. Chem. Phys.*, **2013**, 15, 19831-19844.

[10] D. S. Baranov, B. Gold, S. F. Vasilevsky and I. V. Alabugin, *J. Org. Chem.*, **2013**, 78, 2074-2082.

[11] S. T. Schneebeli, M. Frasconi, Z. C. Liu, Y. L. Wu, D. M. Gardner, N. L. Strutt, C. Y. Cheng, R. Carmieli, M. R. Wasielewski and J. F. Stoddart, *Angew. Chem. Int. Edit.*, **2013**, 52, 13100-13104.

[12] L. E. Polander, A. S. Romanov, S. Barlow, D. K. Hwang, B. Kippelen, T. V. Timofeeva and S. R. Marder, *Org. Lett.*, **2012**, 14, 918-921.

[13] M. Mamada, J. I. Nishida, D. Kumaki, S. Tokito and Y. Yamashita, *J. Mater. Chem.*, 2008, 18, 3442-3447.

Chapter 8

Replacement of Oxygen with Sulfur in NDI for OSCs Acceptor and OTFT Study

The modification of naphthalene diimide (NDI) through one step thionation reaction by Lawensson's Reagent (LR) was studied. By controlling the amount of LR, the number of C=S double bonds could be adjusted. It was found that after thionation, the sulfur substituted NDI had slightly red-shifted absorption and a lower LUMO energy level. In addition, the electron mobility increased simultaneously. Finally, the OSCs performance based on these materials as non-fullerene acceptors was studied but the results were poor. Morphology analysis through AFM suggested that the large crystalline domain might account for the poor OSCs performance and improved electron mobility. It was confirmed that the thionation reaction provides an effective method to modify the structure as well as the properties for the compounds containing C=O double bonds.

*This section has been published substantially as: W. Chen, *et al J. Mater. Chem. C*, **2015**, *3*, 8219–8224

8.1 Introduction

From the discussion in the previous chapter, it is known that although NDI is another promising n-type organic semiconductor for photoelectronic materials, it has several intrinsic shortcomings, which may limit its wide application in OSCs acceptor: 1) Poor absorption below 400 nm and a large bandgap. 2) Higher LUMO energy level around –3.7 eV. 3) Poor charge transport ability. To overcome these problems, in last chapter, an NDI-core-extended building block NTI was developed and its dimer and trimer derivatives were synthesized, which display promising electron mobility and PCE performance. Other strategies to modify the NDI building blocks include narrowing the bandgap through utilizing donor functional groups, e.g. thiophene, to promote the intramolecular charge-transfer as shown in **Fig. 8.1.1**. Acceptors **NDI-2**[1] and **NDI-3**[2] were designed and synthesized following this idea by attaching one or two thiophene molecules as outer wings or inner linker, which extended the absorption spectra to 700 nm. Their photovoltaic properties were also investigated and the PCE was 1.45% and 1.31% respectively for **NDI-2** and **NDI-3.**

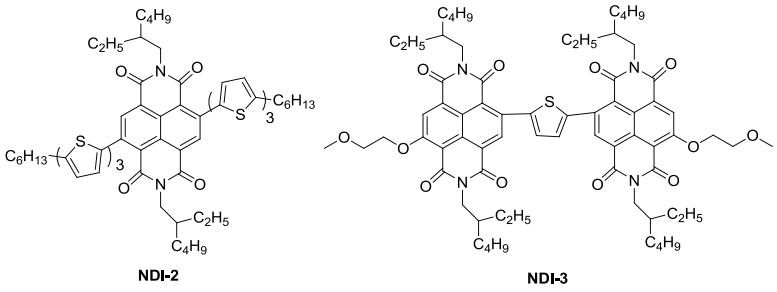

Fig. 8.1.1 Structures of acceptors based on NDI

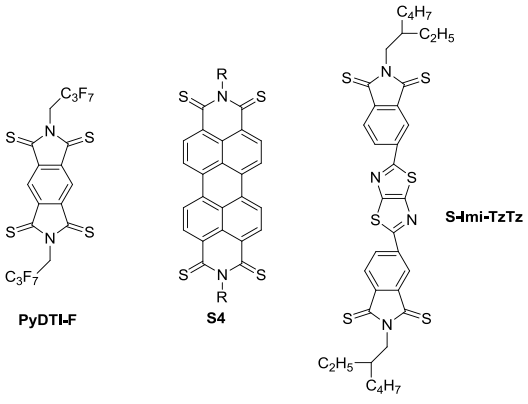

Fig. 8.1.2 Structures of the reported thionated molecules

Thionation reaction is a 2+2 four ring addition reaction usually using Lawesson's Reagent (LR). During the reaction process, the oxygen atom of the C=O double bond is changed to a sulfur atom and physiochemical properties as well as the related electrical character of the molecule may also change subsequently. Compounds **PyDTI-F**[3] and **S4**[4] display much better electron mobility (0.62 and 0.16 $cm^2\ V^{-1}\ s^{-1}$) than their starting reactants as shown in **Fig 8.1.2**, aside from the enhanced absorption spectrum and decreased LUMO energy level,. For **S-imi-TzTz**,[5] its photovoltaic property was also investigated and the authors found out that although the PCE result decreased greatly, the film became much smoother than the controlled group, which provided interesting tips for designing other similar molecules.

In this chapter is studied the sulfur analogue of NDI through thionation reaction and its basic physical and photoelectrical properties are investigated as well as its OPV and OTFT performance. (**Fig. 8.1.3**)

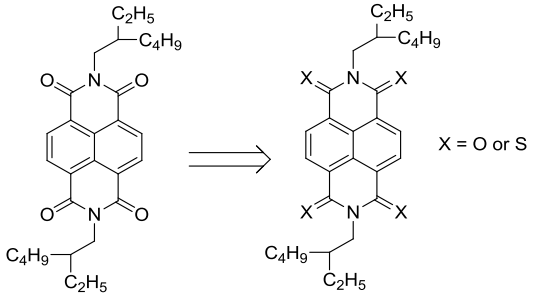

Fig. 8.1.3 Structure of S-NDI compounds in this work

8.2 Experimental Methods

Synthesis of NDI-1S, NDI-2S-trans and NDI-2S-cis

294 mg (0.6 mmol) of NDI and 485 mg (1.2 mmol, 2.0 eq. to NDI) of LR was added into 30 mL of xylene. The solution was heated at 140 ^oC for 2 hs under argon protection. The resulting brown solution was cooled to r.t and the solvent was removed under reduced pressure to give a crude mixture of unreacted **NDI**, **NDI-1S, NDI-2S-trans and NDI-2S-cis**. Further purification through CC by using hexane : DCM = 1:1 to 1: 2 (V/V) gave **NDI-1S, NDI-2S-trans and NDI-2S-cis** in the following yields.

NDI-1S: Green yellow solid, 101mg, Yield: 33%; mp: 175 ^oC (DSC). ^{1}H-NMR (Chloroform-d, 300 MHz) δ 0.96–0.83 (m, 12H), 1.40–1.27 (m, 16H), 1.97–1.91 (m, 1H), 2.18–2.14 (m, 1H), 4.19–4.07 (m, 2H), 4.78–4.65 (m, 2H), 8.62 (d, *J* = 1.2 Hz, 1H),

8.75–8.69 (m, 2H), 9.04 (d, *J* = 9.0 Hz, 1H); ^{13}C-NMR (Chloroform-d, 75 MHz) δ 10.6, 10.7, 14.0, 22.6, 23.0, 24.0, 28.6, 30.7, 31.6, 36.9, 37.9, 44.6, 50.8, 125.0, 125.2, 126.2, 126.6, 126.8, 130.1, 130.5, 130.9, 131.5, 136.0, 160.8, 163.5, 193.5; HRMS: calculated for $C_{30}H_{38}N_2O_3S + Na^+$, 529.2501; found: 529.2498 (M+)

NDI-2S-trans: Brown solid, 12 mg, Yield: 4%. mp: 182 ^{o}C (DSC); ^{1}H-NMR (Chloroform-d, 300 MHz) δ 0.89–0.83 (m, 12H), 1.41–1.27 (m, 16H), 2.21–2.13 (m, 2H), 4.79–4.66 (m, 4H), 8.63 (d, *J* = 9.0 Hz, 2H), 9.04 (d, *J* = 9.0 Hz, 2H); ^{13}C-NMR (Chloroform-d, 75 MHz) δ 10.7, 14.0, 23.1, 24.0, 28.6, 30.7, 36.9, 50.8, 125.0, 125.3, 129.6, 131.0, 136.0, 161.1, 193.5; HRMS: calculated for $C_{30}H_{38}N_2O_2S_2 + H^+$, 523.2453; found: 523.2437 (M+)

NDI-2S-cis: Brown solid, 22 mg, Yield: 7%; m.p: 182 ^{o}C (DSC); ^{1}H-NMR (Chloroform-d, 300 MHz) δ 0.94–0.82 (m, 12H), 1.38–1.26 (m, 16H), 2.22–2.11 (m, 2H), 4.78–4.66 (m, 4H), 8.72 (s, 2H), 8.93 (s, 2H); ^{13}C-NMR (Chloroform-d, 100 MHz) δ 10.7, 14.0, 23.0, 24.0, 28.6, 30.7, 37.0, 50.8, 125.0, 126.3, 128.8, 131.5, 135.5, 161.1, 193.6; HRMS: calculated for $C_{30}H_{38}N_2O_2S_2 + H^+$, 523.2453; found: 523.2459 (M+)

Synthesis of NDI-3S

294 mg (0.6 mmol) of NDI and 1.2 g (3.0 mmol, 5.0 eq. to NDI) of LR was added into 30 mL of xylene. The solution was heated at 140 ^{o}C for 24 hs under argon protection. The resulting brown solution was cooled down to r.t. and the solvent was removed under reduced press to give a crude mixture of **NDI-3S, NDI-2S-trans and NDI-2S-cis**. Further purification through CC by using hexane : DCM = 1:1 to 1: 2 (V/V) gave **NDI-2S-trans** (11% yield), **NDI-2S-cis** (9.2%, yield) and **NDI-3S.**

NDI-3S: red solid, 25 mg, Yield: 4.6%, m.p: 181 ^{o}C (DSC); ^{1}H-NMR (Chloroform-d, 300 MHz) δ 0.95–0.83 (m, 12H), 1.39-1.24 (m, 16H), 2.20–2.12 (m, 1H), 2.35–2.27 (m, 1H), 4.77–4.64 (m, 2H), 5.56–5.41 (m, 2H), 8.57 (d, *J* = 8.1 Hz, 1H), 8.77 (d, *J* = 8.4 Hz, 1H), 8.90–8.87 (m, 2H); ^{13}C-NMR (Chloroform-d, 75 MHz) δ 10.7, 11.0, 14.0, 23.1, 24.0, 24.1, 28.6, 28.7, 30.6, 30.7, 37.0, 37.4, 50.8, 57.5, 121.8, 124.8, 125.1, 128.1, 130.4, 131.0, 131.3, 135.6, 136.7, 137.2, 161.5, 190.8, 193.8; HRMS: calculated for $C_{30}H_{38}N_2OS_3 + H^+$, 539.2225; found: 523.2239 (M+)

8.3 Principal Outcomes

8.3.1 Synthetic route for S-NDI compounds

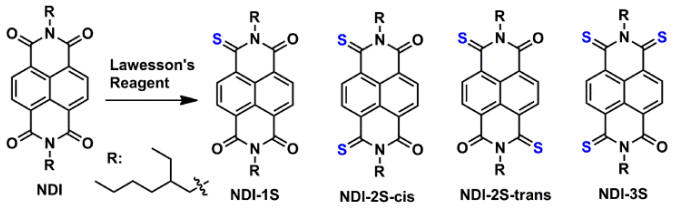

Scheme 8.3.1 Synthetic route for the S-NDI compounds

The synthetic route for the sulfur substituted NDI compounds is displayed in **Scheme 8.3.1**. First of all, the starting reactant NDI was synthesized according to the literature[6] and used as reference material in the following discussion. Meanwhile, it can be observed directly that LR reaction is an efficient one-step reaction for forming C=S bonds from C=O bonds. However, the products are generally a mixture of different thionated NDI compounds with different numbers of sulfur atoms. Thus, the amount of LR and the reaction time need to be controlled precisely to obtain the desired product. For example, using 2.0 eq. of LR and a reaction time of 2 hours, NDI-1S will be formed as the main product in 33% yield while NDI-2S-trans and NDI-2S-cis will be obtained totally with a much lower total yield of 11%. In this case, no NDI-3S was formed but some unreacted starting material NDI. Using 5.0 eq. of LR and a reaction time of 24 hours, NDI-2S-cis, NDI-2S-trans, and NDI-3S were obtained in 9%, 11% and 4.6% yield, respectively while NDI and NDI-1S were not detected. Although a number of reaction conditions (reaction time, ratio, temperature) have been employed to approach NDI-4S, none of them were successful. In addition, it was found out that extremely long reaction times or high temperature have adverse effect on the yield of the target S-NDI products due to the instability of C=S double bond resulting in decomposition.

The ^{1}H-NMR spectra of the S-NDI derivatives were obtained on Bruker AV 300 Spectrometer instrument (300 MHz for ^{1}H-NMR and 75 MHz for ^{13}C NMR) and displayed in **Fig. 8.3.1**. There are several points to which attention must be paid.

First of all, after thionation reaction, the position of H atom on CH_2 connecting to imide group shifts gradually from 4.2 ppm to 4.7 ppm to 5.5 ppm due to the electron-withdrawing ability of the C=S double bond.

Secondly, due to the symmetric structures of NDI, NDI-2S-trans and NDI-2S-cis, there is only one group of peaks corresponding to H atom on CH_2 linked with imide group for these compounds while for NDI-1S and NDI-3S, signals for H atom on CH_2 next to imide group split into two group of peaks.

Thirdly, for NDI-2S-cis compound, because the environment of the two H atoms on the same side of the NDI core is identical, there are two single peaks between 8.5 ppm and 9.0 ppm, which is completely different from NDI-2S-trans compound that exhibits two groups of double peaks.

The structures of all these S-NDI compounds were further confirmed by ^{13}C NMR, and HRMS, whose data were measured on Bruker Autoflex III instrument.

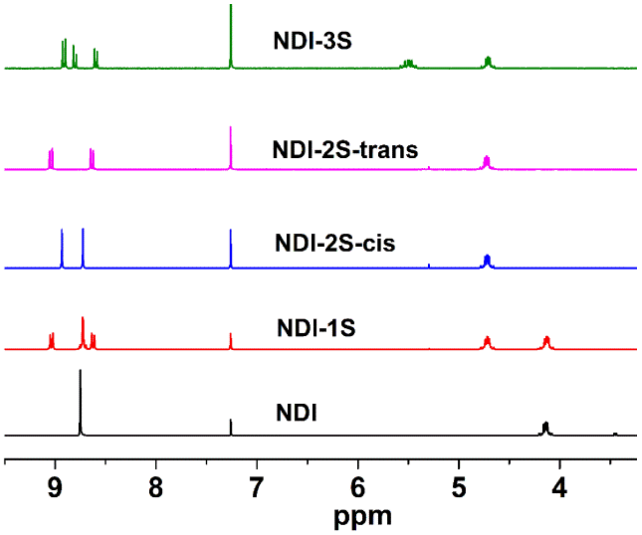

Fig. 8.3.1 Partial ^{1}H-NMR spectra of the S-NDI compounds

8.3.2 Physicochemical properties of S-NDI compounds

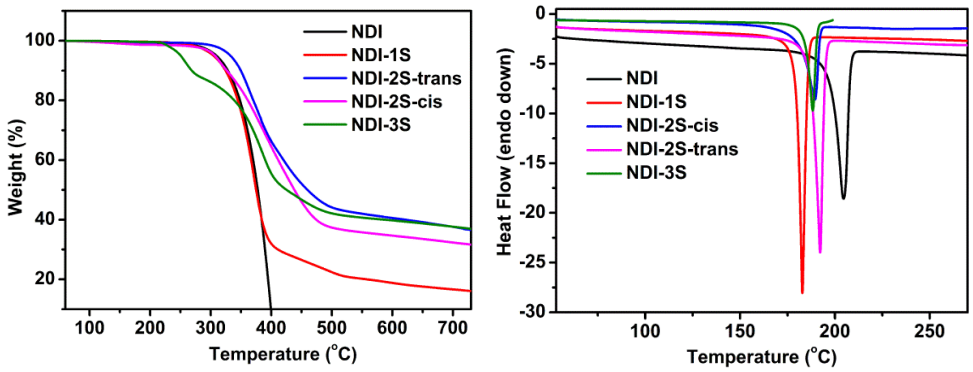

Fig. 8.3.2.1a) TGA and **b)** DSC spectra of S-NDI compounds

TGA spectra shown in **Fig. 8.3.2.1a** were recorded on a NETZSCH STA 409PC instrument at a constant heating rate a 10 ℃ min^{-1} under purified nitrogen gas flow. All the S-NDI compounds, NDI, NDI-1S, NDI-2S-cis and NDI-2S-trans, exhibit a decomposition temperature higher than 320 ^{o}C while NDI-2S-trans seems to be the most stable compound as it decomposed at around 350 ^{o}C. Surprisingly, it is worth noting that NDI-3S is the most susceptible to high temperature and decomposes at around 250 ^{o}C despite it having 3 C=S bonds compared with 2 in the NDI-2S-trans molecule. DSC spectra shown in **Fig. 8.3.2.1b** were recorded on Instrument TAQ-10 at a constant heating rate of 10 ℃ min^{-1} under a nitrogen atmosphere. There are no phase transitions for any of these compounds and their melting peaks are all between 183 ^{o}C and 192 ^{o}C, which are slightly lower than that of the parent compound **NDI** (205 ^{o}C). The reason may be due to the instability of C=S double bond compared with C=O double bond.

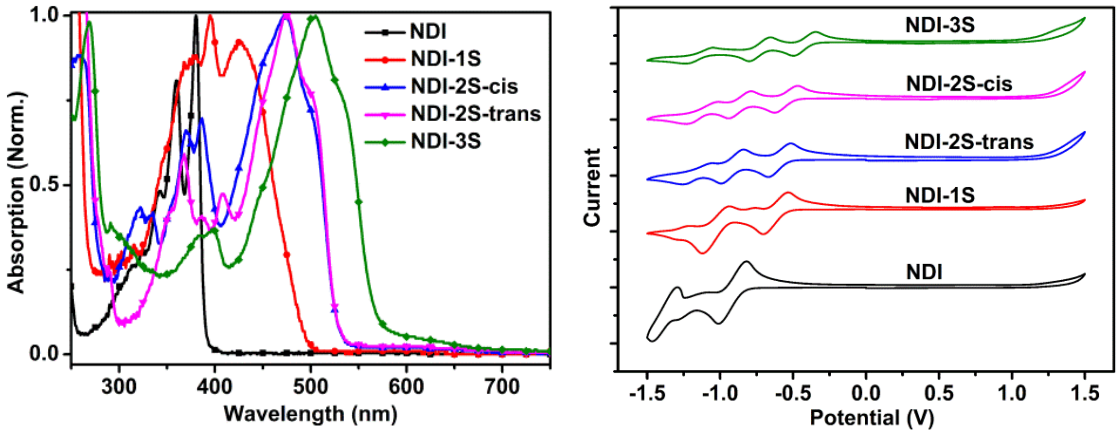

Fig. 8.3.2.2a) Normalized UV-Vis spectra in DCM and **b**) CV of the S-NDI compounds

A SHIMADZU UV-2501PC spectrophotometer was utilized for obtaining the UV–Vis spectrum data and the absorption spectra of the sulfur substituted NDI compounds in DCM are displayed in **Fig. 8.3.2.2a**. With successive formation of C=S double bond from the ketone group in the framework of NDI, the λ_{onsets} of these S-NDI compounds red shift gradually from 400 nm to 580 nm. It is worth mentioning that although the thionation positions for NDI-2S-trans and NDI-2S-cis compounds are different from each other, their λ_{onset} absorptions are almost the same around 530 nm. According to the equation: = 1240nm/λ_{onset}, the bandgap for comparing molecule NDI is 3.20 eV from 1240/388. The bandgaps E_g^{opt} for other S-NDI compounds could also be calculated through this equation and the corresponding values were summarized in **Table 8.3.2.1.** The electrochemical

properties of S-NDI compounds were studied by CV experiments, which were performed on a CHI 660 electrochemical station instrument. All the measured S-NDI compounds were dissolved in anhydrous DCM solution with 0.1 M *n*-Bu_4NPF_6 as supporting electrolytes and scan rate of 100 mV s^{-1}. In addition, all the CV data were obtained through employing 3-electrodes system (Pt disk electrode as WE, one Pt wire as RE and another Pt wire as the CE). Tetrabutylammonium phosphorus hexafluoride (Bu_4NPF_6, 0.1 M) in DCM was used as the supporting electrolyte, and the scan rate was 100 mV s^{-1}. The corresponding CV graphs are displayed in **Fig. 8.3.2.2b** and it can be seen apparently that not only NDI but also S-NDI compounds have two reversible peaks between 0 V to –1.5 V. For the controlled group **NDI**, the onset of reduction potential E_{red}^{onset} was calculated to be –1.14 V according to the equation $E_{red}^{onset} = (E_{1/2} - E_{1/2}(Fc/Fc^+ = +0.23)) = (–0.91–0.23)$ V indicated by note *b* of the table **Table 8.3.2**. Thus, the LUMO energy for NDI was estimated to be –3.66 eV from the E_{red}^{onset} by using the empirical formula:

$E_{LUMO} = –(E_{red}^{onset} + 4.8)$ eV

assuming the absolute energy level of $FeCp_2^{+/0}$ to be 4.8 eV below vacuum. The HOMO energy of NDI is calculated to be 6.86 eV through the equation of HOMO = LUMO $-E_g^{opt}$. Using the same method, the LUMO and HOMO values for 1S, 2S, 3S substituted NDI compounds can also be obtained and the data are summarized in **Table 8.3.2**. Interestingly, in the CV diagram, the LUMO of **NDI-1S** shifted downward about –0.30 eV compared with the LUMO of NDI (–3.66), which is the largest shifted value for the stepwise thionated reaction. Meanwhile, the λ_{onset} UV-Vis absorption for NDI-1S red shifts about 100 nm to 495 nm compared with λ_{onset} of NDI (388 nm), which is also the largest shift value for the thionated reaction, corresponding with the tendency observed CV measurement. Thus, comparing to the other strategies for LUMO level modification,[38] thionation reaction provides an alternative method to adjust LUMO level with a simple one-step synthesis route.

Table 8.3.2 Physiochemical properties for S-NDI compounds

	λ_{onset} (nm)	$E_g^{opt\ a}$ (eV)	$E_{1/2}$ (V)	$E_{red}^{onset\ b}$ (V)	LUMO[c] (eV)	HOMO[d] (eV)
NDI	388	3.20	–0.91	–1.14	–3.66	–6.86

NDI-1S	495	2.51	–0.62	–0.85	–3.95	–6.46
NDI-2S-*trans*	529	2.34	–0.59	–0.82	–3.98	–6.32
NDI-2S-*cis*	529	2.34	–0.55	–0.78	–4.02	–6.36
NDI-3S	571	2.17	–0.42	–0.65	–4.15	–6.32

[a] E_g^{opt} was calculated from 1240nm/λ_{onset}

[b] $E_{red}^{onset} = (E_{1/2} - E_{1/2}(Fc/Fc^+ = +0.23))$

[c] LUMO = $-(E_{red}^{onset} + 4.8)$ eV

[d] HOMO = LUMO $-E_g^{opt}$

8.3.3 OSC and OTFT performance of S-NDI compounds and their characterization

OSCs performance

Firstly, the device structure ITO/PEDOT: PESS/P3HT: NTI-2S-cis/LiF/Al was fabricated and the OSCs performance was studied. Unfortunately, the devices exhibited extremely poor performance with a PCE of 0.013%, V_{oc} of 0.22 V, J_{sc} of 0.25 mA.cm^{-2} and FF of 0.24. AFM was used to find the reason for this poor PCE performance. As shown in **Fig. 8.3.3.1**, the morphology contains lots of large domains due to the crystalline properties of the **NDI-2S-cis**, which deteriorate the PCE performance significantly.

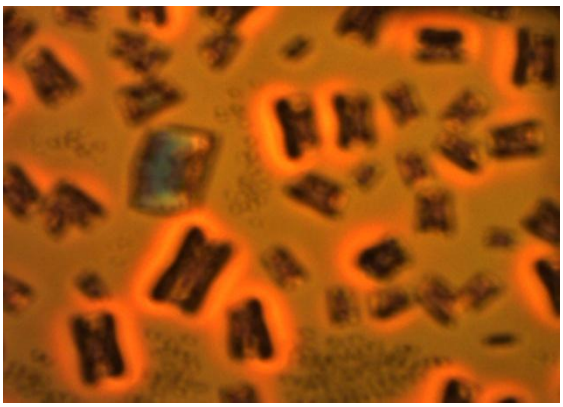

Fig. 8.3.3.1 AFM image for the P3HT: NTI-2S-cis blended film

OTFT performance

To investigate how the sulfur atoms will affect the electron transport property of the S-NDI compounds, thin-film OTFTs were fabricated with bottom gate/top contact configuration and gold as source/drain electrodes. It was found that all the S-NDI compounds all had suitable solubility in common solvents such as chloroform and

toluene etc, except moderate solubility for NDI-3S, which is favorable for solution processed device. It was found that the solubility of S-NDIs strongly depends on the number of C=S double bonds: more C=S double bonds, lower solubility for the compounds. To minimize the systematic error, hexane/chloroform was chose as the processing solvent for all the device fabrication. The measured S-NDI compounds films were formed through spin-coating their regarding solutions onto the SiO_2 (500 nm)/n^{++}Si substrates treated with OTS under ambient conditions. These films then had the TA treatment at different temperatures for the further mobility measurement.

All the devices fabricated from the S-NDI compounds displayed typical n-type behavior under ambient atmosphere and the corresponding transfer curves are depicted in **Fig.8.3.3.2a-d**. The relating parameters regarding to the OTFT, such as the electron mobilities, I_{on}/I_{off} ratios as well as the threshold voltages ($V/_T$) are summarized in **Table 8.3.3**. NDI based OTFT device was also fabricated on the same condition for comparison but displayed no electron mobility. For all the S-NDI compounds, there are several points that one needs to pay attention to.

1) The TA post treatment was beneficial for the improvement of the device performance and the annealing temperature affected the device significantly. Taking the NDI-1S compound as an example, almost no field-effect mobility was measured at 60 ^oC, but the electron mobility increased to 3.0×10^{-4} cm^2 V^{-1} after TA at 140 ^oC with an on/off ratio up to 1.5×10^4. The same tendency was also observed for the other NDI-2S-cis, NDI-2S-trans and NDI-3S compounds. It is worth mentioning that a higher annealing temperature normally ensures higher electron mobility for NDI-1S and NDI-2S compounds, which all exhibited the highest mobility at 140 ^oC, while for NDI-3S compounds, the highest mobility 3.0×10^{-3} cm^2 V^{-1} s^{-1} was measured at 100 ^oC.

2) The device stability for all these S-NDI compounds was different with each other when they are measured under air condition. It was found that with more C=S bond formed, the device stability would increase simultaneously, which might be caused by the decreased LUMO energy when more electron-withdrawing groups were introduced onto the NDI core. For example, NDI-1S based TFT device degraded very quickly when operated in the air and the reproducibility was also very poor. For NDI-2S compounds, both for the cis or trans compounds, although they possessed improved stability than

NDI-1S, their device stability was still not very good under air as shown in Fig. **8.3.3.2e**. It can be observed that the threshold voltage (V_T) shifted from 30 V to 70 V after repeat sweeps in air and the electron mobility also decreased to 8.8×10^{-4} cm^2 V^{-1} s^{-1} from the initial value 4.2×10^{-3} cm^2 V^{-1} s^{-1}. NDI-3S was the most stable compound when operated under air condition and no apparent change for the transfer I-V curves was observed as displayed in **Fig. 8.3.3.2f**. From the above discussion, it can be deduced that the thionation reaction to change the C=O double bond to C=S double bond is a simple and effective method to improve the electron transport ability.

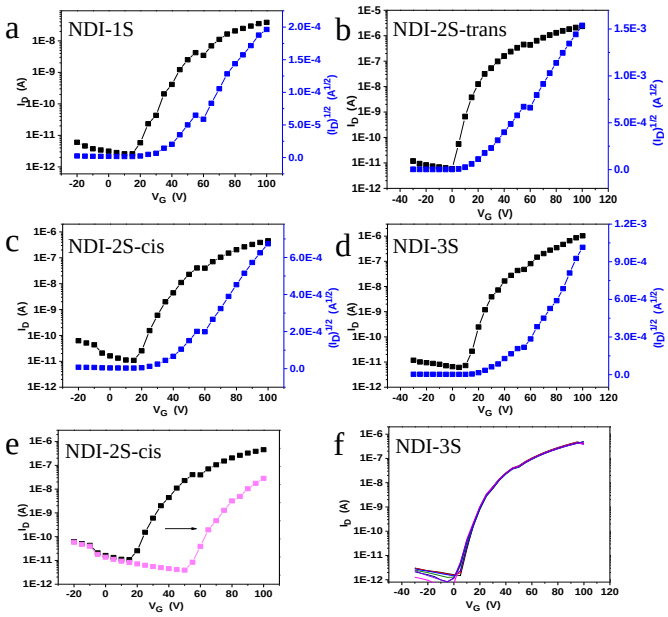

Fig. 8.3.3.2 Typical transfer characteristics OFETs device data of the S-NDI compounds at optimized temperature a, b, c for 140 ^oC and d) for 100 ^oC as well as device repeatability for e, f.

Table 8.3.3 OFETs device data of the S-NDI compounds

	T (^oC)	μ ($cm^2V^{-1}s^{-1}$)	I^{on}/I^{off}	V_T (V)
NDI-1S	60	No Field-effect		
	100	6.1×10^{-5}	5×10^3	27
	140	3.0×10^{-4}	1×10^4	28
NDI-2S-trans	60	2.4×10^{-4}	4×10^2	30
	100	1.7×10^{-3}	2×10^4	16
	140	1.0×10^{-2}	4×10^5	19
NDI-2S-cis	60	4.8×10^{-4}	1×10^4	33

	100	5.6×10^{-4}	4×10^{4}	36
	140	3.7×10^{-3}	4×10^{4}	37
NDI-3S	60	1.7×10^{-3}	4×10^{4}	27
	100	7.3×10^{-3}	2×10^{5}	33
	140	3.0×10^{-3}	4×10^{5}	22

To find out the reason accounting for the increased electron mobility at increased temperature, AFM and XRD were measured to understand the as-fabricated film morphology change at different temperatures.(**Fig.8.3.3.3** and **Fig. 8.3.3.4**). In **Fig. 8.3.3.3**, the morphologies and domain sizes changed significantly at different temperature. When the films were TA at low temperature (60 ℃), there were only small grain and domain sizes on the Si substrate. But when the annealing temperature increased from 60 ℃ to 100 ℃, then 140 ℃, bigger and bigger grains formed with a more ordered films. It is worth mentioning that for NDI-3S film, cracking happened to form large grain boundaries, which might explain its decreased electron mobility. As shown in **Fig. 8.3.3.4**, XRD spectra also indicated that the annealing temperature had great effects on the morphology change. At low annealing temperature, (60 ^{o}C), there was only one weak reflection peak at $2\theta = 4.85^{o}$ observed for all S-NDI compounds' films, corresponding to a d-spacing of 1.89 nm. Thus, it can be calculated that the angle was about 55^{o} between the long axes of the S-NDI derivative and the horizontal Si-substrate plane. But at higher annealing temperature, all the single peaks became stronger, implying improved crystallinity in these films, which corresponded well with the tendency observed through the AFM characterization. Thus, substrate temperature has significant effect on the morphology and crystallinity of microstructures, which are presumed to affect the corresponding charge transport properties of the films. From the above AFM and XRD characterization as well as the typical transfer curves data, it can be summarized that the electron mobility had a close relationship with the film morphology and crystallinity for the microstructure, which is affected greatly by the temperature.

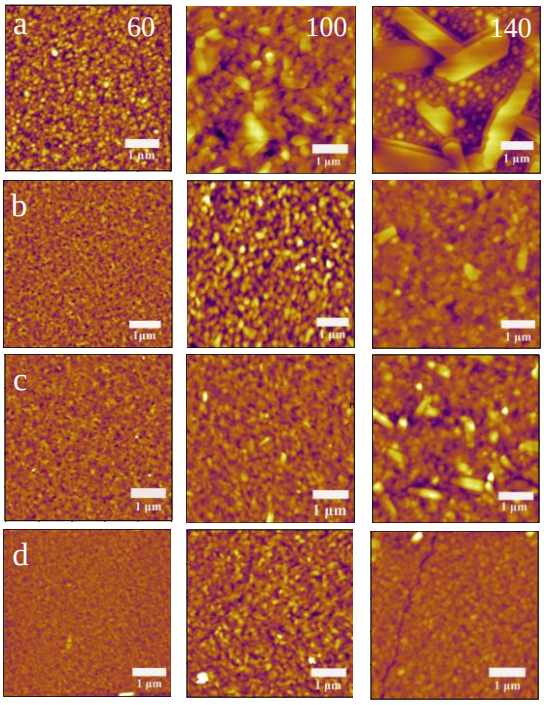

Fig. 8.3.3.3 AFM images of S-NDI Compounds based films (a: **NDI-1S**, b: **NDI-2S-trans**, c: **NDI-2S-cis**, d: **NDI-3S**, size: 5×5 μm; annealed at 60 ℃, 100 ℃ and 140 ℃)

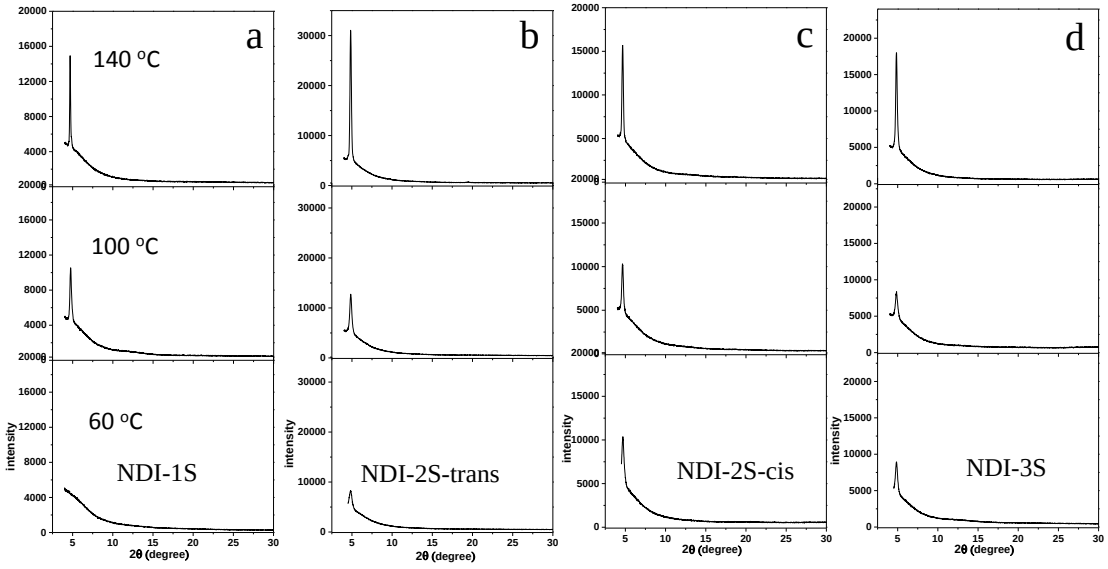

Fig. 8.3.3.4 XRD spectra for the S-NDI compounds

8.4 Conclusions

In this chapter, A series of S-NDI compounds with C=S double bond were designed and synthesized through one simple and effective thionation reaction by adopting the commercial available LR. Their physiochemical properties were studied and these S-NDI displayed red-shift UV-Vis absorption and decreased LUMO energy due to the newly formed electron-withdrawing C=S double bond. Their OSCs and OTFT performance were also investigated at different TA temperature. It found out that these S-NDI compounds had very poor OSCs performance while much improved electron mobility up to 0.01 cm^2 V^{-1} s^{-1}. Further AFM and XRD characterization indicated that higher temperature contributed greatly to the formation of large crystallinity domain, which may be responsible for the poor PCE performance and the better electron mobility. Our research demonstrates that thionation reaction could be an effective way to tune physicochemical and electron properties of carbonyl-containing compounds. In addition, design and synthesize of C=S containing compounds with twisted structure, which can guarantee a suitable film morphology and electron mobility, would be promising non-fullerene acceptor for OSCs.

References

[1] E. Ahmed, G. Q. Ren, F. S. Kim, E. C. Hollenbeck and S. A. Jenekhe, *Chem. Mater.*, **2011**, 23, 4563-4577.

[2] X. Wang, J. H. Huang, Z. X. Niu, X. Zhang, Y. X. Sun and C. L. Zhan, *Tetrahedron*, **2014**, 70, 4726-4731.

[3] T. F. Yang, S. H. Huang, Y. P. Chiu, B. H. Chen, Y. W. Shih, Y. C. Chang, J. Y. Yao, Y. J. Lee and M. Y. Kuo, *Chem. Commun.*, **2015**, 51, 13772-13775.

[4] A. J. Tilley, C. Guo, M. B. Miltenburg, T. B. Schon, H. Yan, Y. N. Li and D. S. Seferos, *Adv. Funct. Mater.*, **2015**, 25, 3321-3329.

[5] Y. Ie, S. Jinnai, M. Nitania and Y. Aso, *J. Mater. Chem. C*, **2013**, 1, 5373-5380.

[6] C. Thalacker, C. Roger and F. Wurthner, *J. Org. Chem.*, **2006**, 71, 8098-8105.

Chapter 9

Design and Synthesis of a K^+ Sensor Based on Naphthalimide Building Blocks.

Developing K^+ probe is significant for in-situ monitoring of sweat change for wearable sensors or evaluating K^+ concentration change within the body. However, the development of novel materials for K^+ probe has progressed rather slowly during the past decades and they generally need multiple steps to synthesize. In this chapter is designed and synthesized a K^+ probe TM-1 based on naphthalimide building block and 1-aza-18-crown-6 within four steps. It displays maximum absorption around 500 nm and weak fluorescence in DMSO solution. Interestingly, with different excited wavelength, this probe exhibits different emission spectrum. Although it turns out that this probe has weak response to K+ in sweat, however, the other components in sweat, such as lactic acid, urea and Na+, are proved to have no influence on this probe. It is infer that the low efficiency for probing K+ may result from the low steric effect and further improvement of the probe is possible

9.1 Introduction

Imbalances in the concentration of K^+ in living organisms can cause certain diseases such as alcoholism, heart disease, anorexia, diabetes, bulimia and even cancer. In addition, rapid development of wearable electronics/sensors has been achieved recently due to its advantage of continuously monitoring an individual's activities without interrupting or limiting the user's motions. Wearable sensors to analyze sweat components change, such as K^+, is important for disease diagnosis, drug abuse detection, and athletic performance optimization.[1] However, design and synthesis of novel materials for K^+ probe is rather slow during the past decades.[2] Thus, developing novel materials or methods for sensitively and selectively detecting potassium is highly desirable. Crown ether is ideal building block for synthesizing K^+ sensors. In this project is developed a K^+ sensor based on the crown ether and naphathlimide.

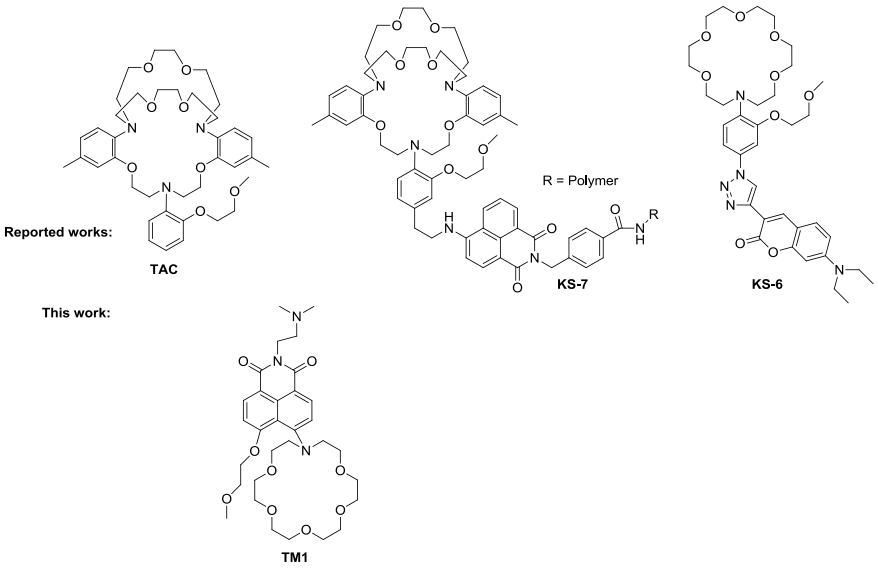

Fig. 9.1.1 Structures of reported and the designed K^+ sensors in this chapter

In the literature review chapter, TAC cryptand was demonstrated to be an effective coordination ligand for K^+ and by connecting with fluorophore part based on n-type semiconductor naphthalimide derivatives, probe KS-7 was designed. It was found that the KS-7 had good selectivity for K+ as a 40 fold excess of Na^+ had almost no effect on its fluorescence intensity. However, one big problem is that the synthesis of a TAC based probe requires multistep reactions.[3] For KS-6, the synthetic procedures become much simpler and it can be obtained in only four steps. In addition, the neighboring 2-

methoxyethoxy has crucial effect on the stability of the probe.[4] Based on the above discussion, probe TM1 was designed and synthesized based on the following points:

1) Naphathlimide derivative can be used as an excellent fluorophore.

2) The synthetic steps should not be too lengthy.

3) The neighboring steric group needs to be introduced.

9.2 Experimental Methods

9.2.1 Preparation of M1-M3 and TM1

Synthesis of M1 and M2:[5]

The title compound was prepared using the modified literature method. 1.072 g anhydride (4.0 mmol) was added to 20 mL of water and then 20 mL (20 mmol) 1M NaOH solution was added and the mixture was stirred to obtain a limpid solution, which was heated to 90-95 ^oC to which was added 20 mmol acetic acid. Bromine (1.56 g, 10 mmol, 2.5 eq.) was injected slowly and the mixture was stirred at 90-95 ^oC for another 24 h. The precipitate was collected by filtration, washed with acetone and dried to give **M1** as a 1.28 g white solid in a yield of 90%, which was used directly in the next step.

1.06 g (3.0 mmol) 1,8-dibromonaphthoic anhydride **M1** and 396 mg (4.5 mmol) ***N,N′***-dimethylethylenediamine was added into a mixed solution of 20 mL ethanol and 20 mL toluene, which was refluxed under argon for 3 h. After the solution was cooled down to r.t., the solvent was removed under reduced pressure and the residue was purified through CC with eluent DCM: Methanol = 20 : 1 (V/V) to give a yellow solid **M2** 710 mg, yield: 55%. ^{1}H-NMR (Chloroform-d, 300 MHz) δ 8.40 (d, *J* = 8.0 Hz, 2H), 8.20 (d, *J* = 8.0 Hz, 2H), 4.32 (t, *J* = 6.9 Hz, 2H), 2.74 (t, *J* = 6.9 Hz, 2H), 2.40 (s, 6H).

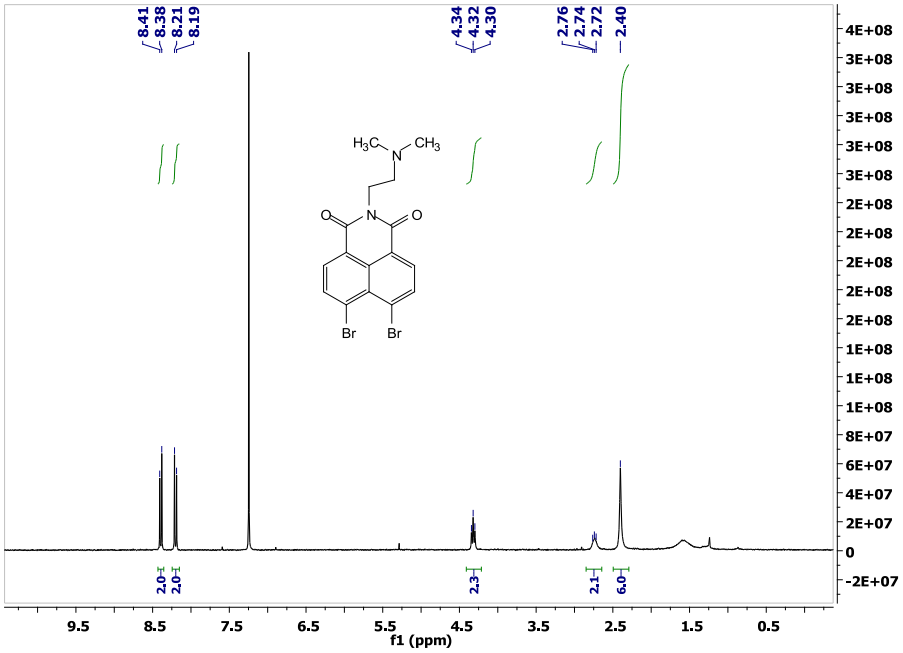

Synthesis of M3:[6]

The title compound was prepared using the modified literature method. A solution of 128 mg **M2** (0.3 mmol) and 44 mg Potassium Carbonate K_2CO_3 (0.32 mmol) was added 5 mL $CH_3OCH_2CH_2OH$. The mixture was heated at 100 ^oC for 2 h. After the solution was cooled down, the solvent was removed under vacuum. The residue was purified through CC with eluent DCM : Methanol = 100 : 6 (V/V) to give 90 mg yellow solid **M3**, Yield: 71%. ^{1}H-NMR (Chloroform-d, 300 MHz): δ 8.59 (d, *J* = 8.0 Hz, 1H), 8.35 (d, *J* = 8.0 Hz, 1H), 8.01 (d, *J* = 8.0 Hz, 1H), 7.12 (d, *J* = 8.0 Hz, 1H), 4.40 (t, *J* = 4.5 Hz, 2H), 4.32 (t, *J* = 6.9 Hz, 2H), 3.97 (t, *J* = 4.5 Hz, 2H), 3.50 (s, 6H), 2.72 (t, *J* = 6.9 Hz, 2H), 2.40 (s, 6H).

Synthesis of TM1:[5]

The title compound was prepared using the modified literature method. 63 mg of **M3** (0.15 mmol) and 79 mg of 1-aza-18-crown-6 (0.30 mmol) was added 4.0 mL of $CH_3OCH_2CH_2OH$. The mixture solution was heated under refluxing for 24 h under Argon. After the solution had cooled down, the solvent was removed under vacuum and the residue was purified through CC with eluent: DCM: Methanol = 100:8 to 5:1 (V/V) to give a sticky yellow solid, 81 mg, yield: 89%. ^{1}H-NMR (Chloroform-d, 300 MHz): δ 8.50 (d, *J* = 8.0 Hz, 1H), 8.43 (d, *J* = 8.0 Hz, 1H), 8.02 (d, *J* = 8.0 Hz, 1H), 7.12 (d, *J* = 8.0 Hz, 1H), 4.42 (t, *J* = 6.9 Hz, 2H), 4.33 (t, *J* = 4.5 Hz, 2H), 3.87 (t, *J* = 4.5 Hz, 2H),

3.75-3.60 (m, 24H), 3.49 (s, 3H), 2.96 (t, *J* = 6.9 Hz, 2H), 2.60 (s, 6H); ^{13}C-NMR (Chloroform-d, 75 MHz): δ 164.4, 164.3, 161.3, 155.9, 133.5, 133.3, 132.8, 117.2, 116.6, 115.0, 113.3, 106.4, 70.7, 70.6, 70.5, 70.3, 70.1, 69.8, 69.5, 68.2, 66.5, 59.0, 56.1, 53.2, 44.5.

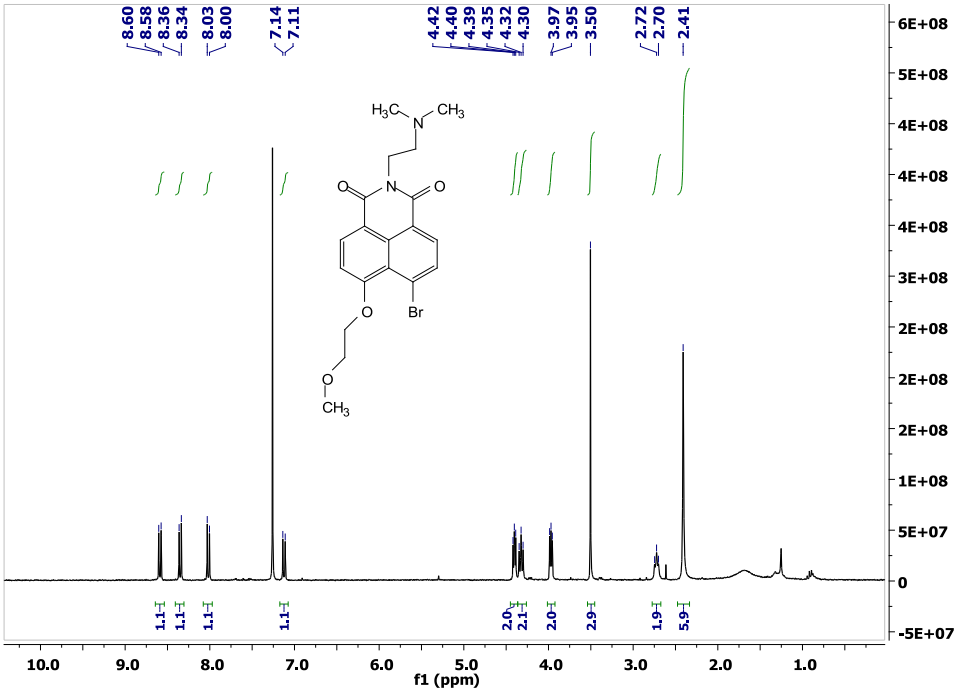

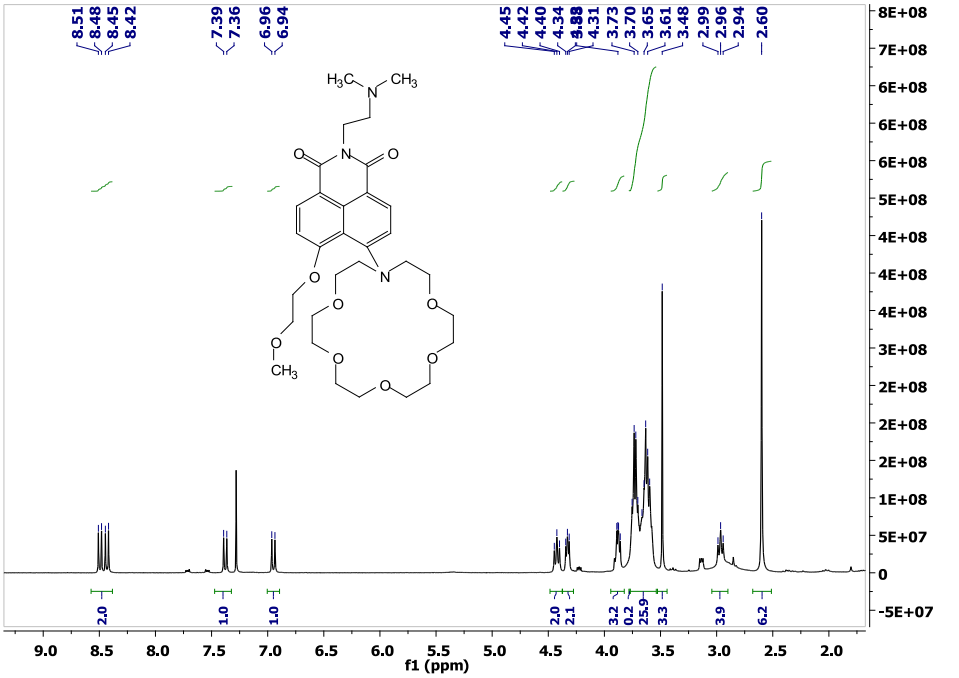

9.2.2 Preparation of the stock solution

In the sweat, the main components are K^+ salt, Na^+ salt, lactic acid and urea while Ca^{2+} salt is in higher concentration than that of trace amount metals Cu^{2+}, Fe^{2+}, Mg^{2+} and Zn^{2+}. Therefore, the concentration of the stock solution for K^+ salt, Na^+ salt, lactic acid and urea are all 1.0 M. The concentrations of the stock solution are 0.1 M for Ca^{2+} and 0.01 M for Cu^{2+}, Fe^{2+}, Mg^{2+} and Zn^{2+} salt. The added volumes for these components are between 3 μL to 30 μL.

9.3 Principal outcomes

9.3.1 Synthetic route for TM-1

The synthetic route for the target molecules TM-1 is displayed in **Scheme 9.3.1**. The NDI anhydride reacted with NBS to introduce the dibromo compound **M1**, which was used directly in the next step and reacted with the *N*,*N*′-dimethylethylenediamine to form **M2** in 55% yield. To obtain **M3** are needed to selectively introduce one alkoxyl group onto **M2**, thus, the amount of base K_2CO_3 was strictly controlled to be 1.0 eq. It turned out that **M3** could be obtained in 71% yield but a byproduct with two alkoxyl groups was also present in the reaction. The mixture of **M3** and 1-aza-18-crwon-6 was refluxed under argon for 24 h. The target molecule TM-1 could be obtained in 89% finally although small amount of the reactant **M3** unreacted. The structure of TM-1 was confirmed by ^1H NMR and ^{13}C NMR respectively.

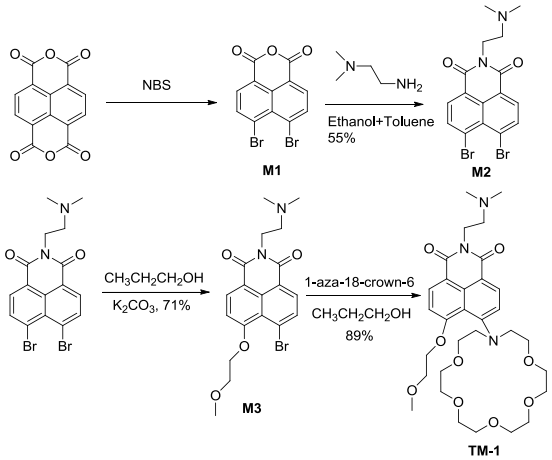

Scheme 9.3.1 Synthetic route for probe TM-1

9.3.2 UV-Vis and fluorescence characterization

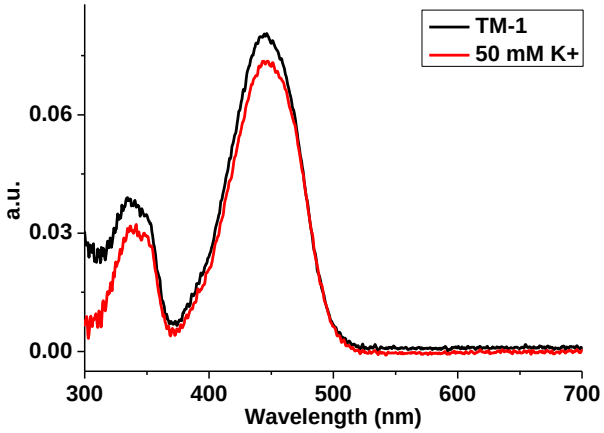

Fig. 9.3.2.1 UV-Vis absorption of TM-1 before and after adding of K^+ (10^{-5} M in DMSO)

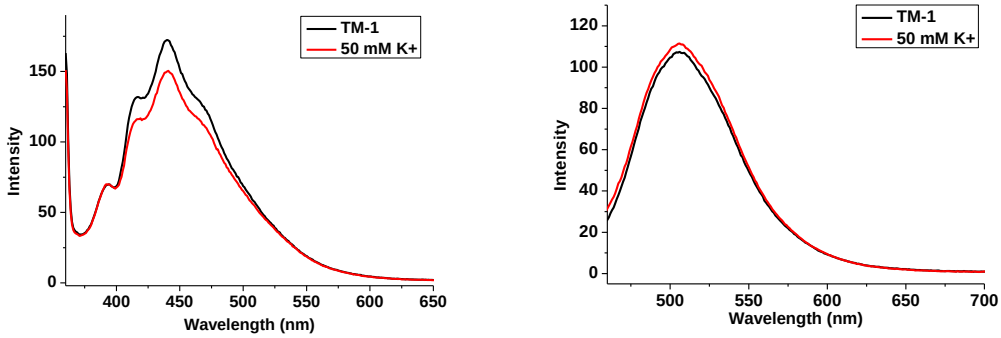

Fig. 9.3.2.2 Fluorescence spectra of TM-1 before and after adding of K^+ (10^{-5} M in DMSO), left: excited at 350 nm; right: excited at 450 nm

The UV-Vis absorption of TM-1 before and after adding K^+ (10^{-5} M in DMSO) is displayed in **Fig. 9.3.2.1**. Before addition of K^+ ion, TM-1 exhibited strong absorption between 400 and 500 nm accompanying by another absorption band between 300 nm and 350 nm. After addition of K^+ ion, the peak intensity decreased slightly, which may indicate weak coordination of K^+ to TM-1. Interestingly, as shown in **Fig. 9.3.2.2**, with different excitation wavelengths, TM-1 displayed different emission spectra. When setting the excited wavelength to 350 nm, the emission spectrum displayed a peak ranging from 360 nm to 550 nm with several shoulders while setting the excitation wavelength as 450 nm, it produced emission ranging from 450 nm to 600 nm, which

indicates that TM-1 may contain different relaxation pathways other than the most common pathway (from the lowest vibrational level of the first excited state to ground state) to emit. Meanwhile, this phenomenon indicated that different excited wavelength might be chosen for different detection requirements. However, after adding K^+ ion, there was only a slightly change in the spectra, which corresponded with the change in the UV-Vis absorption spectrum.

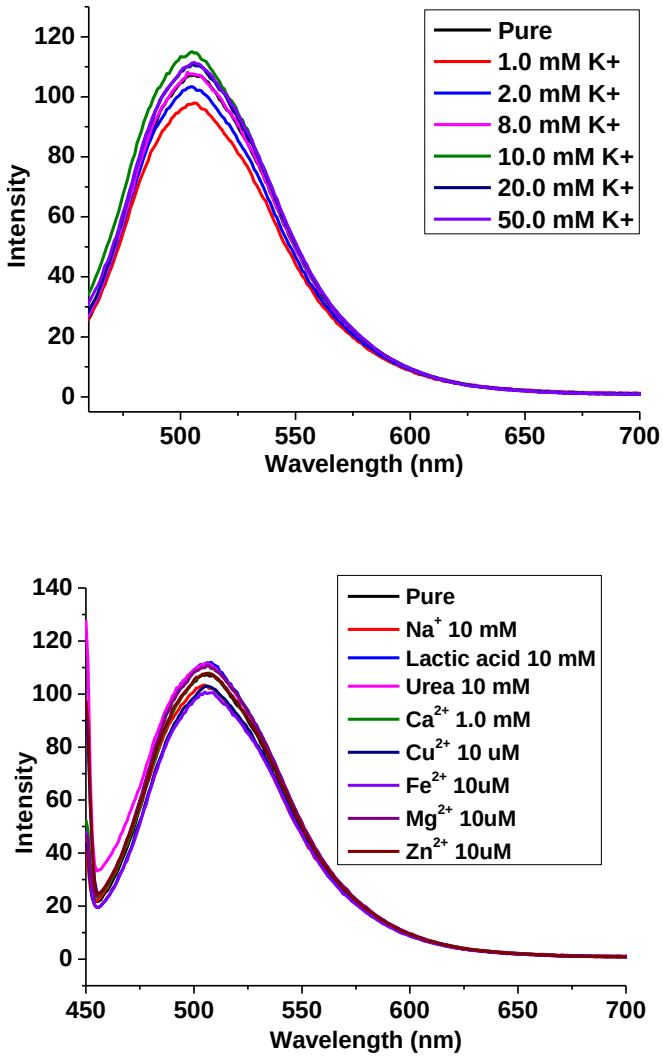

Fig. 9.3.2.3 Fluorescence spectra of TM-1 before and after adding different conc. K^+ and different components (10^{-5} M in DMSO)

The fluorescence spectra of TM-1 before and after adding different concentrations of K^+ and different components (10^{-5} M in DMSO) are displayed in **Fig. 9.3.2.3**. It can be seen

that with different concentrations of K^+, there was a fluorescence intensity variation of about 20%, which might indicate weak coordination of K^+ ion to TM-1 due to the low steric effect of the $CH_3CH_2CH_2O$- group. Further modification of this kind of probe is needed in future work. Meanwhile, the influence of the coexisting components in the sweat on the detection of K+ ion was also tested. Fortunately, there was negligible change of the fluorescence intensity, which indicated that these components might have negligible effect on K+ ion probe.

9.4 Conclusion

In summary, a K^+ probe TM-1 was designed and synthesized based on naphthalimide building block and 1-aza-18-crown-6. It displayed maximum absorption around 500 nm and weak fluorescence in DMSO solution. Interestingly, with different excitation wavelength, this probe exhibited different emission spectra. Although it turned out that this probe has weak response to K^+ in sweat, the other components in sweat, such as lactic acid, urea and Na^+, were proved to have no influence on this probe. It is inferred that the low efficiency for probing K^+ might result from the low steric effect and further improvement of the probe should be possible.

References

[1] Z. Sonner, E. Wilder, J. Heikenfeld, G. Kasting, F. Beyette, D. Swaile, F. Sherman, J. Joyce, J. Hagen, N. Kelley-Loughnane and R. Naik, *Biomicrofluidics*, **2015**, 9 (3), 031301

[2] J. Yin, Y. Hu and J. Yoon, *Chem. Soc. Rev.*, **2015**, 44, 4619-4644.

[3] H. R. He, M. A. Mortellaro, M. J. P. Leiner, R. J. Fraatz and J. K. Tusa, *J. Am. Chem. Soc.*, 2003, **125**, 1468-1469.

[4] S. Ast, T. Schwarze, H. Muller, A. Sukhanov, S. Michaelis, J. Wegener, O. S. Wolfbeis, T. Korzdorfer, A. Durkop and H. J. Holdt, *Chem.-Eur. J.*, 2013, 19, 14911-14917.

[5] Z. Sun and J. S. Wu, *J. Org. Chem.*, **2013**, 78, 9032-9040.

[6] M. Vonlanthen and N. S. Finney, *J. Org. Chem.*, **2013**, 78, 3980-3988.

Chapter 10

Summary/Hypotheses Proven and Disproven/Future Works

Firstly, the contents of the thesis are summarized. A concise and efficient method has been discovered to synthesize n-type building block hetero-aromatic diones through a one-step F-C reaction. Several novel OSCs acceptors based on fullerene and non-fullerene materials have been designed and synthesized. Their basic physicochemical properties and photovoltaics properties have been studied in-depth. It has been discovered that the absorption range, the energy level, the electron mobility and more importantly, the morphology all play crucial effects on the final PCE result for the device. Moreover, a novel K^+ *probe based on n-type materials naphthalene has been designed and synthesized within four steps and its response to potassium ions investigated. Secondly, the extent to which the hypotheses have been proven or not is discussed. For most hypotheses, they are proved to be valid and the expected results were obtained. It seems that non-fullerene acceptor will replace fullerene acceptor sooner or later due to the intrinsic limitation of fullerene. It is still high desirable to develop an efficient* K^+ probe. *Finally, the opportunities and the ideas for future works are proposed. For example, 3-D non-fullerene acceptor may be a possible way to further design the next generation acceptor and NTI is demonstrated to be a powerful building block and further effort can be focused on this field.*

10.1 Summary

In this thesis, I mainly focus on the design and synthesis of novel n-type organic semiconductor materials, including building blocks, small molecules etc, for OSCs acceptors. My Ph. D research can be briefly divided into several parts as shown below.

Firstly, I focused on developing novel building blocks for OSCs acceptors. The intramolecular double Friedel–Crafts acylation strategy was utilized in approaching different types of novel fused heteroaromatic diones, which are promising building blocks for various derivatives with 16%–85% yield.

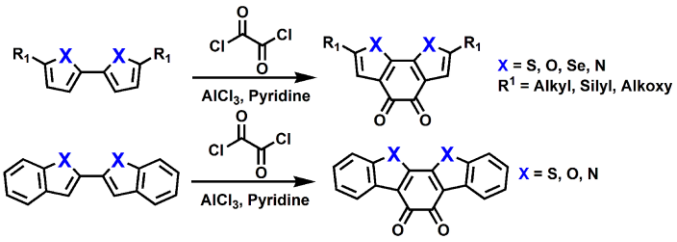

Secondly, I focused on fullerene based OSCs acceptors. I designed and synthesized two novel C_{60} derivatives with absorption group based on quinoxaline, TQMA and TQBA. It turns out that the mono-adducted TQMA exhibits the best PCE results of 2.8% with better film morphology while bis-adducted TQBA shows much poorer performance with the donor P3HT.

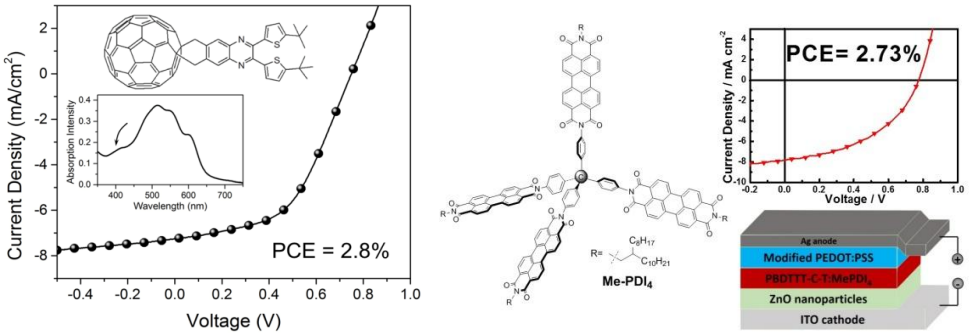

Thirdly, due to the difficulty of functionalizing C_{60} to obtain novel fullerene acceptors, I switched to develop novel non-fullerene acceptors based first on PDI. Considered that fullerene may have isotropic charge transport due to its 3D ball-like shapek, I designed and synthesized a new perylene diimide (PDI)-based acceptor Me-PDI_4 with tetrahedral configuration. It has complementary absorption with donor materials PBDTTT-C-T, amorphous film morphology and suitable energy level and shows a moderate PCE of 2.73%. After studying the carrier transport properties with space charge limited current

(SCLC) method, it turns out that the unbalanced electron-hole mobility may be responsible for the moderate PCE result.

Fourthly, I focused on the non-fullerene acceptors based on NDI. 1) I synthesized a novel building block NTI generated from core-extended NDI, which has α thiophene vacant position for further functionalization. Though coupling, I prepared a series of NTI dimer and trimer, which showed not only good electron mobility 0.4 $cm^2V^{-1}s^{-1}$, but also showed promising PCE results about 2.5%. 2) Through simple one-step thionation of NDI, we obtained a series of S-NDI compounds with enhanced absorption and mobility as well as suitable mobility. However, the PCE is very poor (<0.1%) due to the extremely poor morphology (too large domains). This method provides a useful way for further OSCs acceptor development in the future.

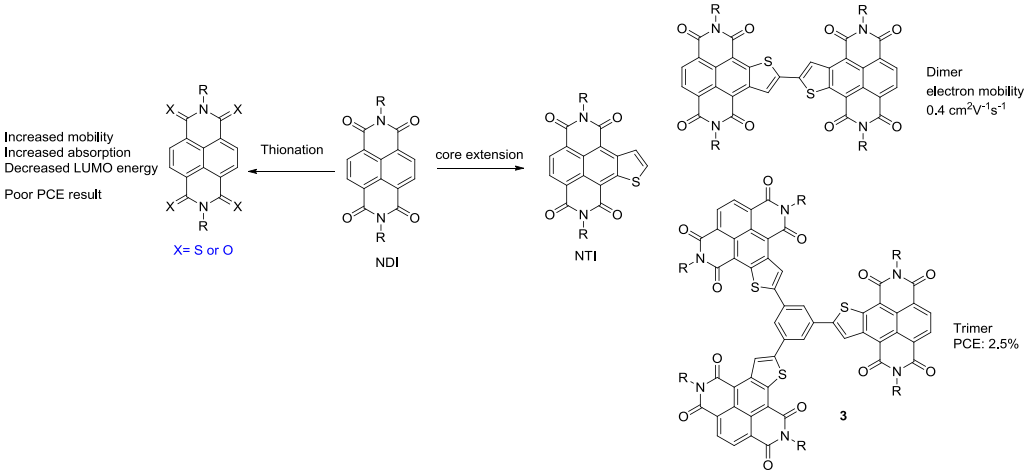

Finally, I designed and synthesized a K^+ probe TM-1 based on naphthalimide building block and 1-aza-18-crown-6 within four steps. Interestingly, with different excitation wavelength, this probe exhibited different emission spectrum. Although it turned out that this probe has weak response to K^+ in sweat, however, the other components in sweat, such as lactic acid, urea and Na^+, were proven to have no influence on this probe. I inferred that the low efficiency for probing K^+ might result from the low steric effect and further improvement of the probe is suggested below.

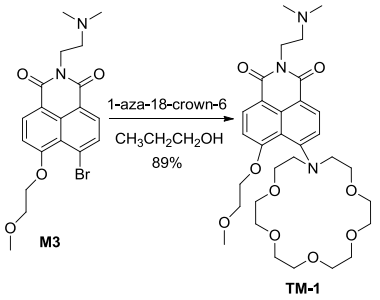

10.2 Hypotheses proven/disproven and future work

10.2.1 Design and synthesis of novel heteroaromatic diones

For organic semiconductors materials, not only using the known building block to synthesize the efficient desired molecules for application in OSCs, OFET etc is important, but also discovering versatile novel building block through simple reaction or cheap catalysis for large scale accumulation and wide application is also urgent and meaningful. In this work, as discussed above, I employed double Friedel–Crafts acylation strategy in approaching different types of novel fused heteroaromatic diones. For this work, there are several highlights:

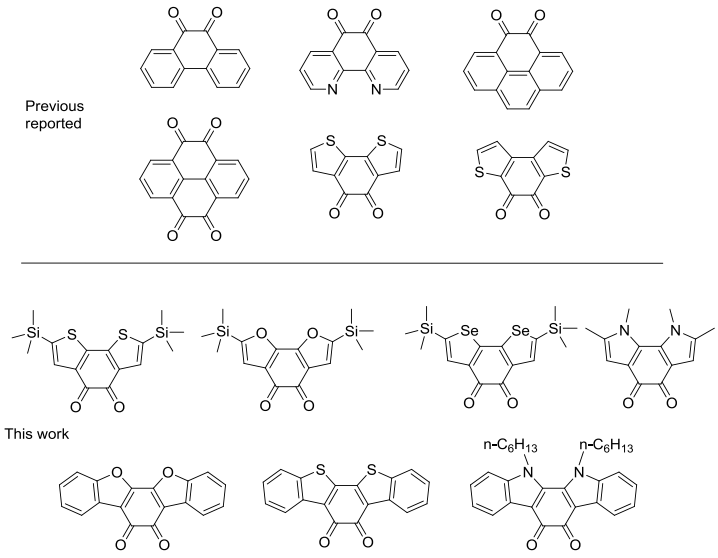

1) I synthesized five more novel diones building blocks in this work.

2) Compared with the former reported diones obtained through different methods, the reported diones in this work are all obtained through the same simple Friedel–Crafts acylation reaction.

3. Different groups could be readily introduced on these building blocks to adjust the solubility. Meanwhile, the sily group can be change to Br group for further functionalization.

Therefore, for future work:

1) To synthesize the derivatives building block based on the published one.

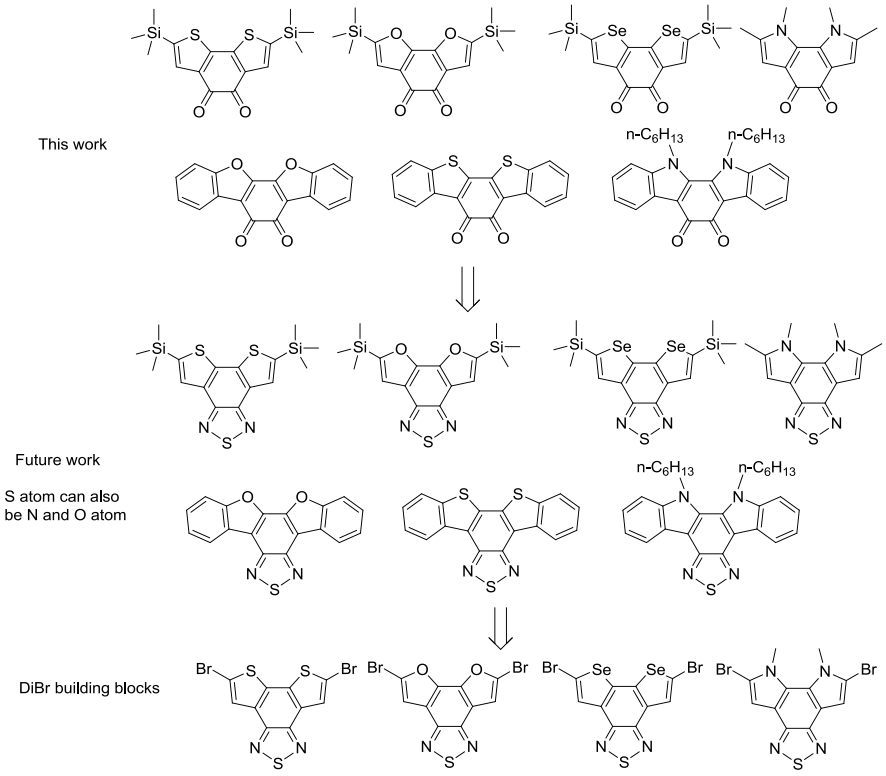

Fig. 10.2.1 Designed molecules for future work about diones

However, there are several points that need to improve for this reaction.

1) The selectivity is poor and the yield ranges from low to moderate. Due to the similar reaction activity of the 3,4 positions of thiophene, there are a lot of intermolecular by product for this reaction. Thus, one possible way to improve that is to decrease the reaction activity of the catalysis $AlCl_3$ and change to other bulky or low reaction activity aluminum catalysis.

2) The second problem for this reaction is that for electron-withdrawing groups, the reactions do not proceed due to the low reaction activity of the substrates.

10.2.2 Fullerene-based acceptor TQMA and TQBA

In this part, I focused on design and synthesis of fullerene-based acceptor. After studying the literatures, to enable superior performance for the OSCs, it was demonstrated that there are generally two methods to modify the C_{60}: one is to widen the absorption spectrum for the acceptor and the other is to increase the LUMO energy of the acceptor. I hypothesized that by combining these two strategies, an efficient fullerene-based acceptor can be obtained. Thus, I designed and synthesized two novel C_{60} derivatives with absorption group based on quinoxaline, mono-adducted acceptor TQMA and bis-adducted acceptor TQBA.

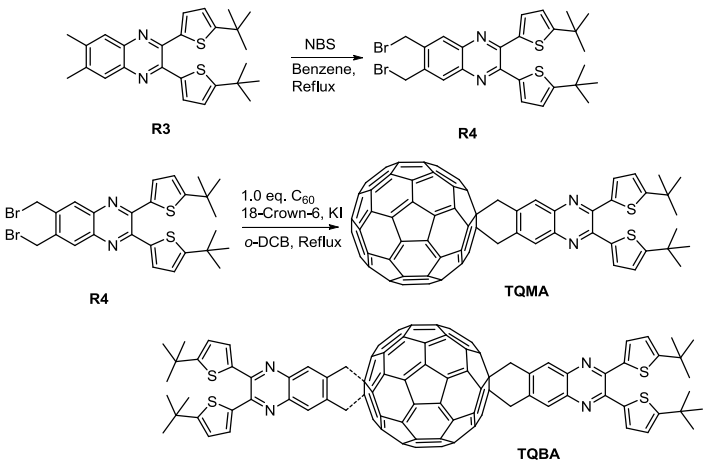

For TQMA, it shows PCE result of 2.8% with donor P3HT while controlled group obtains result of 4.1% by taking $PC_{61}BM$ as the acceptor. For TQBA, much poorer performance was obtained. This work demonstrates that there are some disadvantages of these acceptors.

1. Introducing the absorption group on the fullerene does not guarantee better efficiency. Firstly, although the UV-vis absorption of separated solution at the same concentration for TQMA and TQBA is apparently better than $PC_{61}BM$ but for films, the actual absorption enhancement is not so obvious. Secondly, after introducing the absorption group, it decreases absorption beyond 450 nm area and hence and lowers the absorption for the blend films.

2. For TQBA, maybe due to the too bulky property of the acceptor, the absorption group not only affects the absorption, but also affects other device parameters, such as the

electron mobility and morphology etc, which leads to adverse effects on the final device performance.

3 During preparation of dibromo precursor R4, it is hard to control the reaction since tribromo precursor and monobromo precursor are simultaneously produced. Thus, the separation becomes difficult.

From the above discussion, it seems that it is not so easy to design an efficient fullerene acceptor by combining the two above-mentioned strategies and too many parameters will change at the same time. In addition, the cost of C_{60} is not cheap and the synthesis is difficult. Thus, searching for more efficient non-fullerene acceptor is a better way.

10.2.3 Non-fullerene acceptor Me-PDI$_4$

I designed and synthesized a novel perylene diimide (PDI)-based acceptor Me-PDI$_4$ with tetrahedral configuration. It has complementary absorption with donor materials PBDTTT-C-T, amorphous film morphology and suitable energy level and shows moderate PCE result of 2.73%. After studying the carrier transport properties with space charge limited current (SCLC) method, it turns out that the unbalanced electron-hole mobility may be responsible for the moderate result of PCE.

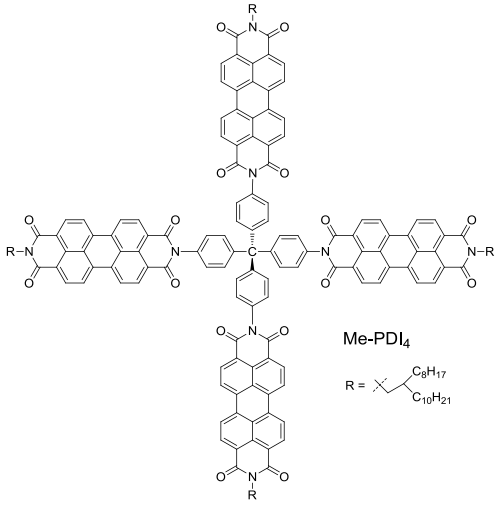

The hypothesis for this work is to design and synthesize a novel 3-D non-fullerene acceptor to mimic the behavior of the fullerene acceptor, which has good isotropic electron transfer capability, amorphous film and miscibility with donor materials etc. This acceptor has the following several highlights:

1. Complementary absorption with donor materials and suitable LUMO energy level for a high V_{oc} (0.77 V).

2. Better film morphology. As is known, controlling the aggregation of PDI unit is the first task in designing a non-fullerene acceptor based on PDI. In this work, the aggregation is perfectly suppressed and the film is amorphous. Even after thermal annealing, the change is not great, which demonstrates the efficiency for 3-D structure non-fullerene acceptor to inhibit the aggregation property.

3. The electron mobility is not too bad in 3-D structure with magnitude of 10^{-5} or 10^{-6}

For further developments of these acceptors, there are basically two methods:

1) Investigate the effects of different alkyl chains.

2) Change the core to triphenylamine or octo-phenylamine POSS core.

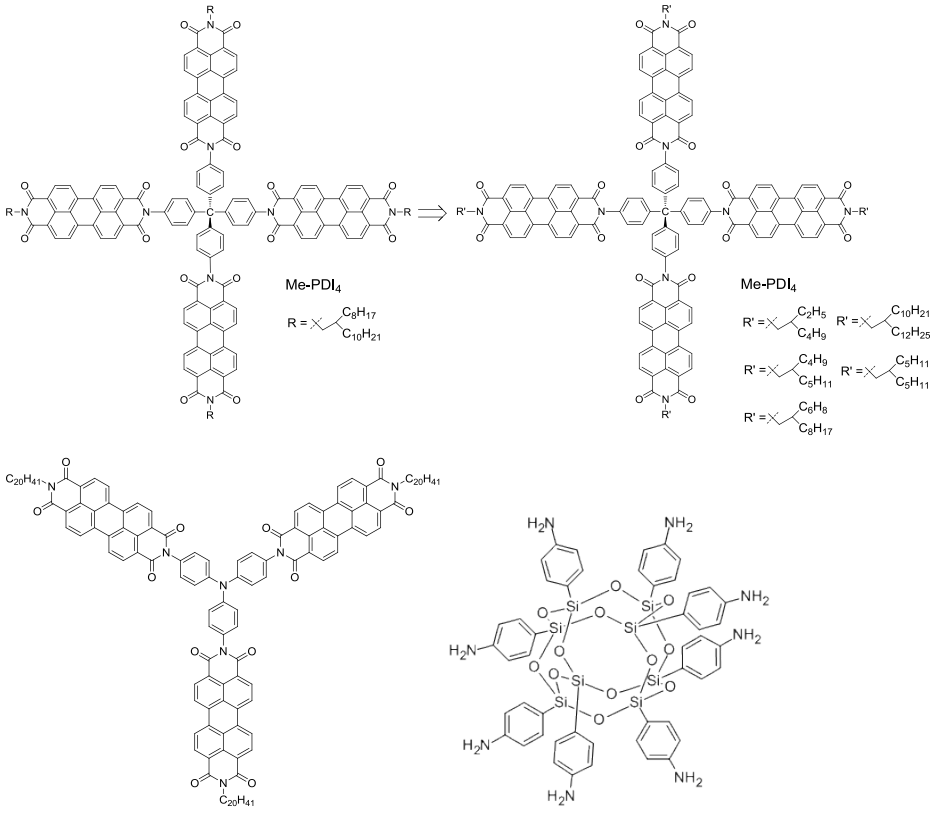

Fig. 10.2.3 Designed molecules for future work using PDI

10.2.4 NTI and S-NDI

In this work, a novel NDI-core-extended building block NTI was developed and though coupling, we synthesized a series of NTI dimer and trimer, which shows not only good electron mobility 0.4 $cm^2V^{-1}s^{-1}$, but also show promising PCE results about 2.5%.

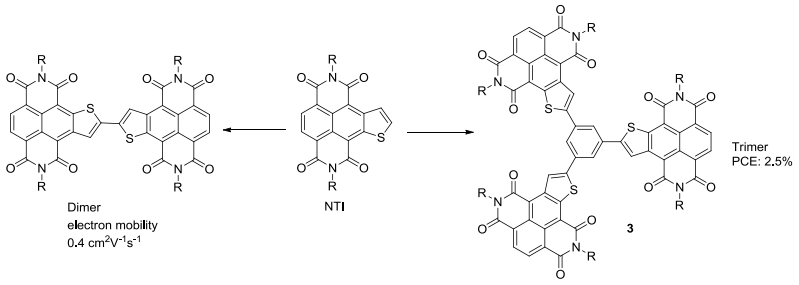

The hypothesis for this work was to design and synthesize a novel building block that shows similar properties as PDI. The new NTI building block exhibits several highlights;

1) Enhanced absorption (λ_{onset} = 500 nm) and suitable LUMO energy (–3.9 eV). For comparison, PDI (λ_{onset} = 540 nm) and LUMO energy (–4.0 eV)

2) Planar structure to ensure good electron mobility

3) One vacant α thiophene position for further functionalization. And the trimer shows PCE of 2.5% with donor PTB7-Th.

Thus, NTI will be the key project for future work.

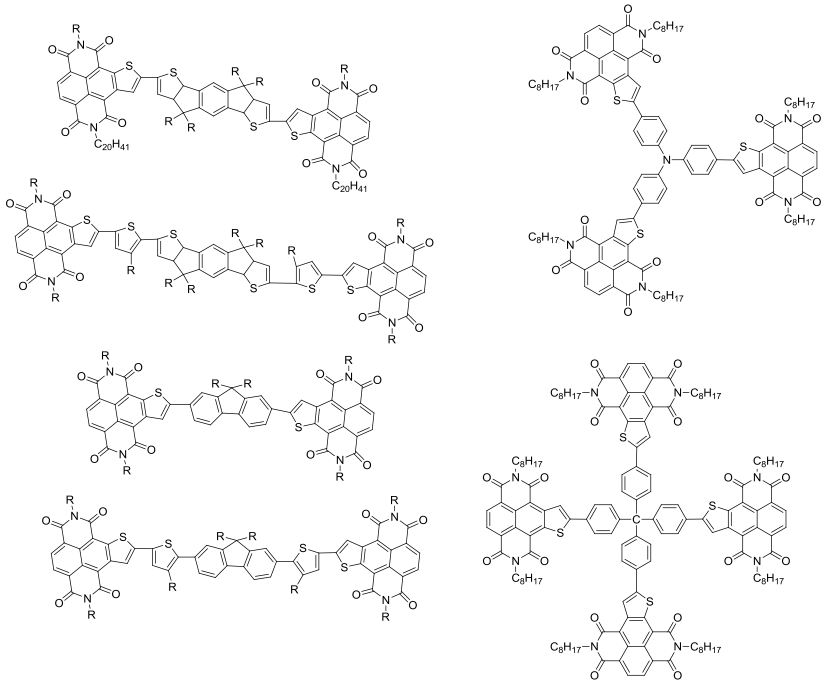

Fig. 10.2.4.1 Designed molecules for future work using NTI

For S-NDI molecules, the hypothesis is similar with that of NTI, the designed building block with similar property to PDI. For the S-NDI compounds, it has the following highlights:

1. Controlled absorption range from 400 to 600 nm and energy levels from –3.8 eV to –4.2 eV.
2. Increased mobility

However, the PCE result is very poor due to the bad morphology, designing a twisted more complex structure may be one possible way to solve that.

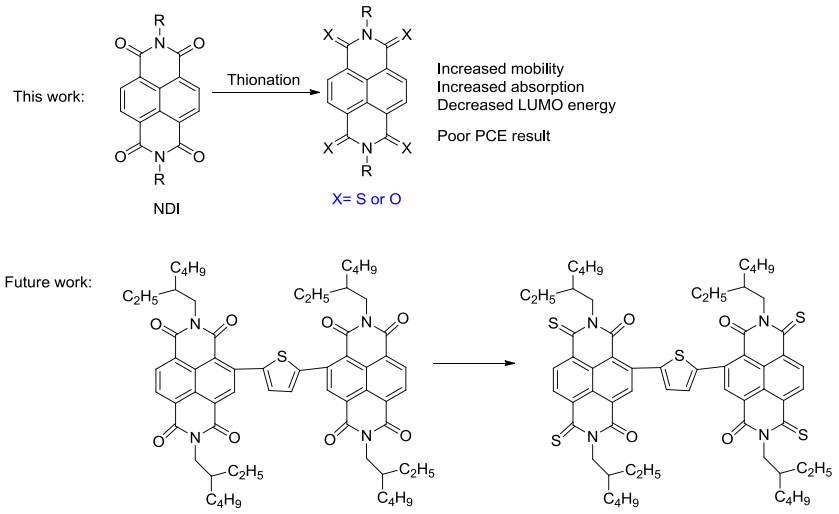

Fig. 10.2.4.2 Designed molecules for future work about S-NDI

10.2.5 Probe TM-1 for K^+ ion

In this thesis, I designed and synthesized the K^+ probe TM-1 based on the concept of combining the naphthalimide and 1-aza-18-crown-6 with a steric alkoxyl group. In addition, I wanted to make the synthetic route not lengthy. It turned out that TM-1 had weak coordination force with K^+ ion maybe due to the weak steric effect of the alkoxyl group. Thus, for the future work, the first molecule so suggested is the molecule TM-2 as displayed below, which may have higher coordination force with K^+ compared with TM-1.

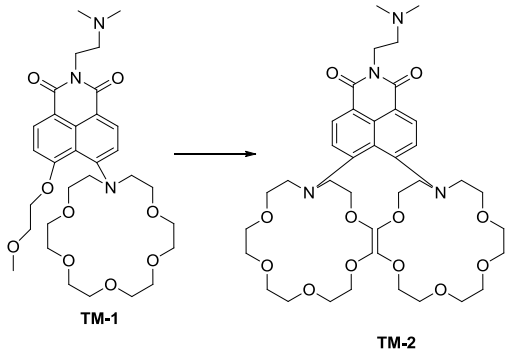

Fig. 10.2.5 Designed molecule for future work about K^+ probe TM-2